# Cavity Optomechanics in Photonic and Phononic Crystals: Engineering the Interaction of Light and Sound at the Nanoscale

Thesis by

Matt Eichenfield

In Partial Fulfillment of the Requirements

for the Degree of

Doctor of Philosophy


California Institute of Technology

Pasadena, California

2010

(Submitted October 19, 2009)

# Abstract

The dynamic back-action caused by electromagnetic forces (radiation pressure) in optical and microwave cavities is of growing interest. Back-action cooling, for example, is being pursued as a means of achieving the quantum ground state of macroscopic mechanical oscillators. Work in the optical domain has revolved around millimeter- or micrometer-scale structures using the radiation pressure force. By comparison, in microwave devices, low-loss superconducting structures have been used for gradient-force-mediated coupling to a nanomechanical oscillator of picogram mass. In this thesis, two different nanometer-scale structures that use combinations of gradient and radiation pressure optical forces are described theoretically and demonstrated experimentally. These structures merge the fields of cavity optomechanics and nanomechanics into nano-optomechanical systsms (NOMS).

The first device, the Zipper optomechanical cavity, consists of a pair of doubly-clamped nanoscale beams separated by approximately 100 nanometers, each beam having a mass of 20 picograms and being patterned with a quasi-1D photonic crystal bandgap cavity. The optical mode of the coupled system is exquisitely sensitive to differential motion of the beams, producing optomechanical coupling right at the fundamental limit set by optical diffraction. The mechanical modes of the beam probed with a background sensitivity only a factor of 4 above the standard quantum limit, and the application of less than a milliwatt of optical power is shown to increase the mechanical rigidity of the system by almost an order of magnitude.

The second device focuses on just one of the doubly-clamped nanoscale beams of the Zipper. We show that, in addition to a photonic bandgap cavity, the periodic patterning of the beam also produces a phononic bandgap cavity with localized me-

chanical modes having frequencies in the microwave regime. We call these photonic and phononic crystal bandgap cavities optomechanical crystals. Because the optical and mechanical modes occupy a volume more than 100,000 times smaller than the volume of a single human cell, the optomechanical interaction in this system is again at the fundamental limit set by optical diffraction. The miniscule effective volume of the mechanical mode corresponds to effective motional masses in the femtogram regime, which, coupled with the enormous optomechanical interaction and high optical and mechanical quality factors, allows transduction of microwave-frequency mechanical motion nearly at the standard quantum limit, with the standard quantum limit easily within reach with simple modifications of the experimental apparatus. The combination of the small motional mass and strong optomechanical coupling allows each trapped photon to drive motion of an acoustic mode with a force more than 15 times the weight of the structure. This provides a powerful method for optically actuating microwave-frequency mechanical oscillators on a chip, and we demonstrate an on-chip phonon laser that emits over 1012 microwave-frequency phonons per second with a ratio of frequency to linewidth of 2 millioncharacteristics similar to those of the first optical lasers. With the ability to readily interconvert photons and microwave-frequency phonons on the surface of a microchip, new chip-scale technologies can be created. We discuss the future of optomechanical crystals and provide new methods of calculating all the otptomechanical properties of the structures.

# Acknowledgements

*If I have seen a little further it is by standing on the shoulders of Giants.* –Isaac Newton, in a letter written to Robert Hooke, 1676.

Figure 1: Cedalion standing on the shoulders of Orion, from *Blind Orion Searching for the Rising Sun*, by Nicolas Poussin, 1658. Metropolitan Museum of Art.

I came into the Painter lab after many people had already poured their blood, sweat, and tears into developing a thriving research program. Oskar, together with

Kartik Srinivasan, Paul Barclay, Matt Borselli, Tom Johnson, Raviv Perahia, Jessie Rosenberg, and Chris Michael built the cleanroom, developed all the processing steps necessary to make nanoscale optical structures, perfected the numerical modeling of optical nanostructures, made every tapered waveguide coupler I ever used, built optical testing setups, and wrote all the code necessary to automate measurements. By the time I joined the group, we were in a stage where ideas could be turned into testable devices in a matter of hours. The amount of work it took to get to that point is staggering, and I owe each and every one of the group members that were senior to me a debt of gratitude that I will, unfortunately, never really be able to repay. I can only say that any success that I have had is every bit as much theirs.

Jasper Chan and Ryan Camacho deserve very special thanks. They came into the lab at a critical time, and none of what I accomplished after their arrival would have been possible without them.

Thanks also to the rest of the Painter group: Qiang Lin, Thiago Alegre, Amir Safavi-Naeini, Jeff Hill, Alex Krause, Justin Cohen, and Dan Chao.

I am indebted to Professors Kerry Vahala, Keith Schwab, Julia Greer, John Dabiri, Chiara Daraio, and Ken Libbrecht. Every one of you has given me ample amounts of your time simply because you were willing to listen and help. I hope I get a chance to repay you somehow.

TJRJ and CPM, if I had to choose to spend four years in a cramped office with anybody, it'd be you two. You are two of the best people I've ever met, and you emit no foul odors. Thank you for putting up with me and keeping me laughing and smiling for the bulk of my graduate career. It turns out you don't think too much about how much time you spend with someone when you're having a good time; so, without my even realizing it, you became my best friends and left before I ever even realized I should be thankful for our time together. I realize it now though and already miss having you guys around.

I wouldn't have done any of this if it weren't for Dave Shelton and Scott Panik. Thanks also to the rest of my family at UNLV: Len Zane, Changfen Chen, Jim Selser, Lon Spight, Steve Lepp, Bernard Zygelman, John Kilburg, Bill O'Donnel, etc., etc...

Dan Koury, Tony Roy, Justus Brevik, Bodhi Sansom, Derek Rinderknecht, Shave Henry, Mike Shearn, Sameer Walavalkar, Will Ford, Lenny Lucas, Eric Brown, Auna Moser, Matt Wahlrab, Jen Dionne, and Jason McClure: you all get a Ph.D. in Awesome (and most of you have a Ph.D. in something else, anyway).

Much love to my mom, dad, Lynne, grandmas, grandpas, and JDO'B. I was fortunate to grow up in such a loving and supportive environment. Donna Driscoll is my surrogate mom in the Caltech Department of Physics; so she deserves to be in here, too.

To Oskar Painter, I couldn't really ask for a better advisor. You took me into your group with enthusiasm at a time when I was struggling to find my place at Caltech. More than just an advisor, you have been an incredible mentor. You are an amazing scientist, and I made sure to soak up everything you said and did while I was in your group. Without your work and support, there is no way I would be where I am. Nothing I say here can do any justice to how much you did for me, but I hope you know how much I appreciate it all.

# Contents

# List of Figures

# List of Tables

# Chapter 1

# Framework

This thesis dissertation is based on four papers [1–4]. These papers describe theoretical and experimental work in cavity optomechanics as they relate to various kinds of photonic crystals, especially patterned nanoscale beams. In this introduction, I hope to briefly describe the significance of this work and how it fits into the fields of cavity optomechanics and the study of mesoscopic mechanical oscillators [5–7]. I will then present some background necessary to understand the optics, mechanics, and optomechanics of these systems.

## 1.1 Introduction

The significance of this work to the field of cavity optomechanics and mesoscale mechanical oscillators close to the ground state is many-fold, but I will try to give a short summary here. As I am trying to highlight the merit of our work, I will clearly focus on the aspects that frame the systems of this work in the best possible light. This is not meant to disparage other systems, as the variety and complexity of all these systems and the problems they are being used to solve allow for many ways to skin virtually every mesoscopic optomechanical cat.

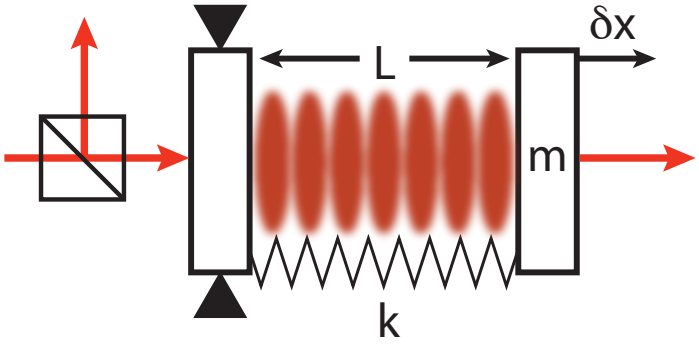


Figure 1.1: Fabry-Perot canonical optomechanical system.

### 1.1.1 A Very Brief Description of the Sensitivity of Optomechanical Systems

Consider the Fabry-Perot cavity in Fig. 1.1 with one of its mirrors attached to a spring. We will imagine using this cavity as both a force sensor and a displacement sensor. The cavity supports many optical modes with frequencies down to the fundamental mode of frequency $\nu_o = c/2L$, where $L$ is the length of the cavity (the spacing between the mirrors). For a displacement of one of the mirrors, $\delta x$ (along the axis of the cavity), the frequency of the optical mode will shift by $\nu_o \delta_x / L = \delta\nu_o$. This is the essence of optomechanical coupling: a mechanical displacement of the cavity induces a change in the state of the light. In this case, one can see that to maximize the effect of a given $\delta_x$, one wants to use the largest possible frequency[1] and the smallest possible cavity length.

The frequency shift of the optical cavity induced by the optomechanical coupling will cause photons in the cavity to accumulate a phase shift proportional to the time the photons spend in the cavity[2], $\tau$. Since our method of measuring displacement will involve some form of mixing theses phase-shifted photons from the cavity with reference photons to measure their interference, we want this accumulated phase

[1]Consider that the wavelength of light is our "ruler" with which we measure displacements. The smaller the wavelength of light (i.e., the higher the frequency), the finer the tick marks on our ruler, and, thus, the greater our ability to measure changes in length.

[2]If photons travel the extra length every round trip, then we want to increase the number of round trips–and thus the time–that the photons spend in the cavity

shift to be as large as possible. The photon lifetime, $\tau$, is related to the *quality factor*, $Q$, of the optical resonator by $2\pi\nu_o\tau = Q$. For the Fabry-Perot cavity with vacuum between the mirrors, the only losses occur at the mirrors themselves; thus, lengthening the cavity increases $Q$ and exactly cancels the corresponding reduction in optomechanical coupling, making the displacement sensitivity independent of length[3] However, for monolithic optical cavities, the losses are often dominated by absorption and scattering in the material that guides the light; thus, for a monolithic cavities, $Q$ is often independent of the length. When this is the case, clearly the displacement sensitivity increases as the length of the cavity decreases. This is the motivation behind nanoscale cavities, where very high optical quality factors can be created in very small (often diffraction-limited) optical resonators. This provides extremely high displacement sensitivity.

A good force sensor is simply a good displacement sensor with a high force responsivity. Thus, we want to keep all the properties that made the cavity optomechanical system a good displacement sensor (small $L$, large $\nu_o$, large $Q$) and add force responsivity. If we consider the force responsivity of a simple harmonic oscillator driven by an impulse or sinusoidal external force, then we can see that we want to minimize the inertial mass of the system[4], $m_{\text{eff}}$, minimize the mechanical stiffness, and minimize the mechanical energy loss rate. Minimizing $m_{\text{eff}}$ is most simply accomplished by reducing the size of the system, which has the benefit of simultaneously increasing the displacement sensitivity. Since the mechanical stiffness is proportional to $m_{\text{eff}}\nu_m^2$, where $\nu_m$ is the frequency of the mechanical oscillator, then minimizing $m_{\text{eff}}$ also means the system is less stiff for a fixed frequency. Unfortunately, for the flexural modes of nanostructures that we will actually consider in this work, decreasing the system size almost universally increases the mechanical frequency; i.e., it makes the structure more mechanically stiff. However, for many reasons[5], high-frequency operation is actually desirable. The *best* one can do for a flexural vibration with mechanical

[3]This is what allows for the exquisite sensitivity of the kilometer-scale gravitational wave interferometers, such as LIGO.

[4]The relevant mass is the effective *motional* mass.

[5]Most notably: lowering thermal occupancy for measuring quantum effects and technological applications, where relevant frequencies are typically in the gigahertz regime.

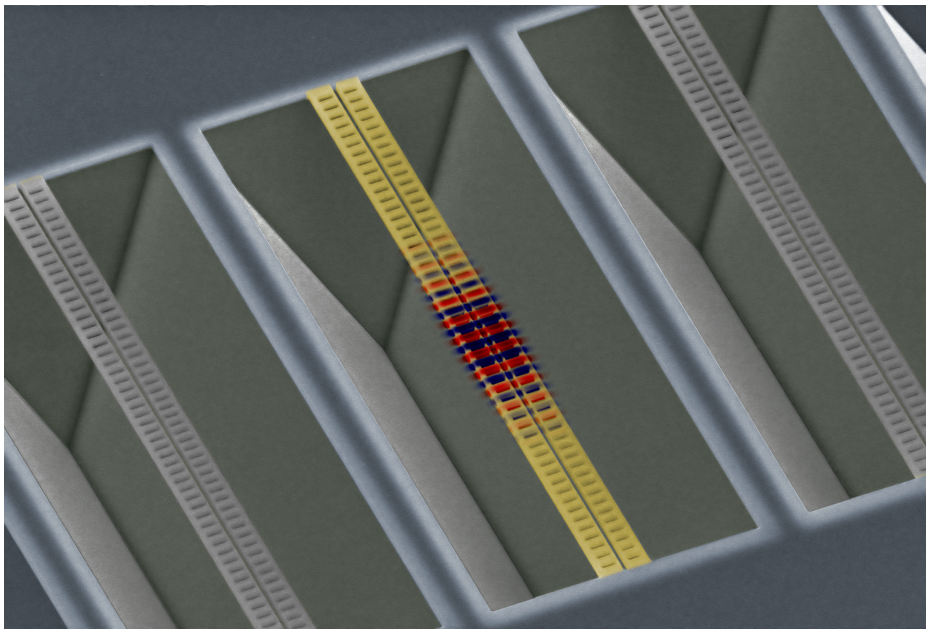

Figure 1.2: SEM image of the "Zipper" optomechanical cavity with the $y$-component of the electric field superposed on the structure.

frequency $\nu_{\mathrm{m}}$ and fixed mass density is to make the size of the system approximately $(\lambda_{\mathrm{sound}}/2)^3$, which is the smallest that the structure can be while still supporting mechanical resonances of wavelength $\lambda_{\mathrm{sound}}$. In addition to making the structure stiff, reducing the system size often *increases* mechanical loss by increasing the fraction of energy in the part of the resonator that contacts the outside world (the structural supports). However, we will show that, in fact, the structure or its supports can often be engineered to avoid these problems by using complete phononic bandgaps, which will thus remove one of the major barriers to reducing system size.

Thus, if we want the penultimate displacement and force sensor in a cavity optomechanical system, we want to make a very small system that can somehow manage to maintain high quality optical and mechanical resonances (low losses). This is a large part of what motivates creating truly nanoscale structures with high-quality optical and mechanical resonances.

### 1.1.2 The Significance of *This* Work

First, in two large jumps, we were able to reduce the effective motional mass of cavity optomechanical systems by more than five orders of magnitude. The state-of-the-art cavity optomechanical system, the microtoroid [5], for several years had the smallest effective motional mass in an optomechanical system: approximately 10 nanograms. Our first serious foray into the field of cavity optomechanics was the "Zipper" (Fig. 1.2), which is a pair of nanoscale beams separated by roughly 100 nanometers, with a photonic bandgap patterned into the beams to localize and store light. This system had an effective motional mass of about 20 picograms, which was an improvement of about 3 orders of magnitude in mass. This was quickly followed by a second "system", the optomechanical crystal, which employed the photonic bandgap cavity of the "Zipper" as a *phononic* bandgap cavity, localizing many acoustic resonances to the same small region in the center of the structure that was previously used to localize light. This localization reduced the mass of the oscillator from the mass of an entire beam (10 picograms) to the mass of just a few of the crossbars in the center, which brought the mass of the system down to about 50 femtograms. Since the system's response to external forces *and* internal radiation pressure forces is inversely proportional to the effective motional mass, this reduction of a factor of 200,000 over the previous state-of-the-art microoptomechanical systems [5–7] dramatically increases the force sensitivity of cavity optomechanical systems.

Next, while reducing the mass of the system by decreasing the system "size", we simultaneously decreased the critical optomechanical length (while maintaining very high optical quality factors). This produced a large increase in the displacement sensitivity, as discussed above. Compared to the microtoroid, this was a decrease in the effective length (and a corresponding increase in the displacement-to-phase transduction) of approximately a factor of 10.

For many measurements, we will show that the sensitivity of the cavity optomechanical system scales inversely with the product $m_{\mathrm{eff}} L_{\mathrm{OM}}^2$, where $L_{\mathrm{OM}}$ is the optomechanical length of the structure (the length of the Fabry-Perot cavity; the radius of

the microtoroid cavity; related to the spacing of the "Zipper" cavity). This makes these systems extremely effective transducers of force and displacement.

The small mass and high sensitivity to motion means that these systems can be used for structures that are much higher frequency than what was previously possible. While gigahertz optomechanical systems had been previoulsy reported [8,9], optomechanical crystals have the potential for quantum-limited motion sensitivity at these high frequencies. As will be discussed in more detail in subsequent chapters, this makes these systems good candidates for observing relatively "hot" objects in their quantum mechanical ground state and opens up many possibilities for technological applications.

Finally, while the field of phononic crystal microstructures and nanostructures is quickly advancing [10], high-frequency operation has been quite limited by electromechanical detection techniques, which involves integration of piezoelectric couplers. Optomechanical crystals allow for low-noise optical measurement of high-frequency phononic crystal waveguides and resonators in any essentially any material with an optical window. In addition, the concepts of dynamical back-action of cavity optomechanics [5] provide methods for manipulating the motion (e.g. amplifying or damping) of phononic crystal systems. By using cavity optomechanical techniques to amplify mechanical motion, optomechanical crystals can be used to produce phonons; by using cavity optomechanical techniques to damp mechanical motion, optomechanical crystals can be used to selectively extract phonons. In the quantum picture, this amounts to the ready interconversion of photons and high-frequency phonons. Since the cavity optomechanical systems demonstrated in this work are planar, chip-scale structures, they (and analogous systems) provide a new novel architecture for the generation, routing, and interaction of photons and phonons on the surface of a microchip.

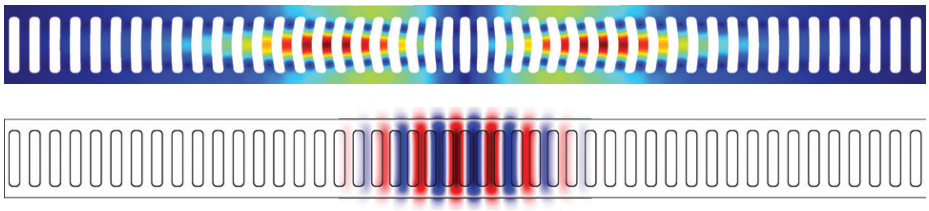

Figure 1.3: Optical (top) and acoustic (bottom) modes of a photonic and phononic crystal nanobeam. The optical mode shown is the fundamental mode of the photonic bandgap cavity. The acoustic mode is a localized "accordion" vibration of the phononic bandgap cavity.

## 1.2 The Optical and Mechanical Systems

Cavity optomechanics involves the mutual coupling of an optical mode to a mechanical mode of a deformable structure. The canonical system is typically a Fabry-Perot cavity with a movable mirror [11] or, more recently, a microtoroid cavity undergoing radial breathing motion [12]. Here, however, we will focus on a nanoscale dielectric beam (or a pair of such beams) suspended on both sides from a large substrate and having a periodic pattern of vertical holes that form a photonic and phononic bandgap cavity[6]. The optical and acoustic modes, examples of which are shown in Fig. 1.3, will be the solutions of the electromagnetic and acoustic wave equations of the structure, and the coupling between them will be determined by a single parameter that characterizes the dispersion of the optical mode due to the displacement of the mechanical mode.

### 1.2.1 Geometry

The general geometry of the photonic and phononic crystal nanobeam is shown in Fig. 1.4(a). A beam of nanoscale cross-section is attached (flush) on both ends to a large substrate of identical material and thickness. The structure is symmetric about the $xy$, $xz$, and $yz$ planes that pass through the center of the structure (which we will also call the origin). The nanobeam, whose geometric parameters are labeled

[6]For many applications, the wavelength of the acoustic mode will be much larger than the periodicity, in which case it will not significantly interact with the holes except to change the mode-averaged mechanical properties of the material

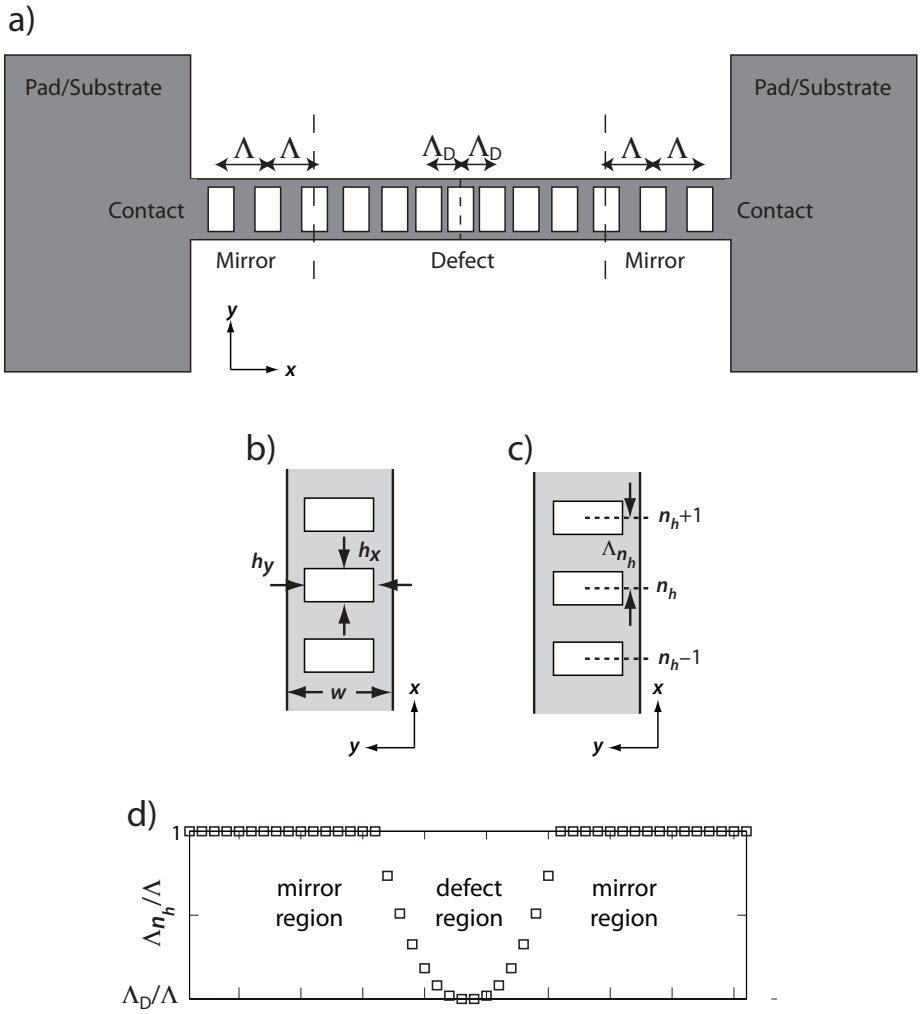


Figure 1.4: **(a)** General geometry of a photonic and phononic crystal nanobeam. **(b)** Spacing of holes in and outside of the defect.

in Fig. 1.4(b), contains a quasi-periodic pattern of $N_{\text{Total}}$ holes with periodicity $\Lambda$, with the center of the structure being a hole ($N_{\text{Total}}$ is odd). For some odd number of holes, $N_{\text{Defect}}$, the spacing between the holes is reduced quadratically around the center hole, such as is shown in Figs. 1.4(c) and (d)[7]. As shown in Fig. 1.4(a), the structure is effectively divided into several portions that will be referred to extensively. The *defect* is the region in the center where the "periodicity" is varied from $\Lambda$ to $\Lambda_{\text{D}}$.

[7]This is just one of many examples of a method for forming a photonic and phononic bandbap cavity in a dielectric nanobeam [13, 14], but it is the only method that will be used in this work. Other methods include changing the hole size, the width, or any combination. In addition, it is also possible to achieve high optical quality factors without a "smooth" defect [13].

The *mirrors* are the two lengths of the structure on either side of the defect with an array of holes with periodicity $\Lambda$. The *substrate* or *pad* is the large (essentially infinite) region on either side of the nanobeam from which it is suspended. The *contacts* are the points where the nanobeam attaches to (or contacts) the substrate. These "portions" of the structure form different regions with qualitatively different electromagnetic and acoustic eigenmodes. The modes of the system are most easily understood by building up the global solution from an understanding of the solutions in these regions, separately.

### 1.2.2 Electromagnetic and Acoustic Eigenvalue Problems

The displacements associated with the deformations of mesoscopic optomechanical systems are generally quite small relative to the structural features, even if the small deformations cause large dispersive shifts of the electromagnetic eigenmodes of the structure. In addition, the frequencies of the optical fields are larger than those of the acoustic fields by at least four orders of magnitude. For these reasons, optomechanical interactions these systems are well-described by a perturbative coupling between the electric and acoustic eigenmodes of the structure in the absence of mechanical motion.

The acoustic displacement field, $\tilde{\mathbf{Q}}(\mathbf{r},t)$, and magnetic induction field, $\tilde{\mathbf{H}}(\mathbf{r},t)$, can both be formulated in terms of eigenvalue problems of their wave equations in the absence of sources. We will assume that the electromagnetic and acoustic properties of the dielectric material are homogenous, locally isotropic (the macroscopic structural geometry clearly breaks the condition of global isotropy), linear, non-piezoelectric, non-magnetic, and free of sources. The fields are also harmonic[8], and only the spatial parts of the fields will be dealt with from here forward; the time-dependence of all fields will be related to their spatial part as $\tilde{\mathbf{F}}(\mathbf{r},t) = \mathbf{F}(\mathbf{r})e^{-i\omega t}$.

[8]Even losses, spatially dependent or otherwise, can be treated as a perturbation on the lossless, harmonic fields, as long as they are not too large. However, we will use numerical techniques to calculate the self-consistent solutions including losses non-perturbatively when we turn to the question of mechanical losses in defect modes of phononic crystals.

#### 1.2.2.1 Acoustic Eigenvalue Problem

Under the above conditions, the acoustic displacement field satisfies the eigenvalue equation [15]

$$\nabla \cdot \left(\mathbf{c} : \nabla_s \mathbf{Q}(\mathbf{r})\right) = -\rho \Omega_{\mathrm{m}}^2 \mathbf{Q}(\mathbf{r}) \,, \tag{1.1}$$

where $\rho$ is the mass density, $\Omega_m$ is the angular frequency of the acoustic field, $\nabla_s \equiv \left(\nabla + \nabla^T\right)/2$ is the symmetric gradient operator, the colon denotes the double scalar (a.k.a. double dot) product of a fourth rank and a second rank tensor, and $\mathbf{c}$ is the (fourth rank) elasticity tensor.

In reduced Voigt notation, the differential operators and elasticity tensor reduce to 2-dimensional matrices, and the wave equation can be written as a matrix equation. As we are treating the material as isotropic, the elasticity tensor reduces in Voigt notation to [15]

$$\mathbf{c}^{-1} = \frac{1}{E} \begin{bmatrix} 1 & -\nu & -\nu & 0 & 0 & 0 \\ -\nu & 1 & -\nu & 0 & 0 & 0 \\ -\nu & -\nu & 1 & 0 & 0 & 0 \\ 0 & 0 & 0 & 2(1+\nu) & 0 & 0 \\ 0 & 0 & 0 & 0 & 2(1+\nu) & 0 \\ 0 & 0 & 0 & 0 & 0 & 2(1+\nu) \end{bmatrix} , \tag{1.2}$$

where $E$ is Young's modulus and $\nu$ is Poisson's ratio. The symmetric gradient reduces to

$$\nabla_S \rightarrow \nabla_{Jj} = \begin{bmatrix} \frac{\partial}{\partial x} & 0 & 0 \\ 0 & \frac{\partial}{\partial y} & 0 \\ 0 & 0 & \frac{\partial}{\partial z} \\ 0 & \frac{\partial}{\partial z} & \frac{\partial}{\partial y} \\ \frac{\partial}{\partial z} & 0 & \frac{\partial}{\partial x} \\ \frac{\partial}{\partial y} & \frac{\partial}{\partial x} & 0 \end{bmatrix} , \tag{1.3}$$

and the divergence reduces to

$$\nabla\cdot \rightarrow \nabla_{iJ} = \begin{bmatrix} \frac{\partial}{\partial x} & 0 & 0 & 0 & \frac{\partial}{\partial z} & \frac{\partial}{\partial y} \\ 0 & \frac{\partial}{\partial y} & 0 & \frac{\partial}{\partial z} & 0 & \frac{\partial}{\partial x} \\ 0 & 0 & \frac{\partial}{\partial z} & \frac{\partial}{\partial y} & \frac{\partial}{\partial x} & 0 \end{bmatrix} . \tag{1.4}$$

In this reduced Voigt notation, the eigenvalue equation reduces to

$$\nabla_{iK} c_{KL} \nabla_{Lj} Q_j = -\rho \Omega_m^2 Q_i \ . \tag{1.5}$$

It is instructive to see the acoustic wave equation written out in component form in regions of spatially constant elasticity. Performing the matrix multiplication yields

$$-k_m^2 Q_x = \left( 2(\nu-1)\frac{\partial^2}{\partial x^2} + (2\nu-1)\left(\frac{\partial^2}{\partial y^2} + \frac{\partial^2}{\partial z^2}\right)\right) Q_x - \frac{\partial^2}{\partial x \partial y} Q_y - \frac{\partial^2}{\partial x \partial z} Q_z \tag{1.6}$$

$$-k_m^2 Q_y = \left( 2(\nu-1)\frac{\partial^2}{\partial y^2} + (2\nu-1)\left(\frac{\partial^2}{\partial x^2} + \frac{\partial^2}{\partial z^2}\right)\right) Q_y - \frac{\partial^2}{\partial y \partial x} Q_x - \frac{\partial^2}{\partial y \partial z} Q_z \tag{1.7}$$

$$-k_m^2 Q_z = \left( 2(\nu-1)\frac{\partial^2}{\partial z^2} + (2\nu-1)\left(\frac{\partial^2}{\partial x^2} + \frac{\partial^2}{\partial y^2}\right)\right) Q_z - \frac{\partial^2}{\partial z \partial x} Q_x - \frac{\partial^2}{\partial z \partial y} Q_y \tag{1.8}$$

where

$$k_m \equiv \frac{\Omega_m}{v_m} \tag{1.9}$$

and

$$v_m = \left( \frac{E}{2(2\nu-1)(\nu+1)\rho} \right)^{1/2} \tag{1.10}$$

is the bulk phase velocity for the material at the frequency of the mode (the speed of sound).

#### 1.2.2.2 Electromagnetic Eigenvalue Problem

Also under the above conditions, Maxwell's equations can be reduced to an eigenvalue-type wave equation for the magnetic induction field $\mathbf{H}(\mathbf{r}) \equiv \mu_0^{-1}\mathbf{B}(\mathbf{r})$ [14],

$$\nabla \times \left( \frac{1}{n^2(\mathbf{r})} \nabla \times \mathbf{H}(\mathbf{r}) \right) = \frac{\omega_o^2}{c^2} \mathbf{H}(\mathbf{r}) \ , \tag{1.11}$$

where $\omega_o$ is the frequency of the optical fields, and $n^2(\mathbf{r}) \equiv \epsilon(\mathbf{r})/\epsilon_0$ is the squared index of refraction. This, together with the transversality constraint, $\nabla \cdot \mathbf{H}(\mathbf{r}) = 0$, completely specifies the magnetic induction.

In regions of spatially constant index of refraction, the component form of the electromagnetic eigenvalue problem becomes

$$-k_o^2 H_x = \left( \frac{\partial^2}{\partial x^2} + \frac{\partial^2}{\partial y^2} + \frac{\partial^2}{\partial z^2} \right) H_x \tag{1.12}$$

$$-k_o^2 H_y = \left( \frac{\partial^2}{\partial x^2} + \frac{\partial^2}{\partial y^2} + \frac{\partial^2}{\partial z^2} \right) H_y \tag{1.13}$$

$$-k_o^2 H_z = \left( \frac{\partial^2}{\partial x^2} + \frac{\partial^2}{\partial y^2} + \frac{\partial^2}{\partial z^2} \right) H_z \tag{1.14}$$

where

$$k_o \equiv \frac{\omega_o}{v_o} \tag{1.15}$$

and

$$v_o = c/n \tag{1.16}$$

is the bulk phase velocity for the material at the frequency of the mode.

Maxwell's equations, together with the harmonic time dependence, allow the electric field to then be calculated directly from the magnetic eigenfields without solving the separate eigenvalue problem for the electric field [14], which gives

$$\mathbf{E}(\mathbf{r}) = \frac{i}{\omega_o}\frac{1}{\epsilon(\mathbf{r})}\nabla \times \mathbf{H}(\mathbf{r}) \; . \tag{1.17}$$

### 1.2.3 Symmetries of the Eigenvalue Problems

We wish to examine the symmetries of the electromagnetic and acoustic eigenvalue problems; i.e., those coordinate transformations that leave the eigenvalue problems unchanged. Consider an operator $\hat{O}$ that acts on vector fields as $\hat{O}\mathbf{F}(\mathbf{r}) \equiv O\mathbf{F}(O^{-1}\mathbf{r})$, where $O$ is a cartesian matrix representation of $\hat{O}$. We will generally want to know whether the electromagnetic and acoustic eigenvalue problems are invariant under the transformation described by an operator and what properties these symmetries give to the modes.

#### 1.2.3.1 Illustrative Example: Mirror Symmetry of the Eigenvalue Problems

As an example, we will consider the operator $\hat{\sigma_x}$, which has the cartesian representation

$$\sigma_x = \begin{bmatrix} -1 & 0 & 0 \\ 0 & 1 & 0 \\ 0 & 0 & 1 \end{bmatrix} \; . \tag{1.18}$$

when acting on polar (covariant) vectors, such as $\mathbf{Q}$, $\mathbf{E}$, and $\mathbf{r}$. When acting on axial (contravariant) vectors, such as $\mathbf{H}$, $\hat{\sigma}_x$ takes the form,

$$\sigma_x = \begin{bmatrix} 1 & 0 & 0 \\ 0 & -1 & 0 \\ 0 & 0 & -1 \end{bmatrix} \; . \tag{1.19}$$

The effect of $\hat{\sigma}_x$ on the acoustic eigenvalue equation is thus captured by the components of $\mathbf{Q}$ transforming as $\{Q_x, Q_y, Q_z\} \rightarrow \{-Q_x, Q_y, Q_z\}$, while differentials transform as $\{dx, dy, dz\} \rightarrow \{-dx, dy, dz\}$ (second differentials are thus unchanged; i.e.,

$\{dx^2, dy^2, dz^2\} \rightarrow \{dx^2, dy^2, dz^2\}$). Thus, in regions of space where the elasticity is constant, one can easily inspect Eqs. (1.6)-(1.8) and see that the eigenvalue problem is invariant under the transformation[9].

Similarly, the effect of $\hat{\sigma}_x$ on the electromagnetic eigenvalue equation is captured by the components of $\mathbf{H}$ transforming as $\{H_x, H_y, H_z\} \rightarrow \{H_x, -H_y, -H_z\}$, with differentials and second differentials transforming as described above. Thus, in regions of space where the index of refraction is constant, one can easily inspect Eqs. (1.12)-(1.14) and see that the electromagnetic eigenvalue problem is invariant under the transformation as well.

#### 1.2.3.2 Differential Operators: Symmetries in Vector-Valued Function Spaces

If we consider the eigenvalue equations being generated by differential operators that act on the space of vector-valued functions, then we correspondingly want to consider the symmetries of the differential operators

$$\hat{\Xi}_m \equiv \nabla \cdot \mathbf{c} : \nabla_s \tag{1.20}$$

and

$$\hat{\Xi}_o \equiv \nabla \times \frac{1}{n^2} \nabla \times \ . \tag{1.21}$$

The eigenvalue equations thus take the form $\hat{\Xi}\mathbf{F}(\mathbf{r}) = \lambda \mathbf{F}(\mathbf{r})$, with $\mathbf{F}$ being either $\mathbf{Q}$ or $\mathbf{H}$, and the corresponding eigenvalue, $\lambda$.

#### 1.2.3.3 Hermiticity

With the inner product in the space of vector-valued functions defined as

$$< \mathbf{F} | \mathbf{G} > \equiv \int \mathrm{d}^3\mathbf{r} \mathbf{F}^*(\mathbf{r}) \cdot \mathbf{G}(\mathbf{r}) \ , \tag{1.22}$$

[9] the new equations are implicitly in the new coordinate system as, for example, $Q_x(x, y, z) \rightarrow -Q_x(-x, y, z)$ or $Q_j(x, y, z) \rightarrow Q_j(-x, y, z)$, where $j$ is $y$ or $z$.

one can easily show[10] that both $\hat{\Xi}_m$ and $\hat{\Xi}_o$ satisfy $< F|\hat{\Xi}G >=< \hat{\Xi}F|G >$ for all vector fields $\mathbf{F}$ and $\mathbf{G}$. In other words, both $\hat{\Xi}_m$ and $\hat{\Xi}_o$ are Hermetian.

Hermiticity endows them with two important properties[11]: the eigenvalues are real, and the inner product of any two eigenmodes *with different eigenvalues* is zero (i.e., nondegenerate modes are orthogonal). In fact, all eigenmodes of a Hermetian operator are orthogonal. It is clear that degenerate modes form a subspace of linearly dependent vectors, since each of the degenerate modes *must* be orthogonal to all other modes with different eigenvalues. Thus we can simply use Gram-Schmidt orthogonalization to generate linear combinations of the degenerate eigenvectors that *are* orthogonal. We conclude that we can always construct a set of eigenvectors of a Hermetian operator that are mutually orthogonal, regardless of degeneracies.

#### 1.2.3.4 Commutativity of Operators and Symmetry Classification of Modes

Because of the invariance of the eigenvalue equations with respect to the operator $\hat{\sigma}_x$, we can either 1) operate on the eigenvector directly with the differential operator or 2) reflect the coordinate system, operate with the differential operator, and then do the inverse reflection on the coordinate system (which is the same as the reflection) to return the system to the original coordinate system. The invariance of the eigenvalue equations guarantees that either of these operations both produce the same eigenvector. Mathematically, this statement is represented as

$$\hat{\Xi}_m \mathbf{Q}(\mathbf{r}) = \hat{\sigma}_x^{-1} \hat{\Xi}_m \hat{\sigma}_x \mathbf{Q}(\mathbf{r}) \tag{1.23}$$

for the acoustic eigenvalue problem, and

$$\hat{\Xi}_o \mathbf{H}(\mathbf{r}) = \hat{\sigma}_x^{-1} \hat{\Xi}_o \hat{\sigma}_x \mathbf{H}(\mathbf{r}) \ . \tag{1.24}$$

[10] The proof for either the acoustic or electromagnetic differential operator involves two applications of inegration by parts. It also mandates that the modes either go to zero at large distances or that they are periodic in any direction for which they do not go to zero, such that the integrals of fields vanishes on the surfaces of integration volumes. See, for example, reference [14].

[11] We state the following properties of Hermetian operators without proof, but these proofs can be looked up in any book on linear algebra or quantum mechanics.

for the electromagnetic eigenvalue problem.

This leads to the concept of commutation; i.e., with the definition $[\hat{A},\hat{B}]\mathbf{F}(\mathbf{r}) \equiv \hat{A}\hat{B}\mathbf{F}(\mathbf{r}) - \hat{B}\hat{A}\mathbf{F}(\mathbf{r})$, then we have

$$[\sigma_x, \hat{\Xi}_m]\mathbf{Q}(\mathbf{r}) = 0 \tag{1.25}$$

and

$$[\sigma_x, \hat{\Xi}_o]\mathbf{H}(\mathbf{r}) = 0\ . \tag{1.26}$$

The commutation of operators allows a further classification of the solutions as follows[12]. Consider a particular acoustic mode, $\mathbf{Q}(\mathbf{r})$, which is a solution of the eigenvalue problem with eigenvalue $\lambda$; i.e., $\hat{\Xi}_m\mathbf{Q}(\mathbf{r}) = \lambda\mathbf{Q}(\mathbf{r})$. Then, a commuting operator $\hat{A}$ satisfies

$$\begin{aligned}
[\hat{A},\hat{\Xi}_m]\mathbf{Q}(\mathbf{r}) &= 0 \\
&= \hat{A}\hat{\Xi}_m\mathbf{Q}(\mathbf{r}) - \hat{\Xi}_m\hat{A}\mathbf{Q}(\mathbf{r}) \\
&= \hat{A}\lambda\mathbf{Q}(\mathbf{r}) - \hat{\Xi}_m\hat{A}\mathbf{Q}(\mathbf{r}) \\
&= \lambda\Big(\hat{A}\mathbf{Q}(\mathbf{r})\Big) - \hat{\Xi}_m\Big(\hat{A}\mathbf{Q}(\mathbf{r})\Big)\ .
\end{aligned} \tag{1.27}$$

The last of these equations means that $\hat{A}\mathbf{Q}(\mathbf{r})$ is also an eigenvector with eigenvalue $\lambda$. If this eigenvalue has no degeneracies, then this guarantees that $\mathbf{Q}(\mathbf{r})$ and $\hat{A}\mathbf{Q}(\mathbf{r})$ can be different only by a multiplicative factor. If we call this factor $\alpha$, then we have demonstrated (for the case of no degeneracy) that $\hat{A}\mathbf{Q}(\mathbf{r}) = \alpha\mathbf{Q}(\mathbf{r})$; that is, $\mathbf{Q}(\mathbf{r})$ is an eigenvector of the operator $\hat{A}$ with eigenvalue $\alpha$.

[12] We will use the acoustic eigenvalue problem as an example, but it clearly applies in an analogous way to the electromagnetic eigenvalue problem

#### 1.2.3.5 Mirror Symmetry Revisited

In the case of the mirror operator, $\hat{\sigma}_x$, which we have already shown commutes with $\hat{\Xi}_m$, we will call the eigenvalue the parity, $p_x$, of $\mathbf{Q}(\mathbf{r})$. Because two applications of the mirror operator maps the coordinate system back into itself (or, in covariant form, $\sigma_x\sigma_x = \mathbf{1}$, where $\mathbf{1}$ is the identity matrix), one can easily see that $p_x^2 = 1$, which means $p_x = \pm 1$. With this restriction on the eigenvalue, we can extract information about the spatial parity of the components of $\mathbf{Q}(\mathbf{r})$. Consider the eigenvalue $p_x = 1$. This implies that $\sigma_x\mathbf{Q}(\sigma_x\mathbf{r}) = \mathbf{Q}(\mathbf{r})$[13]. This breaks into three separate conditions:

$$Q_x(-x,y,z) = -Q_x(x,y,z) \tag{1.28}$$

$$Q_y(-x,y,z) = Q_y(x,y,z) \tag{1.29}$$

$$Q_z(-x,y,z) = Q_z(x,y,z)\ . \tag{1.30}$$

Similarly, for $p_x = -1$, we must have

$$Q_x(-x,y,z) = Q_x(x,y,z) \tag{1.31}$$

$$Q_y(-x,y,z) = -Q_y(x,y,z) \tag{1.32}$$

$$Q_z(-x,y,z) = -Q_z(x,y,z)\ . \tag{1.33}$$

So the parity of the vector field also sets certain restrictions on whether each component is even or odd about the symmetry plane. Analogous relations hold for any mirror operator, and this fact will be important for determining the polarization properties of acoustic and electromagnetic modes, as well as the coupling between acoustic and electromagnetic modes.

An important point to make about scalar parities of vector field components is that the magnetic field (or magnetic induction field) is a contravariant second rank tensor (axial vector), and it is the contravariant representation of the $\hat{\sigma}$ operators that must

[13]Note that $\sigma_x^{-1} = \sigma_x$.

be considered to ascertain the scalar parities of the vector field components. This is simple to do, since the contravariant representation of a mirror operator will just be equal to the negative of the covariant representation. As an example, if the mode has $p_x = +1$, we have for the magnetic induction field:

$$H_x(-x, y, z) = H_x(x, y, z) \tag{1.34}$$
$$H_y(-x, y, z) = -H_y(x, y, z) \tag{1.35}$$
$$H_z(-x, y, z) = -H_z(x, y, z)\ . \tag{1.36}$$

For $p_x = -1$,

$$H_x(-x, y, z) = -H_x(x, y, z) \tag{1.37}$$
$$H_y(-x, y, z) = H_y(x, y, z) \tag{1.38}$$
$$H_z(-x, y, z) = H_z(x, y, z)\ . \tag{1.39}$$

#### 1.2.3.6 Bonded and Anti-Bonded Optical Modes of the "Zipper"

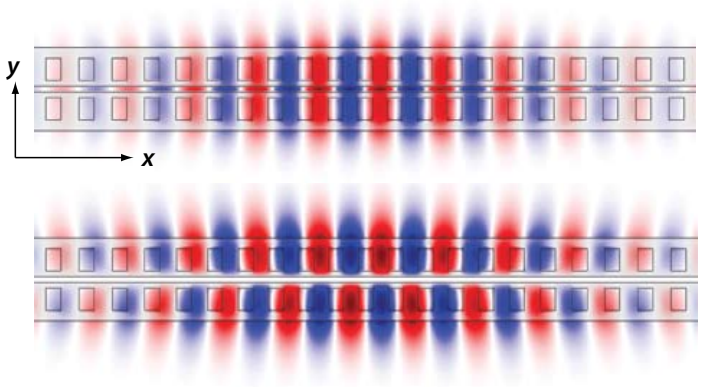


Figure 1.5: $E_y(x, y, z = 0)$ for the "bonded" (top) and "anti-bonded" (bottom) optical modes of the "Zipper" cavity.

The dominant optical field in this work will always be the $y$-component of a $p_z =$

+1 (TE-like) electric field. For the case of the "Zipper" cavity, we will often discuss the difference between "bonded" and "anti-bonded" modes. This analogy derives from a scalar mirror symmetry of electron wavefunctions in covalent bonding of molecules. In this work, "bondedness" refers to is the parity of $E_y$ with respect to the $\hat{\sigma}_y$ mirror plane, since it is this field component that causes the bulk of the energy splitting of optical modes when the gap between the nanobeams is smaller than a wavelength. Referring to Fig. 1.5, we will call the mode with $E_y(x,-y,z) = E_y(x,y,z)$ "bonded", and the mode with $E_y(x,-y,z) = -E_y(x,y,z)$ "antibonded"[14]. The confusion comes about because of the ambiguity in referring to the scalar parity of $E_y$ or the vector parity of the whole field; thus, the mode with $p_y = +1$ is often mistaken for "bonded" and the $p_y = -1$ mode for "anti-bonded". However, one can see that for $p_y = +1$, we have

$$E_x(x,-y,z) = E_x(x,y,z) \tag{1.40}$$
$$E_y(x,-y,z) = -E_y(x,y,z) \tag{1.41}$$
$$E_z(x,-y,z) = E_z(x,y,z)\ , \tag{1.42}$$

whereas for $p_y = -1$, we have

$$E_x(x,-y,z) = -E_x(x,y,z) \tag{1.43}$$
$$E_y(x,-y,z) = E_y(x,y,z) \tag{1.44}$$
$$E_z(x,-y,z) = -E_z(x,y,z)\ . \tag{1.45}$$

So we see from the scalar parity of the dominant field component ($E_y$) that, actually, the mode with $p_y = -1$ is bonded, and the $p_y = +1$ mode is antibonded. Nevertheless, we will still refer to the bonded field as $\mathrm{TE}_+$, but the reader must keep in mind that

[14]The easiest way to identify the modes is from the fact that the anti-bonded mode has $E_y(x,0,z) = 0$, as necessitated by its scalar parity with respect to the $\hat{\sigma}_y$ mirror plane.

the plus does not refer to $p_y = +1$.

It is worthwhile to quickly note the mirror symmetries $p_x$ and $p_z$ of these fields, as these will be the same for both the bonded and anti-bonded modes of the "Zipper", as well as the optical modes of a single beam. First, all the modes will be TE-like. This means the modes of all these structures have $p_z = +1$; i.e., they have the following parity with respect to the $\hat{\sigma}_z$ mirror plane:

$$E_x(x, y, -z) = E_x(x, y, z) \tag{1.46}$$

$$E_y(x, y, -z) = E_y(x, y, z) \tag{1.47}$$

$$E_z(x, y, -z) = -E_z(x, y, z)\ . \tag{1.48}$$

Second, to minimize optical losses[15], the localized optical modes are chosen to have $E_y(-x, y, z) = -E_y(x, y, z)$. This corresponds to $p_x = -1$, for which we have

$$E_x(-x, y, z) = E_x(x, y, z) \tag{1.49}$$

$$E_y(-x, y, z) = -E_y(x, y, z) \tag{1.50}$$

$$E_z(-x, y, z) = -E_z(x, y, z)\ . \tag{1.51}$$

#### 1.2.3.7 Other Symmetries of the Eigenvalue Equations and Point Groups

By methods similar to those in § 1.2.3.1, one can verify that the eigenvalue problems in uniform media are also invariant under all reflections, translations, proper rotations, inversions, and improper rotations[16].

With the addition of geometric structure (such as the nanobeam), the spatial symmetries of the eigenvalue problems and the solutions will be limited by the symmetries of the geometric structure, which is typically some set of rotation, mirror, and

[15] This will be explained in detail in Chapter 2

[16] An improper rotation is the combination of a rotation about an axis and a reflection in a plane perpendicular to the axis. This is also known as a rotary reflection.

inversion symmetries known as the point group of the system. We will now turn to analyzing those symmetries in nanobeams and examining how they affect the modes of the system.

### 1.2.4 Modes and Symmetries of the Projected Mirror Portions

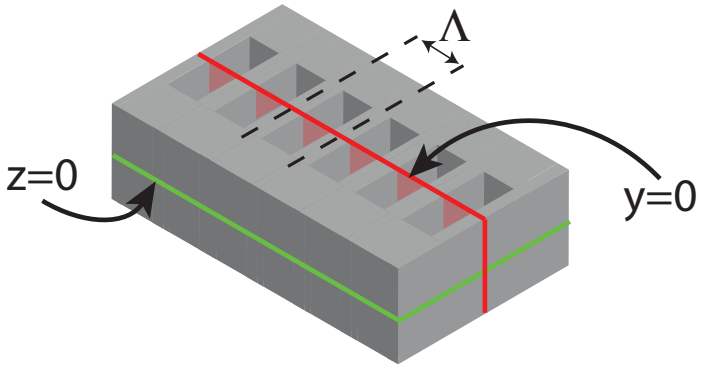


Figure 1.6: Geometry of the "projection" of a nanobeam, showing the periodicity $\Lambda$ and mirror symmetry planes, $z = 0$ and $y = 0$.

Localization of electromagnetic and acoustic energy to the defect region in these nanobeam band gap cavities occurs because propagation in the mirror portions is inhibited for certain ranges of frequencies. Thus an understanding of the acoustic and electromagnetic properties of the mirror portions is critical to understanding the behavior of localized modes.

The mirror portions are periodic such that the elasticity tensor and dielectric function are invariant with respect to translations of length $\Lambda$. If we consider extending the mirror portion infinitely in both directions ($\pm x$), then this construction that has perfect periodicity, $\Lambda$, has solutions that satisfy Bloch's theorem. We will call such an extension of the mirror portion a *projection*. An illustration of the projection geometry is shown in Fig. 1.6.

#### 1.2.4.1 Photonic and Phononic Bands of the Projection

The projection of the nanobeam optomechanical crystal has discrete periodicity, satisfying $\mathbf{n^2}(\mathbf{r}) = \mathbf{n^2}(\mathbf{r} + l\Lambda\hat{\mathbf{x}})$ and $\mathbf{c}(\mathbf{r}) = \mathbf{c}(\mathbf{r} + l\Lambda\hat{\mathbf{x}})$, where $\Lambda$ is the periodicity of the lattice and $l$ is an integer.

Consider an operator that performs discrete translational coordinate transformations on functons of any tensorial rank, the shift of length $\Lambda$ being in the $\hat{\mathbf{x}}$ direction,

$$\hat{T}_\Lambda f(\mathbf{r}) \equiv f(\mathbf{r} + \Lambda\hat{\mathbf{x}}) \ . \tag{1.52}$$

For the projection, $\hat{T}_\Lambda n^2(\mathbf{r}) = n^2(\mathbf{r})$ and $\hat{T}_\Lambda c(\mathbf{r}) = c(\mathbf{r})$ by definition. Together with the fact that differentials are not affected by constant shifts of the coordinate system, this also implies $\hat{T}_\Lambda \hat{\Xi}_m = \hat{\Xi}_m$ and $\hat{T}_\Lambda \hat{\Xi}_m = \hat{\Xi}_m$ in the projection. From this, it is easy to show that $[\hat{T}, \hat{\Xi}_m] = 0$ and $[\hat{T}, \hat{\Xi}_m] = 0$. From § 1.2.3.4, we know that the eigenvectors of the system are also eigenvectors of $\hat{T}_\Lambda$, and we can classify the solutions according to their eigenvalues of $\hat{T}_\Lambda$.

From Bloch's theorem[17], we know that the solutions of the can be expressed as

$$\mathbf{F}(\mathbf{r}) = u(\mathbf{r})e^{ikx} \ , \tag{1.53}$$

where $u(\mathbf{r}) = u(\mathbf{r} + m\Lambda\hat{\mathbf{x}})$ is called the Bloch function. This implies that

$$\hat{T}_\Lambda F(\mathbf{r}) = e^{ik\Lambda} F(\mathbf{r}) \ . \tag{1.54}$$

These solutions can thus be classified according to a wave vector, $k\hat{\mathbf{x}}$. Because of the periodicity of $e^{ik\Lambda}$, all unique eigenvalues are contained in the domain, $k \in [-\pi/\Lambda, \pi/\Lambda]$, which is called the first Brillouin zone[18]. The Bloch function will satisfy a separate differential equation that determines the frequency of the mode as a function of the $k$-vector. As the Bloch function is restricted to a finite region of space

[17] See, for instance, [14].

[18] Time-reversal symmetry and the fact that the frequencies (which are eigenvalues of Hermetian operators) are necessarily real guarantee that positive and negative wave vectors yield identical solutions. This allows the solutions to be further restricted to the first half of the first Brillouin zone, $k \in [0, \pi/\Lambda]$.

(the unit cell) by its periodicity, the solutions for a given $k$ have a discrete spectrum of eigenfrequencies. Thus the eigenfrequencies for the acoustic and electromagnetic modes of the mirror form bands, which we will label by a band index[19], $n$. A diagram that gives the spectrum of frequencies as a function of $k$ in the first Brillouin zone[20] will be called the band diagram of the structure.

#### 1.2.4.2 Mirror Symmetries of the Projection

In addition to translational symmetry, the projection is also symmetric about the $y = 0$ and $z = 0$ planes, as shown in Fig. 1.6. As in § 1.2.3.1 and § 1.2.3.5, the mirror operators, $\sigma_y$ and $\sigma_z$, which have covariant representations

$$\sigma_y = \begin{bmatrix} 1 & 0 & 0 \\ 0 & -1 & 0 \\ 0 & 0 & 1 \end{bmatrix} \quad \sigma_z = \begin{bmatrix} 1 & 0 & 0 \\ 0 & 1 & 0 \\ 0 & 0 & -1 \end{bmatrix}, \tag{1.55}$$

commute with the operators $\hat{\Xi}_m$ and $\hat{\Xi}_o$. The electromagnetic and acoustic modes in the projection can thus be further classified with respect to their vector parity about these planes, each solution having an eigenvalue of the mirror operator such that $\sigma_j \mathbf{Q}(\sigma^{-1}\mathbf{r}) = p_j \mathbf{Q}(\mathbf{r})$, where $j$ can be $y$ or $z$, and $p_j = \pm 1$. We accordingly classify the solutions to the wave equation by the wave vector $k \in [0, \pi/\Lambda]$, $p_y$, and $p_z$.

The band diagram for the acoustic modes of a nanobeam's projection is shown in Fig. 1.7, with the first ten band indices, $n$, labeled a to j, $p_z$ indicated by color, and $p_y$ indicated by line shape. The mechanical displacement profiles of the unit cell are shown for each band at $\Gamma$ and $X$. In the band diagram, the mirror symmetry $\sigma_z$, (across the plane defined by $z = 0$) is indicated by color: red corresponds to even vector parity ($p_z = 1$) and blue to odd vector parity ($p_z = -1$). Mirror symmetry $\sigma_y$ (across the plane defined by $y = 0$) plane is indicated by the line shape: solid corresponds to even vector parity ($p_y = 1$) and dashed to odd vector parity ($p_y = -1$).

[19] Although the band indices may label the frequencies at a given value of $k$ in order of increasing frequency, the bands may cross; so this will not hold in general for all values of $k$.

[20] The two high symmetry points of the first Brillouin zone in a 1D periodic structure are often assigned the names $\Gamma$ for $k = 0$ and $X$ for $k = \pi/\Lambda$.

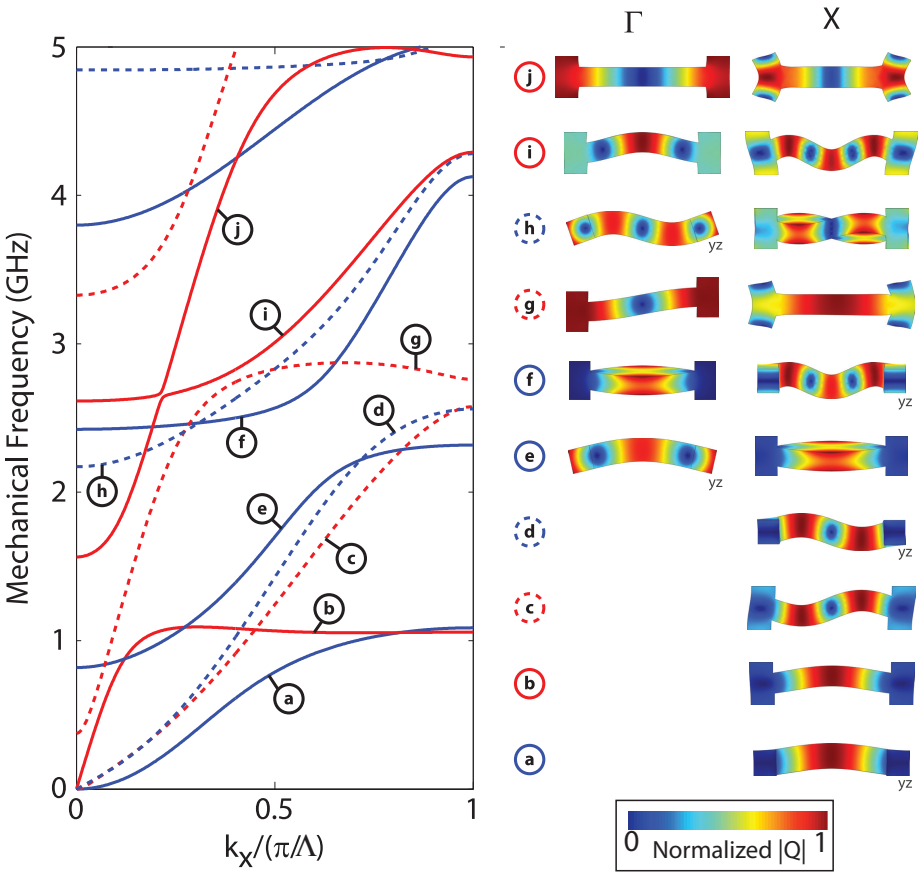


Figure 1.7: Mechanical band diagram and corresponding normalized displacement profiles of the unit cell at the Γ ($k = 0$) and $X$ ($k = \pi/\Lambda$) points. Color and linestyle indicate the symmetries with respect to $\hat{\sigma}_z$ and $\hat{\sigma}_y$, respectively (see text for details).

The mechanical mode profiles are all viewed from a direction normal to the $z = 0$ plane unless labeled "yz", in which case the viewing angle is normal to the $x = 0$ plane. The pinch, accordion, and breathing mode bands are b, i, and j, respectively. As torsional modes can be difficult to interpret without isometric views, it is noted for the reader that the mechanical modes for band e at $X$, band f at Γ, and band h at $X$ are all torsional mechanical modes.

The band diagram for the optical modes of a nanobeam's projection is shown in Fig. 1.8, with the first four band indices, $n$, labeled a to d, and $p_y$ indicated by line shape[21]. As will be the case in all of this work, the structures are much

[21] As in the case of the Fig. 1.7, solid corresponds to even vector parity ($p_y = 1$) and dashed to odd vector parity ($p_y = -1$).

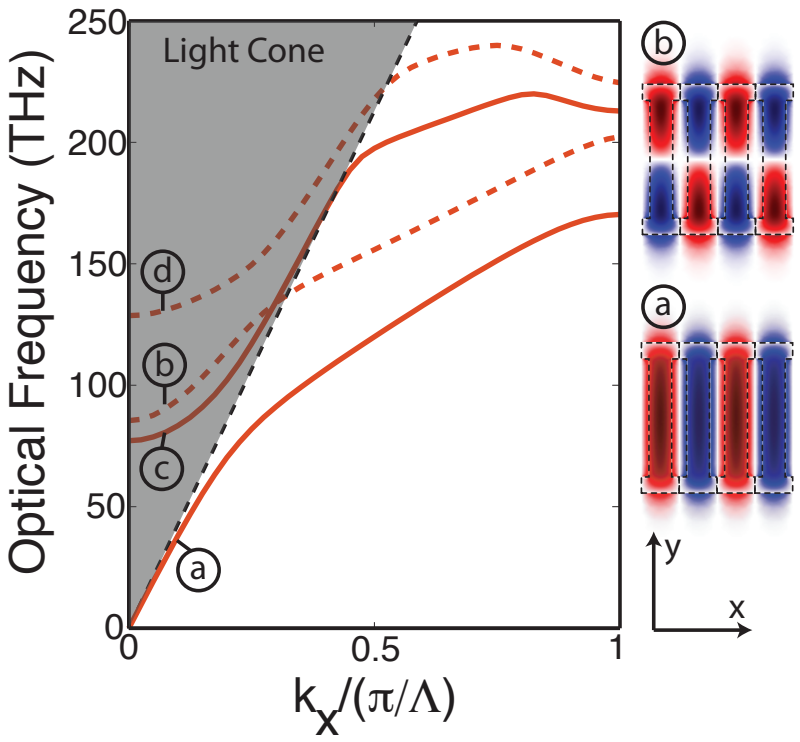


Figure 1.8: Optical band diagram and corresponding normalized displacement profiles of the unit cell at the $\Gamma$ ($k = 0$) and $X$ ($k = \pi/\Lambda$) points. Color and linestyle indicate the symmetries with respect to $\hat{\sigma}_z$ and $\hat{\sigma}_y$, respectively (see text for details). The field profiles shown correspond to $E_y(x, y, z = 0)$.

thinner than they are wide, which makes the energy required to have odd $z$ vector parity very large; thus the TM-like ($z$-odd) modes of the structure do not exist at relevant frequencies. The profile of $E_y(x, y, z = 0)$ for four unit cells are shown for the fundamental (valence) $y$-even and $y$-odd bands at the $X$ point[22].

The optical band diagram also displays another important feature of the optical modes: index guiding. The shaded area of the band diagram, which is called the *light cone*, corresponds to the region $\omega_o > ck$. The line itself, $\omega_o = ck$, is called the *light line*. Above the light line, the modes of the nanobeam are propagating in the direction transverse to the waveguide ($x$). Below the light line, the modes are guided by the index contrast between the material and the air. The concept of index guiding will play a critical role in the localization of optical modes.

[22]The conduction band modes look very similar but have their maxima in the air and nodes in the material

### 1.2.5 Localized Modes and Symmetries

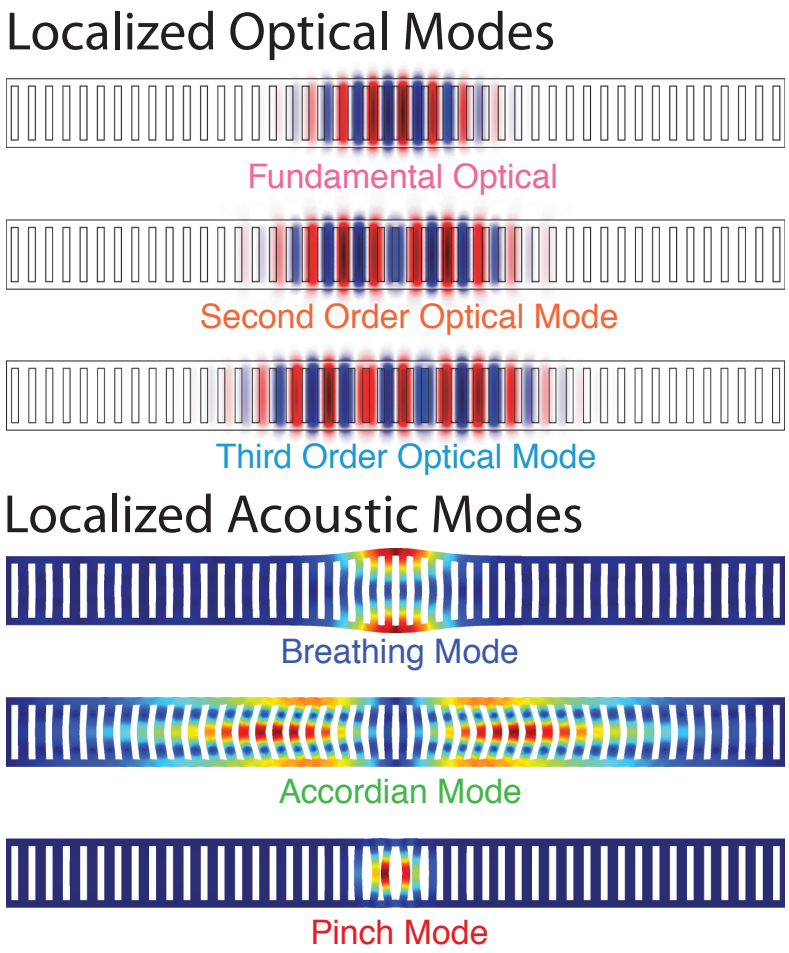


Figure 1.9: Exemplary localized modes of the nanobeam optomechanical crystal.

As described in § 1.2.1 and shown in Fig. 1.4, the defect in the structure (see Fig. 1.4) breaks the discrete periodicity of the mirror section in the $x$ direction, and the solutions to the wave equation (Eq. 1.1) for the structure can no longer be classified by wave vectors and band indices. The structure still retains its $\hat{\sigma}_y$ and $\hat{\sigma}_z$ mirror symmetries. In addition, the structure now has a third mirror plane, $\hat{\sigma}_x$ (the plane $x = 0$), which divides the structure in half in the $x$ direction. As discussed as a general example in § 1.2.3.1, $\hat{\Xi}_m$ and $\hat{\Xi}_o$ commute with the mirror operator, $\hat{\sigma}_x$, where

$$\sigma_x = \begin{bmatrix} -1 & 0 & 0 \\ 0 & 1 & 0 \\ 0 & 0 & 1 \end{bmatrix} \tag{1.56}$$

is the second rank covariant representation of $\hat{\sigma}_x$. Each solution of the wave equation of the full structure is thus an eigenvector of $\hat{\sigma}_j$, with corresponding vector parity $p_j = \pm 1$, $j \in [x, y, z]$.

The solutions to the wave equations in the defect can be viewed as being drawn from the band edges of the projection. Localized modes are formed whenever the modes of the defect exist at a frequency for which the density of states in the projection is small or zero. Thus, many localized mechanical modes are formed at the various band edges. Manifolds of localized modes have identical parities with respect to $\sigma_y$ and $\sigma_z$, and the parity with respect to $\sigma_x$ alternates as one climbs the ladder of states in the manifold.

Examples of localized modes are shown in Fig. 1.9. The three optical modes are derived from the $X$ point of the "a" band of Fig. 1.8. The mechanical modes, which all have $p_x = p_y = p_z = +1$, are derived from various bandedges of Fig. 1.7: breathing, band "j", $\Gamma$ point; accordion, band "i", $\Gamma$ point; and pinch, band "b", $X$ point.

### 1.2.6 Mode Amplitudes, Effective Mode Volumes, and Effective Mass

The optical mode is characterized by a resonant frequency $\omega_{\mathrm{o}} = 2\pi\nu_{\mathrm{o}}$ and electric field $\mathbf{E}(\mathbf{r})$. The mechanical mode is characterized by a resonant frequency $\Omega_{\mathrm{m}} = 2\pi\nu_{\mathrm{m}}$ and displacement field $\mathbf{Q}(\mathbf{r})$, where $\mathbf{Q}(\mathbf{r})$ is the vector displacement describing perpendicular displacements of the boundaries of volume elements. The cavity optomechanical interactions of the distributed structure and its spatially-dependent vector fields, $\mathbf{E}(\mathbf{r})$ and $\mathbf{Q}(\mathbf{r})$, can be reduced to a description of two *scalar* mode amplitudes and their associated mode volumes, with the coupling of the amplitudes parameterized by a single coupling coefficient, $g_{\mathrm{OM}}$.

The mode amplitude, $c$, and complex vector field profile, $\mathbf{e}(\mathbf{r})$, are defined such that the complex electric field is $\mathbf{E}(\mathbf{r}) = c\mathbf{e}(\mathbf{r})$ (the physical field is given by the real part of $\mathbf{E}(\mathbf{r})e^{i\omega t}$). For pedagogical reasons, the amplitude $c$ is normalized such that the time averaged electromagnetic energy is equal to $|c|^2$; i.e. $U = |c|^2 = \frac{1}{2}\int \mathrm{d}V \epsilon |\mathbf{E}|^2$. This forces $\mathbf{e}$ to be normalized such that $1 = \frac{1}{2}\int \mathrm{d}V \epsilon |\mathbf{e}|^2$. In cavity quantum electrodynamics, one typically defines an effective optical mode volume, $V_\mathrm{o} = \int \mathrm{d}V \left(\frac{\sqrt{\epsilon}|\mathbf{E}|}{\max(|\sqrt{\epsilon}\mathbf{E}|)}\right)^2$, in order to gauge the strength of light-matter interactions.

The mechanical vibration's amplitude, $\alpha$, and mode profile (displacement), $\mathbf{q}(\mathbf{r})$, are defined such that $\mathbf{Q}(\mathbf{r}) = \alpha\mathbf{q}(\mathbf{r})$. Here, $\alpha$ is defined as the largest displacement that occurs anywhere for the mechanical field, $\mathbf{Q}(\mathbf{r})$, so that $\max(|\mathbf{q}(\mathbf{r})|) = 1$. The mode amplitude, $\alpha$, must also represent the amplitude of the generalized position, $\beta(t) = \alpha\cos(\Omega t)$, and generalized momentum, $m_\mathrm{eff}\dot{\beta}(t)$, of a simple harmonic oscillator with an energy, $E_\mathrm{mechanical} = \frac{m_\mathrm{eff}}{2}(\Omega^2\beta^2 + \dot{\beta}^2)$. Our particular choice of $\alpha$ determines the mechanical mode's effective volume, $V_\mathrm{m}$, and effective mass, $m_\mathrm{eff} \equiv \rho V_\mathrm{m}$, since this choice of $\alpha$ requires the complimentary definition $m_\mathrm{eff} = \rho\int \mathrm{d}V \left(\frac{|\mathbf{Q}|}{\max(|\mathbf{Q}|)}\right)^2$. To see this note that, at the classical turn-around point, integrating the potential energy of each volume element must give the total potential energy. Thus $E_\mathrm{mechanical} = \frac{1}{2}\Omega^2\int \rho|\mathbf{Q}(\mathbf{r})|^2\mathrm{d}V = \frac{1}{2}m_\mathrm{eff}\Omega^2\alpha^2$, or, in other words, $m_\mathrm{eff}\alpha^2 = \int \rho|\mathbf{Q}(\mathbf{r})|^2\mathrm{d}V$. One can arbitrarily choose the definition of the amplitude or the mass, but choosing one determines the other. In addition, $\alpha$ is the amplitude of zero-point motion of the canonical position operator in a quantized treatment. For a system like a localized mode of a phononic crystal defect cavity, where only a very small, localized portion of the total mass undergoes appreciable motion, the most sensible choice of the mass is the amplitude-squared weighted density integral, which, as stated above, is the choice of mass associated with $\alpha = \max(|\mathbf{Q}(\mathbf{r})|)$.

### 1.2.7 Optical Coupling Between a Standing Wave Resonator and a Traveling Wave Input

The optical cavities in this work will be fed optical power via a nanoscale tapered and dimpled optical fiber [16]. This makes it critical to have a description of the coupling between the waveguide (traveling wave) mode of the fiber and standing wave mode of the resonator. We will be concerned with describing the energy loading of the cavity given experimentally-measurable quantities; we will not be concerned with calculating the coupling rates from the fields, which is the subject of coupled mode theory, excellent treatments of which can be found in References [14, 17, 18].

Consider an optical cavity with two traveling waves represented by the amplitudes, $\tilde{a}$ and $\tilde{b}$, with degenerate frequency $\omega_o$. The field $\tilde{a}$ is fed optical energy at rate $\kappa_e$ by an external driving field, represented by $\tilde{s} = se^{-i\omega t}$, where $|\tilde{s}|^2 \equiv P_0$, where $P_0$ is the incident power. Each of the fields, $\tilde{a}$ and $\tilde{b}$, experience an identical energy loss rate, $\kappa \equiv \kappa_i + \kappa_e$, albeit into different channels: $\tilde{a}$ couples into the direction of the input field (transmission channel), $\tilde{s} = se^{-i\omega t}$, while $\tilde{b}$ couples into the backward direction (reflected channel). In addition, the two fields are coupled together with coherent coupling rate $\beta e^{i\eta}$, where $\mathrm{Im}\{\beta\} = 0$. The amplitudes obey the coupled differential equations [14, 18]

$$\dot{\tilde{a}} = -i\omega_o\tilde{a} + i\beta e^{i\eta}\tilde{b} - \frac{\kappa}{2}\tilde{a} + i\sqrt{\kappa_e}\tilde{s} \tag{1.57}$$

$$\dot{\tilde{b}} = -i\omega_o\tilde{b} + i\beta e^{-i\eta}\tilde{a} - \frac{\kappa}{2}\tilde{b}\,. \tag{1.58}$$

In a frame rotating with $\tilde{s}$, we define the envelopes, $a$ and $b$, such that $\tilde{a} = ae^{-i\omega t}$ and $\tilde{b} = be^{-i\omega t}$. These envelopes then obey the differential equations

$$\dot{a} = i\Delta_0 a + i\beta e^{i\eta}b - \frac{\kappa}{2}a + i\sqrt{\kappa_e}s \tag{1.59}$$

$$\dot{b} = i\Delta_0 b + i\beta e^{-i\eta}a - \frac{\kappa}{2}b\,, \tag{1.60}$$

where $\Delta_0 \equiv \omega - \omega_o$ (blue detuning for $\Delta > 0$).

The steady state amplitudes are found from setting the time derivatives to zero. This gives the solutions

$$a = \frac{i\sqrt{\kappa_e}}{\frac{\kappa}{2} - i\Delta_0 + \frac{\beta^2}{\frac{\kappa}{2} - i\Delta_0}} s \tag{1.61}$$

$$b = \frac{i\beta e^{-i\eta}}{\frac{\kappa}{2} - i\Delta_0} a \; . \tag{1.62}$$

When $\beta \gg \kappa$ (as is the case in photonic crystals, where $\beta$ is equal to the band gap), there is no appreciable amplitude in either mode until $\Delta_0 \approx \pm\beta$. In this case, it can be easily shown that $b \approx \pm e^{-i\eta} a$; in other words, the two fields have equal energies, and we expect they form a standing wave.

With the above in mind, it is useful to make a change of basis:

$$c = \frac{1}{\sqrt{2}} \left(a + e^{i\eta} b\right) \qquad \leftrightarrow \qquad a = \frac{1}{\sqrt{2}} \left(c + d\right) \tag{1.63}$$

$$d = \frac{1}{\sqrt{2}} \left(a - e^{i\eta} b\right) \qquad \leftrightarrow \qquad b = \frac{e^{-i\eta}}{\sqrt{2}} \left(c - d\right) \; . \tag{1.64}$$

One can already see the utility, since, if $b = e^{-i\eta} a$ ($\Delta_0 = \beta$), $d = 0$, whereas if $b = -e^{-i\eta} a$ ($\Delta_0 = -\beta$), $c = 0$. Thus we expect the two fields to decouple. In particular, it can easily be shown that

$$\dot{c} = -\left(\frac{\kappa}{2} + i(\Delta_0 - \beta)\right) c + i\sqrt{\frac{\kappa_e}{2}} s \tag{1.65}$$

$$\dot{d} = -\left(\frac{\kappa}{2} + i(\Delta_0 + \beta)\right) d + i\sqrt{\frac{\kappa_e}{2}} s \; . \tag{1.66}$$

These two two fields are, in fact, decoupled; each standing wave amplitude behaves as an independent field with the original loss rate, $\kappa = \kappa_i + \kappa_e$, but only *half* the input coupling energy rate (i.e. the coefficient in front of the input field is now proportional

to $\sqrt{\kappa_e/2}$). We can now work with a single standing wave amplitude, and the other will never be populated as long as $\beta \gg \kappa$, which is always the case in practice. The master equation for the standing wave amplitude is thus

$$\dot{c} = -\left(\frac{\kappa}{2} + i\Delta\right) c + i\sqrt{\frac{\kappa_e}{2}} s \,, \tag{1.67}$$

where $\Delta \equiv \Delta_0 - \beta = \omega - (\omega_o + \beta)$.

To find the cavity energy, one must construct the electric field, $E = ae^{ikx} + be^{-ikx}$. Then the total (time-averaged) electromagnetic energy density is

$$u = \frac{1}{2}\epsilon_0 |E|^2 = \frac{\epsilon_0}{2}\left(|a|^2 + |b|^2 + 2\cos(2kx)\mathrm{Re}\left\{ab^*\right\} - 2\sin(2kx)\mathrm{Im}\left\{ab^*\right\}\right) \,. \tag{1.68}$$

The total cavity energy is then

$$U = \int_V u \mathrm{d}V \approx \frac{\epsilon_0 V}{2}\left(|a|^2 + |b|^2\right) \,, \tag{1.69}$$

where the equation is exact on resonance and approximately true off resonance for a high-$Q$ cavity, in the sense that the change in $k$ as it is varied from resonance to $\Delta = \kappa$ is proportional to $1/Q$. Thus, if one sets $a \to \sqrt{\frac{2U}{\epsilon_0 V}} a$ (and similarly for $b$), then $U = |a|^2 + |b|^2$.

Because the transformation between standing waves and traveling waves is unitary, $|a|^2 + |b|^2 = |c|^2 + |d|^2$, and, thus, we can finally conclude that

$$U = |c|^2 + |d|^2 \approx |c|^2 \,. \tag{1.70}$$

The steady-state solution to (1.67) is

$$c = \frac{i\sqrt{\frac{\kappa_e}{2}} s}{\frac{\kappa}{2} + i\Delta} \,, \tag{1.71}$$

and, thus, the cavity energy is

$$U = |c|^2 = \frac{2(\kappa_e/\kappa^2)}{1 + 4\left(\frac{\Delta}{\kappa}\right)^2} P_0 \ . \tag{1.72}$$

In order to determine the cavity energy experimentally, one must determine the ratio $\kappa_e/\kappa$. It will now be shown that this quantity is readily measurable via the on-resonance transmission of the cavity mode.

The field transmitted past the waveguide is $s_{out} = ise^{-i\omega t} - \sqrt{\frac{\kappa_e}{2}} c_p(t)$ [14,18], and so the transmission coefficent, $T = |s_{out}/s|^2$ is

$$T = \left| 1 + i\sqrt{\kappa_e} \frac{a}{s} \right|^2 \ , \tag{1.73}$$

and, thus, in our approximation where only $c$ has appreciable amplitude (which is essentially exact in the experimental realizations in this work),

$$T \approx \left| 1 + i\sqrt{\frac{\kappa_e}{2}} \frac{c}{s} \right|^2 = \left| 1 - \frac{\kappa_e}{2} \frac{1}{\frac{\kappa}{2} + i\Delta} \right|^2 = \left| 1 - \frac{\kappa_e/\kappa}{1 + 2i\frac{\Delta}{\kappa}} \right|^2 \ . \tag{1.74}$$

As stated above, the quantity, $T_0 \equiv T(\Delta = 0)$, allows one to experimentally relate the external coupling rate (i.e. the ratio $\kappa_e/\kappa$) to the resonant transmission depth. In particular,

$$T_0 = (1 - \frac{\kappa_e}{\kappa})^2 \ , \tag{1.75}$$

and, since $\kappa_e \leq \kappa$, it follows that

$$\frac{\kappa_e}{\kappa} = 1 - \sqrt{T_0} \ . \tag{1.76}$$

With this expression, one can readily use equation 1.72 to calculate the optical cavity energy.

Another useful relation is the relative linewidth, $\kappa/\kappa_i = 1/\sqrt{T_0}$, which describes the broadening of the resonance due to extrinsic coupling (this follows trivially from the definition $\kappa = \kappa_e + \kappa_i$).

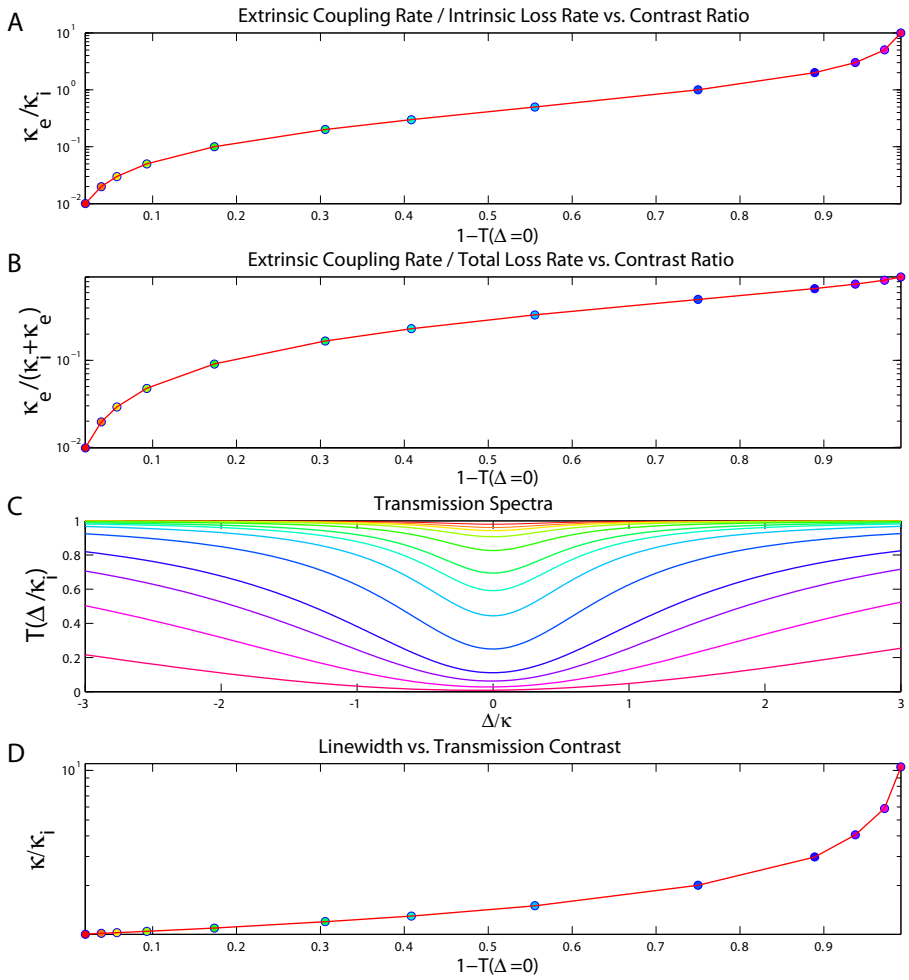


Figure 1.10: Simulated coupling of a traveling wave mode to a standing wave mode. The transmission spectra in c correspond to the colored circles in the other three plots.

## 1.3 Cavity Optomechanics

### 1.3.1 Dispersive Coupling Between the Mechanical and Optical Modes

The optomechanical coupling affects the optical mode by tuning its resonant frequency as a function of displacement, $\omega_o(\alpha)$; whereas the coupling affects the mechanical mode by applying a force, which is expressed as a gradient of the cavity energy, $\mathrm{d}\left|c\right|^2/\mathrm{d}\alpha$. The optical resonant frequency is usually expanded in orders of the (small)

displacement, $\alpha$ around some equilibrium displacement, $\alpha_0$.

$$\omega_{\rm o}(\alpha) = \omega_{\rm o}\Big|_{\alpha=\alpha_0} + (\alpha-\alpha_0)\frac{{\rm d}\omega_{\rm o}}{{\rm d}\alpha}\Big|_{\alpha=\alpha_0} + \frac{1}{2}(\alpha-\alpha_0)^2\frac{{\rm d}^2\omega_{\rm o}}{{\rm d}\alpha^2}\Big|_{\alpha=\alpha_0} + ... \tag{1.77}$$

In the case that the terms higher than first order can be neglected, this equation simplifies to

$$\omega_{\rm o}(\alpha) = \omega_{\rm o}\Big|_{\alpha=\alpha_0} + (\alpha-\alpha_0)\frac{{\rm d}\omega_{\rm o}}{{\rm d}\alpha}\Big|_{\alpha=\alpha_0} \equiv \omega_{\rm o} + (\alpha-\alpha_0)g_{\rm OM} \equiv \omega_{\rm o} + (\alpha-\alpha_0)\frac{\omega_{\rm o}}{L_{\rm OM}}\ , \tag{1.78}$$

where $\omega_{\rm o} \equiv \omega_{\rm o}\Big|_{\alpha=\alpha_0}$ is the equilibrium resonance frequency of the optical mode, $g_{\rm OM} \equiv \frac{{\rm d}\omega_{\rm o}}{{\rm d}\alpha}\Big|_{\alpha=\alpha_0}$ is the derivative of the resonance frequency of the optical mode evaluated at equilibrium, and $L_{\rm OM}$ is the *effective optomechanical length* of the system. The effective length, $L_{\rm OM}$, is a universal parameter that relates displacement to a change in optical frequency (i.e. $\alpha/L_{\rm OM} = \delta\omega_{\rm o}/\omega_{\rm o}$). From the definition, $L_{\rm OM}^{-1} \equiv \frac{1}{\omega_{\rm o}}\frac{{\rm d}\omega_{\rm o}}{{\rm d}\alpha}\Big|_{\alpha=\alpha_0} = g_{\rm OM}/\omega_0$, one can see that reducing $L_{\rm OM}$ maximizes the optomechanical coupling. Moreover, this optomechanical coupling length is "diffraction limited" to $\lambda_{\rm o}/(2n_{\rm eff})$, where $\lambda_{\rm o}$ is the free space optical wavelength and $n_{\rm eff}$ is the effective index of the optical mode. It is simple to show that $L_{\rm OM}$ is equal to the spacing between the mirrors of a Fabry-Perot cavity when one mirror is allowed to move along the cavity axis or the radius of a microtoroid/microdisk for a radial breathing motion, which clearly has a lower limit of half the optical wavelength. For a "Zipper" cavity or double-microdisk, $L_{\rm OM}$ is an exponentially decreasing function of the spacing between the coupled elements, with $L_{\rm OM}$ approaching half the effective optical wavelength of light in the material as the *spacing* approaches zero.

In terms of the coupling parameters, then, the optical force can be written as

$$|F_{\rm optical}| = \frac{{\rm d}\,|c|^2}{{\rm d}\alpha} = \frac{{\rm d}\,|c|^2}{{\rm d}\omega_{\rm o}}\frac{{\rm d}\omega_{\rm o}}{{\rm d}\alpha} = \frac{|c|^2}{\omega_{\rm o}}\frac{{\rm d}\omega_{\rm o}}{{\rm d}\alpha} = \frac{|c|^2}{L_{\rm OM}}\ . \tag{1.79}$$

The perturbation theory of Maxwell's equations with shifting material boundaries

[19] allows one to calculate the derivative of the resonant frequency of a structure's optical modes with respect to some parameterization of a surface deformation, $h(\alpha;\mathbf{r})$, *perpendicular* to the surface of the structure. This results in the derivative of the dispersion with respect to alpha being equal to

$$\frac{\mathrm{d}\omega_\mathrm{o}}{\mathrm{d}\alpha} = \frac{\omega_\mathrm{o}}{2}\frac{\int \mathrm{d}A \frac{\mathrm{d}h}{\mathrm{d}\alpha}\left[\Delta\epsilon\left|\mathbf{E}_\parallel\right|^2 - \Delta(\epsilon^{-1})\left|\mathbf{D}_\perp\right|^2\right]}{\int \mathrm{d}V \epsilon\left|\mathbf{E}\right|^2}\,. \tag{1.80}$$

Thus, if the result of a mechanical simulation is the displacement field, $\mathbf{Q}(\mathbf{r}) = \alpha\mathbf{q}(\mathbf{r}) \equiv \alpha\mathbf{Q}(\mathbf{r})/\max(|\mathbf{Q}|)$, then using the definition of the effective optomechanical coupling length, $L_\mathrm{OM}$, and accounting for field normalizations,

$$\frac{1}{L_\mathrm{OM}} = \frac{1}{4}\int \mathrm{d}A\,(\mathbf{q}\cdot\hat{\mathbf{n}})\left[\Delta\epsilon\left|\mathbf{e}_\parallel\right|^2 - \Delta(\epsilon^{-1})\left|\mathbf{d}_\perp\right|^2\right] \tag{1.81}$$

where $\mathbf{d} = \epsilon\mathbf{e}$, $\hat{\mathbf{n}}$ is the unit normal vector on the surface of the unperturbed cavity, $\Delta\epsilon = \epsilon_1 - \epsilon_2$, $\Delta(\epsilon^{-1}) = \epsilon_1^{-1} - \epsilon_2^{-1}$, $\epsilon_1$ is the dielectric constant of the structure, and $\epsilon_2$ is the dielectric constant of the surrounding medium.

To calculate $L_\mathrm{OM}$ by deforming the structure, one must simulate the fields with a deformation amplitude, $\alpha$, that is large enough to be detectable numerically but small enough that higher order dispersion does not affect the frequency shift. To verify that higher order dispersion is not included, one must simulate the optical fields for a range of displacement amplitudes and extract the linear dispersion. Because perturbation theory can calculate the linear term exactly from a single calculation using the *undeformed* structure, this method has clear advantages over numerical methods using finite deformations.

### 1.3.2 Coupled Equations of Cavity Optomechanics

For a harmonic optical field $\mathbf{E}(\mathbf{r})$[23], which is described by the mode amplitude $c$, and a displacement (acoustic) field $\mathbf{Q}(\mathbf{r})$, described by mode amplitude $\alpha$, the optomechanical interaction of linear order (terms of order $\mathrm{d}^2\omega_\mathrm{o}/\mathrm{d}\alpha^2$ and higher are neglected and $\alpha_0 \equiv 0$) of the fields is governed by the coupled differential equations

$$\dot{c}(t) = \left(-\tfrac{\kappa}{2} - i\omega_\mathrm{o}\left(1 \mp \tfrac{\alpha(t)}{L_\mathrm{OM}}\right)\right)c(t) + i\sqrt{\tfrac{\kappa_e}{2}}se^{-i\omega t} \tag{1.82}$$

$$\ddot{\alpha} + \Gamma_i\dot{\alpha} + \Omega^2\alpha = \pm\frac{|c|^2}{m_\mathrm{eff}L_\mathrm{OM}} \tag{1.83}$$

where $\kappa \equiv \kappa_\mathrm{i} + \kappa_\mathrm{ext}$, $\kappa_\mathrm{i} \equiv \omega_\mathrm{o}/Q_\mathrm{op,i}$ is the intrinsic optical loss rate of the of the cavity; $\kappa_\mathrm{ext}$ is the extrinsic coupling rate between the optical input field and the optical cavity field; $s$ is the amplitude of the input field, normalized such that $|s|^2 \equiv P_0$ is the optical input power impinging on the cavity; $\Omega$ is the acoustic resonance frequency of the cavity[24]; $\Gamma \equiv \Omega/Q_\mathrm{m,i}$ is the intrinsic acoustic loss rate of the cavity; and $m_\mathrm{eff} \equiv \rho V_\mathrm{acoustic}$ is the effective mass of the acoustic mode of the cavity, being the product of the mass density and the effective volume of the acoustic mode. Here we use the convention that the optical resonance frequency is decreasing with increasing $\alpha$ and the optical force is the positive gradient of the cavity energy; this is the typical convention, but it is completely arbitrary[25].

[23]This work will apply to a standing wave optical mode coupled to a traveling wave input field (as discussed in section 1.2.7. To map all the equations derived below to a traveling wave optical mode that is co-directionally-coupled to a traveling wave input field (with no parasitic coupling), one must substitute $\kappa_e/2 \to \kappa_e$, along with the different relation for $\kappa_e/\kappa$. However, this is *all* one must do to move back and forth between these two pictures.

[24]Because the acoustic differential equation is second order, the damping coefficient that multiplies the velocity is the *energy* loss rate, not the amplitude loss rate. Thus $\Gamma$ is the linewidth of the power spectrum of the acoustic mode. The distinction is important, as it can be confusing since it is $\kappa/2$ that appears as the damping coefficient in the first-order optical differential equation, but $\kappa$ is the linewidth (energy damping rate).

[25]This is essentially a statement that the direction that positive $\alpha$ points is arbitrary. The combination of the signs in the coupled differential equations, however, is not arbitrary. One must change the sign of both to make physical sense, since, for instance, whether blue or red detuning induces mechanical gain will be changed if one is changed without the other.

### 1.3.3 Sideband Formalism

One approximate method of solving the linear equations of optomechanics (1.82) and (1.83) is to treat the acoustic mode as a small perturbation of the optical mode, find the effect of the acoustic mode on the optical field, and then calculate what effect the perturbed optical mode has on the acoustic mode. Starting with the premise that the displacement, $\alpha$, is sinusoidal; i.e.

$$\alpha(t) = \alpha_0 \sin(\Omega t) \ , \tag{1.84}$$

the mode amplitude, $c$, is thus described by

$$\dot{c}(t) = \left( -\frac{\kappa}{2} - i\omega_{\mathrm{o}} \left( 1 - \frac{\alpha(t)}{L_{\mathrm{OM}}} \right) \right) c(t) + i\sqrt{\frac{\kappa_e}{2}} s e^{-i\omega t} \ . \tag{1.85}$$

#### 1.3.3.1 Formal Solution

The homogeneous solution to (1.85) is

$$c_h(t) = C_0 \exp\left( \left( -\frac{\kappa}{2} - i\omega_{\mathrm{o}} \right) t - i\frac{\alpha_0}{L_{\mathrm{OM}}} \frac{\omega_{\mathrm{o}}}{\Omega} \cos(\Omega t) \right) \ . \tag{1.86}$$

The particular solution to (1.85) can take the form $c_p(t) = C(t)c_h(t)$, satisfying

$$\dot{C}(t) = \frac{1}{c_h(t)} i\sqrt{\frac{\kappa_e}{2}} s e^{-i\omega t} = is\sqrt{\frac{\kappa_e}{2}} \exp\left( \left( \frac{\kappa}{2} + i\omega_{\mathrm{o}} \right) t + i\frac{\alpha_0}{L_{\mathrm{OM}}} \frac{\omega_{\mathrm{o}}}{\Omega} \cos(\Omega t) - i\omega t \right) \ , \tag{1.87}$$

where $C_0$ has been absorbed into $C(t)$.

Introducing the modulation index

$$\beta \equiv \frac{\alpha_0}{L_{\mathrm{OM}}} \frac{\omega_{\mathrm{o}}}{\Omega} \ , \tag{1.88}$$

the cosine part of the argument of the exponential can be expanded into Bessel functions as

$$\exp\left(\pm i\beta\cos(\Omega t)\right) = \sum_{n=-\infty}^{+\infty} (\pm i)^n J_n(\beta) e^{in\Omega t} \ , \tag{1.89}$$

which is known as the Jacobi-Anger expansion. This allows straight-forward integration of $C$; to wit,

$$C(t) = is\sqrt{\frac{\kappa_e}{2}} \sum_{n=-\infty}^{+\infty} \frac{i^n J_n(\beta)}{\frac{\kappa}{2} + i(n\Omega - \Delta)} e^{i\left(\frac{\kappa}{2} + n\Omega - \omega + \omega_o\right)t} \ . \tag{1.90}$$

Thus

$$c_p(t) = C(t)c_h(t) = is\sqrt{\frac{\kappa_e}{2}} \sum_{n=-\infty}^{+\infty} \frac{i^n J_n(\beta)}{\frac{\kappa}{2} + i(n\Omega - \Delta)} e^{i(n\Omega - \omega)t + i\beta\cos(\Omega t)} \ . \tag{1.91}$$

The general solution is then $c(t) = c_h(t) + c_p(t)$. As $c_h(t)$ is exponentially damped at rate $\kappa$, the general solution rapidly converges to $c_p(t)$, which is the steady-state solution. This optical mode amplitude can thus be used to compute the various properties of the optomechanical system.

#### 1.3.3.2 The Transmission of an Oscillating Cavity

The steady state power exiting the cavity is

$$s_{out} = ise^{-i\omega t} - \sqrt{\frac{\kappa_e}{2}} c_p(t) \ , \tag{1.92}$$

and thus

$$|s_{out}|^2 = |-is_{out}|^2 = \left| se^{-i\omega t} + i\sqrt{\frac{\kappa_e}{2}} c_p(t) \right|^2 = |s|^2 + \frac{\kappa_e}{2} |c_p(t)|^2 - 2\mathrm{Im}\left\{ \sqrt{\frac{\kappa_e}{2}} c_p s^* e^{i\omega t} \right\} \tag{1.93}$$

with

$$-2\mathrm{Im}\left\{\sqrt{\frac{\kappa_e}{2}}c_p s^* e^{i\omega t}\right\} = -\kappa_e \left|s\right|^2 \mathrm{Re}\left\{\sum_{n,m}\frac{i^{(n-m)}J_n(\beta)J_m(\beta)}{\frac{\kappa}{2}+i(n\Omega-\Delta)}e^{i(n+m)\Omega t}\right\} \tag{1.94}$$

and

$$\left|c_p(t)\right|^2 = \frac{\kappa_e}{2}\left|s\right|^2\sum_{n,m}\frac{i^{(n-m)}J_n(\beta)J_m(\beta)}{\left(\frac{\kappa}{2}+i(n\Omega-\Delta)\right)\left(\frac{\kappa}{2}-i(m\Omega-\Delta)\right)}e^{i(n-m)\Omega t}\,. \tag{1.95}$$

#### 1.3.3.3 RF Spectrum of the First Order Sidebands

The experimental arrangement in this work is such that the optical mode is observed by weakly populating the cavity with photons via the tapered optical fiber waveguide and then collecting the transmitted photons via the same waveguide. The RF spectrum of the power transmitted, $\left|s_{out}\right|^2$, is obtained by simple photomixing on an avalanche photodiode (APD). This RF spectrum contains information about the mechanical modes because the mechanical modes modulate the optical mode via the optomechanical coupling. The modulation manifests as a set of sidebands created in the cavity that are transmitted and detected at the APD. If the amount of optical modulation, $\beta$, is small (i.e. $\beta \ll 1$), only the first sideband contributes, as $J_n(\beta \to 0) \approx \frac{1}{n!}\left(\frac{\beta}{2}\right)^n$. In this case, only the product $J_0(\beta)J_{\pm1}(\beta)$ contributes to the signal, and we thus need only consider terms with $n = 0, m = \pm1$ and $n = \pm1, m = 0$ (terms with $n = 0, m = 0$ are DC and do not contribute to the RF spectrum). Also note that, for $\beta \ll 1$, $J_0(\beta) \approx 1$, and $J_{\pm1}(\beta) \approx \pm\frac{\beta}{2}$. As an example, for the breathing mode of a silicon nanobeam, one can have $\omega_o/\Omega \approx 10^5$ and, with $\alpha$ given by the thermal amplitude of oscillation $\alpha = \sqrt{k_B T/m_{\mathrm{eff}}\Omega^2}$, $\alpha/L_{\mathrm{OM}} \approx 2 * 10^{-13}$ m$/5 * 10^{-6}$ m$= 5 * 10^{-8}$, $\beta \approx 5 * 10^{-3}$. Note that this condition is *independent* of the degree of sideband resolution, which is $\Omega/(\kappa/2)$; the system can have small modulation in either the sideband-resolved or sideband-unresolved regimes.

In this small modulation approximation, the power oscillating at $\Omega$ is

$$\begin{aligned}
\frac{|s_{out,\Omega}|^2}{|s|^2} &= -\kappa_e \mathrm{Re}\left\{\frac{-i(\beta/2)e^{-i\Omega t}}{\frac{\kappa}{2}-i\Delta}+\frac{-i(\beta/2)e^{+i\Omega t}}{\frac{\kappa}{2}-i\Delta}+\frac{i(\beta/2)e^{+i\Omega t}}{\frac{\kappa}{2}+i(\Omega-\Delta)}+\frac{i(\beta/2)e^{-i\Omega t}}{\frac{\kappa}{2}+i(-\Omega-\Delta)}\right\} \\
&\quad +\left(\frac{\kappa_e}{2}\right)^2\left\{\frac{-i(\beta/2)e^{-i\Omega t}}{\left(\frac{\kappa}{2}-i\Delta\right)\left(\frac{\kappa}{2}-i(\Omega-\Delta)\right)}\right\} \\
&\quad +\left(\frac{\kappa_e}{2}\right)^2\left\{\frac{-i(\beta/2)e^{+i\Omega t}}{\left(\frac{\kappa}{2}-i\Delta\right)\left(\frac{\kappa}{2}+i(\Omega+\Delta)\right)}\right\} \\
&\quad +\left(\frac{\kappa_e}{2}\right)^2\left\{\frac{i(\beta/2)e^{+i\Omega t}}{\left(\frac{\kappa}{2}+i(\Omega-\Delta)\right)\left(\frac{\kappa}{2}+i\Delta\right)}\right\} \\
&\quad +\left(\frac{\kappa_e}{2}\right)^2\left\{\frac{i(\beta/2)e^{-i\Omega t}}{\left(\frac{\kappa}{2}-i(\Omega+\Delta)\right)\left(\frac{\kappa}{2}+i\Delta\right)}\right\} . \qquad (1.96)
\end{aligned}$$

This expression can be simplified by combining the terms proportional to $(\kappa_e/2)^2$ (those four terms are really just two terms plus their complex conjugates, which can be written as twice the real part of one term). With this simplification, one finds

$$\begin{aligned}
\frac{|s_{out,\Omega}|^2}{|s|^2} &= -\kappa_e \mathrm{Re}\left\{\frac{-i(\beta/2)e^{-i\Omega t}}{\frac{\kappa}{2}-i\Delta}+\frac{-i(\beta/2)e^{+i\Omega t}}{\frac{\kappa}{2}-i\Delta}+\frac{i(\beta/2)e^{+i\Omega t}}{\frac{\kappa}{2}+i(\Omega-\Delta)}+\frac{i(\beta/2)e^{-i\Omega t}}{\frac{\kappa}{2}+i(-\Omega-\Delta)}\right\} \\
&\quad +\frac{\kappa_e^2}{2}\mathrm{Re}\left\{\frac{-i(\beta/2)e^{-i\Omega t}}{\left(\frac{\kappa}{2}-i\Delta\right)\left(\frac{\kappa}{2}-i(\Omega-\Delta)\right)}+\frac{-i(\beta/2)e^{+i\Omega t}}{\left(\frac{\kappa}{2}-i\Delta\right)\left(\frac{\kappa}{2}+i(\Omega+\Delta)\right)}\right\} \\
&\equiv -\kappa_e X+\frac{\kappa_e^2}{2}Y . \qquad (1.97)
\end{aligned}$$

At this point, we must break this into two terms proportional to $\sin(\Omega t)$ and $\cos(\Omega t)$. Then the quadrature sum of those terms will be equal to the total power at $\Omega$.

These terms can be expanded and then simplified to yield

$$
\begin{aligned}
X &= -16\beta\Delta\Omega\frac{\Omega(4\Delta^2-3\kappa^2-4\Omega^2)\cos(\Omega t)+\kappa(4\Delta^2+\kappa^2)\sin(\Omega t)}{(\kappa^2+4\Delta^2)\left(16\Delta^4+8\Delta^2(\kappa^2-4\Omega^2)+(\kappa^2+4\Omega^2)^2\right)} \\
&= -\cos(\Omega t)\left[-\frac{\beta}{2}\left(\frac{2\Delta}{\left(\frac{\kappa}{2}\right)^2+\Delta^2}+\frac{\Omega-\Delta}{\left(\frac{\kappa}{2}\right)^2+(\Omega-\Delta)^2}-\frac{\Omega+\Delta}{\left(\frac{\kappa}{2}\right)^2+(\Omega+\Delta)^2}\right)\right] \\
&\quad -\sin(\Omega t)\left[\frac{\beta\kappa}{4}\left(\frac{1}{\left(\frac{\kappa}{2}\right)^2+(\Omega-\Delta)^2}-\frac{1}{\left(\frac{\kappa}{2}\right)^2+(\Omega+\Delta)^2}\right)\right] \qquad (1.98)
\end{aligned}
$$

$$
\begin{aligned}
Y &= (\beta/2)\left[-\cos(\Omega t)\left(\frac{-\kappa\Omega/2}{\left((\frac{\kappa}{2})^2-\Delta(\Omega-\Delta)\right)^2+\left(\frac{\kappa}{2}\Omega\right)^2}+\frac{\kappa\Omega/2}{\left((\frac{\kappa}{2})^2+\Delta(\Omega+\Delta)\right)^2+\left(\frac{\kappa}{2}\Omega\right)^2}\right)\right. \\
&\quad \left.-\sin(\Omega t)\left(\frac{(\frac{\kappa}{2})^2-\Delta(\Omega-\Delta)}{\left((\frac{\kappa}{2})^2-\Delta(\Omega-\Delta)\right)^2+\left(\frac{\kappa}{2}\Omega\right)^2}-\frac{(\frac{\kappa}{2})^2+\Delta(\Omega+\Delta)}{\left((\frac{\kappa}{2})^2+\Delta(\Omega+\Delta)\right)^2+\left(\frac{\kappa}{2}\Omega\right)^2}\right)\right] \\
&= (\beta/2)\left[\cos(\Omega t)\left(\frac{2\kappa}{\kappa^2+4\Delta^2}\right)\left(\frac{\Omega}{(\frac{\kappa}{2})^2+(\Omega-\Delta)^2}-\frac{\Omega}{(\frac{\kappa}{2})^2+(\Omega+\Delta)^2}\right)\right. \\
&\quad \left.+\sin(\Omega t)\left(\frac{4\Omega}{\kappa^2+4\Delta^2}\right)\left(\frac{\Omega-\Delta}{(\frac{\kappa}{2})^2+(\Omega-\Delta)^2}-\frac{\Omega+\Delta}{(\frac{\kappa}{2})^2+(\Omega+\Delta)^2}\right)\right]. \qquad (1.99)
\end{aligned}
$$

So finally, we have

$$
\begin{aligned}
\frac{|s_{out,\Omega}|^2}{|s|^2} = \cos(\Omega t) \quad & \left[\frac{\kappa_e\beta}{2}\left(-\frac{2\Delta}{\left(\frac{\kappa}{2}\right)^2+\Delta^2}-\frac{\Omega-\Delta}{\left(\frac{\kappa}{2}\right)^2+(\Omega-\Delta)^2}+\frac{\Omega+\Delta}{\left(\frac{\kappa}{2}\right)^2+(\Omega+\Delta)^2}\right)\right. \\
& \left.+\beta\frac{\kappa_e^2}{4}\left(\frac{2\kappa}{\kappa^2+4\Delta^2}\right)\left(\frac{\Omega}{(\frac{\kappa}{2})^2+(\Omega-\Delta)^2}-\frac{\Omega}{(\frac{\kappa}{2})^2+(\Omega+\Delta)^2}\right)\right] \\
+\sin(\Omega t) \quad & \left[\frac{\kappa_e\beta}{2}\left(\frac{\kappa/2}{\left(\frac{\kappa}{2}\right)^2+(\Omega-\Delta)^2}-\frac{\kappa/2}{\left(\frac{\kappa}{2}\right)^2+(\Omega+\Delta)^2}\right)\right. \qquad (1.100) \\
& \left.+\beta\frac{\kappa_e^2}{4}\left(\frac{4\Omega}{\kappa^2+4\Delta^2}\right)\left(\frac{\Omega-\Delta}{(\frac{\kappa}{2})^2+(\Omega-\Delta)^2}-\frac{\Omega+\Delta}{(\frac{\kappa}{2})^2+(\Omega+\Delta)^2}\right)\right].
\end{aligned}
$$

If we say then, that

$$\frac{|s_{out,\Omega}|^2}{|s|^2} = \cos(\Omega t)A_{cos} + \sin(\Omega t)A_{sin} \ , \tag{1.101}$$

then the total power at frequency $\Omega$ (in both quadratures) is

$$|s_{out,\Omega}|^2 = |s|^2 \sqrt{A_{cos}^2 + A_{sin}^2} \ . \tag{1.102}$$

#### 1.3.3.4 Optical Forces

Referring to equations (1.79) and (1.91), the optical force is equal to

$$|c_p(t)|^2 / L_{\rm OM} = \frac{\kappa_e}{2L_{\rm OM}} |s|^2 \sum_{n,m} \frac{i^{(n-m)} J_n(\beta) J_m(\beta)}{\left(\frac{\kappa}{2} + i(n\Omega - \Delta)\right)\left(\frac{\kappa}{2} - i(m\Omega - \Delta)\right)} e^{i(n-m)\Omega t} \ . \tag{1.103}$$

We will again work in the limit of small modulation depth ($\beta \ll 1$). In this caase, the DC force is found by considering the term for which $m = n = 0$ (the next DC term is $m = n = \pm 1$, which is of order $\beta^2$), which is simply proportional to the unperturbed cavity energy,

$$F_{\rm optical,DC} = \frac{1}{L_{\rm OM}} \frac{2(\kappa_e/\kappa^2)}{1 + 4\left(\frac{\Delta}{\kappa}\right)^2} P_0 \ . \tag{1.104}$$

In the limit of small modulation, just as in the consideration of the RF transmission spectrum, there will be four terms at frequency $\Omega$. These are the same four terms, and, in fact, in this approximation, $|c_p(t)|^2 = |s|^2 \kappa_e Y$ (see Eq. (1.99)). Thus the RF force is

$$
\begin{aligned}
F_{\text{optical},\Omega} &\equiv F_Q \cos(\Omega t) + F_I \sin(\Omega t) = F_Q \frac{\dot{\alpha}}{\Omega \alpha_0} + F_I \frac{\alpha}{\alpha_0} \qquad (1.105)\\
&= |s|^2 \frac{\kappa_e \beta}{2L_{\text{OM}}} \Bigg[ \cos(\Omega t) \left( \frac{2\kappa}{\kappa^2 + 4\Delta^2} \right) \left( \frac{\Omega}{(\frac{\kappa}{2})^2 + (\Omega - \Delta)^2} - \frac{\Omega}{(\frac{\kappa}{2})^2 + (\Omega + \Delta)^2} \right) \\
&\quad + \sin(\Omega t) \left( \frac{4\Omega}{\kappa^2 + 4\Delta^2} \right) \left( \frac{\Omega - \Delta}{(\frac{\kappa}{2})^2 + (\Omega - \Delta)^2} - \frac{\Omega + \Delta}{(\frac{\kappa}{2})^2 + (\Omega + \Delta)^2} \right) \Bigg] ,
\end{aligned}
$$

where $F_Q$ and $F_I$ are the in-quadrature and in-phase components of the force, respectively.

We can now rewrite the differential equation for the acoustic mode, Eq. (1.83), to include the effects of the optical mode.

$$
\ddot{\alpha} + \Gamma_i \dot{\alpha} + \Omega^2 \alpha = \frac{1}{m_{\text{eff}}} \left( F_Q \frac{\dot{\alpha}}{\Omega \alpha_0} + F_I \frac{\alpha}{\alpha_0} + F_{\text{DC}} \right) \qquad (1.106)
$$

Thus, we can rewrite the acoustic mode amplitude's differential equation as

$$
\ddot{\alpha} + (\Gamma_i + \Gamma)\dot{\alpha} + \left( \Omega^2 + \delta\Omega^2 \right) \alpha = \frac{1}{m_{\text{eff}}} F_{\text{DC}} \, , \qquad (1.107)
$$

with

$$
\begin{aligned}
\Gamma &\equiv -\frac{1}{m_{\text{eff}} \Omega \alpha_0} F_Q \qquad (1.108)\\
\delta(\Omega^2) \approx 2\Omega\delta\Omega &\equiv -\frac{1}{m_{\text{eff}} \alpha_0} F_I \qquad (1.109)
\end{aligned}
$$

$$
\Gamma = -\frac{\omega_{\text{o}}}{\Omega L_{\text{OM}}^2 m_{\text{eff}}} \left( \frac{2\kappa_e \left| s \right|^2}{\kappa^2 + 4\Delta^2} \right) \left( \frac{\kappa/2}{(\frac{\kappa}{2})^2 + (\Omega - \Delta)^2} - \frac{\kappa/2}{(\frac{\kappa}{2})^2 + (\Omega + \Delta)^2} \right) \qquad (1.110)
$$

$$
\delta\Omega = -\frac{\omega_{\text{o}}}{2\Omega L_{\text{OM}}^2 m_{\text{eff}}} \left( \frac{2\kappa_e \left| s \right|^2}{\kappa^2 + 4\Delta^2} \right) \left( \frac{\Omega - \Delta}{(\frac{\kappa}{2})^2 + (\Omega - \Delta)^2} - \frac{\Omega + \Delta}{(\frac{\kappa}{2})^2 + (\Omega + \Delta)^2} \right) \qquad (1.111)
$$

#### 1.3.3.5 Power Transfer and Effective Temperature

The power transfer between the optical and mechanical mode is (see, for instance, [5])

$$\langle P \rangle = \langle F_{\text{optical}} \cdot \dot{\alpha} \rangle = \left\langle \alpha_0 \Omega_{\text{m}} \left( F_Q \cos(\Omega t)^2 + F_I \sin(\Omega t) \cos(\Omega t) \right) \right\rangle = \frac{\alpha_0 \Omega_{\text{m}}}{2} F_Q \ . \tag{1.112}$$

With equation 1.108, we can thus write $\langle P \rangle = -\frac{\alpha_0^2}{2} m_{\text{eff}} \Omega_{\text{m}}^2 \Gamma = -\langle \alpha^2 \rangle m_{\text{eff}} \Omega^2 \Gamma$.

The free evolution of the average mechanical energy, $E_m$ obeys $\frac{\text{d}}{\text{d}t} \langle E_m \rangle = -\Gamma_i \langle E_m \rangle + k_B T_R \Gamma_i$, where $T_R$ is the reservoir temperature. This gives the expected steady-state result that $\langle E_m \rangle = k_B T_R$. In the presence of the optical field, the loss rate of the mechanical system is modified. However, the optical field does not modify the reservoir temperature [5], which means that the evolution of the mechanical energy changes to $\frac{\text{d}}{\text{d}t} \langle E_m \rangle = -(\Gamma_i + \Gamma) \langle E_m \rangle + k_B T_R \Gamma_i$. Thus the steady-state result gives an effective temperature $T_{eff} = \frac{\Gamma_i}{\Gamma_i + \Gamma} T_R$.

The effective temperature changes the total power of a mechanical mode, whereas the change in linewidth from $\Gamma$ just narrows (or broadens) the mechanical resonance.

### 1.3.4 Calculating the Power Spectral Density

The thermal amplitude of oscillation is defined by

$$\frac{1}{2} m_{\text{eff}} \Omega^2 \alpha_{thermal}^2 = \frac{1}{2} k_B T \ . \tag{1.113}$$

Thus we can define a thermal modulation index given by

$$\beta_{thermal} = \frac{\alpha_{thermal}}{L_{\text{OM}}} \frac{\omega_{\text{o}}}{\Omega} \ . \tag{1.114}$$

Using equations (1.100) - (1.102) and $\beta_{thermal}$, one can find the total transmitted power oscillating at frequency $\nu = \Omega/(2\pi)$, $|s_{out,\nu}|^2$. Only a fraction of this output power reaches the detector, and we'll call this $P_{@det,\nu} = \mu |s_{out,\nu}|^2$

The transimpedance gain of the detector, $G_{TI,0}$, converts optical power to a volt-

age; the gain has a simple pole, however, at frequency $\nu_{det}$. Thus the total gain of the detector at the frequency of the oscillator, $\nu$, is $G_{TI}(\nu) = G_{TI,0}/\left(1 + (\nu/\nu_{det})^2\right)$. This voltage is then fed to the input of a buffered channel amplifier with unity gain and a simple pole at frequency, $\nu_{scope}$ (however, in post-processing, the oscilloscope flattens its own response; so that power spectral densities do not contain the oscilloscope's pole); then the voltage across the load resistor (input impedance $Z$) at the output of the channel amplifier is used to compute a "power", such that

$$P_{RF,\nu} = \left( \frac{\mu \left| s_{out,\nu} \right|^2 G_{TI,0}(\nu)}{(1 + (\nu/\nu_{det})^2)} \right)^2 /Z \ . \tag{1.115}$$

Because the spectrum of a mechanical resonator is distributed over all frequencies, we must calculate how much power is in a given frequency interval, $\mathrm{d}\nu \equiv \mathrm{d}\Omega/(2\pi)$. If the spectrum is a Lorentzian, we must have that

$$P_{RF,\nu} = \int_{-\infty}^{\infty} S^2(\nu)\mathrm{d}\nu' = \int_{-\infty}^{\infty} \frac{S^2(\nu)}{1 + \left(\frac{\nu'-\nu}{\delta\nu/2}\right)^2}\mathrm{d}\nu' = \pi S^2(\nu)\delta\nu/2 = \frac{\pi\nu S^2(\nu)}{2Q_m} \ . \tag{1.116}$$

Thus the power spectral density at the peak is

$$S^2(\nu) = \frac{2Q_m P_{RF,\nu}}{\pi\nu} \ . \tag{1.117}$$

Note that an oscilloscope typically displays $S^2(\nu) * RBW$, where $RBW$ is the resolution bandwidth (the reciprocal of the time record length of the FFT).

### 1.3.5 Extracting the Product $m_{\mathrm{eff}} L_{\mathrm{OM}}^2$ from Experimental RF Spectra

Equation 1.117 allows simple extraction of the total RF power in each mechanical mode. Equations (1.100) - (1.102) can then be used to calculate the product $m_{\mathrm{eff}} L_{\mathrm{OM}}^2$ for each mode, albeit indirectly (since it is not simple to invert the equations). Given $\kappa_e$, $\kappa$, $\Delta$, $\nu_{\mathrm{m}}$, and $\nu_{\mathrm{o}}$, which are all experimentally-measured parameters (and $\Delta$ is directly set to be the $\Delta$ which gives the maximum transduction) the product $m_{\mathrm{eff}} L_{\mathrm{OM}}^2$

uniquely determines the transduced power due to Brownian motion in each mode. Then a numerical root finder can be used to find the product $m_{\text{eff}} L_{\text{OM}}^2$ that gives the correct transduced power from Eq. 1.117.

### 1.3.6 Thermooptic Effects in Cavity Optomechanics

We begin with the set of coupled equations describing mechanical and optical motion,

$$\dot{a} = -(i(\Delta_o - g_{\text{OM}} x) + \Gamma/2)a + \kappa s, \tag{1.118}$$

$$\ddot{x} = -\gamma_M \dot{x} - \Omega_M^2 x - \frac{|a|^2 g_{\text{OM}}}{\omega_o m_x}, \tag{1.119}$$

where $\Delta_o \equiv (\omega_l - \omega_o)$ is the bare laser detuning from the optical cavity resonance ($\omega_o$), $\Gamma$ is the optical cavity (energy) decay rate, $\kappa (= \sqrt{1/\tau_e})$ is the input coupling rate of the laser into the cavity, $|s|^2$ is the optical input power, $g_{\text{OM}} \equiv \mathrm{d}\omega/\mathrm{d}x$ is the optomechanical factor, $\gamma_M$ is the bare mechanical (energy) damping factor, $\Omega_M (= \sqrt{k/m_x})$ is the bare mechanical frequency, $m_x$ is the bare motional mass of the mechanical resonator, and $a$ is the amplitude of the optical cavity field normalized so that $|a|^2$ represents the stored optical cavity energy. The equation for $a$ is written in a slowly varying basis in which the laser frequency, $\omega_l$, has been removed from both $a$ and $s$.

In order to include the effects of thermo-optic tuning of the cavity resonance, we include a third equation for the cavity temperature increase, $\Delta T$:

$$\dot{a} = -(i(\Delta_o - (g_{\text{OM}} x + g_{th} \Delta T)) + \Gamma/2)a + \kappa s, \tag{1.120}$$

$$\ddot{x} = -\gamma_M \dot{x} - \Omega_M^2 x - \frac{|a|^2 g_{\text{OM}}}{\omega_o m_x}, \tag{1.121}$$

$$\dot{\Delta T} = -\gamma_{th} \Delta T + \Gamma_{abs} |a|^2 c_{th}, \tag{1.122}$$

where $g_{th} = -(\mathrm{d}n/\mathrm{d}T)(\omega_o/n_o)$ is the thermo-optic tuning coefficient, $\mathrm{d}n/\mathrm{d}T$ is the

thermo-optic coefficient of the optical and mechanical cavity material, $\Gamma_{abs}$ is the component of the optical energy decay which is due to material absorption, $c_{th}$ is the thermal heat capacity of the cavity, and $\gamma_{th}$ is temperature decay rate.

In order to solve these coupled equations we proceed using a perturbation approach [5]. We assume that the mechanical motion is harmonic in time with small amplitude parameter $\epsilon_x$, $x(t) = x_o + \epsilon_x \cos(\Omega_M t)$. The optical cavity mode amplitude and the cavity temperature increase can be expanded in terms of the small parameter $\epsilon_x$,

$$a(x,t) = \sum_{n=0}^{\infty} \epsilon_x^n a_n(x,t), \tag{1.123}$$

$$\Delta T(x,t) = \sum_{n=0}^{\infty} \epsilon_x^n \Delta T_n(x,t). \tag{1.124}$$

$$\tag{1.125}$$

Keeping terms only to first order in $\epsilon_x$ yields the following sets of coupled equations,

$$0 = -(i\Delta_o' + \Gamma/2)a_0 + \kappa s, \tag{1.126}$$

$$0 = -\Omega_M^2 x_o - \frac{|a_0|^2 g_{\mathrm{OM}}}{\omega_o m_x}, \tag{1.127}$$

$$0 = -\gamma_{th}\Delta T_o + \Gamma_{abs}|a_0|^2 c_{th}, \tag{1.128}$$

and

$$\dot{a}_1 = +i(g_{\mathrm{OM}}x_1 + g_{th}\Delta T_1))a_0 - (i\Delta_o' + \Gamma/2)a_1, \tag{1.129}$$

$$\ddot{x_1} = -\gamma_M \dot{x}_1 - \Omega_M^2 x_1 - \frac{(a_0 a_1^* + a_0^* a_1) g_{\mathrm{OM}}}{\omega_o m_x}, \tag{1.130}$$

$$\dot{\Delta T}_1 = -\gamma_{th}\Delta T_1 + \Gamma_{abs}(a_0 a_1^* + a_0^* a_1)c_{th}, \tag{1.131}$$

where $x_1 \equiv \cos(\Omega_M t)$ and $\Delta_o' = \Delta_o - (g_{\mathrm{OM}}x_o + g_{th}\Delta T_o)$ is the time averaged laser-

cavity detuning. Fourier transforming the first-order perturbation equations to convert them from differential to algebraic ones yields,

$$(i(\omega+\Delta_o')+\Gamma/2)\tilde{a}_1 = +i(g_{\mathrm{OM}}\tilde{x}_1 + g_{th}\tilde{\Delta T}_1)a_0, \tag{1.132}$$

$$(i(\omega-\Delta_o')+\Gamma/2)\tilde{a_1^*} = -i(g_{\mathrm{OM}}\tilde{x}_1 + g_{th}\tilde{\Delta T}_1)a_0^*, \tag{1.133}$$

$$-\omega^2\tilde{x}_1 = -i\omega\gamma_M\tilde{x}_1 - \Omega_M^2\tilde{x}_1 - \frac{(a_0\tilde{a_1^*} + a_0^*\tilde{a}_1)g_{\mathrm{OM}}}{\omega_o m_x}, \tag{1.134}$$

$$(i\omega+\gamma_{th})\tilde{\Delta T}_1 = \Gamma_{abs}(a_0\tilde{a_1^*} + a_0^*\tilde{a}_1)c_{th}, \tag{1.135}$$

Solving for the time-dependent part of the optical cavity energy,

$$(a_0\tilde{a_1^*} + a_0^*\tilde{a}_1) = f(\omega,\Delta_o')\left[i|a_0|^2(g_{\mathrm{OM}}\tilde{x}_1 + g_{th}\tilde{\Delta T}_1)\right], \tag{1.136}$$

where we have defined the transfer function $f$ as,

$$f(\omega,\Delta_o') = \left(\frac{1}{(i(\omega+\Delta_o')+\Gamma/2)} - \frac{1}{(i(\omega-\Delta_o')+\Gamma/2)}\right). \tag{1.137}$$

Substituting for $\tilde{\Delta T}_1$ of eq. (1.135) allows us to solve for the optical cavity energy solely in terms of the mechanical motion,

$$\left(f(\omega,\Delta_o')^{-1} - i\frac{g_{th}\Gamma_{abs}c_{th}|a_0|^2}{i\omega+\gamma_{th}}\right)(a_0\tilde{a_1^*} + a_0^*\tilde{a}_1) = i|a_0|^2 g_{\mathrm{OM}}\tilde{x}_1. \tag{1.138}$$

Defining $f'(\omega,|a_0|^2)$ and $g(\omega,\Delta_o',|a_0|^2)$ as,

$$f'(\omega,|a_0|^2) = -i\frac{g_{th}\Gamma_{abs}c_{th}|a_0|^2}{i\omega+\gamma_{th}}, \tag{1.139}$$

$$g(\omega,\Delta_o',|a_0|^2) = f\left[\frac{1+(f')^*f^*}{|1+f'f|^2}\right], \tag{1.140}$$

allows us to write for the Fourier transform of the time varying component of the cavity energy,

$$(a_0\tilde{a_1^*} + a_0^*\tilde{a}_1) = ig(\omega, \Delta_o', |a_0|^2)|a_0|^2 g_{\rm OM}\tilde{x}_1. \tag{1.141}$$

All of the transfer functions $f$, $f'$, and $g$ have the property that $h(-\omega) = -h(\omega)^*$. With $\tilde{x}_1 = (\delta(\omega - \Omega_M) + \delta(\omega - \Omega_M)/2$, we have for the cavity energy,

$$(a_0\tilde{a_1^*} + a_0^*\tilde{a}_1) = i|a_0|^2 g_{\rm OM}(g(\Omega_M)\delta(\omega - \Omega_M) + g(-\Omega_M)\delta(\omega + \Omega_M))/2 \tag{1.142}$$

$$= -\frac{|a_0|^2 g_{\rm OM}(g(\Omega_M)\delta(\omega - \Omega_M) - g^*(\Omega_M)\delta(\omega + \Omega_M))}{2i}. \tag{1.143}$$

Further simplifying this result yields,

$$(a_0\tilde{a_1^*} + a_0^*\tilde{a}_1) = -|a_0|^2 g_{\rm OM}\Big[\frac{{\rm Re}(g(\Omega_M))(\delta(\omega - \Omega_M) - \delta(\omega + \Omega_M))}{2i} \tag{1.144}$$

$$+\frac{{\rm Im}(g(\Omega_M))(\delta(\omega - \Omega_M) + \delta(\omega + \Omega_M))}{2}\Big]. \tag{1.145}$$

Finally this gives in the time-domain,

$$(a_0 a_1^*(t) + a_0^* a_1(t)) = |a_0|^2 g_{\rm OM}\left[\frac{{\rm Re}(g(\Omega_M))}{\Omega_M}(-\Omega_M \sin\Omega_M t) - {\rm Im}(g(\Omega_M))\cos\Omega_M t\right],$$

$$= |a_0|^2 g_{\rm OM}\left[\frac{{\rm Re}(g(\Omega_M))}{\Omega_M}\dot{x}_1 - {\rm Im}(g(\Omega_M))x_1\right] \tag{1.146}$$

Substituting this result into the equation of motion for $x_1(t)$ in eq. (1.130) allows one to identify renormalized mechanical frequency ($\Omega_M'$) and damping ($\gamma_M'$) terms due to optomechanical and thermo-optic interactions,

$$(\Omega_M')^2 = \Omega_M^2 - \frac{|a_0|^2 g_{\rm OM}^2 {\rm Im}(g(\Omega_M))}{\omega_o m_x}, \tag{1.147}$$

$$\gamma_M' = \gamma_M + \frac{|a_0|^2 g_{\rm OM}^2 {\rm Re}(g(\Omega_M))}{\Omega_M \omega_o m_x}. \tag{1.148}$$

The effects of the thermo-optic tuning of the cavity are manifest in the correction to the pure optomechanical transfer function ($f$) in the equation for $g$ given in eq. (1.140). This correction factor is simply $1/(1 + f'f)$. For $|f'f| \ll 1$ the thermo-optic correction is small, and can be neglected. In order to make connection with previously derived results for the optomechanical spring and gain coefficient, we now consider this correction in the sideband unresolved limit, relevant for the current zipper cavities.

#### 1.3.6.1 Sideband Unresolved Limit ($\Omega_M \ll \Gamma$)

We begin by evaluating $f(\Omega_M)$ in the limit that $\Omega_M \ll \Gamma$,

$$f(\Omega_M) \approx -2\Delta_o' \left( \frac{\Gamma\Omega_M + i\Delta^2}{\Delta^4} \right), \tag{1.149}$$

where we have defined $\Delta^2 = (\Delta_o')^2 + (\Gamma/2)^2$. In the absence of thermo-optic tuning this results in the usual equations for the sideband unresolved optical spring effect and optomechanical gain,

$$(\Omega_M')^2|_{\Delta T_1=0} = \Omega_M^2 + \left( \frac{2|a_0|^2 g_{\mathrm{OM}}^2}{\Delta^2 \omega_o m_x} \right) \Delta_o', \tag{1.150}$$

$$\gamma_M'|_{\Delta T_1=0} = \gamma_M - \left( \frac{2|a_0|^2 g_{\mathrm{OM}}^2 \Gamma}{\Delta^4 \omega_o m_x} \right) \Delta_o'. \tag{1.151}$$

As can be seen, this results in an increase in the mechanical frequency and negative damping (positive *amplification*) of the mechanical motion for blue detuned laser light (relative to the steady-state cavity resonance frequency).

#### 1.3.6.2 Sideband Eesolved Limit ($\Omega_M \gg \Gamma$)

Rewriting $f(\Omega_M)$ in terms of its real and imaginary components we find,

$$f(\Omega_M) = -2\Delta_o' \left( \frac{\Gamma\Omega_M + i\left(\Delta^2 - \Omega_M^2\right)}{\left(\Delta^2 - \Omega_M^2\right)^2 + (\Gamma\Omega_M)^2} \right). \tag{1.152}$$

Substituting this form of $f(\Omega_M)$ into the equations for the optical spring and optomechanical damping/amplification coefficients yields,

$$(\Omega'_M)^2|_{\Delta T_1=0} = \Omega_M^2 + \left( \frac{2|a_0|^2 g_{\rm OM}^2 \left(\Delta^2 - \Omega_M^2\right)}{\left(\left(\Delta^2 - \Omega_M^2\right)^2 + (\Gamma\Omega_M)^2\right)\omega_o m_x} \right) \Delta'_o, \tag{1.153}$$

$$\gamma'_M|_{\Delta T_1=0} = \gamma_M - \left( \frac{2|a_0|^2 g_{\rm OM}^2 \Gamma}{\left(\left(\Delta^2 - \Omega_M^2\right)^2 + (\Gamma\Omega_M)^2\right)\omega_o m_x} \right) \Delta'_o. \tag{1.154}$$

Further simplification for the sideband resolved limit is not generally attainable. Below we consider "optimal" detuning points for maximizing the optomechanical damping/amplification rate, from which we obtain simplifications in both the resolved and unresolved sideband limits.

#### 1.3.6.3 Optimal Detuning Points for Damping/Amplification

Of interest is the maximum optical spring and optomechanical damping/amplification rate that can be obtained for a given cavity energy or input power. Here we study both the resolved and unresolved sideband limits separately.

*Sideband unresolved limit ($\Omega_M \ll \Gamma$)*

One can easily show that the detuning point of maximum damping/amplification, for a given internal cavity energy, occurs at $\Delta'_o \approx (\pm 1/\sqrt{3})(\Gamma/2)$ in the unresolved sideband limit. The corresponding spring and maximum damping/amplification coefficients are,

$$(\Omega'_M)^2|_{\Delta T_1=0,\ \mathrm{SUR},\Delta'_o=\pm\frac{\Gamma}{2\sqrt{3}}} \approx \Omega_M^2 \pm \left( \frac{\sqrt{3}|a_0|^2 g_{\rm OM}^2}{\Gamma\omega_o m_x} \right), \tag{1.155}$$

$$\gamma'_M|_{\Delta T_1,\ \mathrm{SUR},\Delta'_o=\pm\frac{\Gamma}{2\sqrt{3}}} \approx \gamma_M \mp \left( \frac{3\sqrt{3}|a_0|^2 g_{\rm OM}^2}{\Gamma^2\omega_o m_x} \right). \tag{1.156}$$

In the case of fixed input power ($P_i$), the (time averaged) internal cavity energy is also dependent upon the (average) detuning through the cavity Lorentzian transfer

function,

$$|a_0|^2 = \left(\frac{(\Gamma/2)^2}{\Delta^2}\right)\left(\frac{4K}{1+K}\right)\frac{P_i}{\Gamma}, \tag{1.157}$$

where $K$ is the coupling parameter [20] given by the ratio of the *external* loading rate of the cavity (through a waveguide or mirror) to the *intrinsic* cavity damping rate, $K \equiv \Gamma_e/\Gamma_i$. The optimal detuning point for maximum mechanical damping/amplification and fixed input power occurs at $\Delta_o' \approx (\pm 1/\sqrt{5})(\Gamma/2)$ in the resolved sideband limit, with optomechanical coefficients,

$$(\Omega_M')^2|_{\Delta T_1=0,\ \mathrm{SUR},\Delta_o'=\pm\frac{\Gamma}{2\sqrt{3}}} \approx \Omega_M^2 \pm \left(\frac{5\sqrt{5}g_{\mathrm{OM}}^2}{9\Gamma^2\omega_o m_x}\right)\left(\frac{4K}{1+K}\right)P_i, \tag{1.158}$$

$$\gamma_M'|_{\Delta T_1,\ \mathrm{SUR},\Delta_o'=\pm\frac{\Gamma}{2\sqrt{3}}} \approx \gamma_M \mp \left(\frac{50\sqrt{5}g_{\mathrm{OM}}^2}{27\Gamma^3\omega_o m_x}\right)\left(\frac{4K}{1+K}\right)P_i. \tag{1.159}$$

From these equations we see that the maximal damping/amplification in the unresolved sideband limit is strongly dependent upon the optical cavity $Q$ when input power is the fixed parameter.

A final consideration is the ratio of the optical spring effect to the mechanical damping/amplification. We evaluate the normalized ratio of the optical spring to the dampling/amplification factor at the optimal detuning point for fixed input power found above (the optical spring is optimized at a slightly different detuning point, which we ignore here), and find in the sideband unresolved limit,

$$\frac{(\Omega_M' - \Omega_M)/\Omega_M}{(\gamma_M' - \gamma_M)/\gamma_M}|_{\Delta T_1,\ \mathrm{SUR}} \approx -\frac{(\Delta^2 - \Omega_M^2)}{2\Omega_M\Gamma Q_M} \overset{\Delta_o'=\pm\frac{\Gamma}{2\sqrt{5}}}{\approx} -\frac{3\Gamma}{20\Omega_M Q_M}, \tag{1.160}$$

where $Q_M \equiv \Omega_M/\gamma_M$ is the bare mechanical resonator $Q$-factor. The effect of the optical spring in this limit can then be larger than that of the optomechanical damping/amplification in situations where the mechanical $Q$-factor is not too large.

*Sideband resolved limit ($\Omega_M \gg \Gamma$)*

The extrema of the damping/amplification coefficient in the sideband resolved limit ($\Omega_M \gg \Gamma$), for fixed internal cavity energy, occurs approximately at a detuning of $\Delta_o' \approx \pm\Omega_M$. The corresponding coefficients at this optimal detuning point are approximately,

$$(\Omega_M')^2|_{\Delta T_1=0,\ \mathrm{SR},\Delta_o'=\pm\Omega_M} \approx \Omega_M^2 \pm \left(\frac{|a_0|^2 g_{\mathrm{OM}}^2}{2\Omega_M \omega_o m_x}\right), \tag{1.161}$$

$$\gamma_M'|_{\Delta T_1,\ \mathrm{SR},\Delta_o'=\pm\Omega_M} \approx \gamma_M \mp \left(\frac{2|a_0|^2 g_{\mathrm{OM}}^2}{\Gamma\Omega_M \omega_o m_x}\right). \tag{1.162}$$

One sees from the above equations that the maximum damping/amplification for a given internal cavity energy scales only linearly with the optical cavity $Q$-factor (through $\Gamma^{-1}$) in the resolved sideband limit. Also, the optical spring is independent of cavity Q at this detuning point. In this limit then, the most important optomechanical parameters are $g_{\mathrm{OM}}$ and $m_x$, which enter into both the spring and damping/amplification coefficient as $g_{\mathrm{OM}}^2/m_x$.

Similar to the fixed cavity energy case, the optimal detuning point for maximum mechanical damping/amplification and fixed input power occurs at $\Delta_o' \approx \pm\Omega_M$ in the resolved sideband limit, with optomechanical coefficients,

$$(\Omega_M')^2|_{\Delta T_1=0,\ \mathrm{SR},\Delta_o'=\pm\Omega_M} \approx \Omega_M^2 \pm \left(\frac{g_{\mathrm{OM}}^2\Gamma}{8\Omega_M^3 \omega_o m_x}\right)\left(\frac{4K}{1+K}\right) P_i, \tag{1.163}$$

$$\gamma_M'|_{\Delta T_1,\ \mathrm{SR},\Delta_o'=\pm\Omega_M} \approx \gamma_M \mp \left(\frac{g_{\mathrm{OM}}^2}{2\Omega_M^3 \omega_o m_x}\right)\left(\frac{4K}{1+K}\right) P_i. \tag{1.164}$$

From these equations we see that the maximal damping/amplification in the resolved sideband limit is *independent* of the optical cavity $Q$ when input power is the fixed parameter. This is an important point, as it sets a limit to which the threshold input power for regrenerative mechanical oscillation may be lowered by increasing the optical cavity $Q$, and highlights again the importance of the ratio $g_{\mathrm{OM}}^2/m_x$.

As noted in the sideband unresolved case, the detuning point of maximum optical

spring is different than that for maximum damping/amplification. Assuming a small relative optical spring effect ($(\Omega'_M)^2 - \Omega_M^2 \approx 2\Omega_M\left(\Omega'_M - \Omega_M\right)$), we can write for the ratio of the optical spring frequency shift to the mechanical damping/amplification coefficient in the resolved sideband limit,

$$\frac{\left(\Omega'_M - \Omega_M\right)/\Omega_M}{\left(\gamma'_M - \gamma_M\right)/\gamma_M}|_{\Delta T_1,\,\mathrm{SR}} \overset{\Delta'_o = \pm\Omega_M}{\approx} -\frac{\Gamma}{8\Omega_M Q_M}. \tag{1.165}$$

Unlike in the unresolved sideband case, in the limit of resolved sidebands the optical spring effect is much smaller than the effect of damping/amplification on the mechanical resonator properties.

#### 1.3.6.4 Thermo-Optic Response in the Sideband Unresolved Limit

We now consider the thermo-optic response in the sideband unresolved limit, and for a system in which the mechanical frequency is much larger than the thermal decay rate, a situation commonly found in optomechanical microsystems. We begin with $f'$,

$$f'(\Omega_M) = (-\Omega_M\gamma_{th} - i\gamma_{th}^2)\left(\frac{\Delta_{th}}{\Omega_M^2 + \gamma_{th}^2}\right) \approx (-\Omega_M\gamma_{th} - i\gamma_{th}^2)\left(\frac{\Delta_{th}}{\Omega_M^2}\right), \tag{1.166}$$

where we have assumed that the mechanical frequency is much larger than the thermal decay rate ($\Omega_M \gg \gamma_{th}$) and we have associated $g_{th}\Gamma_{abs}c_{th}|a_0|^2/\gamma_{th}$ with the static thermo-optic tuning of the cavity resonance, $\Delta_{th}$. In order to evaluate $g$, we need the unresolved sideband limit of $|f|^2$, $|f'|^2$, and $2\mathrm{Re}(f'f)$,

$$|f(\Omega_M)|^2 \approx \frac{4(\Delta'_o)^2}{\Delta^4}, \tag{1.167}$$

$$|f'(\Omega_M)|^2 \approx \left(\frac{\gamma_{th}\Delta_{th}}{\Omega_M}\right)^2, \tag{1.168}$$

$$2\mathrm{Re}(f'(\Omega_M)f(\Omega_M)) \approx \frac{4\Delta'_o\Delta_{th}\gamma_{th}(\Delta^2\gamma_{th} - \Omega_M^2\Gamma)}{\Omega_M^2\Delta^4}. \tag{1.169}$$

This yields for the transfer function $g(\Omega_M)$ in the sideband unresolved limit and for $\Omega_M \gg \gamma_{th}$,

$$g(\Omega_M) \approx \left(\frac{1}{1+s(|a_o|^2)}\right)\left(f(\Omega_M) + \frac{4(f'(\Omega_M))^*(\Delta'_o)^2}{\Delta^4}\right), \tag{1.170}$$

where we have defined a saturation parameter, $s$, which is equal to,

$$s \approx \left(\frac{2\Delta'_o\gamma_{th}\Delta_{th}(|a_0|^2)}{\Delta^2\Omega_M}\right)^2\left(1+\left(\Delta_{th}(|a_0|^2)\right)^{-1}\left(\frac{\Delta^2}{\Delta'_o} - \frac{\Omega_M^2\Gamma}{\Delta'_o\gamma_{th}}\right)\right). \tag{1.171}$$

Under most situations in which the thermo-optic correction to the bare optomechanics is significant, the static thermo-optic tuning of the cavity resonance dominates all other rates and only the first term contributes to $s$,

$$s \approx \left(\frac{2\Delta'_o\gamma_{th}\Delta_{th}(|a_0|^2)}{\Delta^2\Omega_M}\right)^2. \tag{1.172}$$

One can usefully relate the thermo-optic correction factor in eq. (1.171) to that of the bare optomechanical factor $f$ as,

$$\frac{4(f'(\Omega_M))^*(\Delta'_o)^2}{\Delta^4} \approx \mathrm{Re}(f(\Omega_M))\left(\frac{2\Delta_{th}\Delta'_o\gamma_{th}}{\Omega_M^2\Gamma}\right) + i\mathrm{Im}(f(\Omega_M))\left(\frac{-2\Delta_{th}\Delta'_o\gamma_{th}^2}{\Delta^2\Omega_M^2}\right). \tag{1.173}$$

Substituting eqs. (1.167,1.171) into eqs. (1.148,1.149) yields the following thermo-optic corrections to the optical spring and optomechanical gain coefficients in the sideband unresolved limit and for slow thermal response,

$$(\Omega'_M)^2 \approx \Omega_M^2 + \left(\frac{2|a_0|^2 g_{\mathrm{OM}}^2\Delta'_o}{\Delta^2\omega_o m_x}\right)\left[\frac{1+W}{1+s}\right], \tag{1.174}$$

$$\gamma'_M \approx \gamma_M - \left(\frac{|a_0|^2 g_{\mathrm{OM}}^2\Gamma\Delta'_o}{\Delta^4\omega_o m_x}\right)\left[\frac{1+V}{1+s}\right], \tag{1.175}$$

where the correction factors are,

$$W = -\left(\frac{2\Delta_{th}\Delta_o'\gamma_{th}^2}{\Delta^2\Omega_M^2}\right) = -\left(\frac{2\Delta_{th}}{\Gamma}\right)\left(\frac{\gamma_{th}}{\Omega_M}\right)^2\left(\frac{\Gamma\Delta_o'}{\Delta^2}\right), \tag{1.176}$$

$$V = \left(\frac{2\Delta_{th}\Delta_o'\gamma_{th}}{\Omega_M^2\Gamma}\right) = \left(\frac{2\Delta_{th}}{\Gamma}\right)\left(\frac{\gamma_{th}}{\Omega_M}\right)^2\left(\frac{\Delta_o'}{\gamma_{th}}\right). \tag{1.177}$$

It should be noted that both $W$ and $V$ are dependent upon the (time) average stored cavity energy through the static thermo-optic tuning, $\Delta_{th}$. It is also noteworthy that since the thermo-optic tuning is negative for most cavity materials (heat generates a red shift of the cavity resonance), $W$ will be a positive quantity and $V$ a negative one for blue detuned laser input ($\Delta_o' > 0$). In this way the thermo-optic correction tends to increase the bare optical spring effect and reduce the bare optomechanical gain when one tunes to the blue side of the cavity resonance. This negative correction to the optomechanical gain can then result in an effective mechanical damping on the stable blue-detuned side of the cavity resonance if $|V| > 1$, a case study of which will be explored below. The situation is reversed for a red detuned laser input, with the optical spring effect tending to be reduced and the optomechanical damping being enhanced.

Before proceeding to study specific examples, it is useful to estimate the correction factors and the saturation parameter for detunings close to the maximal bare optomechanical response, $|\Delta_o'| \approx \Gamma/2$. Substituting this detuning into eqs. (1.173,1.177,1.178) yields,

$$|s(|\Delta_o'| = \Gamma/2)| \approx \left(\frac{2\Delta_{th}}{\Gamma}\right)^2\left(\frac{\gamma_{th}}{\Omega_M}\right)^2, \tag{1.178}$$

$$|W(|\Delta_o'| = \Gamma/2)| \approx \left(\frac{2|\Delta_{th}|}{\Gamma}\right)\left(\frac{\gamma_{th}}{\Omega_M}\right)^2, \tag{1.179}$$

$$|V(|\Delta_o'| = \Gamma/2)| \approx \left(\frac{2|\Delta_{th}|}{\Gamma}\right)\left(\frac{\gamma_{th}}{\Omega_M}\right)^2\left(\frac{\Gamma}{2\gamma_{th}}\right). \tag{1.180}$$

The correction factor to the optomechanical gain (damping) is seen to be $\Gamma/2\gamma_{th}$ times larger than that of the correction to the optical spring effect. For optomechanical

systems of micron scale and high optical $Q$, $\Gamma/2\pi \sim 10$ MHz and $\gamma_{th}/2\pi \sim 10$ kHz are reasonable numbers, which means the gain correction is on the order of a thousand times larger than the spring correction. For more modest optical $Q$ systems ($Q \sim 10^5$), the gain correction is a million times larger than the spring correction. The saturation parameter scales similarly to the optical spring correction factor, with an extra factor of $2\Delta_{th}/\Gamma$. Thus, for static thermo-optic tuning greater than the cavity linewidth (thermo-optic bistability) the optical spring correction due to thermo-optic tuning *always* serves to quench the bare optomechanical effect. The optomechanical gain (damping), however, can be enhanced over a useful parameter regime. It is now appropriate to look at a couple of systems in more detail. We begin with the *zipper* optomechanical cavity.

#### 1.3.6.5 Example: The Zipper Optomechanical Cavity

The zipper cavity studied in the manuscript has an optical $Q$-factor on the order of $Q \sim 3 \times 10^4$ ($\Gamma/2\pi \sim 6$ GHz or roughly a $\delta\lambda \sim 50$ pm linewidth), a mechanical frequency $\Omega_M/2\pi \sim 10$ MHz, and a thermal decay rate of roughly $\gamma_{th}/2\pi \sim 8$ kHz (see below). These devices have significant optical absorption at $\lambda \sim 1550$ nm, resulting in a static thermo-optic tuning of roughly $\Delta\lambda_{th} \sim 4$ nm (100 cavity linewidths) for a time-averaged stored cavity energy of 3 fJ ($P_i \sim 5$ mW). The correction and saturation parameters for the zipper cavity under this sort of optical input power and at the "optimal" detuning are,

$$|s(|\Delta_o'| = \Gamma/2)| \approx 2 \times 10^{-3}, \tag{1.181}$$

$$|W(|\Delta_o'| = \Gamma/2)| \approx 8 \times 10^{-6}, \tag{1.182}$$

$$|V(|\Delta_o'| = \Gamma/2)| \approx 10. \tag{1.183}$$

We see that, because of the large thermo-optic tuning and reasonably fast thermal response (a result of the small heat capacity of the zipper cavity geometry), for the zipper cavity the optomechanical gain reverses sign at high enough optical input

power for blue detuned pumping, resulting in strong optomechanical damping of the mechanical motion. This is what we see in our measurements. The optical spring is left unaffected and the overall saturation of the optomechanical coupling is negligible.

#### 1.3.6.6 Example: The Double-disk Optomechanical Cavity

We have also fabricated and measured a "double-disk" gradient force optomechanical devices more similar to the previously studied microtoroid cavity [5]. In the case of the double-disk (results of which will be presented elsewhere [21]), the mechanical frequency and thermal time constant are similar to that of the zipper cavity. The double disk has roughly a factor of 30 times the optical $Q$ of the zipper cavity ($Q \sim 10^6$, $\Gamma/2\pi \sim 200$ MHz). The resulting static thermo-optic tuning is roughly only 8 pm for 3 fJ of stored optical cavity energy, 500 times less than for the zipper cavity and corresponding to 3-4 cavity linewidths. Note that the difference comes partly from the reduced optical absorption in the double disk and partly from the much higher thermal resistance of the long cantilevers with small cross-section in the zipper cavity. For the double disk structure then, the correction and saturation parameters under similar optical pumping conditions as for the zipper cavity are,

$$|s(|\Delta_o'| = \Gamma/2)| \approx 2 \times 10^{-6}, \tag{1.184}$$

$$|W(|\Delta_o'| = \Gamma/2)| \approx 3 \times 10^{-7}, \tag{1.185}$$

$$|V(|\Delta_o'| = \Gamma/2)| \approx 0.014. \tag{1.186}$$

All of the thermo-optic corrections to the optomechanical response in the double-disk structure are then negligible at the power levels studied so far in the lab. Not suprisingly, then, we observe amplification and self-oscillation of the mechanical motion for blue-detuned input light.

### 1.3.7 Thermo-Mechanical Effects

It is also important to consider thermo-mechanical effects (i.e., direct mechanical actuation stemming from thermal effects such as the pressure rise in the gas between the zipper nanobeams or thermal expansion of the nanobeams and surrounding supports) [22]. Thermo-mechanical effects can not only produce a temperature dependent shift in the cavity resonance frequency as described above in the case of the thermo-optic effect, but in addition they can directly produce a force on the nanobeams. On first blush, one might expect that thermo-mechanical effects are responsible for the blue-detuned damping measured in the zipper cavities (for instance, the sign of a thermo-mechanical force due to the pressure rise in the gas between the nanobeams would be opposite that of the optical force). However, even an overly optimistic estimate of the magnitude of thermo-mechanical effects indicates that this is not the case.

The steady-state temperature rise inside the cavity at the largest optical input powers used in this work ($P_i = 5$ mW) is roughly $\Delta T_0 = 60$ K (estimated from the measured thermal tuning rate of the cavity as described below). The optical energy inside the cavity is being modulated by roughly $\beta = 15\%$ of the time-averaged internal cavity energy due to thermal motion of the nanobeams. The component of the zipper cavity temperature oscillating in-phase with the optical cavity energy at the mechanical frequency ($\Omega_M \sim 10$ MHz) is roughly $\Delta T_q \sim (\gamma_{th}/\Omega_M)^2 \beta \Delta T_0$, whereas the in-quadrature component of the zipper cavity temperature is $\Delta T_p \sim (\gamma_{th}/\Omega_M)\beta \Delta T_0$. This assumes of course that $\gamma_{th} \ll \Omega_M$, as is the case for the zipper cavity. Using some of the numbers estimated below, we find $\gamma_{th}/\Omega_M \sim 10^{-3}$, so that the in-phase and in-quadrature modulations in the cavity temperature are at most $\Delta T_q \sim 10^{-5}$ K and $\Delta T_p \sim 10^{-2}$ K, respectively.

We first consider a thermo-mechanical force from the thermal expansion in the nanobeams. The resulting in-plane displacement (which couples to the optical field) is difficult to simply estimate as it sensitivitly depends upon the beam clamping. We have performed finite-element-method (FEM) simulations of our stuctures, with an

accurate representation of our clamping geometry, and find that the resulting in-plane displacement is $\delta x = 80$ pm for $\Delta T_0 = 60$ K at the center of the zipper cavity. From the above estimated in-phase and in-quadrature temperature oscillations for this static temperature shift, we find the corresponding in-phase and in-quadrature thermo-mechanical displacements, $\delta x_q \sim 1.3 \times 10^{-17}$ m and $\delta x_p \sim 1.3 \times 10^{-14}$ m, respectively. The effective in-plane force producing these in-plane displacements is related to the spring constant of the structure, and given by, $\Delta F \sim m_x \Omega_M^2 \delta x$. Putting this all together, we arrive at in-phase and in-quadrature (relative to the mechanical oscillation) components of in-plane force on the nanobeams equal to $\Delta F_q \sim 1.3 \times 10^{-15}$ N and $\Delta F_p \sim 1.3 \times 10^{-12}$ N. The corresponding corrections to the mechancical frequency and damping of the mechanical motion are given by, $\Delta(\Omega_M^2) \sim \Delta F_q/(m_x\sqrt{2}x_{rms})$ and $\Delta(\gamma_M) \sim \Delta F_p/(m_x \Omega_M \sqrt{2} x_{rms})$, where $x_{rms} \approx 6$ pm is the thermal rms amplitude of motion in our case. For $\Omega_M/2\pi = 8$ MHz and $\gamma_M/2\pi = 150$ kHz of the unperturbed zipper cavity $h_{1d}$ mode, we find $\Delta(\Omega_M^2)/\Omega_M^2 \sim 1.4 \times 10^{-6}$ and $\Delta(\gamma_M)/\gamma_M \sim 7.5 \times 10^{-2}$. The measured (frequency)$^2$ shift is $\sim 10^6$ times larger than this estimate, indicating that the measured spring effect is not a result of this sort of thermo-mechanical coupling. The measured mechanical damping factor is $\Delta\gamma_M/\gamma_M \sim 8$, which is two-orders of magnitude larger than be expected from thermo-mechanical coupling due to thermal expansion of the nanobeams.

Another possible thermo-mechanical force is that due to the temperature dependent pressure changes in the gas (nitrogen) surrounding the nanobeams. Treating a worst case scenario in which the gas between the nanobeams is unable to expand (molecules cannot escape), the in-phase and in-quadrature pressure increases would be approximately $\Delta P_q \sim (\Delta T_q/T_0)P_0 \sim 3 \times 10^{-8} P_0$ and $\Delta P_p \sim (\Delta T_p/T_0)P_0 \sim 3 \times 10^{-5} P_0$, respectively, near room temperature ($T_0 = 300$ K). The area of the gap-side of the nanobeams in the zipper cavity is $10^{-11}$ m$^2$, yielding a best-case scenario in-phase and in-quadrature force of $\Delta F_q \sim 3 \times 10^{-14}$ N and $\Delta F_p \sim 3 \times 10^{-11}$ N, respectively. The corresponding corrections to the mechancical frequency and damping of the mechanical motion are $\Delta(\Omega_M^2)/\Omega_M^2 \sim 3 \times 10^{-5}$ and $\Delta(\gamma_M)/\gamma_M \sim 1.7$. Again, the measured (frequency)$^2$ shift is $\sim 10^5$ times too small to account for the measured spring effect.

The predicted mechanical-amplitude damping factor is within an order of magnitude of the measured value, although still a factor of 5 times too small even with the extremely "optimistic" estimate for the pressure rise. As such, it is unlikely that this thermo-mechanical effect is contributing significantly to the observed mechanical damping either.

A final comment relates to the difference between the thermo-optic effect studied here and direct thermo-mechanical damping/amplification present in other nanomechanical and cavity-optomechanical devices [22, 23]. In these previously studied devices, if the pure optical force were removed the system would behave in a similar fashion. In the case of the thermo-optic effect, the thermo-optic tuning only serves to enhance or quench the bare optomechanical coupling, effectively riding on top of the optomechanical response. Turning off the optical force, then, eliminates the coupling of the thermo-optic effect to the mechanical degrees of freedom of the system.

# Chapter 2

# Optical and Mechanical Design of a "Zipper" Photonic Crystal Optomechanical Cavity

This chapter is reproduced and adapted from Ref. [2].

## 2.1 Summary

Design of a doubly-clamped beam structure capable of localizing mechanical and optical energy at the nanoscale is presented. The optical design is based upon photonic crystal concepts in which patterning of a nanoscale-cross-section beam can result in strong optical localization to an effective optical mode volume of 0.2 cubic wavelengths ($(\lambda_c)^3$). By placing two identical nanobeams within the near field of each other, strong optomechanical coupling can be realized for differential motion between the beams. Current designs for thin film silicon nitride beams at a wavelength of $\lambda = 1.5$ $\mu$m indicate that such structures can simultaneously realize an optical $Q$-factor of $7 \times 10^6$, motional mass $m_u \sim 40$ picograms, mechanical mode frequency $\Omega_M/2\pi \sim 170$ MHz, and an optomechanical coupling factor ($g_{\mathrm{OM}} \equiv \mathrm{d}\omega_c/\mathrm{d}x = \omega_c/L_{\mathrm{OM}}$) with effective length $L_{\mathrm{OM}} \sim \lambda = 1.5$ $\mu$m.

## 2.2 Introduction

At a macroscopic level, the interaction of light with the mechanical degrees of freedom of a dielectric object can be calculated by considering the flux of momentum into or out of an object using the Maxwell stress-energy tensor. At a microscopic level, as in the case of atomic physics, one can define an interaction Hamiltonian between an atom and the light field in order to derive the various mechanical forces on the atom's center of mass, which in general depends upon both the external and internal degrees of freedom of the atom [24]. In the case of a dielectric mechanical resonator, a direct relationship between the macroscopic dielectric and microscopic atomic theories can be made, and useful analogies may be forged [5, 6]. The interactions of light with mechanically resonant objects is currently being actively explored in the field of cavity optomechanics as a means to obtain ground-state cooling of a macroscopic mechanical resonator [6, 25–31]. The strength of optomechanical interactions in these system can be quantified on a per-photon basis by the rate of change of the cavity resonance frequency ($\omega_c$) with mechanical displacement amplitude ($u$), $g_{\rm OM} \equiv {\rm d}\omega_c/{\rm d}u = \omega_c/L_{\rm OM}$. $L_{\rm OM}$ is an effective length over which a cavity photon's momentum can be exchanged with the mechanical system. In this work we describe a simple doubly clamped nanobeam system (a so-called *zipper* cavity) which allows for the combined localization of optical and mechanical energy in a nanoscale structure so as to provide extremely large optomechanical coupling due to the gradient optical force. Optical energy is localized within the center of the nanobeam using a one-dimensional photonic crystal in combination with total internal reflection. Beyond the analysis provided here, future optimization of both the optical and mechanical properties of these chip-based structures should allow for a variety of new applications from precision metrology [32] to tunable photonics [33, 34].

The outline for the paper is as follows. We begin with the optical design of a one-dimensional photonic crystal in a siliocn nitride nanobeam. Finite-element-method electromagnetic simulations are used to deduce the level of optical localization and the relevant optical losses within the struture. The mechanical properties of the zipper

cavity are studied next, with numerical simulations used to determine the lower-lying mechanical eigenmodes. The tuning properties of a double nanobeam photonic crystal are then computed to estimate the strength of the optomechanical coupling for the differential in-plane motion of the beams. We conclude with a comparison of the zipper cavity properties with other more macroscopic optomechanical systems, and a discussion of the future prospects for these sorts of chip-based gradient optical force devices.

## 2.3 Optical Design and Simulation

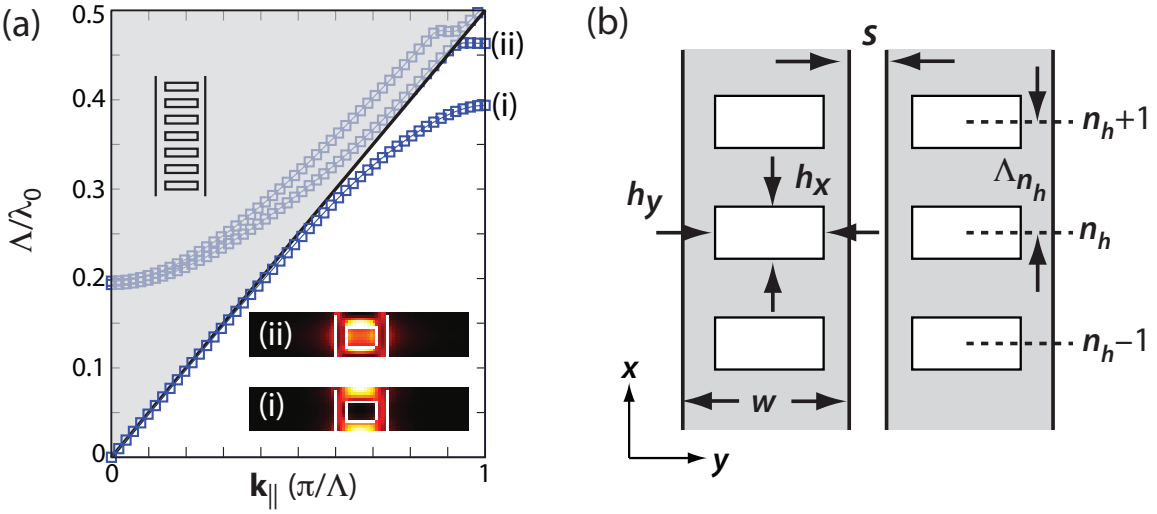


Figure 2.1: Bandstructure properties of the photonic crystal nanowire. (a) Axial bandstructure of the single beam photonic crystal structure, with nominal width and thickness. $\mathbf{k}_{||}$ is the wavevector of light in the direction of the 1D photonic lattice, $a$ is the lattice period, and $\Lambda/\lambda_0$ is the "normalized" optical frequency for free-space wavelength $\lambda_0$. The light cone, denoted by the grey area and deliniated by the black light line, represents regions of frequency-wave-vector space in the bandstructure diagram in which light can radiate into the two transverse directions orthogonal to the axis of the photonic lattice. The two inset images show the electric field energy density of the valence (i) and conduction (ii) band-edge modes (the white outline is a contour plot of the refractive index of the nanowire). (b) Schematic of the double beam zipper cavity indicating the slot gap ($s$), the lattice constant ($a$), the beam width ($w$), and the axial and transverse hole lengths, $h_x$ and $h_y$, respectively.

The optical design of the zipper cavity utilizes a quasi-1D photonic crystal struc-

ture to localize optical modes to the center of a nanoscale cross-section beam. There are a number of different, but related, design methodologies used to form low-loss optical resonances in such photonic crystal "nanowires" [35–40]. In this paper we utilize concepts based upon an envelope picture of the guided photonic crystal modes [41] in the patterned nanobeam. We choose to work with "acceptor"-type modes formed from the lower-lying band of modes (the so-called "valence" band in reference to electronic semiconductor crystals) at the Brillouin zone boundary. In this way, the mode frequencies are as far away from the light line as possible, reducing leakage into the surrounding air-cladding of the nanobeam. Owing to the optically thin photonic wires considered in this work, the modes of predominantly in-plane polarization (TE-like modes) are most strongly guided and are the modes of primary interest here. In order to form acceptor modes, the bandedge of the valence band must be increased near the center of the cavity, and decreased in the mirror sections defining the end of the cavity. This is a result of the negative group velocity dispersion of the valence band modes [41].

We have chosen to perform designs based upon thin films of silicon nitride, as opposed to higher refractive index materials such as silicon-on-insulator (SOI), for several reasons. One reason is that silicon nitride can be grown on silicon wafers with very high optical quality across a wide range of wavelengths covering the visible to the mid-infrared. We have measured [42] optical $Q$-factors in excess of $3 \times 10^6$ for whispering-gallery modes of microdisks formed from stoichiometric silicon nitride deposited by low-pressure-chemical-vapor-deposition (LPCVD). A second reason is that LPCVD-deposited stoichiometric silicon nitride films on silicon have a large internal tensile stress, which has been shown to be critical in producing high-$Q$ mechanical resonances in doubly-clamped nanobeams [43, 44]. An additional concern is the two-photon absorption present in smaller bandgap semiconductors such as silicon and gallium arsenide, which results in additional free-carrier absorption (FCA), and which can result in significant parasitic effects such as thermo-optic and free-carrier dispersion in small-volume photonic crystal nanocavities [20]. Silicon nitride, with its large bangap ($\sim$ 3 eV), requires three (as opposed to two) 1 eV photons to be absorbed

simultaneously, greatly reducing nonlinear absorption in the near-IR. An obvious drawback of using silicon nitride thin films, is the lower refractive index ($n \sim 2$) of these films in comparison to semiconductor films ($n \sim 3.4$). As is shown below (and in Ref. [40]), with carefully chosen designs, high-$Q$ photonic crystal optical cavities of sub-cubic-wavelength mode volume can still be formed in silicon nitride thin films.

The bandstructure of a single beam silicon nitride nanowire, calculated using the MIT photonic bands software package [45], is displayed in Fig. 2.2. As described in more detail below, the simulation is performed for a "nominal" structure defined by a lattice normalized beam thickness ($\bar{t} = t/\Lambda = 2/3$) and beam width ($\bar{w} = w/\Lambda = 7/6$). The refractive index of the silicon nitride beam is taken as $n = 2$, and a resolution of 64 points per axial lattice period is used to ensure accurate band frequencies. Our coordinate convention is (see Fig. 2.4): (i) $x$ the in-plane coordinate along the long axis of the cavity, (ii) $y$ the in-plane transverse coordinate, and (iii) $z$ the out-of-plane transverse coordinate. Only the lower-lying bands with modes of even parity in the $\hat{z}$-direction and odd parity in the $\hat{y}$-direction are shown, corresponding to the fundamental TE-like modes of the beam waveguide. As indicated by the electric field energy density plots of the two lowest lying band-edge modes (inset to Fig. 2.2(a)), the valence band lies predominantly in the region of the high refractive index silicon nitride beam, whereas the upper "conduction" band mode lies predominantly in the region of the air hole patterning.

The formation of localized optical cavity resonances is accomplished by introducing a "defect" into the photonic lattice. The defect region in the structures studied here consists of a quadratic grade in the lattice constant of the linear array of air holes near the cavity center. In order to reduce transverse radiation loss, we choose to use a defect which supports an odd symmetry fundamental mode along the axial direction. Since the valence band modes tend to have electric field intensity predominantly inside the high-dielectric region (and nodes of the electric field in the low-dielectric constant air holes), a defect in which an air hole is at the center of the cavity yields an odd parity fundamental mode along the axial direction. Here, and in what follows, we use a cavity defect region consisting of the central 15 holes, with the lattice

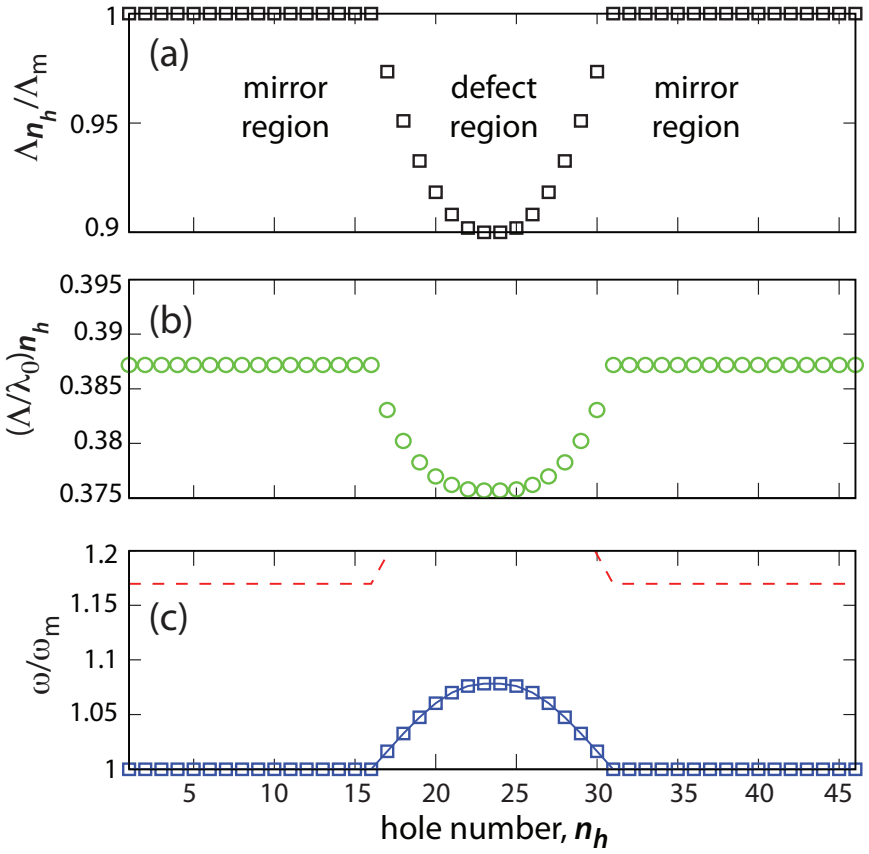


Figure 2.2: Geometry and photonic properties of the defect portion. **a** Lattice constant (normalized to the lattice period in the mirror section of the cavity, $\Lambda_m$) versus hole number ($n_h$) within the photonic lattice of the cavity. **a,b** Resulting frequency of the valence band-edge mode versus hole number. **b** Normalized frequency in terms of the local lattice constant, $(\Lambda/\lambda_0)_{n_h}$, is displayed. **c** The local band-edge frequency is referenced to the valence band-edge in the mirror section of the cavity. The solid blue (dashed red) curve is the valence (conduction) band-edge.

period varied from a nominal value in the outer *mirror* section ($a_m$) to 90% of the nominal value at the center of the defect region. This was found to provide a good balance between axial-localization of the cavity modes and radiation loss into the $y$-$z$ transverse directions of the nanobeams. In Fig. 2.2(c) we plot the *local* lattice period, defined as $a_{n_h} = x(n_h + 1) - x(n_h)$, versus air hole number $n_h$ along the length of the cavity. In Fig. 2.2(d) we plot the corresponding lattice-normalized frequency of the local TE-like valence band-edge modes of the single beam cavity. The small variation in lattice-normalized frequency is a result of the distortion in the aspect ratio of the

(perfectly periodic) structure as the lattice period is changed. More useful is the plot in Fig. 2.2(e) which shows the frequency of the local valence band-edge (blue solid curve) and conduction band-edge (red dashed curve) modes normalized to the valence band-edge mode frequency in the mirror section of the cavity. The quadratic grade in lattice constant results in a nearly-harmonic shift in the valence band-edge frequency versus position in the center of the cavity, with the band-edge frequency at the cavity center lying approximately mid-gap between the valence and conduction band-edges in the mirror section of the cavity.

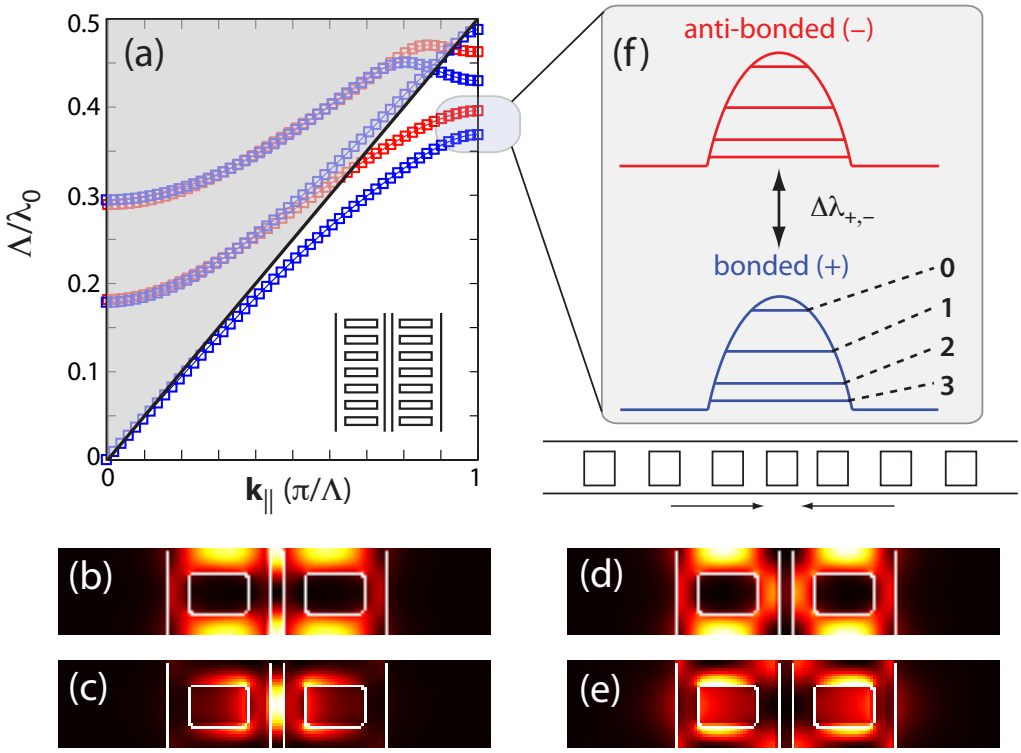


Figure 2.3: Optical design principle of the zipper cavity. (a) Axial bandstructure of the double beam quasi-1D photonic crystal structure, with nominal width, thickness, and slot gap. The blue curves are the bonded bands and the red curves are the anti-bonded bands. Valence and conduction band-edge modes of the bonded (b,c) and anti-bonded (d,e) bands, respectively. (f) Illustration of the defect cavity formation at the Brillouin-zone boundary. The splitting between the two manifolds is indicated by $\Delta\lambda_{+,-}$.

For the double-beam design of the zipper cavity, two photonic crystal nanowires are placed in the near-field of each other as illustrated in Fig. 2.2(b). The strong cou-

pling between two nearly-identical nanobeams results in a bandstructure consisting of even and odd parity superpositions of the TE-polarized single beam photonic bands (Fig. 2.3(a)). We term the even parity supermodes, *bonded* modes, and the odd parity supermodes, *anti-bonded* modes [33]. The anti-bonded manifold of resonant modes are shifted to higher frequency than the bonded manifold of modes, with splitting ($\Delta\lambda_{+,-}$) being dependent upon the slot gap ($s$) between the nanobeams. The electric field energy density plots of the bonded valence and conduction band-edge modes are shown in Figs. 2.3(b) and 2.3(c), respectively. The corresponding anti-bonded modes, with noticeably reduced energy density in the slot gap, are displayed in Figs. 2.3(d)-(e). Owing to the negative curvature of the valence band forming the localized cavity modes, the fundamental mode of the cavity for each manifold has the highest frequency, with the higher-order modes having reduced frequencies (schematically illustrated in Fig. 2.3(f)). In what follows, we will primarily be interested in the bonded mode manifold due to the larger electric field intensity of these modes in the slot gap.

With the zipper cavity now defined, we perform a series of finite-element-method (FEM), fully vectorial, 3D simulations of the localized cavity modes [46]. In these simulations we use the graded cavity design described above. The numerical mesh density is adjusted to obtain convergent values for the frequency and optical $Q$-factor of the cavity modes, and the structure is simulated with all available symmetries taken into account allowing for 1/8th the simulation volume. Scattering boundary conditions are used in the outer axial and transverse boundaries to provide a nearly-reflectionless boundary for out-going radiation. In the transverse direction ($y$-$z$) a cylindrical outer boundary is also used to reduce the total simulation volume. Finally, a check of the accuracy of our FEM simulations was also performed through a series of equivalent simulations using finite-difference time-domain code (Lumerical [47]). Figures 2.4(a) and 2.4(c) display the FEM-calculated electric field mode profiles of the fundamental bonded ($TE_{+,0}$) and anti-bonded ($TE_{-,0}$) modes, respectively, of the double beam zipper cavity. Cross-sectional electric field profiles, displayed in Figs. 2.4(b) and 2.4(d), clearly show the even and odd parity of the modes. Also shown

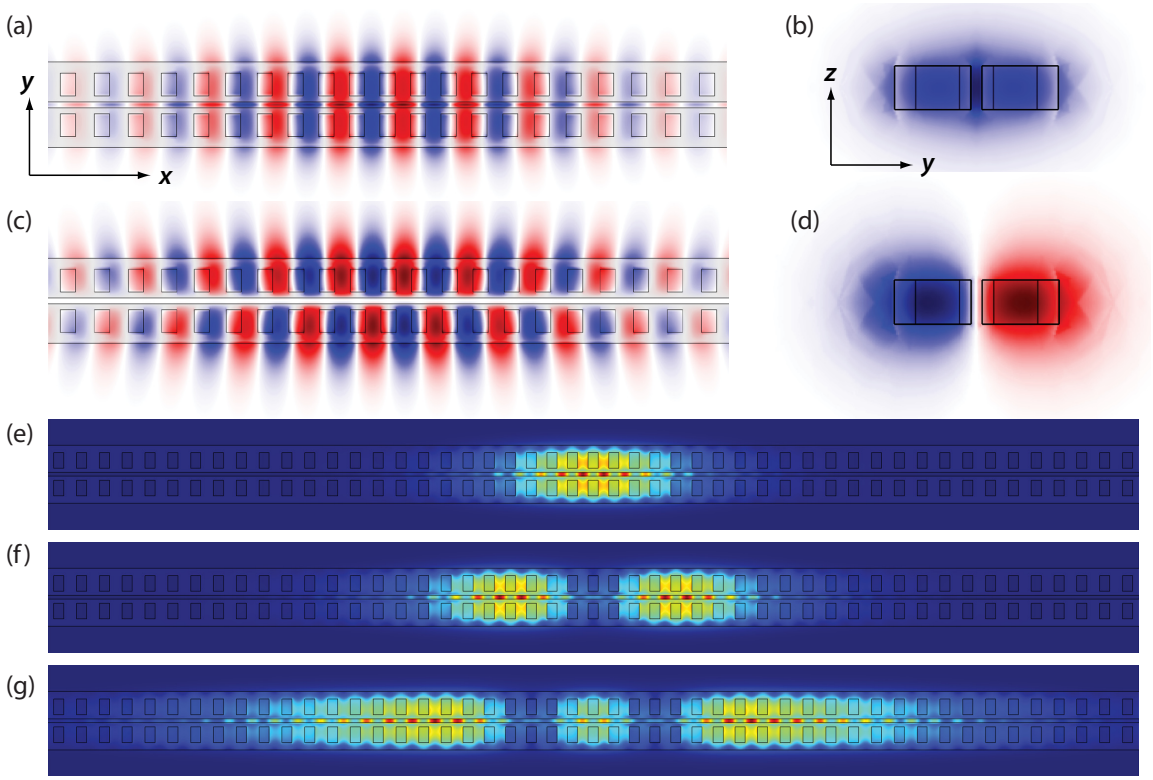


Figure 2.4: Transverse electric field ($\mathbf{E}_y$) mode profile of the fundamental bonded mode ($\mathrm{TE}_{+,0}$): (a) top-view, (b) cross-section. Transverse electric field ($\mathbf{E}_y$) mode profile of the fundamental anti-bonded mode ($\mathrm{TE}_{-,0}$): (c) top-view, (d) cross-section. The field colormap corresponds to +1 (red), 0 (white), and -1 (blue). Electric field energy density of the (e) fundamental ($\mathrm{TE}_{+,0}$), (f) second-order ($\mathrm{TE}_{+,1}$), and (g) third-order ($\mathrm{TE}_{+,2}$) bonded optical modes. The intensity colormap ranges from +1 (red) to 0 (blue).

in Figs. 2.4(e)-2.4(g) are the electric field intensity of the lowest three bonded cavity mode orders, $\mathrm{TE}_{+,0}$, $\mathrm{TE}_{+,1}$, and $\mathrm{TE}_{+,2}$.

Design variations of the zipper cavity are performed around a "nominal" structure with the following (normalized) dimenensions: (i) beam width, $\bar{w} \equiv w/\Lambda_m = 700/600$, (ii) beam thickness, $\bar{t} \equiv t/\Lambda_m = 400/600$, (iii) axial hole length, $\bar{h}_x \equiv h_x/\Lambda_m = 267/600$, (iv) axial hole width, $\bar{h}_y \equiv h_y/\Lambda_m = 400/600$, and (v) slot gap, $\bar{s} \equiv s/\Lambda_m = 100/600$, where $\Lambda_m$ is the lattice periodicity in the cavity mirror section. The length of the beam is set by the number of air hole periods in the cavity, which for the nominal structure is $N_h = 47$ (23 holes to the left and right of the central hole, with

the central 15 holes defining the defect region). The filling fraction of the air holes in the nominal structure is $f = 25.4\%$. For a fundamental bonded mode wavelength of $\lambda \sim 1500$ nm, the nominal lattice constant is $\Lambda_m = 600$ nm, hence the normalization by 600 in the above expressions for normalized dimensions.

Figure 2.5 shows the simulated $Q$-factor of the fundamental bonded cavity mode ($TE_{+,0}$) versus the total number of periods $N_h$ of the cavity for the nominal structure. The normalized cavity resonance frequency is calculated to be $\Lambda_m/\lambda_c = 0.3927$. The radiation loss from the cavity is broken into two parts, yielding two effective $Q$-factors: (i) the axial radiation loss out the ends of the nanobeams (yielding $Q_{||}$), and (ii) the radiation loss transverse to the long axis of the zipper cavity and intercepted by the transverse boundary (yielding $Q_{\perp}$). In Figure 2.5, $Q_{||}$ is seen to rise exponentially as a function of $N_h$, with an order of magnitude increase in $Q$-factor for every 6 additional periods of air holes. The transverse $Q$ is seen to rise initially with hole periods, but then levels off and saturates at a value of $Q_{\perp} = 7 \times 10^6$. The variation in $Q_{\perp}$ for structures with small $N_h$, and low $Q_{||}$, is a result of weak coupling between radiation loss into these (arbitrarily chosen) directions. Small reflections at the end of the nanobeams results in a small amount of axial radiation making its way to the transverse boundary. Nevertheless, a structure with $N_h > 47$ results in a total radiation $Q$-factor limited by the transverse $Q$-factor of $7 \times 10^6$. This value is very large given the modest refractive index of the silicon nitride film and small cross-section of the nanobeams (large air filling fraction).

In order to study the dependence of $Q$-factor on the hole size, we have also simulated the nominal structure with varying axial and transverse hole size, as shown in Figs. 2.6 and 2.7. In each of the plots the axial $Q$-factor increases with increasing hole size, but then saturates, as the hole size approaches that of the nominal structure. For hole sizes larger than the nominal structure, the $Q_{||}$ slightly drops, as does the transverse $Q$-factor. This drop in transverse $Q$-factor is a result of the increased normalized frequency of the mode (higher air filling fraction), which pushes the mode closer to the air-cladding light line, increasing radiation into the cladding (the drop in $Q_{||}$ is a result of low-angle transverse radiation making its way to the boundary at

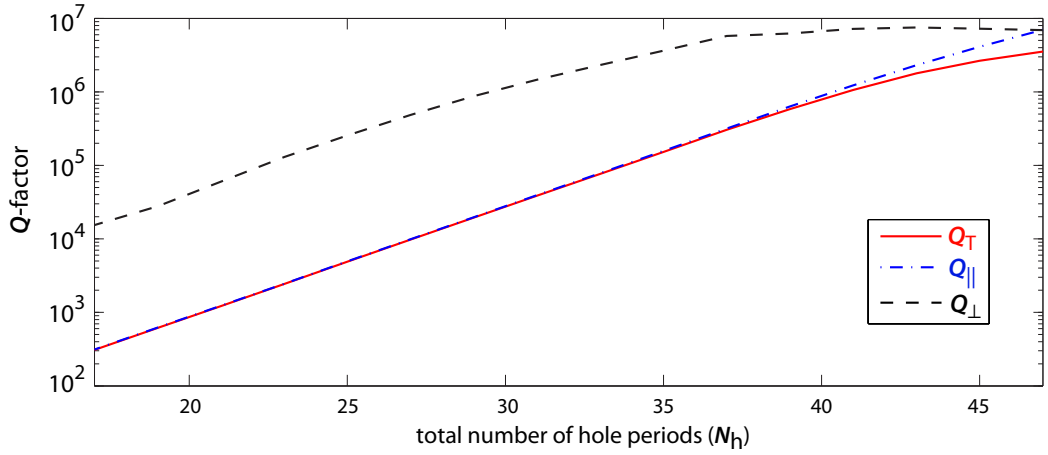


Figure 2.5: Optical $Q$-factor (axial, transverse, and total) versus number of hole periods in the cavity, $N_h$. In these simulations the defect region is maintained the same, with only the number of periods in the mirror section varied. The nominal structure corresponds to the maximum hole number in this plot, $N_h = 47$.

the end of the nanobeams). Therefore, the nominal structure represents an optimal structure in this regard, allowing for tight axial localization of the mode, without decreasing the transverse $Q$-factor.

The strength of light-matter interaction depends upon a position-dependent effective optical mode volume of a resonant cavity,

$$V_{\text{eff}}(\mathbf{r}_0) \equiv \frac{\int \varepsilon(\mathbf{r})|\mathbf{E}(\mathbf{r})|^2 \mathrm{d}^3\mathbf{r}}{\varepsilon(\mathbf{r}_0)|\mathbf{E}(\mathbf{r}_0)|^2}, \tag{2.1}$$

where $\varepsilon(\mathbf{r})$ is the position dependent dielectric constant and $\mathbf{r}_0$ is the position of interest. In the case of the zipper cavity, the strength of the optomechanical coupling depends upon $V_{\text{eff}}(\mathbf{r}_0)$ evaluated in the slot gap of the nanobeams. Similarly, in the field of cavity-QED, the effective mode volume can be used to estimate the coherent coupling rate between an "atom" and the cavity field. In Fig. 2.8 we plot the effective mode volume versus slot gap size, $s$, between the nanobeams for the $\text{TE}_{0,+}$ mode of the nominal structure. We plot two different effective mode volumes: (i) $V_g$, the effective mode volume evaluated at the center of the nanobeam gap near the center of the cavity where the field is most intense, and (ii) $V_p$, the minimum effective mode volume evaluated at the position of peak electric field energy density in the cavity.

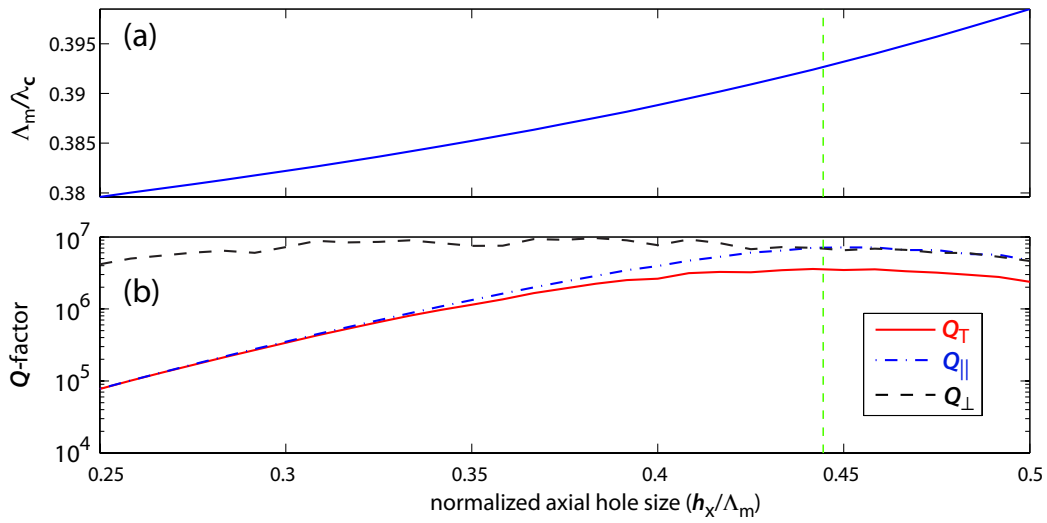


Figure 2.6: (a) Normalized frequency and (b) Optical $Q$-factor (axial, transverse, and total) versus normalized axial hole length, $\bar{h}_x$. The nominal structure is indicated by the dashed green line.

For normalized gap widths, $\bar{s} < 1/6$ the modes of the nanobeam are strongly coupled resulting in a peak electric field intensity in between the slot gap (hence the two effective mode volumes track each other). The effective mode volumes approach a value of $V_{\text{eff}} = 0.1(\lambda_c)^3$ as the slot gap approaches zero. This small value is a result of the discontinuity in the dominant polarization of the TE mode ($E_y$) as it crosses into the slot gap [48]. For slot gaps $\bar{s} > 1/6$, the minimum effective mode volume saturates at a value of $V_p = 0.225(\lambda_c)^3$ corresponding to that of a single nanobeam (i.e., no enhancement from energy being pushed into the slot gap). The effective mode volume evaluated at the center of the slot gap, on the otherhand, continues to rise with slot gap due to the exponential decay of the field in the gap.

A final variation considered is the nanobeam width. In Fig. 2.9 the nominal structure is varied by adjusting the normalized beam width while holding the filling fraction of the air holes fixed. This is done by scaling the the transverse hole length with the beam width. The axial $Q$-factor increases with the beam width due to the increased effective index of the guided mode, and thus increased effecive contrast of the quasi-1D photonic crystal. Due to the reduced lateral localization of the cavity mode, the effective mode volumes also increase with beam width. In contrast, the

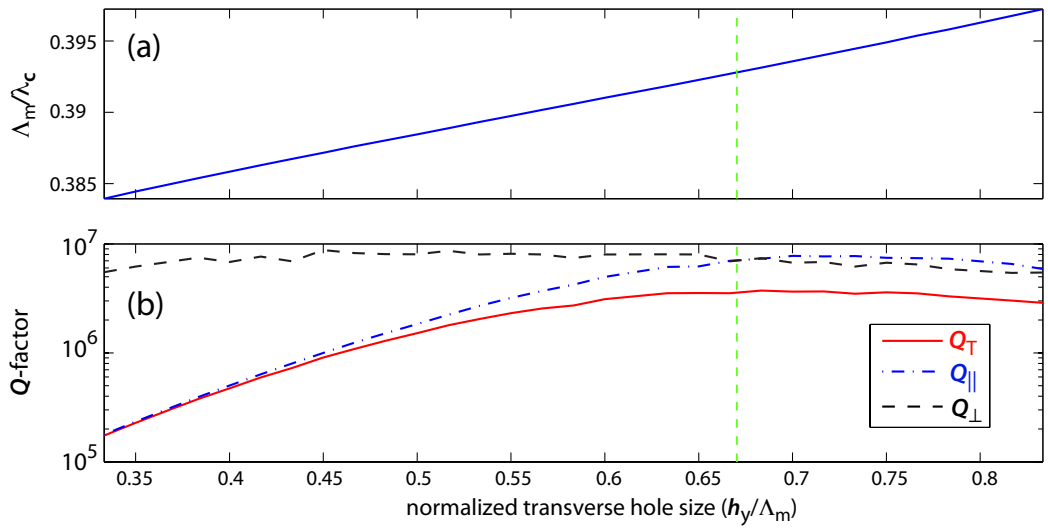


Figure 2.7: (a) Normalized frequency and (b) Optical $Q$-factor (axial, transverse, and total) versus normalized transverse hole length, $\bar{h}_y$. The nominal structure is indicated by the dashed green line.

transverse $Q$-factor remains approximately constant.

## 2.4 Mechanical Mode Analysis

The mechanical modes of the zipper cavity can be categorized into common and differential modes of in-plane (labeled $h$) and out-of-plane motion (labeled $v$) of the two nanobeams. In addition there are compression (labeled $c$) and twisting (labeled $t$) modes of the beams. In this work we focus on the in-plane differential modes, $h_{qd}$, as these modes are the most strongly opto-mechanically coupled due to the large change in the slot gap per unit (strain) energy. We use FEM numerical simulations to calculate the mechanical mode patterns and mode frequencies, the first few orders of which are shown in Fig. 2.10. The material properties of silicon nitride for the FEM simulations were obtained from a number of references. Where possible we have used parameters most closely associate with stoichiometric, low-pressure-chemical-vapor-deposition (LPCVD) silicon nitride deposited on $\langle 100 \rangle$ Si: mass density $\rho = 3100$ kg/m$^3$, Young's modulus $Y \sim 290$ GPa, internal tensile stress $\sigma \sim 1$ GPa [43, 44], coefficient of thermal expansion $\eta_{TE} = 3.3 \times 10^{-6}$ K$^{-1}$, thermal conductivity $\kappa_{th} \sim 20$

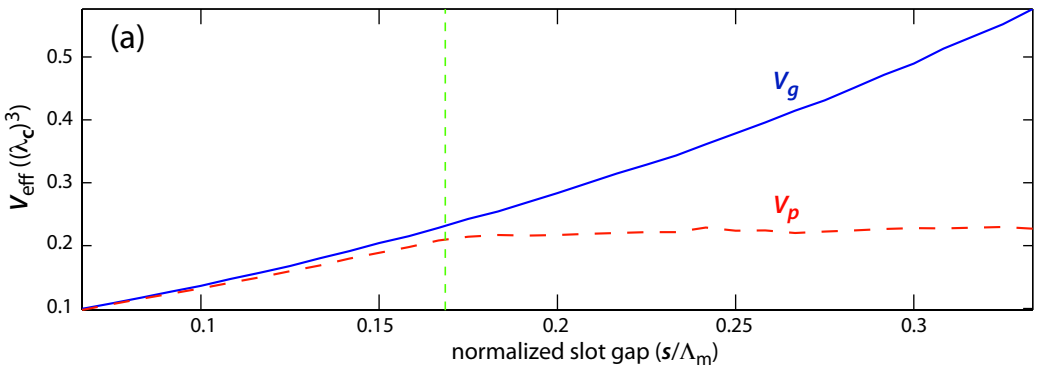


Figure 2.8: Effective mode volume of the $TE_{0,+}$ mode versus normalized slot gap, $\bar{s}$. The nominal structure is indicated by the dashed green line.

W/m/K, and specific heat $c_{sh} = 0.7$ J/g/K.

For the mechanical mode properties tabulated in Table 2.1 we have analyzed the nominal zipper cavity structure at an operating wavelength of $\lambda \approx 1.5$ $\mu$m, corresponding to a geometry with $\Lambda_m = 600$ nm, $t = 400$ nm, $s = 100$ nm, $w = 700$ nm, $h_x = 267$ nm, and $h_y = 400$ nm. The total number of air holes is set to $N_h = 55$, ensuring a theoretical $Q$-factor dominated by transverse radiation ($Q_\perp$), yielding a cavity length of $l = 36$ $\mu$m. The zipper cavity is clamped at both ends using fixed boundary conditions at the far ends of the "clamping pads" shown in Fig. 2.10. This clamping scheme is suitable for estimating the mechanical mode eigenfrequencies, although more complex clamping schemes envisioned for real devices will likely introduce modified splittings betweeen nearly-degenrate common and differential modes. The effective spring constant listed in Table 2.1 for each mode is based upon a motional mass equal to that of the true physical mass of the patterned nanobeams, $m_u \approx 43$ picograms (see below for self-consistent definition of motional mass).

The resulting frequency for the fundamental $h_{1d}$ mode is $\Omega/2\pi \approx 8$ MHz. The in-plane mode frequency of a doubly clamped beam, with $l \gg w, t$, is approximately given by [43]:

$$\Omega_q/2\pi = \frac{q^2\pi}{2l^2}\sqrt{\frac{YI_y}{\rho A}}\sqrt{1+\frac{\sigma A l^2}{q^2 Y I_y \pi^2}}, \tag{2.2}$$

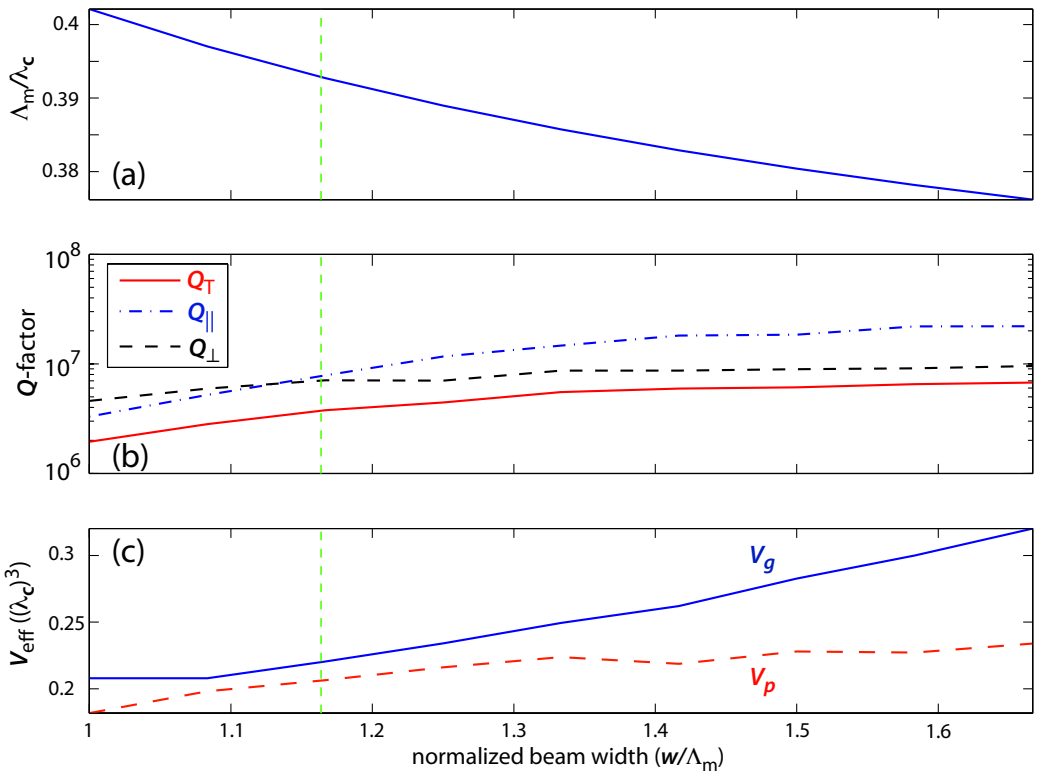


Figure 2.9: (a) Normalized frequency, (b) $Q$-factor and (c) Effective mode volume versus normalized beam width. The nominal structure is indicated by the dashed green line.

where $q$ is the mode index (approximately an integer), $A = tw$ is the cross-sectional area of the beams, and $I_y = tw^3/12$ is the cross-sectional moment of inertial about the in-plane axis ($\hat{y}$) of the beam. This fits the numerical data reasonably accurately assuming an effective beam width of $w' = (1 - f)w$. From the scaling in eq. (2.2), one finds that for mode number $q \geq 3$ (where internal stress can be neglected and $\Omega_q/2\pi \approx \frac{q^2\pi}{2l^2}\sqrt{\frac{YI_y}{\rho A}}$) that the in-plane frequency scales inversely with the square of the beam length, linearly with the beam width, and independent of the beam thickness. Therefore, a linear increase in the resonant frequency can be obtained by moving to shorter optical wavelengths and scaling the structure with wavelength. For much larger increases in mechanical resonance frequency, one must resort to higher-order in-plane modes of motion. Optomechanical coupling to these modes is discussed below.

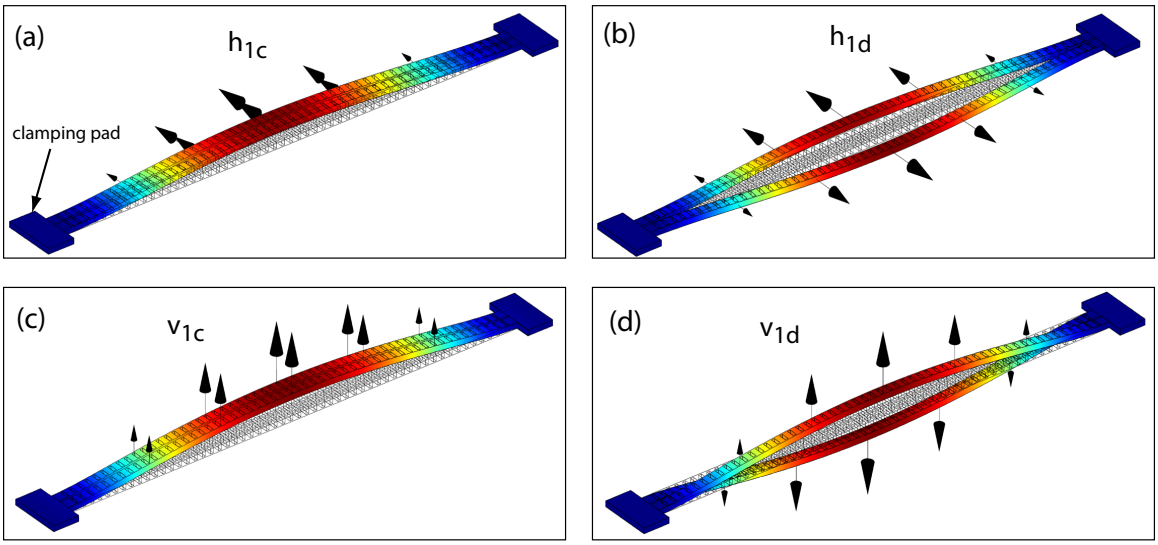


Figure 2.10: Mechanical eigenmode displacement plots: (a) 1st-order in-plane common mode, (b) 1st-order in-plane differential mode, (c) 1st-order out-of-plane common mode, and (d) 1st-order out-of-plane differential mode. The color represents total displacement amplitude, as does the deformation of the structure. The arrows indicate the local direction of displacement.

We have also studied the expected thermal properties of the zipper cavity, again assuming a 1.5 $\mu$m wavelength of operation. Due to the air-filling-fraction of the etched holes in the zipper cavity nanobeams, the thermal conductivity of the patterned beams is approximately $\Gamma_{th} = 75\%$ of the bulk value. A simple estimate for the thermal resistance of the zipper cavity due to conduction of heat through the nitride nanobeams themselves is $R_{th} \sim l/(8tw\Gamma_{th}\kappa_{th}) \approx 1.15 \times 10^6$ K/W, where the factor of 1/8 comes from the ability for heat to escape out either end of the nanobeams and in either direction. The physical mass of the zipper cavity, taking into account the etched holes, is approximately $m = 43$ picograms. The heat capacity of the zipper cavity is then $c_h \approx 3 \times 10^{-11}$ J/K. From the heat capacity and the conductive thermal resistance, the thermal decay rate (appropriate for high vacuum conditions in which convection is negligible) is estimated to be $\gamma_{th} = 1/R_{th}c_h \sim 2.9 \times 10^4$ s$^{-1}$. Finite-element-method simulations of the thermal properties of the zipper cavity yield an effective thermal resistance of $R_{th} = 1.09 \times 10^6$ K/W and a thermal decay rate of $\gamma_{th} = 5.26 \times 10^4$ s$^{-1}$ for temperature at the center of the zipper cavity, in reasonable

Table 2.1: Summary of mechanical mode properties. Optomechanical coupling factor is for the $TE_{0,+}$ mode.

| Mode label | $\Omega_M/2\pi$ (MHz) | $k_u$ (N/m) | $g_{\mathrm{OM}}$ (in units of $\omega_c/\lambda_c$) |
|---|---|---|---|
| $v_{1c}$ | 5.95 | 60 | |
| $v_{1d}$ | 6.15 | 64 | |
| $v_{2c}$ | 12.3 | 257 | |
| $v_{2d}$ | 12.7 | 274 | |
| $v_{3c}$ | 19.2 | 626 | |
| $v_{3d}$ | 20.0 | 679 | |
| $h_{1d}$ | 7.91 | 106 | 1.24 |
| $h_{1c}$ | 7.94 | 107 | $\sim 0$ |
| $h_{2d}$ | 18.2 | 562 | $\sim 0$ |
| $h_{2c}$ | 18.3 | 568 | $\sim 0$ |
| $h_{3d}$ | 31.8 | 1717 | 1.16 |
| $h_{3c}$ | 32.0 | 1738 | $\sim 0$ |
| $h_{9d}$ | 167.7 | $4.77 \times 10^4$ | 0.63 |
| $h_{9c}$ | 168.0 | $4.79 \times 10^4$ | $\sim 0$ |
| $t_{1d}$ | 41.0 | 2854 | |
| $t_{1c}$ | 41.1 | 2868 | |
| $c_{1c}$ | 78.6 | $1.05 \times 10^4$ | |
| $c_{1d}$ | 79.4 | $1.07 \times 10^4$ | |

correspondence to the estimated values.

## 2.5 Optomechanical Coupling

With the optical and mechanical modes of the zipper cavity now characterized, we proceed to consider the optomechanical coupling of the optical and mechanical degress of freedom. As described at the outset, the parameter describing the strength of optomechanical coupling is the frequency shift in the cavity mode frequency versus mechanical displacement, $g_{\mathrm{OM}} \equiv \mathrm{d}\omega_c/\mathrm{d}u$, where $\omega_c$ is the cavity resonance frequency and $u$ represents an amplitude of the mechanical displacement. In the case of the commonly studied Fabry-Perot cavity [29], $g_{\mathrm{OM}} = \omega_c/L_c$, where $L_c$ is approximately

the physical length of the cavity. A similar relation holds for whispering gallery structures, such as the recently studied microtoroid [5], in which the optomechanical coupling is proportional to the inverse of the radius of cavity ($R$), $g_{\rm OM} = \omega_c/R$. Both these devices utilize the radiation pressurce, or scattering, force of light. By comparison, the zipper cavity operates using the gradient force for which the optomechanical coupling length can be on the scale of the wavelength of light, $L_{\rm OM} \sim \lambda_c$. Similar to the scaling found in the previous section for the effective mode volume, the optomechanical coupling length scales exponentially with the slot gap, $L_{\rm OM} \sim \lambda_c e^{\alpha s}$, where $\alpha$ is proportional to the refractive index contrast between the nanobeams forming the zipper cavity and the surrounding cladding.

In Fig. 2.11(a) we plot the tuning curve for the nominal zipper cavity structure studied in the previous two sections versus the normalized slot gap width, $\bar{s} \equiv s/\Lambda_m$. Due to the strong intensity of the bonded mode in the center of the slot gap, it tunes more quickly than the anti-bonded mode. This tuning curve can be used to estimate the optomechanical coupling for the in-plane differential mode of motion of the zipper cavity nanobeams. The in-plane common mechanical modes and both types of vertical mechanical modes are expected to provide a much smaller level of optomechanical coupling due to the reduced change in slot gap with these types of motion. For complex geometries and motional patterns, one must use a consistent definition of displacement amplitude, $u$, in determing $g_{\rm OM}$, $m_{\rm eff}$ (motional mass), and $k_{\rm eff}$ (effective spring constant). In this work we use a convention in which $u(t)$ represents the amplitude of motion for a normalized mechanical eigenmode displacement field pattern:

$$\mathbf{u}_n(\mathbf{r},t) = u_n(t)\frac{\sum_i \mathbf{f}_n(x;i)}{\sqrt{\sum_i \frac{1}{l}\int_0^l |\mathbf{f}_n(x;i)|^2 \mathrm{d}x}}, \tag{2.3}$$

where $n$ is a mode label, $l$ is the length of the nanobeams, and for the simple two-beam geometry considered here, $i$ is an index indicating either the first or second nanobeam and we write the displacement vector only as a function of position along the long axis of the nanobeams ($x$). With this definition of *amplitude*, the effective motional

mass is simply the total mass of the two nanobeams ($m_u = 43$ picograms), and the effective spring constant is defined by the usual relation $k_u = m_u \Omega_M^2$, with $\Omega_M$ the mechanical eigenmode frequency. The amplitude associated with zero-point motion and used in the equipartition theorem to determine the thermal excitation of the mechanical mode is then $u_n(t)$. Note, an alternative, but equally effective method, defines the amplitude first, and then adjusts the effective motional mass based upon the strain energy of the mechanical motion.

Our chosen normalization prescription yields (approximately) for the $q$th odd-order in-plane differential mechanical mode,

$$\mathbf{u}^{\mathrm{o}}_{h_{qd}}(x,t) \approx u_{h_{qd}}(t)\left(\hat{y}_1 \cos(q\pi x/l) + \hat{y}_2 \cos(q\pi x/l)\right) \tag{2.4}$$

, where $\hat{y}_1$ and $\hat{y}_2$ are (transverse) in-plane unit vectors associated with first and second nanobeams, respectively, and which point in opposite directions away from the center of the gap between the nanobeams. The even-order modes are anti-symmetric about the long axis of the cavity and are given approximately by,

$$\mathbf{u}^{\mathrm{e}}_{h_{qd}}(z,t) \approx u_{h_{qd}}(t)\left(\hat{y}_1 \sin(q\pi x/l) + \hat{y}_2 \sin(q\pi x/l)\right) \ . \tag{2.5}$$

To be consistent then, with this definition of mode displacement amplitude, $g_{\mathrm{OM}}$ must be defined in terms of the rate of change of cavity frequency with respect to *half* the change in slot gap ($g_{\mathrm{OM},0} \approx \mathrm{d}\omega_c/\frac{1}{2}\mathrm{d}\delta s$), as the amplitude $u_{h_{qd}}(t)$ corresponds to a (peak) change in slot gap of $\delta s = 2u_{h_{qd}}(t)$.

Fig. 2.11(b) plots the optomechanical coupling length for each of the bonded and anti-bonded fundamental modes from the derivative of their tuning curves in Fig. 2.11(a). This plot shows that for a normalized slot gap of $\bar{s} = 0.1$ (or roughly $s = 0.04\lambda_c$), the optomechanical coupling length to the fundamental bonded optical mode can be as small as $L_{\mathrm{OM}}/\Lambda_m \approx 2$. For the normalized frequency of the bonded mode ($\Lambda_m/\lambda_c \approx 0.4$), this corresponds to $L_{\mathrm{OM}} \approx 0.8\lambda_c$, as expected from the arguments laid out in the introduction. The $\mathrm{TE}_{-,0}$ has a significantly smaller optomechanical coupling due to its reduced electric field energy in the slot.

An estimate of the optomechanical coupling to the mechanical modes can be found by averaging the displacement amplitude field pattern of the mechanical mode weighted by the (normalized) optical intensity pattern of the zipper cavity optical modes [49] (an exact calculation of the optomechanical coupling factor suitable for complex dielectric geometries and mixed cavity field polarization can be performed using the pertubation theory for shifting boundaries in Ref. [50]). For the specific case of the in-plane differential modes, the optomechanical coupling factor to the $\mathrm{TE}_{+,0}$ optical mode is approximately given by,

$$g_{\mathrm{OM},h_{qd}} \approx g_{\mathrm{OM},0} \frac{\left| \int \overline{\mathbf{f}}_{h_{qd}}(x;i) |\widetilde{\mathbf{E}}_{\mathrm{TE}_{+,0}}(x)|^2 \mathrm{d}x \right|}{\int |\widetilde{\mathbf{E}}_{\mathrm{TE}_{+,0}}(x)|^2 \mathrm{d}x}, \tag{2.6}$$

where $\overline{\mathbf{f}}_{h_{qd}}(x;i)$ is the normalized displacement vector of either of the nanobeams (=cos($q\pi x/l$) (sin($q\pi x/l$)) for the odd(even)-order in-plane differential mode), $\widetilde{\mathbf{E}}_{\mathrm{TE}_{+,0}}(x)$ is the Gaussian-like envelope of the $\mathrm{TE}_{+,0}$ optical cavity mode along the long-axis of the nanobeams, and $g_{\mathrm{OM},0}$ is the optomechanical coupling factor as calculated from the tuning curve of Fig. 2.11.

Given the odd symmetry of the even-order $h_{qd}$ mechanical modes, and the even symmetry of the optical intensity for the zipper cavity optical modes, the optomechanical coupling to the even-order $h_{qd}$ modes is approximately zero. The odd-order in-plane differential modes, on the otherhand, have an anti-node of mechanical displacement at the optical cavity center and an even long-axis symmetry. For mode numbers small enough that the half-wavelength of the mechanical mode is roughly as large, or larger, than the effective length of the optical cavity mode along the axis of the beam, the optical mode will only sense the central half-wave displacement of the mechanical mode and the optomechanical coupling should still be quite large. As an example, from the intensity plot of the $\mathrm{TE}_{+,0}$ fundamental bonded optical mode in Fig. 2.4, the effective length of the optical mode along the long-axis of the nanobeams is $L_{\mathrm{eff}} \sim 7\Lambda_m = 4.2$ $\mu$m (for $\lambda_c = 1.5$ $\mu$m). The mechanical mode index $q$ is roughly equal to the number of half-wavelengths of the mechanical mode along the axis of the zipper cavity. Therefore, for the zipper cavity of length $l = 36$ $\mu$m studied above,

the 9th order in-plane differential mechanical mode with $\Omega_{h_{9d}}/2\pi \approx 170$ MHz has a half-wavelength equal to 4 $\mu$m $\approx L_{\text{eff}}$. The resulting optomechanical coupling of the $h_{9d}$ mechanical mode to the $\text{TE}_{+,0}$ optical mode is then still relatively large, equal to approximately half that of the coupling to the fundamental $h_{1d}$ mechanical mode. The optomechanical coupling factor to the $\text{TE}_{+,0}$ for each of the in-plane differential modes is tabulated along with the mechanical mode properties in Table 2.1.

There are several physical ways of understanding the strength of the optomechanical coupling represented by $g_{\text{OM}}$. The per-photon mechanical force is given by $F_{ph} = \hbar g_{\text{OM}}$. For the zipper cavity, this yields a per-photon force of $F_{ph} \approx \hbar\omega_c/\lambda_c$, which at near-infrared wavelengths corresponds to 0.2 pN/photon. Such a force could be measured using other, non-optical techniques, and could provide a means for detecting single photons in a non-demolition manner. Also, through the optomechanical coupling, intra-cavity light can stiffen [28, 51–53] and dampen [25–29, 54] the motion of the coupled mechanical oscillator [5]. A perturbative analysis shows that in the sideband unresolved limit ($\Omega_M \ll \Gamma$) the effective mechanical frequency ($\Omega'_M$) and damping rate ($\gamma'_M$) are given by the following relations (see Ref. [5]):

$$(\Omega'_M)^2 = \Omega_M^2 + \left(\frac{2|a_0|^2 g_{\text{OM}}^2}{\Delta^2 \omega_c m_u}\right)\Delta'_o, \tag{2.7}$$

$$\gamma'_M = \gamma_M - \left(\frac{4|a_0|^2 g_{\text{OM}}^2 \Gamma}{\Delta^4 \omega_c m_u}\right)\Delta'_o, \tag{2.8}$$

where $\Omega_M$ and $\gamma_M$ are the bare mechanical properties of the zipper cavity, $|a_0|^2$ is the time-averaged stored optical cavity energy, $\Delta'_o \equiv \omega_l - \omega_c$ is the laser-cavity detuning, $\Gamma$ is the waveguide-loaded optical cavity energy decay rate, and $\Delta^2 \equiv (\Delta'_o)^2 + (\Gamma/2)^2$. The maxmimum "optical spring" effect occurs at a detuning point of $\Delta'_o = \Gamma/2$. Extrapolating equation (3.1) down to the single photon level (ignoring quantum fluctuations for arguments sake), for this laser-cavity detuning a single stored cavity photon introduces a shift in the mechanical frequency corresponding to $\Delta(\Omega_M^2)/\Omega_M^2 = (2Q\hbar\omega_c)/(\lambda_c^2 k_{\text{eff}})$. For the zipper cavity, with $Q = 5 \times 10^6$, $\lambda_c = 1$ $\mu$m, and $k_{h_{1d}} = 100$ N/m, the resulting single-photon mechanical frequency shift is

approximately $\Delta(\Omega_M)/\Omega_M = 1\%$.

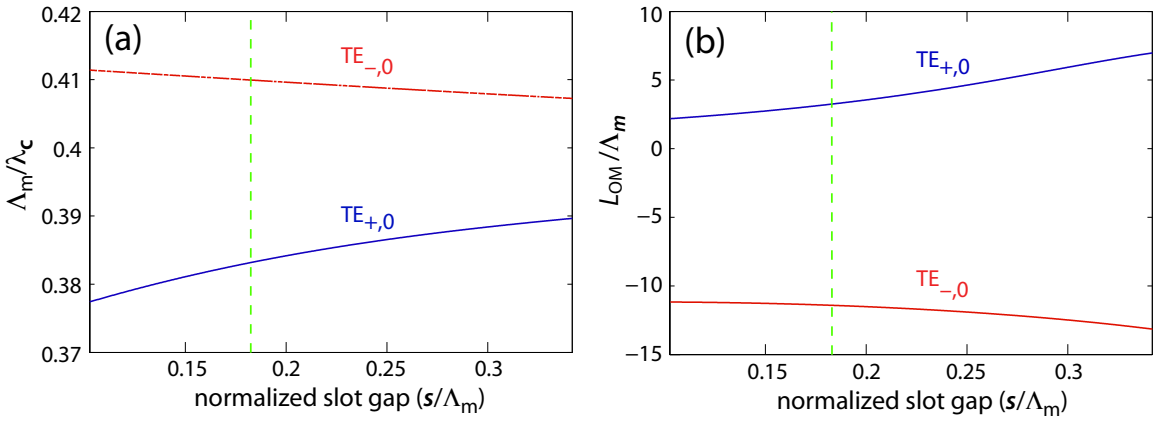


Figure 2.11: (a) Bonded and anti-bonded mode tuning curves versus normalized nanobeam gap. (b) Corresponding normalized effective optomehcanical coupling length, $\overline{L}_{\rm OM} \equiv L_{\rm OM}/\Lambda_m$. The nominal structure is indicated by the dashed green line.

## 2.6 Summary and Discussion

Using photonic crystal concepts, we have designed an optomechanical system in which optical and mechanical energy can be co-localized in a cubic-micron volume and efficiently coupled through the gradient optical force. In the particular design studied here, a "zipper" cavity consisting of two nanoscale beams of silicon nitride, doubly clamped and patterned with a linear array of air holes, is used to form the optical cavity and the mechanical resonator. Mechanical oscillations consisting of differential motion of the doubly-clamped silicon nitride nanobeams results in an optomechanical coupling constant as large as $g_{\rm OM} \sim \omega_c/\lambda_c$, where $\omega_c$ and $\lambda_c$ are the optical resonant cavity frequency and wavelength, respectively. This coupling is several orders of magnitude larger than has been demonstrated in high-Finesse Fabry-Perot cavities, and is more than order of magnitude larger than for whispering-gallery micrototoid structures, both of which rely upon the radiation pressure force. Finite-element-method (FEM) simulations of the zipper cavity show that a structure with an optical $Q = 5 \times 10^6$, mechanical resonance frequency of $\Omega_M/2\pi \approx 170$ MHz, and motional

mass of $m_u \approx 40$ picograms is possible. In the future, further increase in the mechanical frequency and reduction in the motional mass may be attained by using planar phononic crystals [55] to form the mechanical resonator. The combination of phononic and photonic crystals would also provide an integrated, chip-scale platform for routing and coupling optical and mechanical energy.

Beyond cavity optomechanics, the zipper cavity may also find application in the field of cavity QED. In particular, the zipper cavity as described here is suitable for a broad range of wavelengths from the visible to the mid-infrared. The optical mode volume is made smaller by the sub-wavelength slot gap between the nanobeams [48], with $V_{\text{eff}} \sim 0.2(\lambda_c^3)$ for a slot gap of $s \sim \lambda_c/10$. As an example, one can imagine placing nanoparticles of diamond (a popular solid-state system for quantum information processing [56–61]) in the gap between the nanobeams. Such "pick-and-place" techniques have been used with other, larger, optical cavities with good success [62–64]. In the zipper cavity case, the small $V_{\text{eff}}$ would produce a coherent coupling rate with the zero-phonon-line (ZPL) of the $NV^-$ transition of approximately, $g_{\text{ZPL}}/2\pi \sim 3$ GHz, even after accounting for the $3-5\%$ branching ratio for the ZPL line. This is more than 100 times the radiative-limited linewidth measured for the $NV^-$ transition (12 MHz), and more than 10 times the theoretical zipper cavity decay rate (90 MHz), putting the coupled system deep within the strong coupling regime. The additional benefit provided by the zipper cavity is the ability to rapidly tune the cavity frequency into and out of resonance with the ZPL of the $NV^-$ transition. If mechanical resonance frequencies could be increased towards GHz values, using the suggested phononic crystal concepts for instance, then new approaches to photon-mediated quantum interactions and quantum state transfer can be envisioned for solid-state cavity QED systems.

# Chapter 3

# Experimental Demonstration of a Picogram and Nanometer Scale Photonic Crystal Optomechanical Cavity

This work is reproduced and adapted from Ref. [1].

## 3.1 Summary

Recently, there has been keen interest [6] in dynamic back-action caused by electromagnetic forces in optical [25–29, 54] and microwave [31] cavities. Back-action cooling, for example, is being pursued as a means to achieve quantum ground-state cooling of a macro-scale mechanical oscillator. Work in the optical domain has revolved around milli- or micro-scale structures utilizing the radiation pressure force. By comparison, in microwave devices, low-loss superconducting structures have been used for gradient-force mediated coupling to a nanomechanical oscillator of picogram mass [31]. Here we describe measurements of an optical system consisting of a pair of specially patterned nanoscale beams in which optical and mechanical energy are simultaneously localized to a cubic-micron-scale volume, and for which large per-photon optical gradient forces are realized. The resulting scale of the per-photon force and the mass of the structure enable new cavity-optomechanical regimes to be explored, where for example, the mechanical rigidity of the structure is dominantly provided

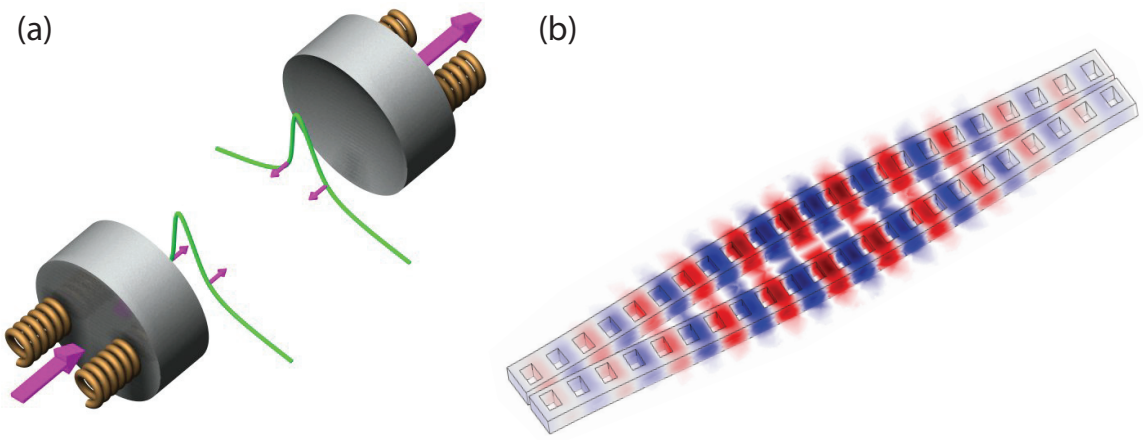


Figure 3.1: Comparison of optomechanical systems. **a**, Fabry-Perot optomechanical system with two mirrors on springs. **b**, Photonic crystal optomecachanical systems.

by the internal light field itself. In addition to precision measurement and sensitive force detection [32], nano-optomechanics may find application in reconfigurable and tunable photonic systems [65], RF-over-optical communication [66], and to generate giant optical nonlinearities for wavelength conversion and optical buffering [34].

## 3.2 Introduction to the Zipper Optomechanical System

Optical forces arising from near-field effects in guided-wave structures have been proposed [33], and recently demonstrated [67, 68], as a means of providing large optomechanical coupling between the field being guided and the dielectric mechanical structure providing the guiding. The resulting optical force can be viewed as an intensity gradient force much like that used to *tweeze* dielectric particles or to trap cold gases of atoms [69]. In the devices studied in this work, doubly-clamped silicon nitride nanobeams are converted into optical resonant cavities through the patterning of a linear array of etched holes (Fig. 3.1(b)). Bringing two such cavities into the near-field of each other forms a super cavity supporting even and odd superpositions of the individual beams modes. This "zipper" cavity, so-named due to its resemblence

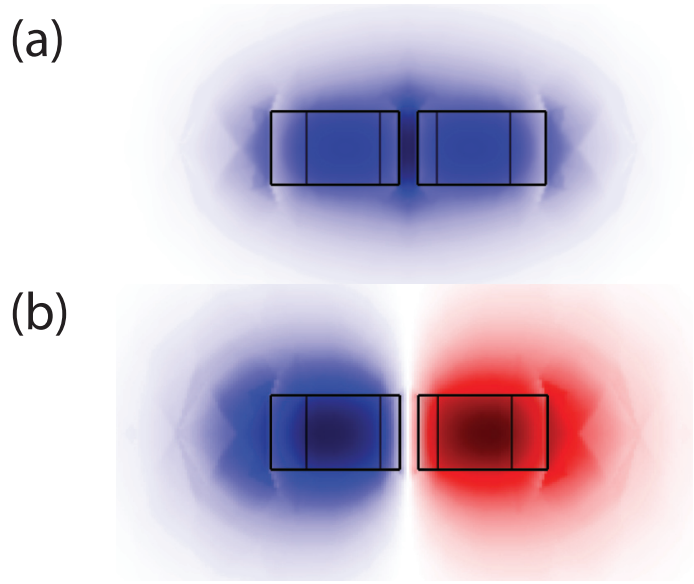


Figure 3.2: Finite-element-method simulated **a**, bonded and **b**, anti-bonded supermodes of the zipper optical cavity, shown in cross-section.

to the mechanical fastner, allows for sensitive probing and actuation of the differential motion of the beams through the internal, optical, cavity field.

A figure of merit for cavity-optomechanical systems is the coupling constant $g_{\mathrm{OM}} \equiv \mathrm{d}\omega_c/\mathrm{d}x$, which represents the differential frequency shift of the cavity resonance ($\omega_c$) with mechanical displacement of the beams ($x$). For the commonly studied Fabry-Perot cavity structure (Fig. 3.1(a)), momentum transfer between the circulating light field and the mechanically-compliant end mirror(s) occurs at a rate of $2\hbar\mathbf{k}_{ph}$ per round trip time, resulting in an optomechanical coupling constant that scales with the inverse of the cavity length ($L_c$), $g_{\mathrm{OM}} = \omega_c/L_c$. Similarly for whispering-gallery-mode structures, such as the recently studied microtoroid [5], $g_{\mathrm{OM}}$ scales with the perimeter length through the radius of the cavity $R$, $g_{\mathrm{OM}} = \omega_c/R$. In the case of the zipper cavity the optomechanical coupling is exponentially proportional to the slot gap ($s$) between the beams, $g_{\mathrm{OM}} = \omega_c/L_{\mathrm{OM}}$ with $L_{\mathrm{OM}} \sim w_o e^{\alpha s}$. The minimum value of $L_{\mathrm{OM}}$ is set by $w_o$ which is approximately equal to the beam width, while the decay constant $\alpha$ is set by the wavelength of light ($\lambda$) and the refractive index contrast of the nanobeam system. Thus, for beam widths on the order of the wavelength of light and

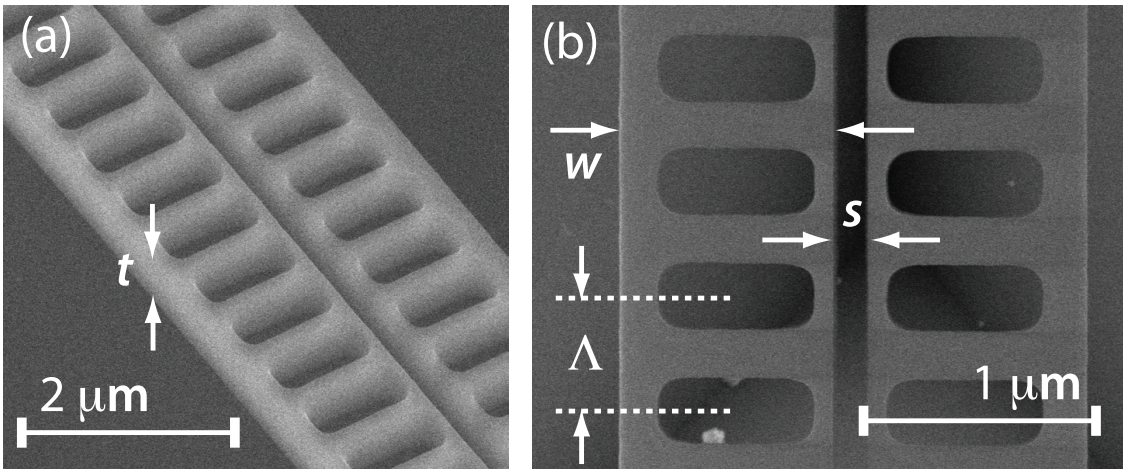


Figure 3.3: **a,b**, Scanning-electron-microscope (SEM) images of a typical zipper cavity, indicating the slot width ($s$), the cantilever width ($w$), and the photonic crystal lattice constant ($\Lambda$).

for a sub-wavelength slot gap, $L_{\rm OM} \sim \lambda$, independent of the length of the nanobeams (see Fig. 3.5(a,b)). This yields an optomechanical coupling more than an order of magnitude larger than can be accomplished in high-Finesse Fabry-Perot cavities [70] or glass microtoriod structures [5]. In addition, this large optomechanical coupling is realized in a versatile geometry in which motional mass and mechanical stiffness can be greatly varied, and for which the mechanical displacement energy density and optical energy density can be efficiently co-localized at optical wavelengths in the visible-NIR and for mechanical frequencies in the MHz-GHz frequency range.

## 3.3 Fabrication

For the devices studied in this work, optically thin ($t = 400$ nm) stoichiometric silicon nitride ($Si_3N_4$) is deposited using low-pressure-chemical-vapor-deposition on a silicon wafer in order to form the optical guiding layer and the mechanical beams. Electron-beam lithography is used to pattern the zipper cavity consisting of beams of length $l = 25 - 40$ $\mu$m, widths of $w = 0.6$-$1.4$ $\mu$m, and with an inter-beam gap of $s = 60$-$250$ nm (Fig. 3.3(b)). The optical cavity is created in the nanobeams by patterning holes to form a quasi-1D photonic bandgap for light (see Figs. 3.6). A $C_4F_8/SF_6$-based

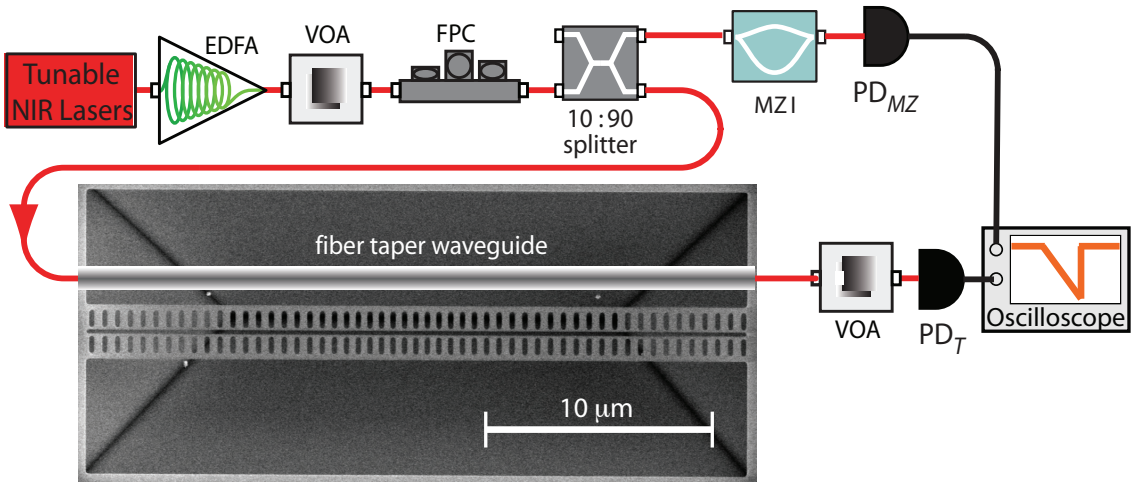


Figure 3.4: Experimental set-up used to probe the optical and mechanial properties of the zipper cavity. Acronyms are: erbium-doped fiber amplifier (EDFA), variable optical attenuator (VOA), fiber polarization controller (FPC), fiber Mach-Zender interferometer (MZI), and photodetected Mach-Zender transmission ($PD_{MZI}$) and zipper cavity transmission ($PD_T$).

plasma etch is then used to transfer the nanobeam and photonic crystal pattern into the $Si_3N_4$. This is followed by a wet chemical etch of KOH which selectively etches the underlying Si subtrate and releases the patterned beams.

## 3.4 "DC" Optical Spectroscopy

As shown in Figure 3.4, optical excitation and probing of the zipper cavity is performed using a high-efficiency optical fiber taper coupler [71] in conjunction with a bank of tunable external-cavity diode lasers. A fiber polarization controller is used to adjust the polarization to selectively excite the transverse electric (TE) polarization modes of the zipper cavity. The zipper optical cavity design is based upon a graded lattice concept [2, 71, 72] in which the lattice period is varied harmonically from the center to the ends of the nanobeam. This results in an optical potential for photons which increases harmonically as one approaches the cavity center. Localized modes form from photonic bands near the zone boundary with negative group velocity dispersion [41], with the fundamental mode of the cavity having the *high-*

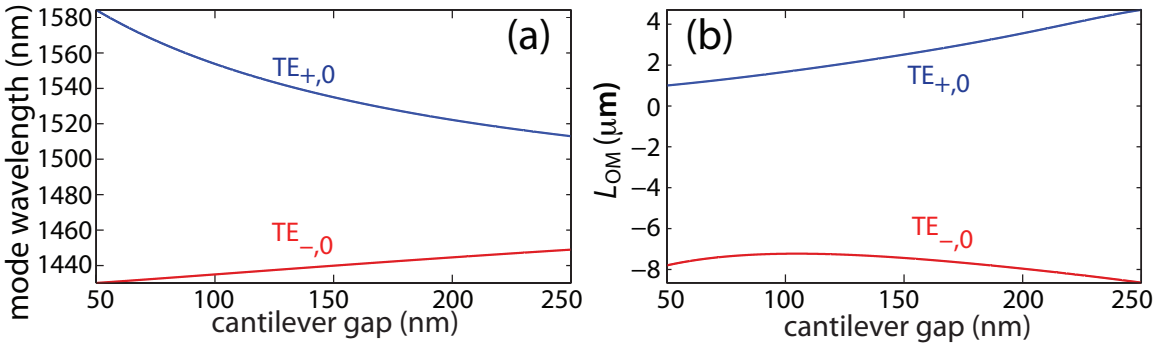


Figure 3.5: Finite-element-method simulation of the **a**, wavelength tuning versus nanobeam slot gap and **b**, effective optomechanical coupling length parameter ($L_{\rm OM}$) for the bonded and anti-bonded fundamental zipper cavity optical modes ($w$ = 650 nm).

*est* frequency and higher-order cavity modes *decreasing* in frequency (see inset of Fig. 3.6). Owing to the strong optical coupling between the pair of nanobeams, the photonic bands in the zipper cavity break into pairs of positive and negative parity super-mode bands. The positive-parity superposition, designated $\mathrm{TE}_{+}$, corresponds to a manifold of modes which have an even mode profile for the TE electric field polarization and a peak electric field intensity in the center of slot gap between the beams (Fig. 3.2(a)). These we term *bonded* modes [33]. The negative-parity $\mathrm{TE}_{-}$ manifold of modes (the *anti-bonded* modes) have an odd parity mode profile and a node at the slot gap center (Fig. 3.2(b)).

By systematically varying the lattice constant of the devices, and measuring the parity of the cavity modes using the fiber taper as a near-field probe [71], one can identify the various zipper cavity modes. For example, for a zipper cavity with $a$ = 640 nm, beam width $w$ = 650 nm, and slot gap $s$ = 120 nm, the measured transmission scan across the $\lambda$ = 1420-1625 nm range is shown in Fig. 3.6. From shortest to longest wavelength, the resonance peaks all have an even mode profile and are associated with the $\mathrm{TE}_{+,0}$ through $\mathrm{TE}_{+,4}$ modes of the *bonded* manifold of modes. Wavelength scans of a different zipper cavity, with larger beam width $w$ = 1.4 $\mu$m and slot gap $s$ = 250 nm, exhibits a spectrum in which the bonded and anti-bonded mode manifolds overlap (Fig. 3.7(a)). The measured on-resonance transmission contrast

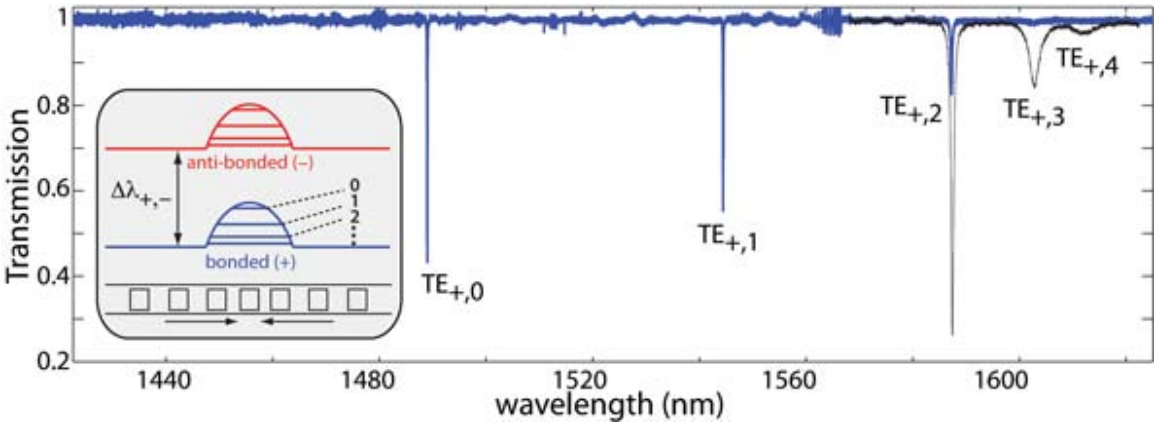


Figure 3.6: DC optical spectroscopy of the zipper cavity. Measured optical transmission of a zipper cavity with $w = 650$ nm and $s = 120$ nm showing four orders of the bonded ($TE_+$) resonant modes. Inset: schematic of the graded photonic crystal lattice design and resulting bonded and anti-bonded resonance manifolds.

versus lateral taper position for each of the modes is shown in Fig. 3.7(b,c), indicating their even (bonded) and odd (anti-bonded) mode character. The optical $Q$-factor of the zipper cavity $TE_{+,0}$ mode can theoretically reach a value well above $10^6$ even in the modest refractive index afforded by the silicon nitride [2,40]. Experimentally we have measured zipper cavity modes with $Q$-factors in the range of $Q = 10^4 - 10^5$ (Finesse $\mathcal{F} \sim 10^4$), depending largely upon the fill-fraction of the air holes and their scattering of light transverse to the axis of the quasi-1D photonic bandgap. For devices at the high end of the measured $Q$ range ($Q \sim 3 \times 10^5$), we find a significant contribution to optical loss from absorption (see Methods).

## 3.5 RF Optical Spectroscopy

Mechanical motion of the zipper cavity nanobeams is imprinted on the transmitted optical intensity through the phase modulation of the internal cavity field [5]. Figure 3.9(a) shows the high-temporal-resolution (blue curve) and low-pass filtered (red curve) transmitted signal as the input laser wavelength is swept across the $TE_{1,+}$ mode of the zipper cavity of Fig. 3.6 at low optical input power ($P_i = 12$ $\mu$W). The zoomed-in temporal response of the transmitted intensity for a detuning on the

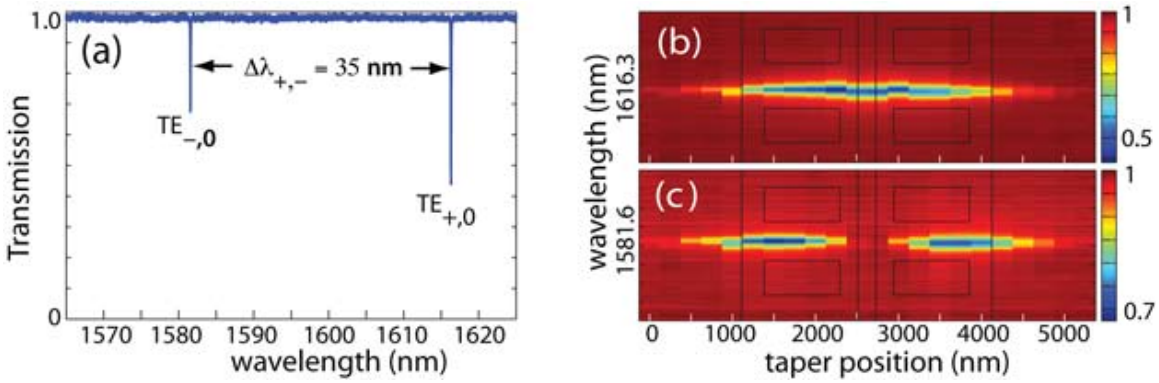


Figure 3.7: **a**, Measured optical transmission of a zipper cavity with a larger beam width and gap ($w$ = 1400 nm, $s$ = 250 nm) showing the bonded and anti-bonded lowest order optical resonances. **b,c**, Optical transmission versus fiber taper lateral position for each of the bonded and anti-bonded resonant modes of **a**, indicating the even and odd parity of the modes. Black outline corresponds to position of zipper cavity.

side of the Lorentzian lineshape (Fig. 3.9(b)) shows an oscillating signal of frequency $\sim 8$ MHz and peak-to-peak amplitude of roughly a third of the transmission contrast of the resonance. Finite-element-method (FEM) simulations (Fig. 3.9(a,b)) indicate that the lowest order in-plane common ($h_{1c}$) and differential ($h_{1d}$) mechanical modes of the pair of coupled nanobeams have frequencies of 8.19 and 8.16 MHz (mass, $m_x \approx 43$ picograms, and spring constant $k_{h1} \approx 110$ N/m; see Methods), respectively, when accounting for $\sim$ 0.75 GPa of internal tensile stress in the nitride film [43]. The corresponding mechanical amplitude of oscillation is calibrated by fitting $g_{\rm OM}$ from the optical spring effect as discussed below and in the Methods section, yielding $L_{\rm OM} = 1.58$ $\mu$m ($g_{\rm OM}/2\pi = 123$ GHz/nm) and an inferred rms amplitude of motion of approximately $x_{\rm rms} \sim 5.8$ pm. This is in good correspondence with both the FEM-simulated optomechanical coupling constant for this device ($L_{\rm OM} = 2.1$ $\mu$m for $s = 120$ nm in Fig. 3.6(b)) and the expected thermal amplitude for the $h_{1d}$ mode ($\langle x_{th}^2 \rangle^{1/2} = \sqrt{k_B T/k_{h1}} = 6.2$ pm).

The RF spectrum of the transmitted optical intensity out to 150 MHz is shown in Fig. 3.9(c). Comparison to FEM mechanical simulations [2] allows us to identify many of the resonances in the RF spectrum, with in-plane mechanical resonances up

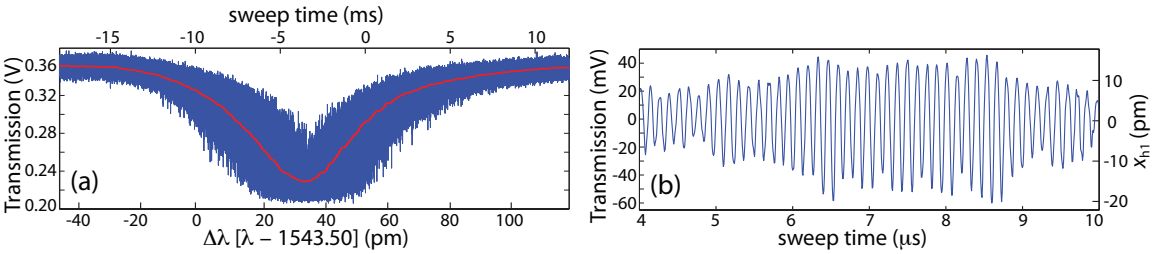


Figure 3.8: RF optical spectroscopy. **a**, Optical transmission through the zipper cavity of Fig. 3.6(c). The red curve corresponds to the low-pass-filtered (bandwidth 10 kHz) transmission signal showing the underlying Lorentzian-like cavity resonance. **b**, Temporal oscillations in optical transmission for fixed detuning, showing large-scale optical power oscillations of frequency $\sim 8$ MHz.

to 9th-order being visible. The strength of the corresponding spectral peaks oscillates for odd and even orders of in-plane motion, consistent with the odd-order mechanical modes having an anti-node of displacement at the center of the zipper cavity and the even-order modes having a node. The mechanical $Q$-factor of the resonances are measured to vary between $Q_M \sim 50 - 150$, limited by gas-damping [73] in the nitrogen test environment used in this work. For the $h_1$ mechanical resonances (Fig. 3.9(d)) at 8 MHz, the RF spectrum shows two other interesting features. The first is the interference between the two resonances as evidenced by the asymmetry in each peak and the narrow central dip. As will be detailed elsewhere, this is due to coupling between the common and differential modes of mechanical oscillation for which the common-mode motion is *dark* with respect to our optical read-out method. The second feature of interest is the slight shift of the $h_1$ resonance peaks to lower (higher) resonance frequencies for red (blue) laser-cavity detuning. Both of these features are absent for the $h_3$ resonance peaks centered around 28 MHz (Fig. 3.9(e)) for which the optomechanical coupling is weaker and the frequency-splitting between independent nanobeam motion is much larger than for the $h_1$ modes.

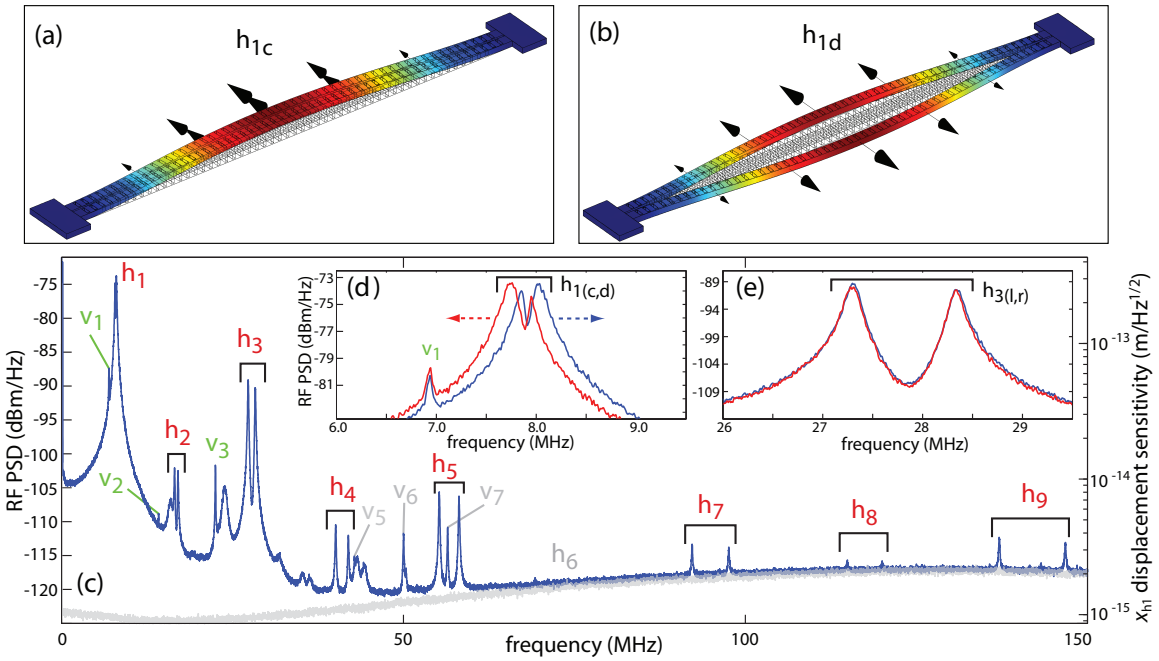


Figure 3.9: FEM-modeled lowest order **a**, common and **b**, differential mechanical resonances. Mechanical deformation and color indicates displacement amplitude, while arrows indicate direction. **c**, Detected RF spectrum with horizontal ($h$) and vertical ($v$) cantilever modes of motion indicated. Grey colored labels indicate either "missing" resonances or modes of questionable description. Grey colored curve is the electronic detector noise floor. Insets: zoomed-in RF spectrum of the **d**, hybridized fundamental $h_1$ mechanical modes and **g**, distinct left and right cantilever modes of third-order in-plane motion ($h_3$). In **f** and **e** the red curves correspond to RF spectra taken for red detuning and the blue curves correspond to blue-detuned spectra.

## 3.6 Optical Spring and Damping

The optically driven zipper cavity not only allows for sensitive mechanical displacement detection, but can also strongly modify the mechanical motion in two distinct ways. Optical stiffening of the mechanical resonant structure [5, 28] (the so-called "optical spring") results from the component of optical cavity energy (and gradient force) oscillating in-phase with the mechanical motion. On the otherhand, the finite cavity photon lifetime introduces a non adiabatic, time-delayed, component of optical force acting in-quadrature with the mechanical motion. This velocity dependent force results in detuning-dependent amplification or damping of the mechanical motion. A perturbative analysis shows that in the sideband unresolved limit ($\Omega_M \ll \Gamma$) the ef-

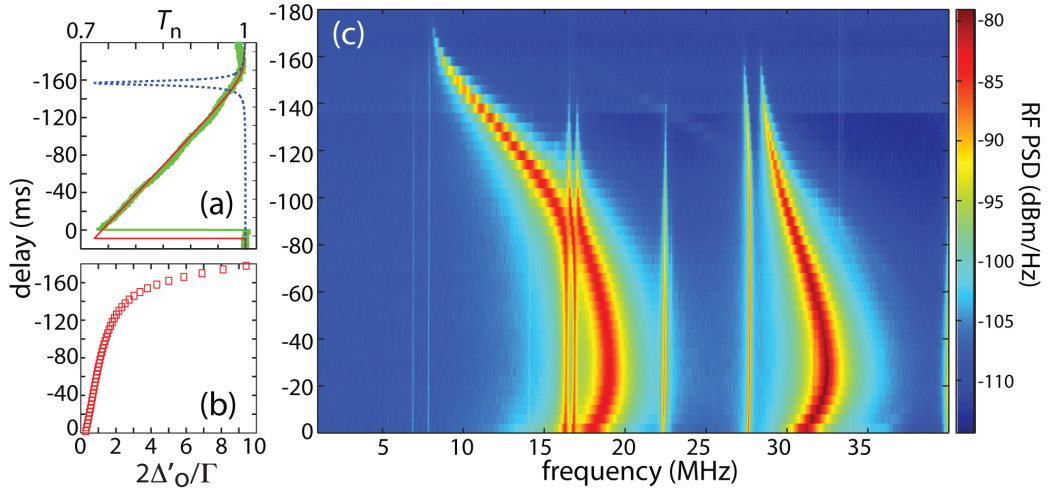


Figure 3.10: Optical Spring and Damping. **a**, Measured (green curve) and fit model (red curve) normalized optical transmission versus wavelength sweep in units of sweep time. Dashed blue curve corresponds to low power model curve. **b**, Conversion between sweep time delay and normalized cavity detuning, fit from model curve in (a), with zero time delay corresponding to zero laser-cavity detuning. **c**, Intensity image of the measured RF power spectrum versus cavity detuning (time delay) of the optical transmission signal from the zipper optical cavity of Fig. 3.6(c) at an input optical power of 5.1 mW (dropped power of 1.4 mW).

fective mechanical frequency ($\Omega'_M$) and damping rate ($\gamma'_M$) are given by the following relations (see Ref. [5] and § 1.3):

$$(\Omega'_M)^2 = \Omega_M^2 + \left(\frac{2|a_0|^2 g_{\mathrm{OM}}^2}{\Delta^2 \omega_c m_x}\right)\Delta'_o, \tag{3.1}$$

$$\gamma'_M = \gamma_M - \left(\frac{2|a_0|^2 g_{\mathrm{OM}}^2 \Gamma}{\Delta^4 \omega_c m_x}\right)\Delta'_o, \tag{3.2}$$

where $\Omega_M$ and $\gamma_M$ are the bare mechanical properties of the zipper cavity, $|a_0|^2$ is the time-averaged stored optical cavity energy, $\Delta'_o \equiv \omega_l - \omega_c$ is the laser-cavity detuning, $\Gamma$ is the waveguide-loaded optical cavity energy decay rate, and $\Delta^2 \equiv (\Delta'_o)^2 + (\Gamma/2)^2$.

As is shown in Fig. 3.10, for higher optical input powers ($P_i = 5$ mW) the internal optical cavity field provides significant stiffness to mechanical motion of modes in the zipper optomechanical cavity. The large optomechanical coupling ($L_{\mathrm{OM}} = 1.58$ $\mu$m) and comparitively small motional mass ($m_x \sim 43$ picograms) of the $h_{1d}$-zipper-cavity

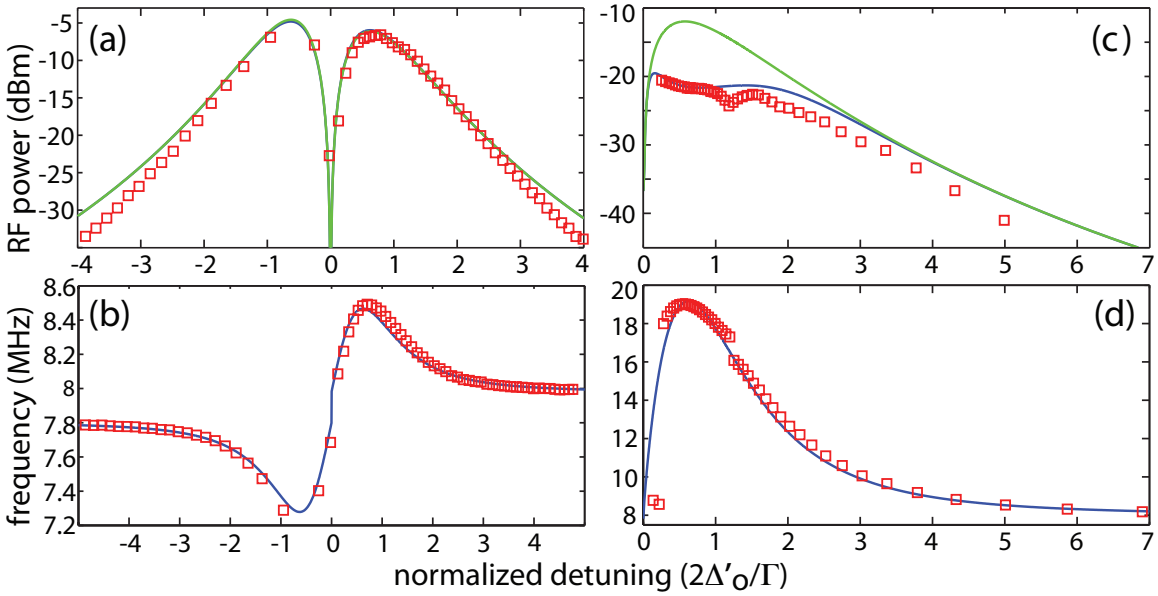


Figure 3.11: Optical Spring and Damping. **a**, Measured (green curve) and fit model (red curve) normalized optical transmission versus wavelength sweep in units of sweep time. Dashed blue curve corresponds to low power model curve. **b**, Conversion between sweep time delay and normalized cavity detuning, fit from model curve in (a), with zero time delay corresponding to zero laser-cavity detuning. **c**, Intensity image of the measured RF power spectrum versus cavity detuning (time delay) of the optical transmission signal from the zipper optical cavity of Fig. 3.6(c) at an input optical power of 5.1 mW (dropped power of 1.4 mW). Measured and modeled **d**,**f** total RF power and **e**,**g** resonance frequency of the $h_{1,d}$ mechanical mode, versus detuning. **d**,**e** correspond to low optical input power ($P_i = 127$ $\mu$W) while **f**,**g** are for high optical input power ($P_i = 5.1$ mW). Blue (green) curves correspond to a model with (without) optomechanical damping. Red squares are measured data points.

mechanical mode results in a giant optical spring effect [28], shifting the mechanical frequency from 8 to 19 MHz (Fig. 3.10(c)). This corresponds to an optical stiffness greater than five times that of the intrinsic mechanical stiffness of the silicon nitride cantilevers. For the $h_{3d}$ in-plane mode, the frequency shift is smaller due to the slightly reduced optomechanical coupling factor of this mode and its larger bare frequency. An additional feature in Fig. 3.10(d) is the mechanical mode mixing that occurs as the optical spring tunes the $h_{1d}$ mode through other mechanical resonances. The mode mixing is most prevelant as the $h_{1d}$ sweeps away from the $h_{1c}$ mode and through the $h_2$ in-plane modes near $\Omega/2\pi = 16$ MHz (Fig. 3.10(e)). This mixing of mechanical

modes is due to the highly anisotropic and motion-dependent optical stiffness and its renormalizing of the mechanical eigenmodes of the structure, and will be discussed in more detail elsewhere.

Figures 3.11(a-d) compare the measured integrated RF power in the $h_{1d}$ mechanical resonance line and its mechanical frequency to a nonlinear optical model of the zipper cavity system including the optical gradient force and thermo-optic tuning of the cavity (see Methods section). At low optical power (Figures 3.11(a,b)), a single estimate for $g_{\rm OM}$ based upon optical FEM simulations fits both the total measured RF power (or $\langle x^2 \rangle$) and optical frequency of the $h_{1d}$ mode over a large detuning range. At higher powers (Figures 3.11(c,d)), the same estimated $g_{\rm OM}$ fits the optical frequency tuning of the $h_{1d}$ mode, but severely over estimates the total RF power (green curve in Fig. 3.11(c)) where the optomechanical interaction is strongest. Damping of the mechanical motion is quite unexpected for blue-detuned laser excitation [5]. FEM numerical simulations of the zipper cavity indicate thermomechanical effects [22,23] produce a response several orders of magnitude too small to explain the observed damping; however, a theoretical analysis of the cavity dynamics including the thermo-optic effect (see § 1.3.6) shows that the severely phase-lagged and damped thermo-optic tuning of the cavity introduces a significant correction to eq. (3.2). Owing to the small heat capacity of the zipper cavity, thermo-optic tuning reverses the sign of the damping coefficient of the bare optomechanical response for blue-detuned pumping (the correction to the optical spring is found to be small, at the $10^{-4}$ level). The numerical model including the thermo-optic correction to the spring and damping terms is shown as a blue curve in Figs. 3.11(a,c), with the fit to the high power data now in much better agreement. The model indicates that at a detuning of $\Delta_0' \approx \Gamma/4$ (Fig. 3.11(c)) the thermal motion of the $h_{1d}$ resonance is being damped from $x_{\rm rms} \approx 7$ pm down to 1 pm, at a bath temperature of 360 K.

## 3.7 Prospects of the "Zipper" Optomechanical system

Beyond the giant optical spring effect afforded by the large optomechanical coupling and picogram-scale mass of the zipper cavity, thin-film photonic crystals offer a highly flexible, chip-scale architecture for coupling optical and mechanical degrees of freedom. In the area of quantum cavity-optomechanics, significant improvements in optical $Q$ to values approaching $5 \times 10^6$ ($\mathcal{F} \sim 10^6$) can be expected with new processing technqiues [2, 74], which along with increased mechanical frequency ($> 100$ MHz), will push the system into the important sideband resolved limit [30, 75]. Applications to optical cavity QED [70] also exist, where rapid cavity frequency shifting may be utilized for single-photon generation and quantum-state transfer. Finally, by combining phononic [55] with photonic crystal concepts, simultaneous routing and localization of acoustic and optical waves can be envisioned. Such a platform would expand both quantum and classical applications, and enable integration not possible in current optomechanical microsystems.

## 3.8 Optomechanical Coupling, Effective Mass and Spring Constant

For complex geometries and motional patterns, one must use a consistent definition of displacement amplitude, $x$, in determing $g_{\mathrm{OM}}$, $m_x$ (motional mass), and $k_{\mathrm{eff}}$ (effective spring constant). In this work we use a convention in which $x(t)$ represents the amplitude of motion for a normalized mechanical eigenmode displacement field pattern:

$$\mathbf{u}_n(z,t) = x_n(t)\frac{\mathbf{f}_n(z)}{\sqrt{\frac{1}{l}\int_0^l |\mathbf{f}_n(z)|^2 \mathrm{d}z}}, \tag{3.3}$$

where $n$ is a mode label, $l$ is the length of cantilever, and, for the simple cantilever

geometry considered here, the displacement vector is only a function of position along the axis of the cantilevers ($z$). With this definition of amplitude, the effective motional mass is simply the total mass of the two cantilevers ($m_x = m_c = 43$ picograms) and the effective spring constant is defined by the usual relation $k_{\rm eff} = m_c\Omega_M^2$, with $\Omega_M$ the mechanical eigenmode frequency. The amplitude associated with zero-point motion and used in the equipartition theorem to determine the thermal excitation of the mechanical mode is then $x_n(t)$. In the case of the fundamental differential mechanical mode of motion for the two cantilevers of the zipper cavity, this normalization prescription yields $\mathbf{u}_{h1d}(z,t) \approx x_{h1d}(t)\,(\sin(\pi z/l)\hat{x}_1 + \sin(\pi z/l)\hat{x}_2)$, where $\hat{x}_1$ and $\hat{x}_2$ are in-plane unit vectors associated with the two nanobeams of the zipper cavity and pointing in opposite directions away from the center of the gap between the nanobeams. Thus, to be consistent, $g_{\rm OM}$ for the $h_{1d}$ mode must be defined approximately as the rate of change of cavity frequency with respect to *half* the change in slot gap ($g_{\rm OM} \approx {\rm d}\omega_c/\frac{1}{2}{\rm d}\delta s$), as the amplitude $x_{h1d}(t)$ corresponds to a change in slot gap of $2x_{h1d}(t)$ near the center of the cavity.

## 3.9 Optical Transmission, Measured RF Spectra, and Motional Sensitivity

RF spectra are measured by direct detection of the optical power transmitted through the zipper cavity using a 125 MHz bandwidth photodetector (noise-equivalent-power NEP= 2.5 pW/Hz$^{1/2}$ from 0-10 MHz and 22.5 pW/Hz$^{1/2}$ from 10-200 MHz, responsivity $R = 1$ A/W, transimpedance gain $G = 4\times10^4$ V/A) and a high-speed oscilloscope (2 Gs/s sampling rate and 1 GHz bandwidth). As shown in Fig. 3.4, a pair of "dueling" calibrated optical attenuators are used before and after the zipper cavity in order to vary the input power to the cavity while keeping the detected optical power level constant. The measured electrical noise floor is set by the circuit noise of the photodetector for the optical power levels considered in this work, corresponding to $-125$ dBm/Hz near 10 MHz. The motional sensitivity of the $h_{1d}$ mechanical mode is

measured at $9 \times 10^{-16}$ m/Hz$^{1/2}$ for an optical input power of 12 $\mu$W (corresponding to a dropped power of 3.5 $\mu$W, and an estimated 660 stored cavity photons). At the power levels considered in this work, optical force noise contribution to the motional sensitivity is negligible.

## 3.10 Calibration of Input Power and Intra-Cavity Photon Number

A fiber-taper optical coupling technique was used to in-couple and out-couple light from the zipper cavity. The fiber taper, although extremely low-loss on its own (88% transmission efficiency in this work), was put in contact with the substrate near the zipper cavity in order to mechanically anchor it during all measurements (thus avoiding power-dependent movement of the taper due to thermal and/or optical forces). The total fiber taper transmission after mechanical anchoring of the taper to the substrate is 53%. In order to accurately determine the optical power reaching the cavity (determined by the optical loss in the taper section before the cavity) we measure the cavity response at high optical power (resulting in thermo-optic tuning of the cavity and optical bistability in the transmission response) with the input sent in one direction and then in the other of the taper. From the asymmetry in the thermo-optic tuning in the cavity for both directions one can determine the asymmetry in the optical loss, and thus determine the optical loss before and after the zipper cavity. Finally, this method along with calibrated measurements of the optical power at the input and output of the taper, can determine accurately the optical power reaching the zipper cavity (the *input* power) and dropped by the cavity. From calibration of the wavelength sweep using the fiber Mach-Zender interferometer one can also accurately measure the cavity linewidth and the corresponding loaded cavity $Q$. The average stored photon number can then be determined from the dropped power and the loaded cavity $Q$. The $TE_{1,+}$ mode is chosen to study in detail, instead of the $TE_{0,+}$ fundamental mode, due to its spectral alignment with the EDFA gain bandwidth,

allowing for the higher power measurements presented in Fig. 3.11.

## 3.11 Calibration of Laser-Cavity Detuning

The transduction from mechanical motion to modulated intra-cavity power, and consequently measured RF photodector spectrum, depends sensitively on the detuning point of the laser from the cavity resonance. Accurate measurement of the laser-cavity detuning, even for large detunings ($> 5$ half-cavity-linewidths), is required to compare the theoretical model with measured data for the optical spring and damping shown in Fig. 3.11. Several methods exist to determine the laser-cavity detuning, including calibration of the transduced modulated photodector signal for a known mechanical or optical modulation, or simple inversion of the normalized optical transmission signal using the measured Lorentzian response of the cavity. For the swept measurements presented in this work, we have opted to calibrate accurately the laser wavelength versus sweep time using a fiber-based Mach-Zender interferometer (FSR= 1.57 pm at $\lambda \sim 1480$ nm), and to use this to fit and convert sweep time to laser-cavity detuning by comparing with a nonlinear model of the cavity system that incorporates thermo-optic and gradient-force tuning (see § 3.13). The thermo-optic cavity tuning versus temperature was measured to be 14.9 pm/K by direct measurement of the resonance wavelength shift over a 20 K temperature range. The optomechanical coupling constant $g_{\rm OM}$ was estimated from both simulation, based upon an FEM model of scanning-electron-microscope (SEM) images taken of the cavity geometry, and a fit to the peak measured mechanical frequency shift. The nonlinear cavity model, incorporating the measured thermo-optic effect and the fit $g_{\rm OM}$, then provides an accurate conversion between wavelength and detuning from the cavity. The above method for calibrating laser-cavity detuning is simple to employ with the swept wavelength method used in this work, and found to be much more accurate than relying on the low-pass-filtered optical transmission contrast to infer detuning (especially for large detunings where the transmission contrast is below the percent level).

## 3.12 Zipper Cavity Optical Loss

As mentioned above, although the optical force dominates the cavity tuning at MHz frequencies, the static tuning of the cavity is still largely ($\sim 80\%$) provided by the thermo-optic effect through optical absorption and subsequent heat generation within the zipper cavity. As discussed in the § 3.13.4, calculation of the thermal resistance of the silicon nitride zipper cavity indicates that optical absorption accounts for approximately 6% of the total optical cavity loss for the device in Fig. 3.11(a) (an absorption-limited $Q \sim 4.8 \times 10^5$). We attribute the optical absorption loss in the zipper cavity to surface-states [74] of the "holey" silicon nitride beams, rather than absorption in the bulk of the silicon nitride film, due to the much larger $Q$ values we have measured in less surface-sensitive microdisks formed from the same silicon nitride material. Properly chosen chemical surface treatments should enable $Q$-factors approaching the bulk-absorption-limited value of $Q_b \sim 5 \times 10^6$ at $\lambda = 1.5$ $\mu$m, and perhaps even higher at shorter wavelengths where optical absorption from overtones of the vibrational modes of the N-H bond is reduced.

These set of notes describe cavity optomechanics in the presence of additional thermo-optic tuning of the cavity resonance. We find that thermo-optic tuning results in correction factors to both the optical spring and optomechanical gain. In addition there is an overall saturation of the optomechanical coupling. These effects can be large for systems with large static thermo-optic tuning and fast thermal decay relative to the mechanical frequency. Analysis of the zipper optomechanical cavity indicates that optical damping can be realized with blue detuned light, in direct opposition to the bare optomechanical effect. Thermo-mechanical effects are also considered, and found to be negligible on the scale of the measured properties of the zipper cavity system. Finally, methods and parameters used in fitting a steady-state nonlinear optical model, including the gradient optical force and thermo-optic tuning, to the measured zipper optomechanical cavity response are provided at the end of the notes.

## 3.13 Steady-State Nonlinear Optical Model of the *Zipper* Optomechanical Cavity

### 3.13.1 Optical Properties

The fiber Mach-Zender interferometer is used to calibrate the wavelength scans of the zipper cavity modes. For the zipper cavity mode ($TE_{+,1}$) of the device studied in Fig. 2(c), Fig. 3, and Fig. 4, the taper-loaded optical $Q$-factor was measured to be $Q_T = 2.8 \times 10^4$ with a transmission contrast (fractional dropped power) of $\Delta T = 27.5\%$. The resonance wavelength is $\lambda \sim 1543$ nm. The fit value (see below) of the component of optical loss attributed to absorption is $Q_a = 4.5 \times 10^5$.

### 3.13.2 Geometry

As discussed in the main text, the zipper cavity device under study had $l = 36$ $\mu$m, $w = 650$ nm, $s = 120$ nm, and $t = 400$ nm, as measured by calibrated SEM inspection. The etched air holes were measured to be 330 nm by 330 nm in area. The total number of air holes per beam is 55.

### 3.13.3 Silicon Nitride Material Properties

The material properties of silicon nitride were scoured from a number of sources and journal articles. Where possible we have used parameters most closely associate with LPCVD silicon nitride on $\langle 100 \rangle$ Si. The density of LPCVD silicon nitride is taken to be $\rho = 3100$ kg/m$^3$, the Young's modulus $Y \sim 290$ GPa, the tensile stress $S \sim 0.75$ GPa, the coefficient of thermal expansion $\eta_{TE} = 3.3 \times 10^{-6}$ K$^{-1}$, the thermal conducivity $\kappa_{th} \sim 20$ W/m/K, and the specific heat $c_{sh} = 0.7$ J/g/K.

### 3.13.4 Thermal Properties of the Zipper Cavity

Due to the air-filling-fraction of the etched holes in the zipper cavity nanobeams, the thermal conductivity of the patterned beams was taken as $\Gamma_{th} = 75\%$ of the

bulk value. A simple estimate for the thermal resistance of the zipper cavity is then given by $R_{th} \sim l/(8tw\Gamma_{th}\kappa_{th}) \approx 1.15 \times 10^6$ K/W, where the factor of 1/8 comes from the ability for heat to escape out either end of the nanobeams and in either direction. The physical mass of the zipper cavity, taking into account the etched holes, is approximately $m = 43$ picograms. The heat capacity of the zipper cavity is then roughly $c_h = 3 \times 10^{-11}$ J/K. From the heat capacity and the thermal resistance, the thermal decay rate is estimated to be $\gamma_{th} = 1/R_{th}c_h \sim 2.9 \times 10^4$ $s^{-1}$. Finite-element-method simulations of thermal properties of the zipper cavity yield an effective thermal resistance of $R_{th} = 1.09 \times 10^6$ K/W and a thermal decay rate of $\gamma_{th} = 1/R_{th}c_h \sim 5.26 \times 10^4$ $s^{-1}$ for temperature at the center of the zipper cavity, in reasonable correspondence to the estimated values. The thermal tuning rate (dominated by the thermo-optic effect) for the device under study was measured to be $\delta\lambda_c/\delta T \sim 0.0149$ nm/K using a thermo-electrically heated stage and a thermo-couple placed a few millimeters from the sample.

### 3.13.5 Optomechanical Properties of the Zipper Cavity

The bare mechanical resonance frequency of the $h_{1d}$ zipper cavity is measured to be $\Omega_M \sim 8$ MHz, in good corresondence with the FEM-simulated value when $S = 0.75$ GPa of tensile stress is introduced into the silicon nitride film. The measured mechanical $Q$-factor is approximately $Q_M \sim 50$ for the differential mode, and roughly $Q_M \sim 150$ for the common mode of motion of the nanobeams. This difference is attributed to the squeeze-film-like damping [76] of the differential motion due to gas "squeezed" in between the beams. It should be mentioned that all measurements in the work described here were done in a nitrogen purged box (i.e., not under vacuum). The FEM-simulated optomechanical coupling length, based upon SEM images of the device under test, is $L_{\rm OM} = 2.09$ $\mu$m. The inferred optomechanical coupling length value, based upon the peak measured optical spring effect for various optical input powers, is $L_{\rm OM} = 1.575$ $\mu$m. Although good correspondence is found between simulated and measured $L_{\rm OM}$, the measured value of $L_{\rm OM} = 1.575$ $\mu$m is used to fit

the remaining cavity parameters as described below.

### 3.13.6 Wavelength-Scan Fitting

The steady-state equations of motion of the zipper cavity, as given by eqs. (1.126-1.128), are numerically solved with variable parameter $Q_a$ (all other parameters are fixed to values given above). The resulting wavelength dependent transmission curve is then fit to the measured (low-pass filtered) curve for a variety of optical input powers in order to determine the fit value of $Q_a$. Optical input power is calibrated as described in the Methods section using a calibrated power meter and measuring the system response for optical power sent in both directions down the fiber taper. From the fit transmission curve (Fig. 4(a)), the laser-cavity detuning (Fig. 4(b)) at each point within the intensity image of Fig. 4(c) can be determined. Calculating the optomechanical damping versus laser-cavity detuning, with and without the thermo-optic correction, is then used to model the expected RF power in the mechanical resonance line using eqs. (1.175-1.178).

# Chapter 4

# Design and Simulation Principles of Photonic and Phononic Crystal Optomechanical Resonators: Optomechanical Crystals

This chapter is reproduced and adapted from Ref. [4].

## 4.1 Summary

Periodically structured materials can sustain both optical and mechanical excitations which are tailored by the geometry. Here we analyze the properties of dispersively coupled planar photonic and phononic crystals: optomechanical crystals. In particular, the properties of co-resonant optical and mechanical cavities in quasi-1D (patterned nanobeam) and quasi-2D (patterned membrane) geometries are studied. It is shown that the mechanical $Q$ and optomechanical coupling in these structures can vary by many orders of magnitude with modest changes in geometry. An intuitive picture is developed based upon a perturbation theory for shifting material boundaries that allows the optomechanical properties to be designed and optimized. Several designs are presented with mechanical frequency $\sim$ 1-10 GHz, optical $Q$-factor $Q_o > 10^7$, motional masses $m_{\rm eff} \approx 100$ femtograms, optomechanical coupling length $L_{\rm OM} < 5$ $\mu$m, and a radiation-limited mechanical $Q$-factor $Q_m > 10^7$.

## 4.2 Introduction

It has previously been shown that "defects" in a planar periodic dielectric structure can simultaneously confine optical and mechanical resonances to sub-cubic-wavelength volumes [77]. As the co-localized resonances share the same lattice, and thus the same wavelength, the ratio of the optical to mechanical frequency of these modes is proportional to the ratio of their velocities. More recently, it was demonstrated that such co-localized resonances in a Silicon structure can strongly couple, via motion-induced phase modulation of the internal optical field, resulting in sensitive optical read-out and actuation of mechanical motion at GHz frequencies [3]. In this paper we aim to further develop the theory and design of these coupled photonic and phononic systems, laying the groundwork for what we term "optomechanical crystals". Here we choose a cavity-centric viewpoint of the interaction between photons and phonons, using the terminology and metrics from the field of cavity optomechanics [5–7]. An alternative viewpoint, more appropriate for guided-wave structures, may also be taken in which the interactions are described from a nonlinear optics (Raman-like scattering) perspective [78, 79].

We focus on two cavity devices in particular, a quasi-one-dimensional (quasi-1D) patterned nanobeam and a quasi-two-dimensional (quasi-2D) patterned nanomembrane, both of which have been studied extensively in the past [35, 80] for their photonic properties. The strength of the (linear) optomechanical coupling in such structures is found to be extremely large, approaching a limit corresponding to the transfer of photon momentum to the mechanical system every optical cycle [2]. Simultaneously, the effective motional mass [49] of the highly confined phonon modes is small, less than few hundred femtograms for a cavity system operating at a wavelength of 1.5 $\mu$m and a mechanical frequency of  2 GHz. This combination of parameters makes possible the optical transduction of high-frequency (multi-GHz) mechanical vibrations [8, 9, 78, 79] with near quantum-limited displacement sensitivity [81, 82]. Additionally, dynamical back-action [83] between the photon and phonon fields can be used to dampen [26, 27, 54, 84, 85] and amplify [86–88] mechanical motion, provid-

ing an optical source of coherent phonons [89,90] which can then be used within other phononic circuit elements [10, 91–94]. Planar optomechanical crystals then, should enable a new generation of circuits where phonons and photons can be generated, routed, and made to interact, all on a common chip platform.

Unlike the simple motion of a mirror on a spring in more conventional cavity optomechanical systems [51, 95], the complex mechanics of optomechanical crystal structures makes it difficult to intuit the origin or strength of the optomechanical coupling. Nonetheless, understanding the nature of the coupling is crucial to the engineering of optomechanical crystal devices as the degree of coupling between different optical and mechanical mode pairs can vary by orders of magnitude within the same structure, with even subtle changes in the geometry inducing large changes in the optomechanical coupling. In the experimental demonstration of a nanobeam optomechanical crystal [3], it was shown that the perturbation theory of Maxwell's equations with shifting material boundaries [19] provides an accurate method of estimating the optomechanical coupling of these complex motions. Here we describe how this perturbation theory can be used to create an intuitive, graphical picture of the optomechanical coupling of simultaneously localized optical and mechanical modes in periodic systems.

The outline of the paper is as follows. We first analyze the quasi-1D nanobeam optomechanical crystal system. This nanobeam structure provides a simple example through which the salient features of optomechanical crystals can be understood. The mechanical $Q$ of the structure is modeled using absorbing regions that provide a radiation condition for outgoing mechanical vibrations. The various types of mechanical losses are analyzed, and methodologies for minimizing or avoiding these losses are discussed. The dispersive coupling between the optical and mechanical modes is studied next. We use the aforementioned perturbation theory to analyze the optomechanical coupling strength, and which we display as an optomechanical coupling density on the surface of the structure. We use the density of optomechanical coupling picture to illustrate how the structure can be optimized to maximize the optomechanical coupling. Finally, we analyze the optomechanical coupling of a quasi-2D membrane

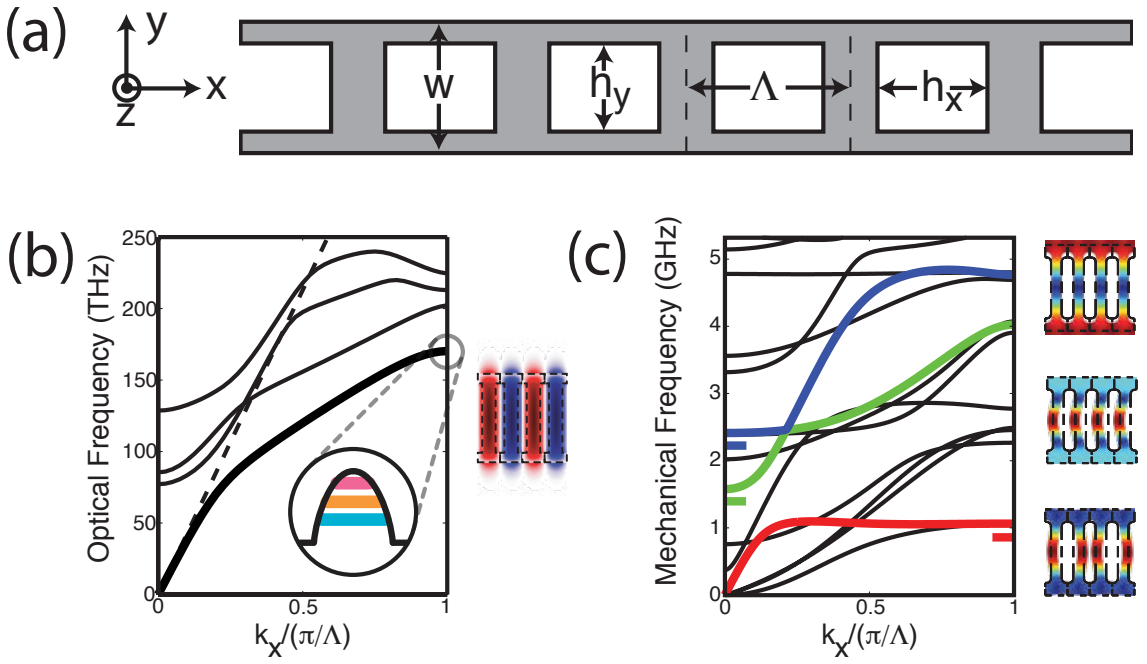


Figure 4.1: **(a)** General geometry of the periodic nanobeam structure's projection (infinite structure, no defect). **(b)** Optical band diagram of the nanobeam's projection. The band from which all localized optical modes will be derived is shown in dark black, with $E_y$ of the optical mode at the $X$ point shown to the right of the diagram. The harmonic spatial potential created by the defect, along with the first three optical modes are shown as emanating from the $X$-point band-edge. **(c)** Mechanical band diagram of the nanobeam's projection. The three bands that form defect modes that will be discussed in this work are colored. The bottom-most mode is from the $X$ point of the red band; the $\Gamma$ points of the green and blue bands correspond to the middle and top mechanical modes, respectively. The frequencies of the defect modes that form from the band edges are shown as short, horizontal bars.

structure, the well-known double-heterostructure photonic crystal cavity [72]. We show how the optical and mechanical modes and their coupling can be understood in terms of the quasi-one-dimensional nanobeam example.

## 4.3 One-Dimensional Optomechanical Crystal Systems: An Example

To illustrate the nature of the optomechanical coupling and losses in OMCs, we will use a quasi-1D nanobeam structure which has been demonstrated experimentally [3]. Figure 4.1(a) shows the general geometry of a periodic, quasi-one-dimensional OMC system made in a silicon beam of nanoscale cross-section. The system consists of an infinitely periodic array of $h_x$ by $h_y$ rectangular holes with center-to-center spacing, $\Lambda$, in a beam of width $w$ and thickness, $t$ (not shown). Although the actual structure will employ a defect to localize energy to a small portion of the beam, it is useful to consider the modes of this infinitely-periodic structure, since the structure has discrete translational invariance, allowing the optical and mechanical modes of the system to be classified according to their wavevector, $k_x$, and a band index. We shall call the infinitely-periodic structure the *projection* of the system. The band picture provided by the projection allows a simple description of localized optical and mechanical modes as existing between two "mirrors" in which propagating modes at the frequency of the defect have a small or vanishing density of states; the mirrors surround a perturbation region where propagation at the modal frequency is allowed, localizing the propagating mode between the mirrors. The optical and mechanical bands of the OMC's projection are shown in Fig. 4.1(b) and 4.1(c), respectively, for the structure $\Lambda = 360$ nm, $w = 1400$ nm, $h_y = 990$ nm, $h_x = 190$ nm, and $t = 220$ nm. The material properties are parameterized by an isotropic Young's modulus, $E = 169$ GPa, and an index of refraction, $n = 3.49$. The optical bands are computed with the MIT Photonic Bands package [96], while the mechanical bands are computed with COMSOL Mutliphysics [97], a finite element method (FEM) solver. The structure does not possess a complete stop band for either the mechanics or the optics; nevertheless a defect in this structure can simultaneously produce highly-confined, low-loss optical and mechanical modes.

The primary optical mode of interest will be the first TE-like (dominantly polarized in the $y$-direction) "valence" band mode at the edge of the first Brillioun zone

(the edge of the first Brillioun zone is called $X$ and the origin is called $\Gamma$). The electric field profile, $E_y$, is shown next to the band diagram. As described in detail in previous work on "zipper" optomechanical resonators [1,2] using general momentum-space design rules of photonic crystal cavities [98], the localized modes that come from this band-edge mode are as far as possible from the light line while having a minimal amount momentum near $k_x = 0$ (and identically zero momentum at $k_x = 0$) when used with a structure that is symmetric about a hole in the center. This reduces the radiation loss out of the structure. Because of the finite index contrast of the system, the optical $Q$ is limited by radiation from optical momentum components that are close to $k_x = 0$, since the system can only guide momentum components that are above the critical angle for total internal reflection. This governs the design and choice of optical modes of the structure. Because the optical band has negative curvature at the $X$ point, the frequency of the mode at the band edge must be increased to confine an optical mode coming from this band. This can be accomplished by decreasing $\Lambda$ (making the holes closer together without changing the size of the hole). As has been shown [1, 2, 13, 36–40, 99] both theoretically and experimentally, these nanobeam systems are capable of achieving very high radiation-limited $Q$-factors.

Unlike light, mechanical energy cannot radiate into the vacuum. This makes the design rules for creating low-loss mechanical defect modes qualitatively different than those discussed above for optical defect modes, as will be discussed in the next section. Just as true *photonic* band-gaps are not necessary to achieve high confinement and low optical losses in nanowire structures, true *phononic* bandgaps are also unnecessary to achieve low mechanical losses. A quasi-stop-band, where a defect mode of a particular polarization, frequency, and $k$-vector cannot couple a *significant* amount of energy to the waveguide modes of the mirror portion will be enough to acheive mechanical energy localization. Unlike in optics, all mechanical modes are "guided" by the structure, regardless of their $k$-vector, which allows localized mechanical modes to be created from either of the high symmetry points, $\Gamma$ or $X$. In fact, it will be shown that it is advantageous to draw mechanical modes from the $\Gamma$ point, as this generally produces larger optomechanical coupling than drawing from $X$. Clearly the

mechanical mode should be localized by the same defect as the optical mode; if this is not the case, then the target mechanical band-edge should be essentially unaffected by the defect that creates the optical mode, and a separate defect must be found that can localize the mechanics without significantly affecting the optical mode. Finally, the localized defect mode that is formed from the band edge must be sufficiently optomechanically coupled to the localized optical mode(s) of interest.

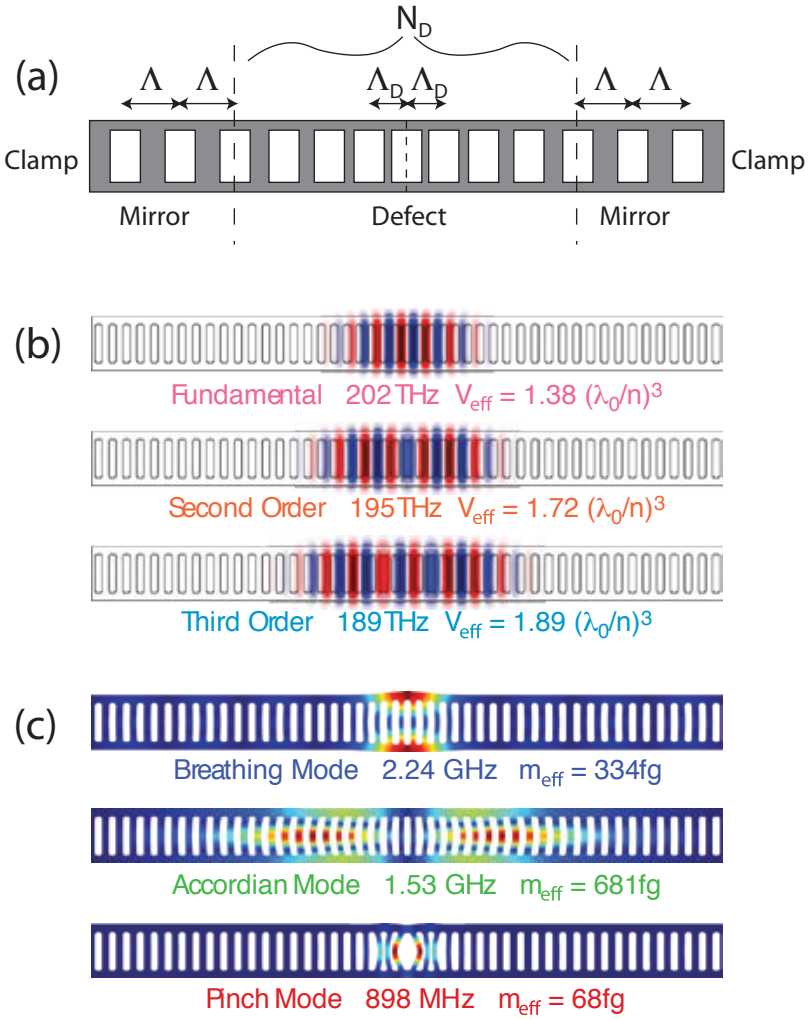


Figure 4.2: **(a)** Schematic illustration of actual nanobeam optomechanical crystal with defect and clamps at substrate. **(b)** Localized optical modes of the nanobeam OMC. The colors of the names correspond to the illustration of the inverted potential in Fig. 4.1(b). Localized, optomechanically-coupled mechanical modes of the nanobeam OMC. The colors of the names correspond to the colored bands and horizontal bars showing the modal frequencies in Fig. 4.1(c).

The defect that will be employed to localize optical and mechanical energy to the center of the structure consists of a decrease in the lattice constant for the otherwise periodic array of $N_{\text{total}}$ holes in the beam, as illustrated in Fig. 4.2(c). For the modes that are localized by the defect, this effectively divides the structure into a "defect" portion where propagation is allowed, surrounded by "mirrors", where the localized modes are evanescent, as discussed above. The particular defect used here consists of some odd number of holes, $N_{\text{D}}$, with the spacing between the holes varying quadratically from the background lattice constant, $\Lambda$, to some value $\Lambda_{\text{D}}$, with the spacing varying symmetrically about the center hole (the hole dimensions are held fixed throughout the structure). The complete geometry, which we will refer to as "the nominal structure" is: $N_{\text{total}} = 75$, $\Lambda = 360$ nm, $w = 1400$ nm, $h_y = 990$ nm, $h_x = 190$ nm, $t = 220$ nm, $N_{\text{D}} = 15$, and $\Lambda_{\text{D}} = 0.85\Lambda$. In the nanobeam structure described here, this defect simultaneously localizes many mechanical and optical modes.

For localized modes, the quasi-harmonic spatial defect creates a quasi-harmonic potential for the optical and mechanical mode envelopes [41]. This creates a ladder of states for each band edge with approximately Hermite-Gauss spatial dependencies along the cavity axis ($x$), in direct analogy to the harmonic potential of 1D quantum mechanics. As discussed above, the localized optical modes of interest come entirely from a single band-edge (the darkened band in Fig. 4.1(b)); the first three cavity modes of the defect from that band are shown in Fig. 4.2(b). Many localized mechanical modes with linear optomechanical coupling exist in this system. As examples, we will examine an exemplary optomechanically-coupled mechanical cavity mode from three different band-edges, even though each of these band edges produces a manifold of defect modes which may or may not have optomechanical coupling. The three modes are shown in Fig. 4.2(c), with the colors of the bands of Fig. 4.1(c) corresponding to the colors of the modes' label in the figure.

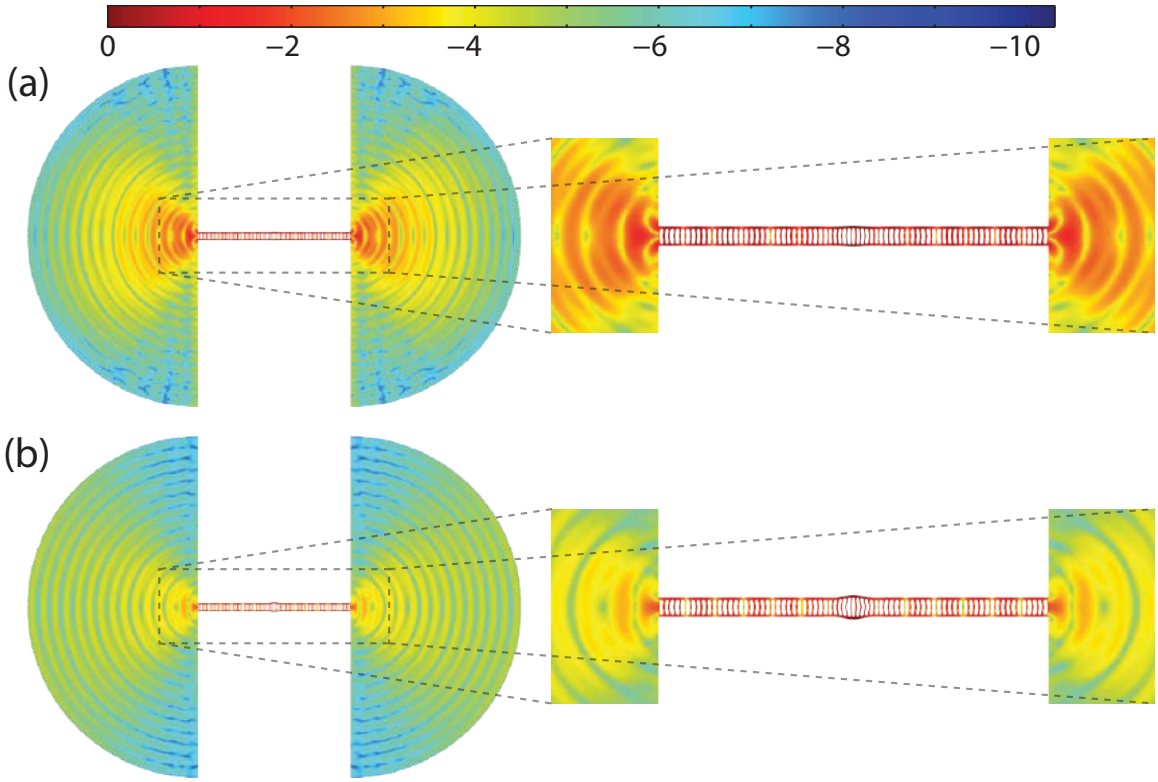


Figure 4.3: **(a)** In-phase and **(b)** in-quadrature mechanical displacement field ($\log_{10}(|\mathbf{q}|^2/\max(|\mathbf{q}|^2))$ of the fundamental breathing mode of nanobeam OMC structure with weakly absorbing "pad", showing the propagating nature of the radiated mechanical waves in the pad region.

## 4.4 Modal Cross-Coupling and Mechanical Losses

Periodic structures can be fabricated to have phononic band gaps [93,100–102], where mechanical energy loss by linear elastic coupling to the environment can be made arbitrarily small. Eventually, more fundamental losses [103, 104] such as thermoelastic loss [105–108], non-equilibrium energy redistribution [104, 109], phonon-phonon scattering [110], and the movement of dislocations and impurities [104, 111] should be accessible in these systems. First, however, the linear interaction of the optomechanical crystal and its surrounding substrate, which acts as a bath, must be understood and minimized. With this in mind, we use a finite element method model with weakly absorbing "bath" regions to model the losses in the system due to coupling of the mechanical energy into modes that are not confined. This method captures inter-modal

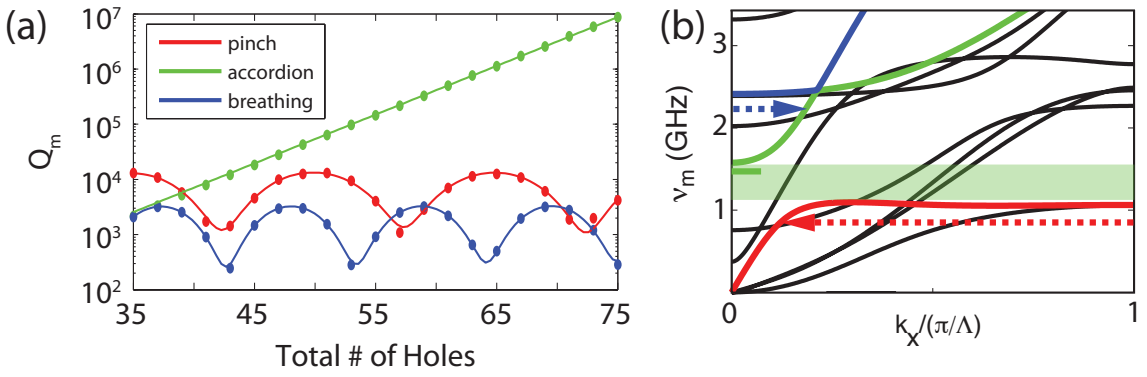


Figure 4.4: **(c)** Dependence of $Q_\mathrm{m}$ on the total length of the structure; the number of mirror holes on each side is $(N_T - 15)/2$. This shows the oscillatory $Q_\mathrm{m}$ of the pinch and breathing modes, which are coupled to waveguide modes, and the exponentially-increasing $Q_\mathrm{m}$ of the accordion mode. **(d)** Mechanical band structure of the nanobeam OMC, with arrow tails indicating the frequency and high-symmetry point of the breathing (blue) and pinch (red) modes, and arrow heads indicating the equi-frequency waveguide mode that acts as the dominant source of parasitic coupling. The effective bandgap of the accordion mode is shown in transparent green, with its frequency indicated as a horizontal green bar at the $\Gamma$ point.

coupling between the localized modes and all other mechanical modes of the system, some of which act as parasitic loss channels into the surrounding "bath".

The lack of a mechanical bandgap means that the superposition of $k$-vectors necessary to create a localized mode in the defect coincide with $k$-vectors of equi-frequency propagating modes of the phononic crystal mirrors. The localized modes and propagating modes of equal frequency will hybrizide and couple whenever the symmetries of the modes do not forbid it. In addition to the propagating modes, there are "body modes" that exist purely because of the boundary conditions (and thus not represented in the band structure), such as vibrations, density waves, and torsions of the finite, clamped structure. If the simulated exterior boundary conditions allow energy in the propagating and body modes to be lost, the propagating and body modes that couple to the localized mode will act as parasitic loss channels for the localized mode.

In a fabricated structure, the cantilever is attached to a substrate at both ends, rather than a hard boundary at the end of the cantilever. These more realistic boundaries must be included to model propagating and body mode losses. The propagating

modes travel down the nanobeam and partially reflect at the contacts due to an effective impedance mismatch caused by the geometric change between the nanobeam and the bulk. The rest of the power radiates into the bulk, causing a loss of mechanical energy. Thus the localized mode is coupled to a propagating mode with identical frequency that can radiate part or all of its energy into the surrounding "bath". This propagating mode also forms a coupled cavity resonance with the localized mode because of the reflections at the clamp points. The body modes have a softer boundary condition than $\mathbf{q} = 0$ at the boundaries, extending the body mode amplitude into the substrate. The part of the body mode that extends into the substrate can excite radiative modes of the substrate. The body mode then acts as a loss channel for any localized mode to which it is coupled. The localized, propagating, and body modes form a set of coupled resonators. Since the body and propagating modes are very sensitive to the total length of the structure, the self-consistent solution, which determines the loss of the localized mode, is very sensitive to the exact boundary conditions. Thus, to accurately simulate the true spatial profiles and losses of localized mechanical modes, one needs a simulation that reflects the true boundary conditions.

To model the loss due to coupling to radiative modes of the substrate, we include a large, semi-circular "pad" on each side of the nanobeam, with the same material constants as the nanobeam. To make the pad act like a "bath", we introduce a phenomenological imaginary part of the speed of sound in the pad region; i.e., $\mathrm{v}_{\mathrm{pad}} \rightarrow \mathrm{v}_{\mathrm{Silicon}}(1 + i\eta)$, where $\mathrm{v} = \sqrt{E/\rho}$. This creates an imaginary part of the frequency, and the mechanical $Q$ can be found by the relation, $Q_{\mathrm{m}} = \mathrm{Re}\left\{\nu_{\mathrm{m}}\right\}/(2\mathrm{Im}\left\{\nu_{\mathrm{m}}\right\})$. By adding loss to the pad material, propagating modes will reflect part of their power at the contacts (the interface between the cantilever and the substrate) because of the change in the impedance from the absorption, not just the geometric change in impedance. From this point of view, $\eta$ should be made as small as possible, since this contribution to the reflection coefficient is an artifact of the simulation and is not present in the real system. However, $\eta$ must also be large enough that the self-consistent solution includes a propagating, radiated wave, which only happens if the wave is appreciably attenuated by the time it reflects from the edge of the simulation

(where $\mathbf{q} = 0$) and returns to the contact. Thus, the pad is made as large as possible, given computational constraints, and the absorption is increased until $Q_{\mathrm{m}}$ changes appreciably, which gives the threshold value for $\eta$ at which the reflectivity of the contacts has an appreciable contribution from the absorption. The simulation is then performed with a value of $\eta$ that produces a propagating wave in the pad without causing an artificial reflectivity at the contact. Propagation in the pad is easily verified if the position of the nodes/antinodes swap between the in-phase and in-quadrature parts of the mechanical cycle (the nodes/antinodes of a standing wave are stationary). Figure 4.4(a) and 4.4(b) show the in-phase and in-quadrature (respectively) parts of the mechanical cycle of the breathing mode, clearly showing a propagating radiative mode in the weakly absorbing pad, with $\log_{10}(|\mathbf{q}|^2/\max(|\mathbf{q}|^2)$ plotted to elucidate the attenuation of mechanical radiation in the pad.

Limiting the artificial reflection at the interface of the non-absorbing and absorbing portions sets the maximum absorptivity, which in turn sets the minimum size of the pad (to guarantee that the radiation is completely attenuated before returning to the source). This size/absorptivity trade-off can be improved by making $\eta$ vary as a function of position in the pad, starting out at zero and increasing radially outward (quadratically, say). This is analogous to a mechanical perfectly matched layer (PML) [112], which has the benefit of increasing the round-trip absorption while maintaining a minimum reflectance at the clamp *due to* absorption. This provides the same reflection-free absorption of mechanical radiation in a more compact simulation space, making better use of computational resources.

Changing the length of the structure changes the resonance condition for both the propagating and body modes. This changes the amount of coupling to the localized mode in the self-consistent solution of the system. Thus the parasitc losses into a waveguide mode should be periodic. Figure 4.4(c) shows $Q_{\mathrm{m}}$ for the pinch, accordion, and breathing mode as the total number of holes (i.e., the length of the optomechanical crystal) is varied. For the breathing and pinch modes, the mechanical losses oscillate as a function of the total length of the nanobeam. For this particular geometry, the losses are dominated by propagating modes, and the oscillation period

of the $Q$ can be matched to a $k$-vector of a waveguide mode in the band structure in Fig. 4.4(d) (shown as a dotted line extending from the defect frequency). Thus the length of the structure can be tuned to minimize mechanical losses in cases where a complete mechanical bandgap is not present. Interestingly, the $Q$ of the accordion mode increases exponentially with the number of holes, indicating that the mode is evanescent in the mirror portions. Examining the four bands that cross through at the frequency of the accordion mode, we find that all four bands have a mirror symmetry about either the $x-z$ or $x-y$ planes that forbids any hybridization or coupling between to the accordion mode. This creates an effective bandgap (shown in translucent green). Practically speaking, this is a much weaker stop-band than a true bandgap, because any defect in the structure that breaks the symmetry of the accordion mode about the mirror planes will cause a coupling to the waveguide modes in the gap. However, it is exactly this kind of symmetry-dependent effective bandgap that is responsible for the high *optical* $Q$ [1,3,13,99] of the experimentally-fabricated structures. This gives some confidence that it is possible to fabricate structures that are defect-free to the degree necessary to achieve high $Q_{\mathrm{m}}$.

## 4.5 Optomechanical Coupling: Definition and Integral Representation

Cavity optomechanics[1] involves the mutual coupling of two modes of a deformable structure: one optical and one mechanical. The optical mode is characterized by a resonant frequency $\omega_{\mathrm{o}} = 2\pi\nu_{\mathrm{o}}$ and electric field $\mathbf{E}(\mathbf{r})$. The mechanical mode is characterized by a resonant frequency $\Omega_{\mathrm{m}} = 2\pi\nu_{\mathrm{m}}$ and displacement field $\mathbf{Q}(\mathbf{r})$, where $\mathbf{Q}(\mathbf{r})$ is the vector displacement describing perpendicular displacements of the boundaries of volume elements. The cavity optomechanical interactions of the distributed structure and its spatially-dependent vector fields, $\mathbf{E}(\mathbf{r})$ and $\mathbf{Q}(\mathbf{r})$, can be reduced to a description of two *scalar* mode amplitudes and their associated mode volumes, with

[1]This section is a partial reproduction from Chapter 1. See relevant sections of Chapter 2 for a more extensive discussion.

the coupling of the amplitudes parameterized by a single coupling coefficient, $g_{\mathrm{OM}}$.

The mode amplitude, $c$, and complex vector field profile, $\mathbf{e}(\mathbf{r})$, are defined such that the complex electric field is $\mathbf{E}(\mathbf{r}) = c\mathbf{e}(\mathbf{r})$ (the physical field is given by the real part of $\mathbf{E}(\mathbf{r})e^{i\omega t}$). For pedagogical reasons, the amplitude $c$ is normalized such that the time averaged electromagnetic energy is equal to $|c|^2$; i.e. $U = |c|^2 = \frac{1}{2}\int \mathrm{d}V \epsilon |\mathbf{E}|^2$. This forces $\mathbf{e}$ to be normalized such that $1 = \frac{1}{2}\int \mathrm{d}V \epsilon |\mathbf{e}|^2$. In cavity quantum electrodynamics, one typically defines an effective optical mode volume, $V_{\mathrm{o}} = \int \mathrm{d}V \left(\frac{\sqrt{\epsilon}|\mathbf{E}|}{\max(|\sqrt{\epsilon}\mathbf{E}|)}\right)^2$, in order to gauge the strength of light-matter interactions.

The mechanical vibration's amplitude, $\alpha$, and mode profile (displacement), $\mathbf{q}(\mathbf{r})$, are defined such that $\mathbf{Q}(\mathbf{r}) = \alpha\mathbf{q}(\mathbf{r})$. Here, $\alpha$ is defined as the largest displacement that occurs anywhere for the mechanical field, $\mathbf{Q}(\mathbf{r})$, so that $\max(|\mathbf{Q}(\mathbf{r})|) = 1$. It is important to note that this particular choice of $\alpha$ determines the mechanical mode's effective volume and effective mass, $V_{\mathrm{m}}$ and $m_{\mathrm{eff}} \equiv \rho V_{\mathrm{m}}$, respectively. In order to represent an energy and be consistent with the equipartition theorem, this choice of $\alpha$ requires the complimentary definition $m_{\mathrm{eff}} = \rho \int \mathrm{d}V \left(\frac{|\mathbf{Q}|}{\max(|\mathbf{Q}|)}\right)^2$. To see this, note that the free evolution of the mechanical oscillator has, by definition, a time-independent total energy $E_{\mathrm{mechanical}} = \frac{m_{\mathrm{eff}}}{2}(\Omega^2\alpha^2 + \dot{\alpha}^2)$. On the other hand, integrating the total energy of each volume element must *also* give this same total energy. If we pick the point in phase space at which all the mechanical energy is potential energy (i.e. the classical "turn-around point"), we must have that $E_{\mathrm{mechanical}} = \frac{1}{2}\Omega^2 \int \rho|\mathbf{Q}(\mathbf{r})|^2\mathrm{d}V = \frac{1}{2}m_{\mathrm{eff}}\Omega^2\alpha^2$, or, in other words, $m_{\mathrm{eff}}\alpha^2 = \int \rho|\mathbf{Q}(\mathbf{r})|^2\mathrm{d}V$. One can arbitrarily choose the definition of the amplitude or the mass, but choosing one determines the other. Note that $\alpha$ is also the amplitude of zero-point motion of the canonical position operator in a quantized treatment. For a system like a localized mode of a phononic crystal defect cavity, where only a very small, localized portion of the total mass undergoes appreciable motion, the most sensible choice of the mass is the amplitude-squared weighted density integral, which, as stated above, is the choice of mass associated with $\alpha = \max(|\mathbf{Q}(\mathbf{r})|)$.

The optomechanical coupling affects the optical mode by tuning the optical resonant frequency as a function of displacement, $\omega_{\mathrm{o}}(\alpha)$; whereas the coupling affects the

mechanical mode by applying a force, which is expressed as a gradient of the cavity energy, $\mathrm{d}\left|c\right|^2/\mathrm{d}\alpha$. The optical resonant frequency is usually expanded in orders of the (small) displacement, $\alpha$ around some equilibrium displacement, $\alpha_0$.

$$\omega_{\mathrm{o}}(\alpha) = \omega_{\mathrm{o}}\Big|_{\alpha=\alpha_0} + (\alpha-\alpha_0)\frac{\mathrm{d}\omega_{\mathrm{o}}}{\mathrm{d}\alpha}\Big|_{\alpha=\alpha_0} + (\alpha-\alpha_0)^2\frac{\mathrm{d}^2\omega_{\mathrm{o}}}{\mathrm{d}\alpha^2}\Big|_{\alpha=\alpha_0} + ... \tag{4.1}$$

In the case that the terms higher than first order can be neglected, this equation simplifies to

$$\omega_{\mathrm{o}}(\alpha) = \omega_{\mathrm{o}}\Big|_{\alpha=\alpha_0} + (\alpha-\alpha_0)\frac{\mathrm{d}\omega_{\mathrm{o}}}{\mathrm{d}\alpha}\Big|_{\alpha=\alpha_0} \equiv \omega_{\mathrm{o}} + (\alpha-\alpha_0)g_{\mathrm{OM}} \equiv \omega_{\mathrm{o}} + (\alpha-\alpha_0)\frac{\omega_{\mathrm{o}}}{L_{\mathrm{OM}}}\ , \tag{4.2}$$

where $\omega_{\mathrm{o}} \equiv \omega_{\mathrm{o}}\Big|_{\alpha=\alpha_0}$ is the equilibrium resonance frequency of the optical mode, $g_{\mathrm{OM}} \equiv \frac{\mathrm{d}\omega_{\mathrm{o}}}{\mathrm{d}\alpha}\Big|_{\alpha=\alpha_0}$ is the derivative of the resonance frequency of the optical mode evaluated at equilibrium, and $L_{\mathrm{OM}}$ is the *effective optomechanical length* of the system. The effective length, $L_{\mathrm{OM}}$, is a universal parameter that relates displacement to a change in optical frequency (i.e. $\alpha/L_{\mathrm{OM}} = \delta\omega_{\mathrm{o}}/\omega_{\mathrm{o}}$). From the definition, $L_{\mathrm{OM}}^{-1} \equiv \frac{1}{\omega_{\mathrm{o}}}\frac{\mathrm{d}\omega_{\mathrm{o}}}{\mathrm{d}\alpha}\Big|_{\alpha=\alpha_0} = g_{\mathrm{OM}}/\omega_0$, one can see that reducing $L_{\mathrm{OM}}$ maximizes the optomechanical coupling. It is simple to show that $L_{\mathrm{OM}}$ is equal to the spacing between the mirrors of a Fabry-Perot cavity when one mirror is allowed to move along the cavity axis or the radius of a microtoroid/microdisk for a radial breathing motion. For a "Zipper" cavity or double-microdisk, $L_{\mathrm{OM}}$ is an exponentially decreasing function of the spacing between the coupled elements, with $L_{\mathrm{OM}}$ approaching half a wavelength of light as the spacing approaches zero.

The perturbation theory of Maxwell's equations with shifting material boundaries [19] allows one to calculate the derivative of the resonant frequency of a structure's optical modes, with respect to some parameterization of a surface deformation *perpendicular* to the surface of the structure. If the result of a mechanical simulation is the displacement field, $\mathbf{Q}(\mathbf{r}) = \alpha\mathbf{q}(\mathbf{r}) \equiv \alpha\mathbf{Q}(\mathbf{r})/\max(|\mathbf{Q}|)$, then

$$\frac{1}{L_{\mathrm{OM}}} = \frac{1}{4}\int \mathrm{d}A\,(\mathbf{q}\cdot\hat{\mathbf{n}})\left[\Delta\epsilon\left|\mathbf{e}_{\parallel}\right|^2 - \Delta(\epsilon^{-1})\left|\mathbf{d}_{\perp}\right|^2\right] \tag{4.3}$$

where $\mathbf{d} = \epsilon\mathbf{e}$, $\hat{\mathbf{n}}$ is the unit normal vector on the surface of the unperturbed cavity, $\Delta\epsilon = \epsilon_1 - \epsilon_2$, $\Delta(\epsilon^{-1}) = \epsilon_1^{-1} - \epsilon_2^{-1}$, $\epsilon_1$ is the dielectric constant of the structure, and $\epsilon_2$ is the dielectric constant of the surrounding medium.

To calculate $L_{\mathrm{OM}}$ by deforming the structure, one must simulate the fields with a deformation amplitude, $\alpha$, that is large enough to be detectable numerically but small enough that higher order dispersion does not affect the frequency shift. To verify that higher order dispersion is not included, one must simulate the optical fields for a range of displacement amplitudes and extract the linear dispersion. Because perturbation theory can calculate the linear term exactly from a single calculation using the *undeformed* structure, this method has clear advantages over numerical methods using finite deformations.

## 4.6 Optomechanical Coupling: Visual Representation and Optimization

In addition to being computationally simpler than deformation methods, the perturbative method of calculating the optomechanical coupling allows one to represent the optomechanical coupling as a density on the surface, with different parts of the structure contributing different amounts of optomechanical coupling. This yields much more information than just the value of $L_{\mathrm{OM}}$, itself. The optomechanical coupling density is given by

$$\zeta_{\mathrm{OM}}(\mathbf{r}) \equiv \frac{1}{4}(\mathbf{q}\cdot\hat{\mathbf{n}})\left[\Delta\epsilon\left|\mathbf{e}_{\parallel}\right|^2 - \Delta(\epsilon^{-1})\left|\mathbf{d}_{\perp}\right|^2\right]. \tag{4.4}$$

The optomechanical coupling density can further be broken down into a mechanical part (the normal displacement profile)

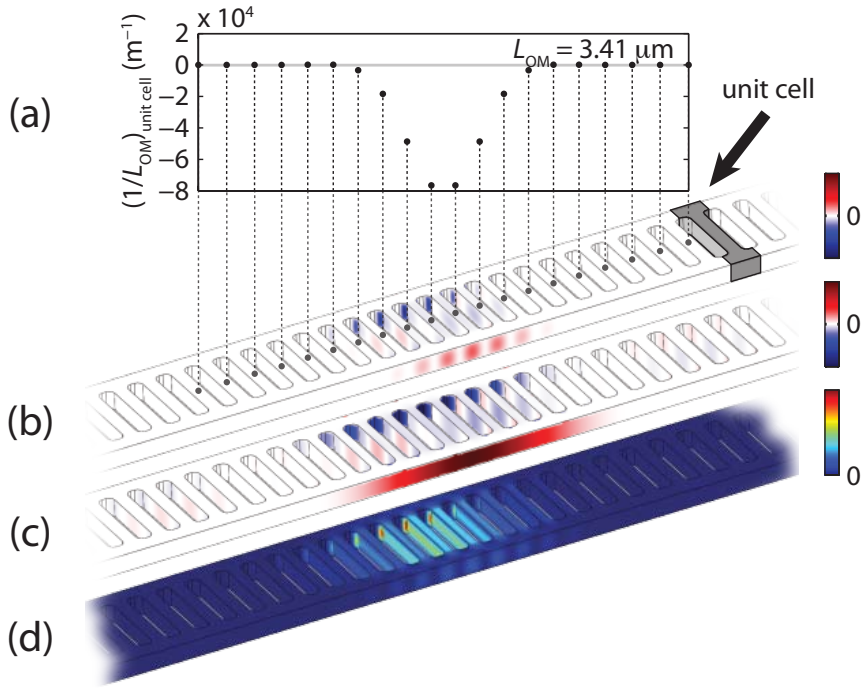


Figure 4.5: For the fundamental breathing mode and the fundamental optical mode in the nominal structure, **(a)** FEM simulation of individual unit cell contributions to the total optomechanical coupling (each point computed by integrating $\zeta_{\mathrm{OM}}$ (Equation 5.1) over the respective unit cell), **(b)** surface plot of the optomechanical coupling density, $\zeta_{\mathrm{OM}}$. **(c)** surface plot of the normal displacement profile, $\Theta_{\mathrm{m}}$ (Equation 4.5), **(d)** surface plot of the electromagnetic energy functional, $\Theta_{\mathrm{o}}$ (Equation 4.6). In (d), there is significant optomechanical coupling density in the corner of the holes, where the crossbar meets the rail. Without the fillets, the field amplitude is concentrated in the corner and difficult to see. For this reason, the corners have been filleted to allow the optomechanical coupling density in the corners to be visualized. The fillets do not significantly affecting the optomechanical coupling (confirmed by simulation).

$$\Theta_{\mathrm{m}}(\mathbf{r}) \equiv \mathbf{q} \cdot \hat{\mathbf{n}} \tag{4.5}$$

and an optical part (the electromagnetic energy functional)

$$\Theta_{\mathrm{o}}(\mathbf{r}) \equiv \Delta\epsilon \left|\mathbf{e}_{\parallel}\right|^2 - \Delta(\epsilon^{-1}) \left|\mathbf{d}_{\perp}\right|^2 \ , \tag{4.6}$$

which can be separately visualized on the surface. This provides a quantitative method of assessing the separate optical and mechanical contributions and allows

an intuitive approach to individually engineering the optical and mechanical properties of the structure to enhance the optomechanical coupling of specific modes.

Figure 4.5(a) shows the contribution to the optomechanical coupling, $L_{\mathrm{OM}}^{-1}$, of the breathing mode and fundamental optical mode from each "unit cell" of the structure. Summing the contributions from each unit cell yields $L_{\mathrm{OM}}^{-1}$. Figs. 4.5(b)-(d) show $\zeta_{\mathrm{OM}}$, $\Theta_{\mathrm{m}}$, and $\Theta_{\mathrm{o}}$, plotted on the surface of the nanobeam OMC for the fundamental breathing mode and the fundamental optical mode. In Fig. 4.5(b), it can be seen that there are two dominant and opposite contributions to the optomechanical coupling: one from the outside face of the rails and one from the inside face of the rails (in the corners of holes). Minimizing the cancellation between these two contributions is critical to achieving a small $L_{\mathrm{OM}}$ for the breathing mode (i.e. strong optomechanical coupling). The geometry of the "nominal" structure optimizes the coupling between the fundamental optical mode and the breathing mode, as shown below.

Since the breathing mode is drawn from a band edge at the $\Gamma$ point, adjacent unit cells are mechanically in-phase with each other and add constructively to the optomechanical coupling. This is in contrast to defect modes drawn from band edges at the $X$ point, such as the pinch mode, where adjacent unit cells are mechanically out-of-phase, resulting in neighboring unit-cell contributions that tend to cancel. This cancellation reduces the optomechanical coupling unless it is specifically mitigated with extremely tight modal envelopes (see description of pinch mode optomechanical coupling below).

The degree to which the different faces of the rails cancel each other's contribution to $L_{\mathrm{OM}}^{-1}$ is set by the attenuation of the optical field between the two edges, as the mechanical displacement of the two rails is fairly uniform. Thus, one would expect that varying the rail thickness, which changes the relative amplitude of the optical field on the two rail faces, would have a significant impact on the coupling. Figure 4.6(a) shows $L_{\mathrm{OM}}$ as a function of rail thickness, with $L_{\mathrm{OM}}$ of the nominal structure (190 nm rail thickness) circled in green. For rail thicknesses smaller than 190 nm (such as the 100 nm rail width, circled in red in Fig. 4.6(a) and shown in Fig. 4.6(b)), the amplitude of the optical field on the inside and outside edge of the field is becoming

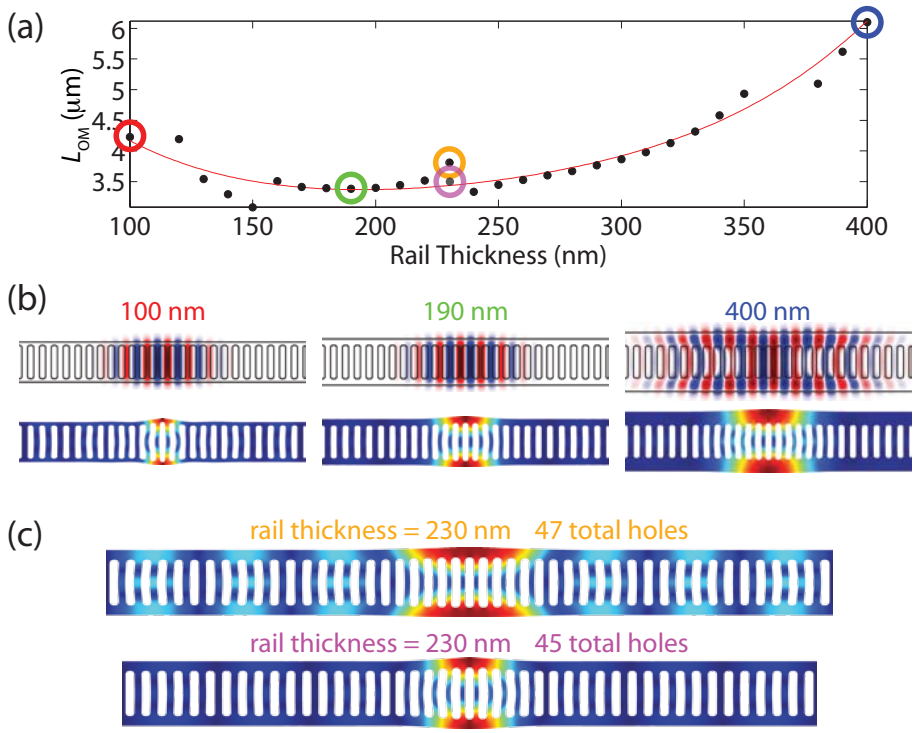


Figure 4.6: For the fundamental breathing mode and the fundamental optical mode, **(a)** the dependence of the optomechanical coupling on the rail thickness (with oscillations in the data arising from accidental degeneracies with the cantilever modes), **(b)** the optical and mechanical mode profiles for rail thicknesses of 100 nm, 190 nm and 400 nm circled in red, green and blue respectively in (a), **(c)** comparison of the mechanical mode profiles when coupled (orange) and not coupled (purple) to cantilever modes, with the corresponding effect on in $L_{\mathrm{OM}}$ highlighted in (a).

more and more similar. This results in a larger cancellation between the contributions to $L_{\mathrm{OM}}^{-1}$ on the inside and outside of the rails, decreasing the optomechanical coupling. This reasoning might lead one to believe that increasing the rail thickness should monotonically decrease $L_{\mathrm{OM}}$ (increase optomechanical coupling). However, for rail thicknesses larger than 190 nm (such as the 400 nm rail width, circled in blue in Fig. 4.6(a) and shown in Fig. 4.6(b)), there is significant decrease in confinement of the optical mode because the light can partially "spill around" the holes through the wide rails. The mechanical mode, in contrast, stays relatively confined. The net effect is that the optical energy is "wasted" on parts of the structure that do not have significant motion, and the optomechanical coupling is again decreased.

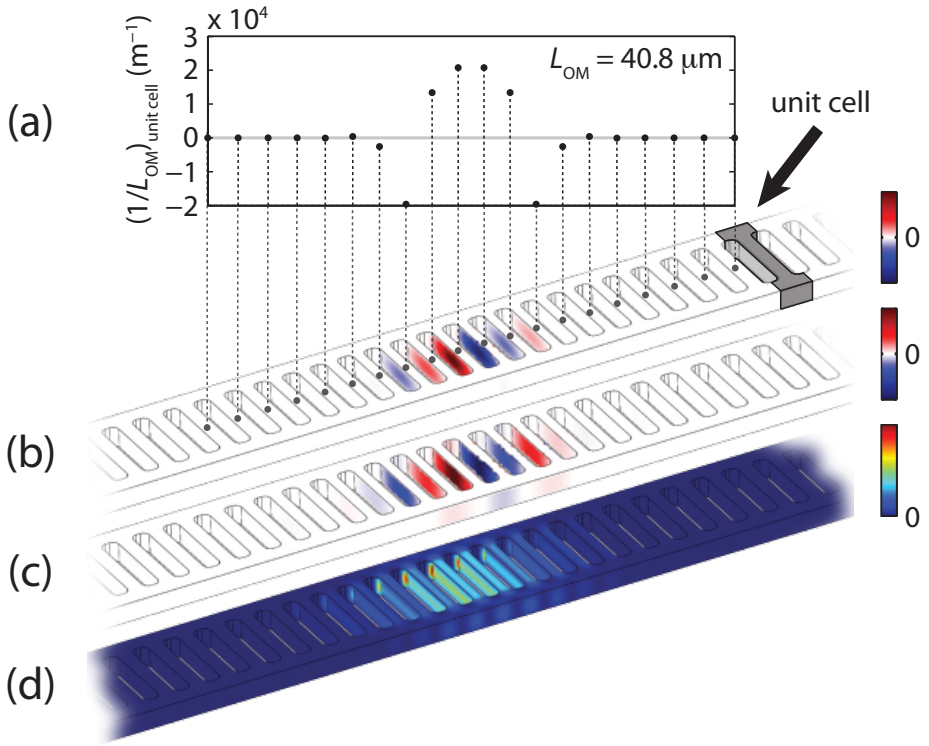


Figure 4.7: For the fundamental pinch mode and the fundamental optical mode in the nominal structure, **(a)** FEM simulation of individual unit cell contributions to the total optomechanical coupling, **(b)** surface plot of the optomechanical coupling density, **(c)** surface plot of the normal displacement profile (Equation 4.5), **(d)** surface plot of the electromagnetic energy functional (Equation 4.6).

Just as $Q_{\mathrm{m}}$ is affected by hybridization of the breathing mode with propagating and body modes, $L_{\mathrm{OM}}$ is affected by hybridization as $\mathbf{q}(\mathbf{r})$ is modified by the coupling to waveuide or body modes. This is responsible for the oscillations in $L_{\mathrm{OM}}$ seen in Fig. 4.6(a). The impact of coupling to the nanobeam body modes can be clearly seen in Fig. 4.6(c), where the breathing mode in a structure with a rail thickness of 230 nm has been plotted for two different beam lengths (number of total holes). For 47 total holes (circled in orange in Fig. 4.6a)), the breathing mode shape is altered significantly by the hybridization, causing the $L_{\mathrm{OM}}$ to deviate from the trend indicated by the red line in Fig. 4.6a). Shortening the structure by 2 holes (one on each side) decreases the coupling of the breathing mode to the propagating mode, returning $L_{\mathrm{OM}}$ to the trend line.

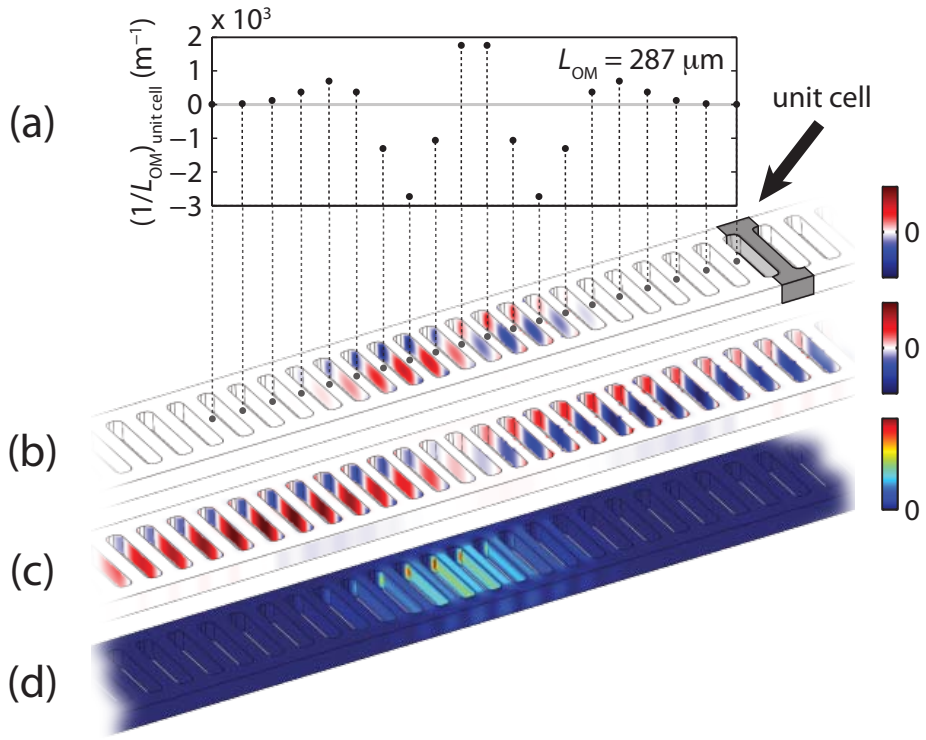


Figure 4.8: For the accordion mode and the fundamental optical mode in the nominal structure, **(a)** FEM simulation of individual unit cell contributions to the total optomechanical coupling, **(b)** surface plot of the optomechanical coupling density, **(c)** surface plot of the normal displacement profile (Equation 4.5), **(d)** surface plot of the electromagnetic energy functional (Equation 4.6).

The pinch mode is a localized, in-plane differential acoustic vibration. Each neighboring crossbar vibrates 180 degrees out of phase with its nearest neighbors, since the pinch mode is drawn from a band edge at the $X$ point. So although the optomechanical coupling contribution from each half of the structure (with respect to the $y$-$z$ plane) is equal, such that the two halves add constructively to $L_{\mathrm{OM}}^{-1}$, on either side of the $y$-$z$ plane, contributions to $L_{\mathrm{OM}}^{-1}$ from neighboring crossbars tend to cancel. This puts a premium on mechanical localization, as a more localized pinch mode has a larger difference (and thus a reduced cancellation) between neighboring crossbars. Although the envelope of the pinch mode's displacement profile is gaussian, each crossbar is very rigid, so the displacement of the compression and tension faces of each beam is essentially identical (but opposite). The gaussian envelope only

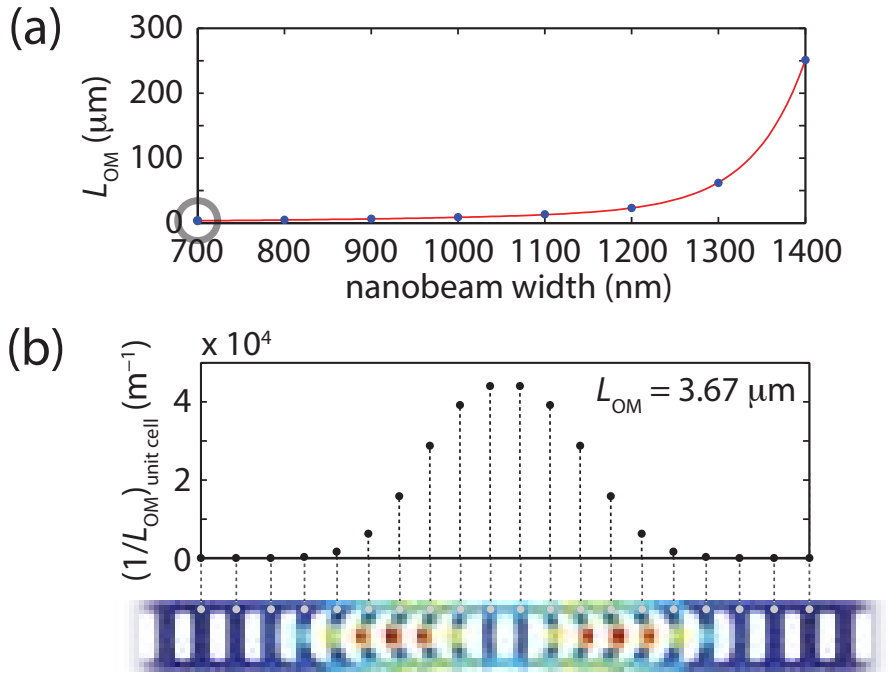


Figure 4.9: For the accordion mode with the fundamental optical mode, **(a)**, the effective length as a function of total beam width, **(b)**, individual unit cell contributions to the total optomechanical coupling for a structure with a beam width of 700 nm (circled in (a)), mode frequency of 3.97 GHz and effective motional mass of 334 fg, with accompanying mechanical mode plot. The narrower mechanical mode (represented here by the deformation of the structure with color indicating relative strain) envelope results in drastically different optomechanical coupling contributions compared to Fig. 4.8.

serves to change the relative vibration amplitudes of neighboring crossbars. The optomechanical coupling contribution from each beam would be approximately *zero* if it weren't for the rapid variation of the optical mode's envelope, and the contribution of each crossbar to $L_{\mathrm{OM}}^{-1}$ depends primarily on the difference in the optical energy density across the width of the beam. This would then lead one to believe that tighter localization, both optically and mechanically, would produce better optomechanical coupling for this structure. Indeed, although the $L_{\mathrm{OM}}$ of the pinch mode in the structure shown is quite modest ($\approx$ 41 $\mu$m), $L_{\mathrm{OM}}$ can be reduced to less than 3 $\mu$m by more tightly confining the optical and mechanical modes by reducing the number of holes involved in the defect region. There is, however, a loss of optical $Q$ associated with the increased confinement due to the larger optical momentum

components associated with tighter spatial localization. However, the structure as shown has a radiation-limited optical $Q$ greater than 10 million; so it can be quite reasonable to trade optical $Q$ for higher optomechanical coupling.

The last type of mechanical mode to be considered is the accordion mode (Fig. 4.8). The relatively poor $L_{\mathrm{OM}}$ for the accordion mode in the nominal structure is partly due to the fact that the rails recoil against the motion of the cross bar, producing opposing optomechanical contributions within each unit cell. In addition, the coupling of the broad first order Hermite-Gauss envelope of the mechanical mode with the narrower optical mode induces cancellations in the optomechanical coupling contributions at the inflection points of the mechanical mode envelope.

As discussed above, the accordion mode has a large effective mechanical bandgap. The dramatically increased $Q_{\mathrm{m}}$ that results makes it worthwhile to investigate whether the structure can be modified to produce smaller $L_{\mathrm{OM}}$. By reducing the width of the nanobeam, it can be seen from Fig. 4.9(a) that the coupling is dramatically improved by almost two orders of magnitude when the width of the structure is reduced. As shown in Fig. 4.9(b), for a beam width of 700 nm, the contributions within each unit cell no longer cancel, due to the comparatively narrower mechanical mode envelope, and the structure yields $L_{\mathrm{OM}} = 3.67\ \mu$m. In addition, simulations of the $Q_{\mathrm{m}}$ show that the effective bandgap for this narrower structure is approximately 2 GHz, yielding an extremely large $Q_{\mathrm{m}}$ for a given number of holes in the mirror section ($Q_{\mathrm{m}} \approx 10^8$ for 35 total holes). It should be noted that the frequency of the accordion mode of the narrower structure is approximately 4 GHz, up from 1.5 GHz in the wider structure.

## 4.7 Optomechanical Coupling in Two-Dimensional Optomechanical Crystals

As a final example of how these methods can be used to understand the optomechanical coupling in periodic structures with complex mechanical and electric field profiles, we model a double heterostructure hexagonal photonic crystal slab resonator. This

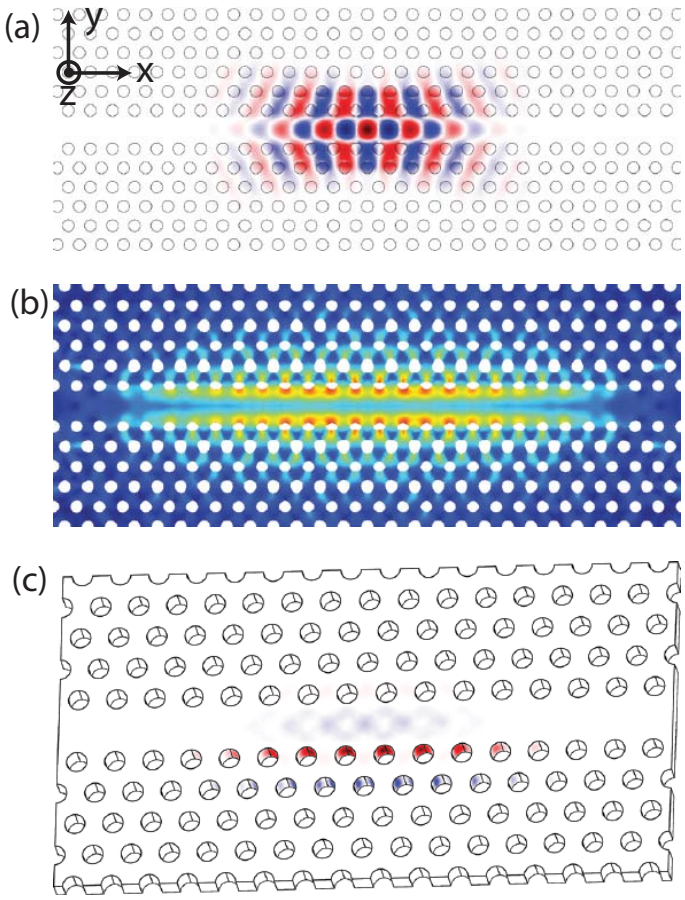


Figure 4.10: **(a)** Fundamental optical mode of the double-heterostructrure OMC (geometry identical to that described in Ref. [72]), with $\lambda_0 \approx 1.5\ \mu$m, $Q_{\rm rad} \approx 2.7\times10^7$, and $V_{\rm eff} = 1.2\ (\lambda_0/n)^3$. **(b)** Breathing mechanical mode of the double-heterostructure OMC, with $\nu_{\rm m} = 9.3$ GHz, and $m_{\rm eff} = 322$ femtograms. **(c)** Optomechanical coupling integrand plotted on the double-heterostructure OMC system's surface; the structure has an $L_{\rm OM} = 1.75\ \mu$m for the optical-mechanical mode-pair from 4.10(a) and 4.10(b).

is a well-known optical system, which has been found to have radiation-limited quality factors in excess of twenty million, with experimental demonstrations exceeding quality factors of two million [72]. The system consists of a hexagonal lattice of air holes in a silicon slab, with a single row of holes removed to create a waveguide mode within the optical stop band (the defect pulls the waveguide mode from the conduction band); in addition, the spacing in the direction of the waveguide is abruptly decreased twice to provide longitudinal confinement. This structure is essentially equivalent to the nanobeam structure, with the optical and mechanical modes guided

by Bragg reflection in the lateral direction, as opposed to total internal reflection and hard boundaries in the nanobeam. With this in mind, we expect very similar optical and mechanical modes wherever lateral propagation out of the waveguide is prohibited by Bragg reflection.

The fundamental optical cavity mode of the structure (the geometry is identical to that described in Ref. [72]) has been reproduced by FEM simulation and shown in Fig. 4.10(a). The structure also exhibits a lateral mechanical breathing mode at 9.3 GHz with a motional mass of 300 femtograms, modulating the width of the waveguide in a way that is analogous to the mechanical breathing mode of the nanobeam. The breathing mode displacement profile is shown in Fig. 4.10(b).

Figure 4.10(c) shows the integrand of the optomechanical coupling integrand (Eq. 5.1) between the the optical mode and the mechanical breathing mode plotted on the surface of the structure. The structure is shown slightly tilted to allow the insides of the holes to be seen, which give the dominant contributions to the optomechanical coupling. It is interesting to note that the coupling comes almost entirely from the movement of a small part of the interior of the holes (i.e., the region of the inner sidewall of the hole, closest to the center defect region); this can be seen by comparing the top half of the structure to the bottom half (since the integrand is symmetric about the $x$-$z$ plane). Since each row of holes provides an opposite contribution to its neighbors, it is necessary to have a rapidly decaying optical envelope to achieve small $L_{\mathrm{OM}}$, which is the case for the optical mode shown here. There is also a very small, opposing contribution from the center waveguide due to buckling/extrusion of the structure as the width is modulated. Just as in the case of the nanobeam, this optical-mechanical mode-pair has a very strong dispersive coupling, and evaluating the integral yields an effective length of only 1.75 $\mu$m.

Optically, the structure has a complete photonic bandgap for in-plane propagation, but, with a hole size to lattice constant ratio of $r/\Lambda = 0.26$, there is no corresponding in-plane mechanical bandgap. This makes the structure susceptible to mechanical loss mechanisms similar to those of the nanobeam. However, the two-dimensional hexagonal lattice, as well as other two dimensional Bravais lattices, can have simul-

taneous optical and mechanical bandgaps [113, 114], allowing the possibility of highly localized, low-loss optical-mechanical mode-pairs with very small effective lengths and motional masses.

# Chapter 5

# Experimental Demonstration of Optomechanical Coupling of Localized Acoustic and Optical Modes of a Photonic and Phononic Crystal

This work is reproduced and adapted form Ref. [3].

## 5.1 Summary

Structured, periodic optical materials can be used to form photonic crystals capable of dispersing, routing, and trapping light. A similar phenomena in periodic elastic structures can be used to manipulate mechanical vibrations. Here we present the design and experimental realization of strongly coupled optical and mechanical modes in a planar, periodic nanostructure on a silicon chip. 200-Terahertz photons are co-localized with mechanical modes of Gigahertz frequency and 100-femtogram mass. The effective coupling length, $L_{\mathrm{OM}}$, which describes the strength of the photon-phonon interaction, is as small as 2.9 $\mu$m, which, together with minute oscillator mass, allows all-optical actuation and transduction of nanomechanical motion with near quantum-limited sensitivity. Optomechanical crystals have many potential applications, from RF-over-optical communication to the study of quantum effects in mesoscopic mechanical systems.

## 5.2 Introduction

Periodicity in materials yields interesting and useful phenomena. Applied to the propagation of light, periodicity gives rise to photonic crystals [115], which can be precisely engineered to, among other things, transport and control the dispersion of light [116,117], tightly confine and trap light resonantly [118], and enhance nonlinear optical interactions [119]. Photonic crystals can also be formed into planar lightwave circuits for the integration of optical and electrical microsystems [120]. Periodicity applied to mechanical vibrations yields phononic crystals, which harness mechanical vibrations in a similar manner to optical waves in photonic crystals [10,91–94,101,102]. As has been demonstrated in studies of Raman scattering in epitaxially grown vertical cavity structures [78] and photonic crystal fibers [121], the simultaneous confinement of mechanical and optical modes in periodic structures can lead to greatly enhanced light-matter interactions. A logical next step is thus to create planar circuits that act as both photonic *and* phononic crystals [77]: optomechanical crystals. In this spirit, we describe the design, fabrication, and characterization of a planar, silicon-chip-based optomechanical crystal capable of co-localizing and strongly coupling 200 THz photons and 2 Gigahertz phonons. These planar optomechanical crystals bring the powerful techniques of optics and photonic crystals to bear on phononic crystals, providing exquisitely sensitive (near quantum-limited), optical measurements of mechanical vibrations, while simultaneously providing strong non-linear interactions for optics in a large and technologically-relevant range of frequencies.

## 5.3 Acoustic and Optical Modes

The geometry of the optomechanical crystal structure considered here is shown in Fig. 5.1(a). The effectively one-dimensional (1D) optomechanical crystal consists of a silicon nanobeam (thickness $t$ not shown) with rectangular holes and thin cross-bars connected on both sides by thin rails (we will refer to infinitely periodic constructs such as this as the "projection" of the finite structure). Fig. 5.1(b) shows a finite-

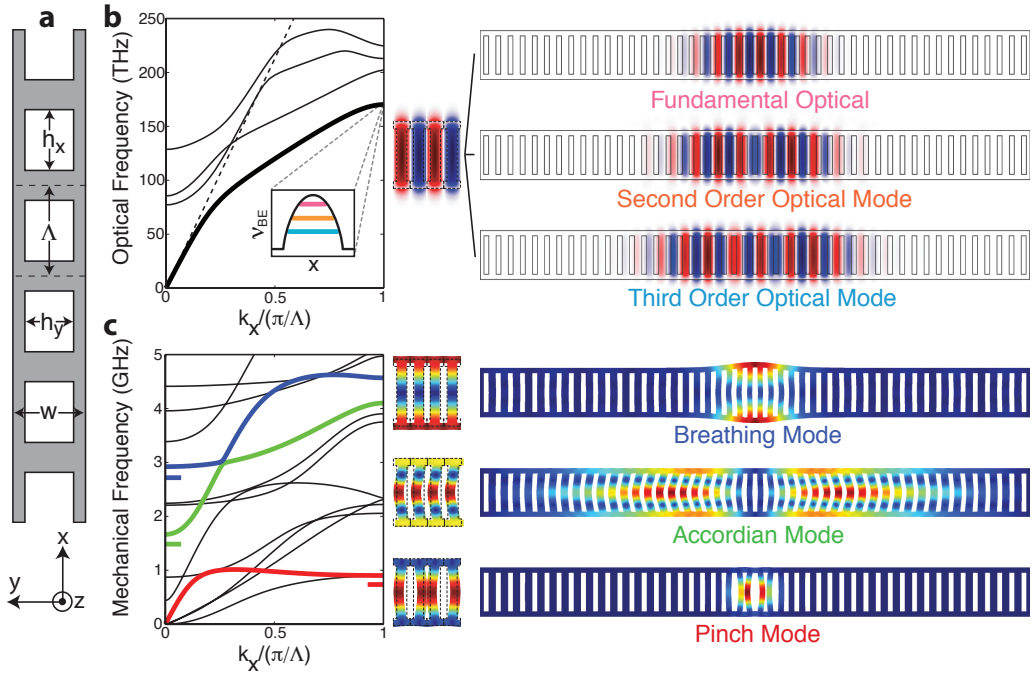


Figure 5.1: **(a)**, Geometry of nanobeam structure. **(b)**, Optial and **(c)**, mechanical bands and defect modes calculated via FEM for the projection of the experimentally-fabricated silicon nanobeam ($\Lambda$ = 362 nm, $w$ = 1396 nm, $h_y$ = 992 nm, $h_x$ = 190 nm, and $t$ = 220 nm; isotropic Young's modulus of 168.5 GPa; $n$ =3.493). In this particular structure, which will be referred to as "Device 1", $N_{\text{defect}}$ = 15 holes, $N_{\text{total}}$ = 75 and the spacing between the holes varies quadratically from the lattice constant of the projection (362 nm) to 85% of that value (a "15% defect") for the two holes straddling the central cross-bar (the other parameters of Device 1 are as listed above).

element-method (FEM) simulation of the optical band structure of the projection of a nanobeam (see caption for parameters). The electric field profile for modes at the band edge ($k_x = \pi/\Lambda$, the boundary of first Brillouin zone) are shown to the right of the band structure. The finite structure terminates at its supports on both ends, forming a doubly-clamped beam. To form localized resonances in the center of the structure, the discrete translational symmetry of the patterned beam is intentionally disrupted by a "defect", consisting of a quadratic decrease in the lattice constant, $\Lambda$, symmetric about the center of the beam for some odd number of holes, $N_{\text{defect}} < N_{\text{total}}$. The defect forms an effective potential for optical modes at the band edges, with the spatial dependence of the effective potential closely following

the spatial properties of the defect [2] (as illustrated in the inset of the optical band diagram). Thus the optical modes of the infinitely-periodic structure are confined by a quasi-harmonic potential. This effective potential localizes a "ladder" of modes with Hermite-Gauss envelopes, analogous to the modes of the 1D harmonic potential of quantum mechanics. The localized optical modes of the finite structure (hereafter referred to as Device 1) are also found by FEM simulation and shown in Fig. 5.1(b) to the right of the corresponding mode of the projection.

Analogously, Fig. 5.1(c) shows a FEM simulation of the mechanical band structure of the nanobeam's projection. Mechanical modes at the band edge experience an effective potential analogous to the optical modes, localizing certain types of vibrations to the defect region. The colored bands give rise to mechanical modes that, when localized by the defect, yield "ladders" of modes with strong dispersive coupling to the localized optical modes (the frequency of the fundamental defect mode is indicated by a horizontal bar of the same color). We classify these optomechanically-coupled mechanical modes, from lowest to highest frequency, as "pinch", "accordian", and "breathing" modes. The localized mechanical modes of Device 1 are shown to the right of the corresponding mode of the projection.

## 5.4 Optomechanical Coupling

The two kinds of waves, mechanical and optical, are on equal footing in this structure. Each mechanical mode has a frequency $\nu_{\mathrm{m}} = \Omega_{\mathrm{m}}/2\pi$ and displacement profile $\mathbf{Q}(\mathbf{r})$; each optical mode has a frequency $\nu_{\mathrm{o}} = \omega_{\mathrm{o}}/2\pi$ and electric field profile $\mathbf{E}(\mathbf{r})$. Just as the optical mode volume, $V_{\mathrm{o}} = \int \mathrm{d}V \left( \frac{\sqrt{\epsilon}|\mathbf{E}|}{\max(|\sqrt{\epsilon}\mathbf{E}|)} \right)^2$, describes the electromagnetic localization of the optical mode, the mechanical mode volume, $V_{\mathrm{m}} \equiv \rho \int \mathrm{d}V \left( \frac{|\mathbf{Q}|}{\max(|\mathbf{Q}|)} \right)^2$ (see § 1.2.6), describes the strain energy-averaged localization of the mechanical mode. For both the localized optical and mechanical modes of the patterned beam cavity, the effective mode volume is less than a cubic wavelength. The effective motional mass, being proportional to the mode volume ($m_{\mathrm{eff}} \equiv \rho V_{\mathrm{m}}$), is between 50 and 1000

femtograms for the mechanical modes shown in Fig. 5.1(c) ($\rho_{Si} = 2.33$ g/cm$^3$).

Drawing on recent work in the field of cavity optomechanics [6,7], we describe the coupling between optical and mechanical degrees of freedom (to lowest order) by an effective coupling length $L_{\mathrm{OM}} \equiv (\frac{1}{\nu_\mathrm{o}}\frac{\mathrm{d}\nu_\mathrm{o}}{\mathrm{d}\alpha})^{-1}$ (see § section:dispersivecoupling), where $\delta\nu_\mathrm{o}$ is the change in the frequency of an optical resonance caused by the mechanical displacement parameterized by $\alpha$. For this work, $\alpha$ is defined as the maximum displacement that occurs *anywhere* for the mechanical mode. By definition then, the smaller $L_{\mathrm{OM}}$, the larger the optical response for a given mechanical displacement. $L_{\mathrm{OM}}$ is also the length over which a photon's momentum is transferred into the mechanical mode as it propagates within the structure, and thus is inversely proportional to the force per-photon applied to the mechanical system.

To calculate $L_{\mathrm{OM}}$, we employ a perturbative theory of Maxwells equations with respect to shifting material boundaries [19]. The derivative $\frac{\mathrm{d}\nu_\mathrm{o}}{\mathrm{d}\alpha}$ around some nominal position, where the optical fields are known, can be calculated *exactly* without actually deforming the structure for a surface-normal displacement of the boundaries, $h(\alpha;\mathbf{r}) \equiv \mathbf{Q}(\mathbf{r})\cdot\hat{\mathbf{n}} = \alpha\mathbf{q}(\mathbf{r})\cdot\hat{\mathbf{n}}$, where $\mathbf{q}(\mathbf{r}) = \mathbf{Q}(\mathbf{r})/\alpha = \mathrm{d}\mathbf{Q}(\mathbf{r})/\mathrm{d}\alpha$ is the unitless displacement profile of the mechanical mode, and $\alpha$ parameterizes the amplitude of the displacement. Using this perturbative formulation of Maxwell's equations, we find

$$\frac{1}{L_{\mathrm{OM}}} = \frac{1}{2}\frac{\int \mathrm{d}A\left(\frac{\mathrm{d}\mathbf{Q}}{\mathrm{d}\alpha}\cdot\hat{\mathbf{n}}\right)\left[\Delta\epsilon\left|\mathbf{E}_\parallel\right|^2 - \Delta(\epsilon^{-1})\left|\mathbf{D}_\perp\right|^2\right]}{\int \mathrm{d}V\epsilon\left|\mathbf{E}\right|^2} \tag{5.1}$$

where $\hat{\mathbf{n}}$ is the unit normal vector on the surface of the unperturbed cavity, $\mathbf{D}(\mathbf{r}) = \epsilon(\mathbf{r})\mathbf{E}(\mathbf{r})$, $\Delta\epsilon = \epsilon_1 - \epsilon_2$, $\Delta(\epsilon^{-1}) = \epsilon_1^{-1} - \epsilon_2^{-1}$, $\epsilon_1$ is the dielectric constant of the periodic structure, and $\epsilon_2$ is the dielectric constants of the surrounding medium ($\epsilon_2 = \epsilon_0$ in this case). This method of calculating the coupling provides a wealth of intuition about the nature of the coupling and can be used to engineer the structure for strong optomechanical coupling.

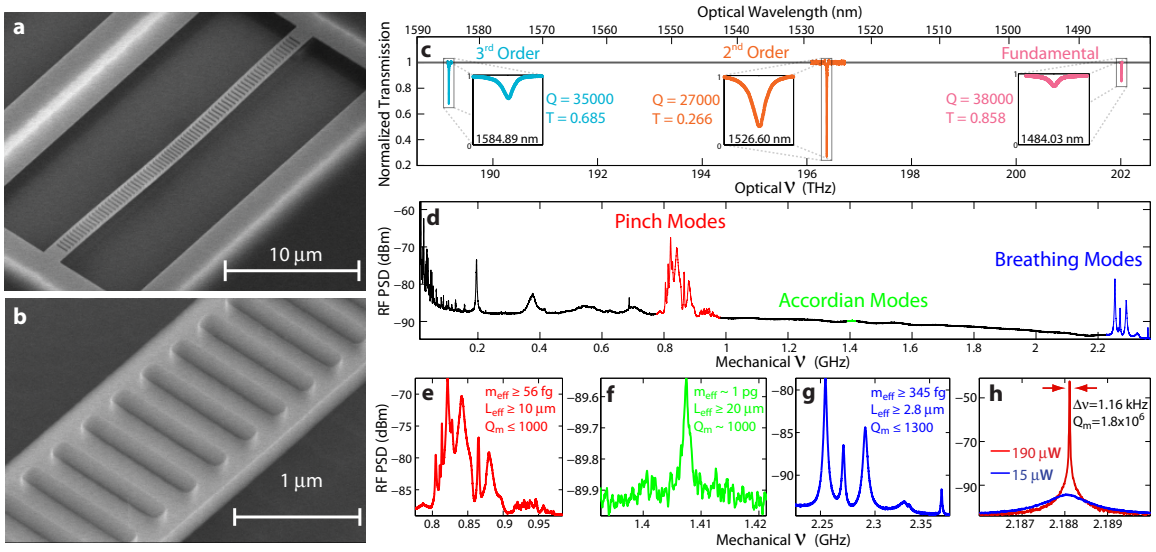


Figure 5.2: **(a)**, and **(b)**, show SEM images of the fabriced silicon nanobeam optomechanical crystal. **(c)**, Optical spectroscopy of Device 1 with the taper waveguide in contact. **(d)**, Mechanical spectroscopy of Device 1 with taper waveguide in contact. **(e)-(g)**, Zoomed RF mechanical spectra of Device 1 showing pinch (red), accordian (green), and breathing (blue) modes.

## 5.5 "DC" and RF Optical Spectroscopy

Figs. 5.2(a) and 5.2(b) show scanning electron microscope (SEM) images of a fabricated silicon nanobeam with the parameters of Device 1. The optical modes of the nanobeam are probed with a tapered and dimpled optical fiber [16] in the near-field of the defect cavity, simultaneously sourcing the cavity field and collecting the transmitted light in a single channel. Fig. 5.2(c) shows the low-pass filtered optical transmission spectrum of Device 1 at low optical input power ($\sim 30\ \mu$W). The optical cavity resonances are identified by comparison to FEM modeling of the optical modes of the structure (see § 5.14.1). Looking in the radio frequency (RF) spectrum provides information about the mechanical modes of the structure, as mechanical motion gives rise to phase and amplitude modulation of the transmitted light. Figs. 5.2(c)-(f) show the measured photodetector RF power spectral density (PSD) of the optical transmission through the second order cavity resonance (this mode was used due to its deep on-resonance coupling). A series of lower frequency modes can be seen in

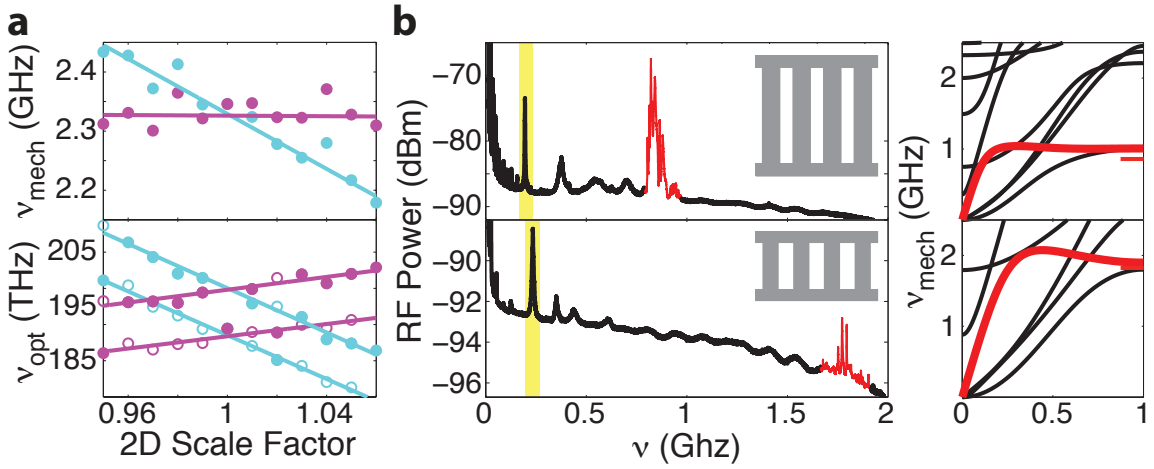


Figure 5.3: **(a)**, Geometric scaling (planar) of the fundamental breathing mode. Device 1 is the device with scale factor 1.03. The best linear least-squares fit lines in the top panel correspond to the mechanical frequency changing by $-0.9\% \pm 0.2\%$ per device; the normalized frequency changes by $-0.01\% \pm 0.2\%$ per device. The optical frequency of the mode used to make the mechanical measurement is filled (the other optical mode is open). **(b)**, Engineering of pinch mode frequencies, showing two devices with pinch mode frequencies of 850 MHz and 1.75 GHz. The mechanical band diagrams of each structure are shown to the right of the measured RF spectrum, with the pinch mode band highlighted in red.

the spectra ($\sim$ 200 MHz and harmonics), corresponding to compression of modes of the entire beam, followed by groups of localized phononic modes of the lattice at 850 MHz (pinch), 1.41 GHz (accordian), and 2.25 GHz (breathing). The transduced signal at low optical power corresponds to thermally-excited motion of the mechanical modes, and is inversely proportional to $m_{\text{eff}} L_{\text{OM}}^2$ (see below). At higher optical input power ($\sim$ 100 $\mu$W; see 5.2(h) and § 5.11, optical excitation of regenerative mechanical oscillation [6] of the breathing modes is possible due to the small mass and short optomechanical coupling length of the co-localized phonon and photon modes.

## 5.6 Engineering of the Mechanical Frequencies

Fig. 5.3(a), top panel, shows how the frequency of the fundamental mechanical breathing mode scales with a uniform geometric scaling in the plane. A series of 12 devices have been fabricated, identical except that the entire geometry in the plane is scaled

incrementally by 1% per device. For each device, one of the first two optical modes is selected and used to measure the mechanical frequency of the fundamental breathing mode (cyan dots, top panel). The frequencies plotted in magenta are the normalized frequencies, i.e. the bare frequencies (cyan) times the scale factor for the device. Because the beams are thin, causing the crossbars to behave approximately like "Euler beams", the frequency of the mechanical mode scales perfectly with the two-dimensional scale factor. This is in contrast to the optical modes (Fig. 5.3(a), bottom panel), which clearly do not scale with the planar geometry, a result of the coupling of in-plane and vertical optical mode confinement (scaling in all three dimensions is thus required). Since the planar scaling for the lattice-localized mechanical modes is trivial, this method could be used with a larger span of devices to measure the frequency dependence of the Young's (or bulk) modulus of the material.

Significant shifts in the frequency of the lattice-localized mechanical modes can be obtained through a non-uniform planar scaling. Fig. 5.3(b) shows the RF PSD for Device 1 and a second device, Decice 2, which has an essentially identical lattice constant, $\Lambda = 365$ nm, and total length, $L$, as compared to Device 1, but a considerably smaller width ($w = 864$ nm, $h_y = 575$ nm, $h_x = 183$ nm). Simulations show that the pinch modes are the lowest-frequency group of localized and optomechanically-coupled mechanical modes in both structures (see right panels of Fig. 5.3(b)). Experimentally, the ratio of the localized pinch mode frequencies (highlighted in red) in these two devices is 1.749 GHz/805 MHz = 2.17. The ratio of the frequency of the localized pinch-mode manifold, after accounting for the defect, is theoretically 1.826 GHz/846 MHz = 2.16. It is interesting to note that the mechanical modes of the entire doubly-clamped beam (as opposed to the lattice-localized modes) depend very weakly on the structural differences between Device 1 and Device 2. For instance, the second-order acoustic vibration mode of the nanobeam (highlighted in yellow in Fig. 5.3(b)) has a frequnecy which should be $\frac{3\pi}{2L}\sqrt{\frac{E}{\langle\rho\rangle}}$, where $E$ is Young's modulus and $\langle\rho\rangle$ is the average linear density. The frequency of this mode is measured to be 234 MHz/195 MHz = 1.20 times higher in Device 2 than for Device 1, which is in good agreement with the ratio $\sqrt{\langle\rho_1\rangle/\langle\rho_2\rangle} = 1.23$. The difference between the change in the frequencies

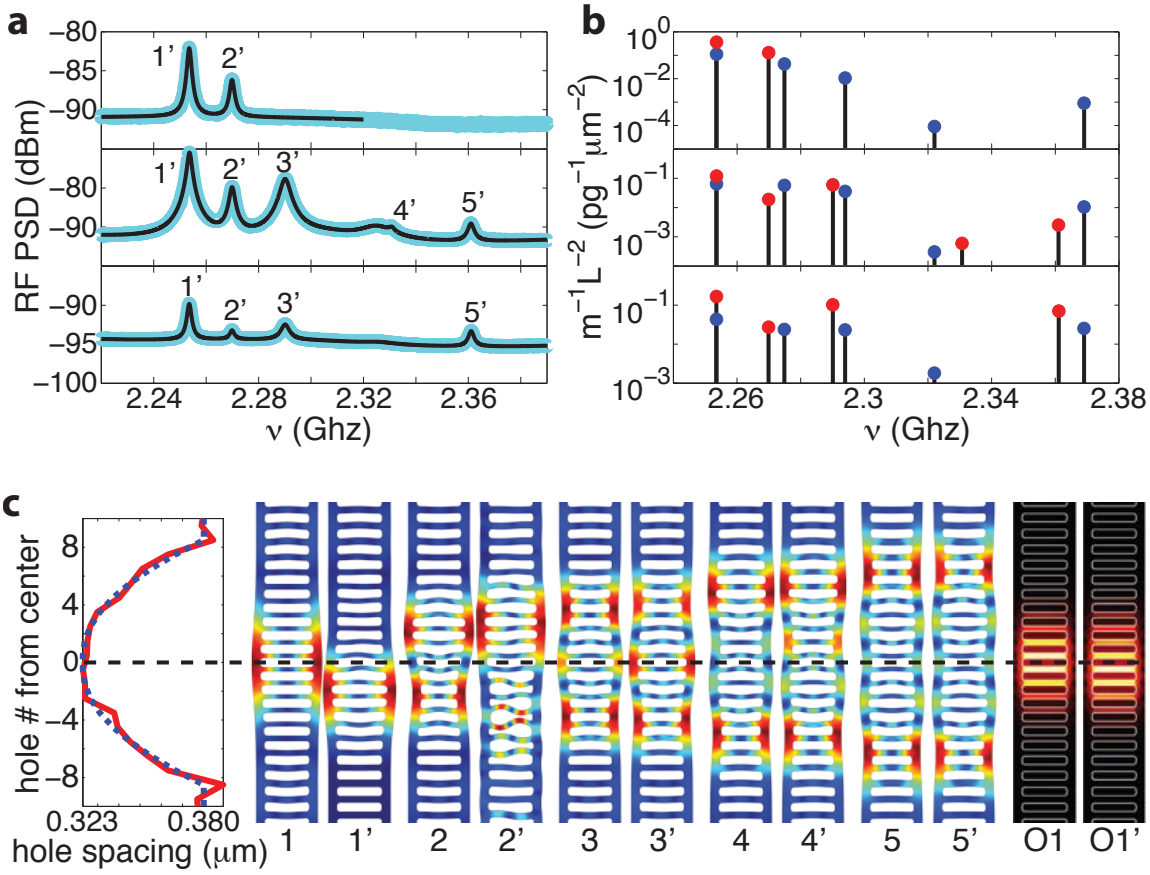


Figure 5.4: **(a)**, Transduction of breathing mode motion. **(c)**, Ideal and actual ("primed") modes of the silicon nanobeam optomechanical crystal due to the ideal (dashed) and actual defect (solid, red).

of the lattice-localized versus beam modes illustratres the independence of these two "systems"; once the wavelength of the global beam modes approach the scale of the lattice periodicity, the vibrations become localized and behave independently of the global beam structure (such as the end clamps).

## 5.7 Measuring Thermal Power in Mechanical Modes and the Product $m_{\rm eff}L^2_{\rm OM}$

Fig. 5.4(a) shows the RF optical transmission spectrum due to Brownian motion of the breathing modes of Device 1 (i.e., at low optical input power), for the three op-

tical modes shown in Figs. 5.1(c) and 5.2(c). Because the various optical modes have different spatial profiles, each mechanical mode has a *different* $L_{\mathrm{OM}}$ *for each optical mode*. The root-mean-square (rms) mechanical amplitude of a mode due to Brownian motion is $\langle \alpha^2 \rangle = k_B T/(m_{\mathrm{eff}}\Omega^2)$. It can be shown analytically that the factor $1/(m_{\mathrm{eff}}L_{\mathrm{OM}}^2)$ uniquely determines the transduction of the Brownian motion for these sideband-resolved optomechanical oscillations (see § 1.3.5). To the right of each measured spectrum (Fig. 5.4(b)) is the experimentally-extracted mechanical frequency and value of $1/(m_{\mathrm{eff}}L_{\mathrm{OM}}^2)$, together with the values of these quantities obtained from the FEM model (using Eq. 5.1 to determine $L_{\mathrm{OM}}$). Good correspondence, in both frequency and transduced signal amplitude, is found across all optical and mechanical mode pairs. In order to achieve this level of correspondence, imperfections in the fabricated structure are taken into account by extracting the geometry from high-resolution SEM images of the device and calculating the modified optical and mechanical modes (Fig. 5.4(c)). The resulting measured value for optomechanical coupling between the fundamental breathing and optical mode (assumming a FEM-calculated motional mass of $m_{\mathrm{eff}} = 330$ fg) is $L_{\mathrm{OM}} = 2.9$ $\mu$m, approaching the limit of the wavelength of light. The sensitivity of the mechanical transduction of the fundamental breathing mode can be appreciated by comparing the mode's rms thermal amplitude at $T = 300$ K, $\alpha_{th} = 245$ fm, to its quantum zero-point motion of $\alpha_{zp} = 3.2$ fm. The sensitivity limit, as given by the background level in the middle panel of Fig. 5.4(c), is thus a factor of $\sim 7.5$ times that of the standard quantum limit.

## 5.8 Mechanical Energy Loss

The loss of mechanical energy from confined mechanical modes of a phononic crystal can, in principal, be made arbitrarily low (and thus the mechanical $Q$ arbitrarily high) by including a large number of unit cells outside the localizing potential region. Of course, other forms of mechanical damping, such as thermo-elastic damping, phonon-phonon scattering, or surface damping effects, would eventually become dominant

[122]. This makes optomechanical crystals ideal structures for studying these loss mechanisms. The fundamental breathing mode of the 1D phononic crystal structure studied here, at 2.254 GHz, has a room temperature mechanical $Q$ of 1300 in air, and in contact with the taper waveguide (power-dependent measurements confirm that this mechanical Q is not enhanced by dynamical back-action). This corresponds to a frequency-$Q$ product of $3 \times 10^{12}$ Hz, a value close to largest demonstrated to date [123]. Although further tests (as a function of temperature and lattice periods) are required to determine the contribution of various mechanical loss mechanisms, numerical simulations show that mode coupling between localized and leaky phonon modes exist in these 1D cavity structures and can significantly limit the $Q$-factor (§ 5.14.4 and § 4.4). This obstacle can be overcome in two-dimensional periodic slab structures, which have been shown to possess complete gaps for both optical and mechanical modes simultaneously [113].

## 5.9 Summary and Conclusion

The experimental demonstration of optomechanical coupling between 200 Terahertz photons and 2 Gigahertz phonons in a planar optomechanical crystal paves the way for new methods of probing, manipulating, and stimulating linear and non-linear mechanical and optical interactions in a chip-scale platform. As the study of quantum mesoscale mechanical oscillators has nearly become a reality [25, 28, 29, 124, 125], high frequency mechanics will provide a distinct experimental advantage due to the lower thermal phonon occupancy. In addition, optomechanical crystals with full phononic bandgaps provide a platform to decouple the direct decoherence (phonon leakage) of mechanical modes from their supports. This could allow the preparation of mechanical vibrations with ultra-long lifetimes, the study of the intrinsic mechanical material losses, and narrow-linewidth Gigahertz frequency sources. Optomechanical crystals could also be used as high-spatial resolution mass sensors; with $m_{\rm eff} = 62$ fg and $\nu_{\rm m} = 850$ MHz, the mass of a single Hemoglobin A protein ($\sim 10^{-19}$ g) would change the frequency of the pinch mode by 700 Hz, allowing sensitivity paralleling NEMS

zeptogram mass sensors [126].

## 5.10 Measured and Simulated Optomechanical Coupling and Mechanical $Q$

Table 5.1 summarizes the properties of the breathing mechanical modes. Measured values are denoted with a tilde. The necessary RF amplitudes and linewidths are extracted from the spectra of Fig. 5.4(a) using a nonlinear least squares fit with linear background and a sum of as many Lorentzian functions as are visible in the spectrum. Simulated values are calculated using methods described below.

Table 5.1: Measured and Simulated properties of the breathing mechanical modes. Tildes indicate measured quantities. The experimental effective lengths, $L_{\mathrm{OM}}$, between each breathing mode and the first three optical cavity modes are calculated using the experimentally extracted $m_{\mathrm{eff}} L_{\mathrm{OM}}^2$ (see Fig. 5.4(b)) and dividing by the $m_{\mathrm{eff}}$ from the model. The superscript, $n$, in ${}^{n}L_{\mathrm{OM}}$, indicates coupling of that mechanical mode to the $n$th optical mode (see Fig. 5.1(b)). $L_{\mathrm{OM}}$ has units of microns; masses are in femtograms; and mechanical frequencies have units of gigahertz. See §5.14.4 for discussion on modeling $Q_m$.

| # | $\nu_{\mathrm{m}}$ | $\widetilde{\nu_{\mathrm{m}}}$ | $m_{\mathrm{eff}}$ | ${}^{1}L_{\mathrm{OM}}$ | $\widetilde{{}^{1}L_{\mathrm{OM}}}$ | ${}^{2}L_{\mathrm{OM}}$ | $\widetilde{{}^{2}L_{\mathrm{OM}}}$ | ${}^{3}L_{\mathrm{OM}}$ | $\widetilde{{}^{3}L_{\mathrm{OM}}}$ | $Q_m$ | $\widetilde{Q_m}$ |
|---|---|---|---|---|---|---|---|---|---|---|---|
| 1 | 2.254 | 2.254 | 329 | 4.9 | 2.9 | 6.4 | 5.1 | 7.8 | 4.4 | 2050 | 1280 |
| 2 | 2.275 | 2.270 | 399 | 7.1 | 4.5 | 6.2 | 12 | 9.5 | 9.8 | 1180 | 1130 |
| 3 | 2.294 | 2.290 | 628 | 11 | N/A | 6.2 | 5.3 | 7.7 | 4.1 | 1290 | 613 |
| 4 | 2.322 | 2.326 | 704 | 110 | N/A | 64 | 49 | 26 | N/A | 387 | 973 |
| 5 | 2.369 | 2.361 | 665 | 38 | N/A | 11 | 25 | 7.1 | 4.7 | 21600 | 950 |

## 5.11 Optical Actuation: Amplification and Regenerative Oscillation

Fig. 5.5a shows the fundamental breathing mode of the optomechanical crystal nanobeam, pumped using the fiber taper probe coupled to the fundamental optical mode (this particular device has a scale factor 1.07 in Fig. 5.8a, which is nominally identical to Device 1 of the main text but uniformly scaled by 4%). The mechanical $Q$ at a

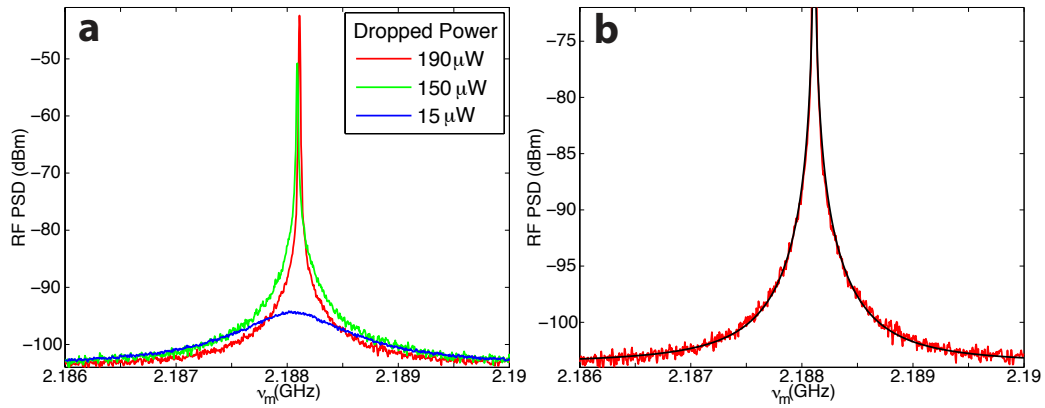


Figure 5.5: **(a)** 2.19 GHz breathing mode showing spectral narrowing from 800 kHz to 1.16 kHz with increasing optical input power. **(b)** Nonlinear least-squares fit (black) to redacted high power (red) curve in **a**.

dropped optical power of 15 $\mu$W (input power is 74 $\mu$W with 20 percent of the power coupled to the device) is approximately $Q_m = 2700$. Upon increasing the dropped power to 190 $\mu$W (an 11 dB increase), the mechanical mode power rises dramatically and the linewidth narrows to below the 4.8 kHz resolution limit of the oscilloscope (the resolution-limited effective $Q$ is thus 460,000). This sort of regenerative oscillation [5, 127] (sometimes called paramteric instability) arises due to the retarded part of the optical force on the mechanical mode, which, for a blue detuned laser input, results in amplification of the mechanical motion. Even though a large part of the signal is below the resolution bandwidth, the linewidth at 931 $\mu$W can still be extracted, as there is more than 20 dB of signal to noise at the point where the lineshape becomes wider than the resolution limit. Fig. 5.5b shows the nonlinear least-squares fit to the redacted dataset, which is an excellent fit to the data and gives a linewidth of 1.16 kHz (effective $Q_m = 1.8 \times 10^6$).

## 5.12 Experimental Setup

The experimental setup used to measure the optical, mechanical, and optomechanical properties of the silicon optomechanical crystal nanobeam is shown in Fig. 5.6. The setup consists of a bank of fiber-coupled tunable infrared lasers spanning ap-

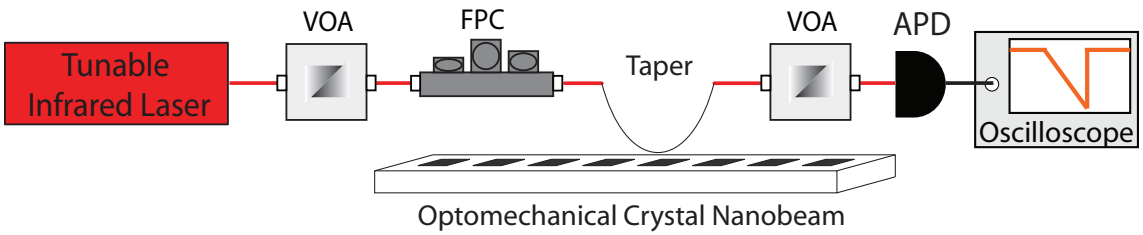


Figure 5.6: Experimental setup used to measure optical, mechanical, and optomechanical properties of silicon optomechanical crystal nanobeam.

proximately 200 nm, centered around 1520 nm. After a variable optical attenuator (VOA) and fiber polarization controller (FPC), light enters the tapered and dimpled optical fiber, the position of which can be controlled with nanometer-scale precision (although vibrations and static electric forces limit the minimum stable spacing between the fiber and device to about 50 nm). The transmission from the fiber is (optionally) passed through another VOA and finally reaches an avalanche photodiode (APD) with a transimpedance gain of 11,000 and a bandwidth (3 dB rolloff point) of 1.2 GHz. The APD has an internal bias tee, and the RF voltage is connected to the 50 Ohm input impedance of the oscilloscope. The oscilloscope can perform a Fourier transform (FT) to yield the RF power spectral density (RF PSD). The RF PSD is calibrated using a frequency generator that outputs a variable frequency sinusoid with known power.

## 5.13 Fabrication

The optomechanical crystal nanobeam is formed in the 220 nm thick silicon device layer of a [100] Silicon-On-Insulator (SOI) wafer. The pattern is defined in electron beam resist by electron beam lithography. The resist pattern is transfered to the device layer by an inductively-coupled plasma reactive ion etch with a $C_4F_8/SF_6$ gas chemistry. The nanobeam is then undercut and released from the silica BOX layer by wet undercutting with hydrofluoric acid.

## 5.14 Numerical Modeling

Modeling of both the optical and mechanical modes is done via finite element method (FEM), using COMSOL Multiphysics [97]. Mechanical band structures are done in COMSOL. Photonic bands are done with MIT Photonic Bands [96]. The following subsections provide the description of the method used to define the FEM model of the optomechanical crystal system.

### 5.14.1 Extracting the Geometry in the Plane

To model the optomechanical crystal system, the geometry of the as-fabricated structure must be measured. As the features are smaller than an optical wavelength, the measurements must be done by scanning electron microscope (SEM). FIG. 5.7(a) shows an "eagle's-eye" high-resolution SEM micrograph of a portion of device 1, with the defect centered in the image.

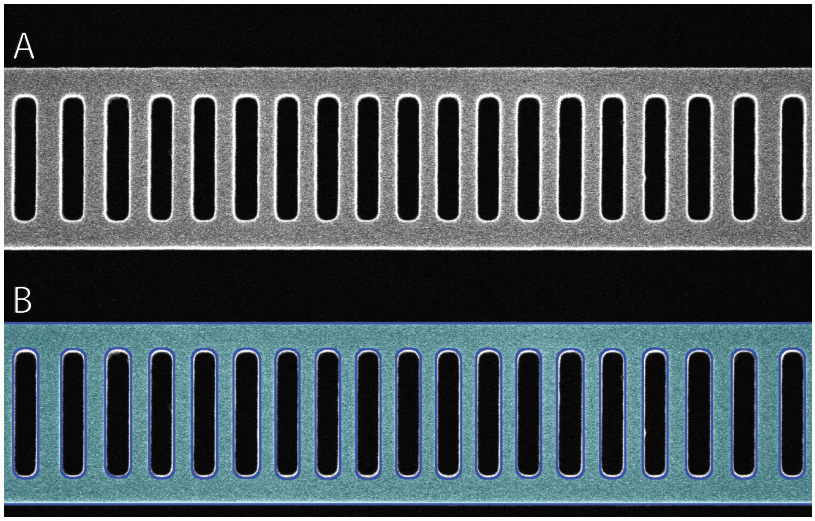


Figure 5.7: **(a)**, Scanning electron micrograph of fabricated silicon optomechanical crystal. **(b)**, Approximated geometry shown as blue overlay on SEM micrograph from **(a)**.

Digital line-scans of the micrograph are used to detect the edges of the geometry. From the extracted edge positions, the geometry is approximated as a series of rectangular holes with two filleted ends inside of a rectangle (the beam), giving an

approximate planar geometric representation of the structure shown as an overlay in Fig. 5.7(b). This geometric representation takes into account the size, position, and any curvature of each hole, giving an accurate approximation of the geometry. In the defect region, each hole is given by its measured value. Outisde the defect region, a series of holes is used to get the average hole shape, which is used in the model.

The SEM has been calibrated, and the dimesnions as measured by the SEM are too large by 5%. Thus, the entire planar geometry is uniformly scaled down by 5%. Since the lattice constant, $\Lambda$, is a center-to-center distance between features, it is not affected by erosion during processing, which makes it the most reliable measure of distance on the sample. After applying the SEM calibration factor, the average lattice constant outside of the defect as measured by the SEM agrees with the value written by the electron beam lithography tool to better than 1%. Since the SEM and lithography tool are independent, this is yet another confirmation that the geometry has been measured correctly (the fine spectral features of the simulation are the other way to check the geometry measurements, after comparing to measured mechanical and optical spectra).

The SOI wafer thickness is specified as 220 nm by the manufacturer. We will assume that the planar geometry extends uniformly into the vertical direction for the entire 220 nm, since the "eagle's-eye" view used to measure the planar geometry does not capture any asymmetries in the vertical dimension. These vertical asymmetries are much more difficult to extract without sacrificing the device (by focused ion beam, cleaving, etc.).

### 5.14.2 Young's Modulus and Index of Refraction

The nanobeam structures are fabricated such that the long axis ($\hat{x}$) is parallel to the SOI wafer flat, which is oriented along [110] ($\pm 0.5^\circ$). We decompose the displacement field in FEM simulations along the crystal axes and find the majority of the strain energy is primarily stored in deformations along the family of equivalent directions specified by $\langle 110 \rangle$. Because the strain for the modes of interest are primarily along

$\langle 110 \rangle$, an isotropic elasticity tensor (two independent elements) derived from a single Young's modulus and Poisson's ratio is appropriate for the current level of detail. The index of refraction will also be treated as an isotropic scalar.

As the Young's modulus, $E$, and index of refraction, $n$, determine the phase velocity of the waves (and thus the frequency), they can be "tuned" to make a single simulated frequency (mechanical for $E$ and optical for $n$) come out exactly as measured. The free spectral range of the modes and the relative frequencies of different types of modes are determined by the details of the geometry, in conjunction with $E$ and $n$; so although a single frequency can always be made to match experiment exactly by scaling $E$ or $n$, the wider details of the spectrum are a more accurate reflection of whether the model is a good match to the experimental values.

After accounting for the planar geometry and scale factor, the Young's modulus and index are tuned until the fundamental optical mode and the fundamental breathing mechanical mode each come out exactly as measured, which occurs for $E = 168.5$ GPa and $n = 3.493$ (the Poissons's ratio, $\nu$, is 0.28 in this work). These parameters, along with the measured geometry (as discussed above) yields a model that produces the values in Table 5.1 and Fig.5.4(c) in the main text.

### 5.14.3 Optics: Mode Maps and Modeling

Fig. 5.8a shows all the optical modes measured for a series of 20 devices, which are identical up to a uniform planar scaling that changes by 1% per device (Device 1 is the device with scale factor 1.03; this figure is just an expanded version of the bottom panel of Fig. 5.3(a) in the main text). Because of the limited laser range, only a limited number of modes can be measured on any given device. By measuring this series of uniformly scaled devices, a large number of modes can be seen as they are "scanned" through the laser range.

The devices, taken together, display a lot of information about the optical spectrum, which contains a number of conspicuous features that match well with an FEM model of the optical properties. First, the devices display a series of five relatively

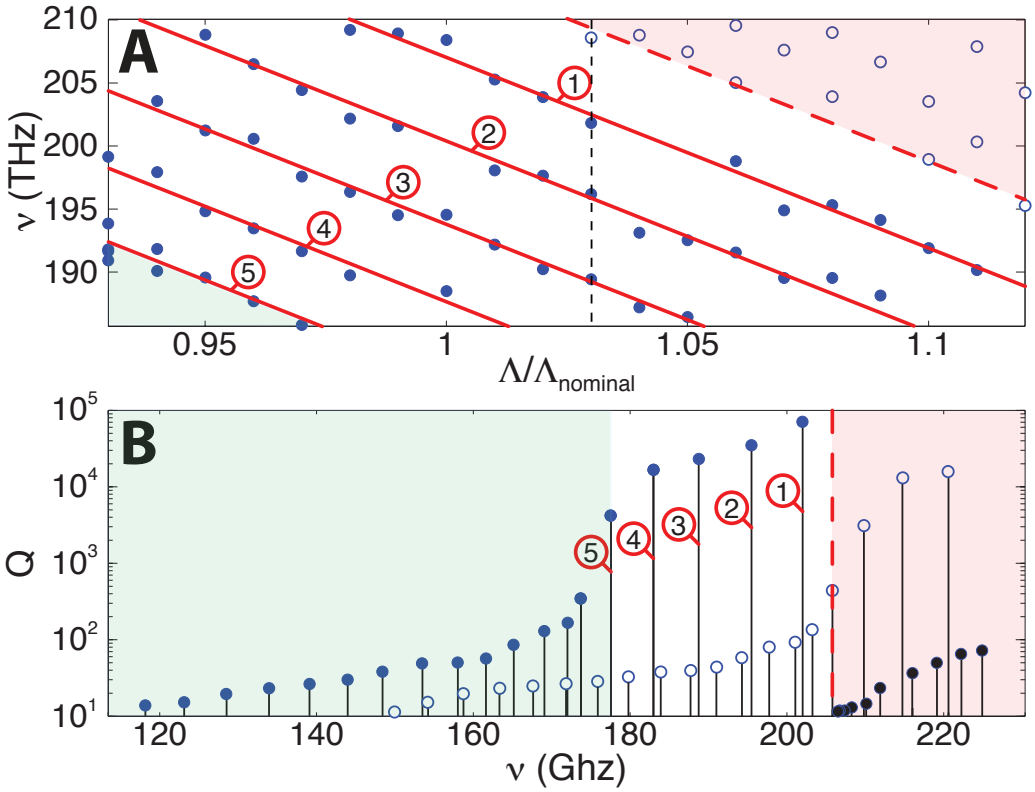


Figure 5.8: **(a)** Optical modes measured in a 200 nm laser wavelength span for a series of 20 devices. **(b)** Simulation of Device 1, which is the device with scaling factor 1.03 (dashed line). Filled blue circles correspond to modes of the fundamental (valence) optical band; the region shaded blue corresponds to frequencies that are no longer within the defect potential barrier hight (i.e. propagating modes). Open blue circles correspond to transverse valence band modes; the pink shaded region shows the edge of the effective optical potential for the transverse valence band modes. Black circles correspond to conduction band modes.

high $Q$ modes (analogous modes of different devices are connected with red lines across different device measurements). Second, the smallest devices show a number of low-$Q$ modes at frequencies below the fifth mode. Finally, at high frequencies, the devices display another set of low-$Q$ modes, which are higher-$Q$ than waveguide-like modes but not as high-$Q$ as the other five modes.

These features are all consistent with the FEM optical model of Device 1. Fig. 5.8(b) shows the simulated modes of Device 1, plotted as a function of their optical $Q$. The simulation shows that the defect confines 5 modes, with a precipitous drop in $Q$ as the modal frequencies exit the defect potential (go below the negative energy barrier

height); the region of frequency space below the negative barrier height is shaded in light blue in Figs. 5.8(a) and (b). The simulation also explains the series of modes higher in frequency, which are *not* the conduction band modes. These modes, indicated with open circles in both Fig. 5.8(a) and 5.8(b) (as opposed to filled) circles, are the Hermite-Gauss ladder of modes with a single node transverse to the direction of propagation ($y$ direction). These modes have a lower effective index, which reduces their radiation-limited $Q$ relative to modes without transverse nodes. The simulated effective optical potential for the transverse optical modes is shown in pink. Conduction band modes (which are not measured due to their very low optical $Q$) are shown as filled black circles.

While the optical information provided by any single device would be difficult to unravel, the measurements of the series of devices coupled with simulation allow us to unambiguously identify the optical spectra of every device in the series.

### 5.14.4 Modeling Mechanical Q

Simulations of an isolated optomechanical crystal nanobeam (hard boundary conditions at the edges) show that the confined modes can couple to modes of longer wavelength, the effect of which is to produce a standing wave within the structure that is not attenuated outside the defect. In the real structures, these long-wavelength modes will travel down the nanobeam and partially reflect at the contacts due to an effective impedance mismatch between the nanobeam and the bulk, with the rest of the power leaving the structure into the bulk. Thus the isolated mode is coupled to a mode with long wavelength but identical frequency that can radiate into the surrounding "bath".

To model the loss due to this resonant coupling to radiative modes, we include a large, semi-circular silicon "pad" on each side of the nanobeam. To make the pad act like a "bath", we introduce a phenomenological imaginary part of the speed of sound in pad region; i.e., $\mathrm{v}_{\mathrm{pad}} \rightarrow \mathrm{v}_{\mathrm{Silicon}}(1 + i\eta)$, where $\mathrm{v} = \sqrt{E/\rho}$. This creates an imaginary part of the frequency, and the mechanical $Q$ can be found by the relation,

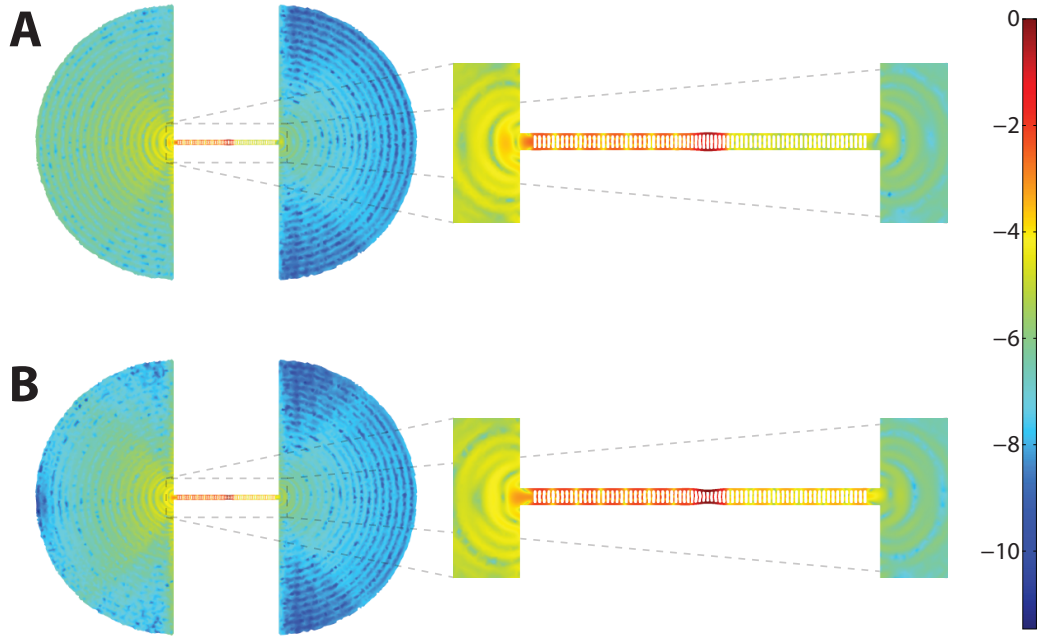


Figure 5.9: **(a)**, In-phase and **(b)**, in-quadrature mechanical displacement field of fundamental breathing mode with absorbing "pad". This simulation includes asymmetries in the structure and correspondingly exhibits an asymmetric radiation pattern in the substrate.

$Q_m = \mathrm{Re}\{\nu_\mathrm{m}\}/(2\mathrm{Im}\{\nu_\mathrm{m}\})$.

By adding loss to the pad material, part of the power reflected at the contacts will be due to the change in the impedance from the absorption. From this point of view, $\eta$ should be made as small as possible, since this contribution to the reflection coefficient is not present in the real system. However, $\eta$ must also be large enough that the self-consistent solution includes a radiated wave that *propagates* for a significant portion of the pad, which only happens if the wave is appreciably attenuated by the time it reflects from the edge of the simulation and returns to the contact. Thus, the pad is made as large as possible, given computational constraints, and the absorption is increased until the $Q_m$ changes appreciably, which gives the threshold value for $\eta$ at which the reflectivity of the contacts has an appreciable contribution from the absorption. The simulation is thus performed with a value of $\eta$ that produces a propagating wave in the pad without causing an artificial reflectivity at the contact; propagation in the pad is easily verified if the position of the nodes/antinodes swap between the

in-phase and in-quadrature parts of the mechanical cycle (the nodes/antinodes of a standing wave are stationary). Figs. 5.9(a) and 5.9(b) show the in-phase and in-quadrature (respectively) parts of the optical cycle, showing a propagating radiative mode in the pad. The simulated values of $Q_m$ can be found in Table 1. Most of the values of mechanical $Q$ calculated this way are in fair agreement with the measured values except for the fifth breathing mode, which, by this method, appears to have a $Q_m$ of over $22,000$; in reality, the $Q$ of this mode may be limited by coupling with a leaky mode caused by defects that are not modeled (such as vertical defects), material losses, or the presence of the taper waveguide.

# Bibliography

[1] M. Eichenfield, R. Camacho, J. Chan, K. J. Vahala, and O. Painter, "A picogram- and nanometre-scale photonic-crystal optomechanical cavity," Nature **459**(7246), 550–555 (2009).

[2] J. Chan, M. Eichenfield, R. Camacho, and O. Painter, "Optical and mechanical design of a "zipper" photonic crystal optomechanical cavity," Opt. Express **17**(5), 3802–3817 (2009).

[3] M. Eichenfield, J. Chan, R. Camacho, K. J. Vahala, and O. Painter, "Optomechanical Crystals," arXiv:0906.1236v1 (2009).

[4] M. Eichenfield, J. Chan, A. Safavi-Naeini, K. Vahala, and O. Painter, "Modeling Dispersive Coupling and Losses of Localized Optical and Mechanical Modes in Optomechanical Crystals," ArXiv:0908.0025v1 (2009).

[5] T. J. Kippenberg and K. J. Vahala, "Cavity Optomechanics," Opt. Express **15**(25), 17172–17205 (2007).

[6] T. J. Kippenberg and K. J. Vahala, "Cavity Optomechanics: Back-Action at the Mesoscale," Science **321**(5893), 1172–1176 (2008).

[7] I. Favero and K. Karrai, "Optomechanics of deformable optical cavities," Nat Photon **3**(4), 201–205 (2009/04//print).

[8] T. Carmon and K. J. Vahala, "Modal Spectroscopy of Optoexcited Vibrations of a Micron-Scale On-Chip Resonator at Greater than 1 GHz Frequency," Phys. Rev. Lett. **98**(22), 123901 (2007).

[9] M. Tomes and T. Carmon, "Photonic Micro-Electromechanical Systems Vibrating at X-band (11-GHz) Rates," Physical Review Letters **102**(11), 113601 (pages 4) (2009).

[10] R. H. O. III and I. El-Kady, "Microfabricated phononic crystal devices and applications," Measurement Science and Technology **20**(1), 012002 (13pp) (2009).

[11] A. Dorsel, J. McCullen, P. Meystre, E. Vignes, and H. Walther, "Optical Bistability and Mirror Confinement Induced by Radiation Pressure," Physical Review Letters **51**(17), 1550–1553 (1983).

[12] H. Rokhsari, T. J. Kippenberg, T. Carmon, and K. J. Vahala, "Radiation-pressure-driven micro-mechanical oscillator," Opt. Express **13**(14), 5293–5301 (2005).

[13] P. B. Deotare, M. W. McCutcheon, I. W. Frank, M. Khan, and M. Lončar, "High quality factor photonic crystal nanobeam cavities," Applied Physics Letters **94**(12), 121106 (pages 3) (2009).

[14] J. D. Joannopoulos, S. G. Johnson, J. N. Winn, and R. D. Meade, *Photonic Crystals: Molding the Flow of Light*, 2nd ed. (Princeton University Press, 2008).

[15] B. A. Auld, *Acoustic Fields and Waves in Solids*, vol. I and II (Wiley-Interscience, New York, 1973).

[16] C. P. Michael, M. Borselli, T. J. Johnson, C. Chrystal, and O. Painter, "An optical fiber-taper probe for wafer-scale microphotonic device characterization," Opt. Express **15**(8), 4745–4752 (2007).

[17] A. W. Snyder and J. D. Love, *Optical Waveguide Theory* (Chapman and Hall, New York, NY, 1983).

[18] H. A. Haus, *Waves and Fields in Optoelectronics*, 1st ed. (Prentice-Hall, Englewood Cliffs, New Jersey, 1984).

[19] S. G. Johnson, M. Ibanescu, M. A. Skorobogatiy, O. Weisberg, J. D. Joannopoulos, and Y. Fink, "Perturbation theory for Maxwell's equations with shifting material boundaries," Phys. Rev. E **65**(6), 066611 (2002).

[20] P. E. Barclay, K. Srinivasan, and O. Painter, "Nonlinear response of silicon photonic crystal microcavities excited via an integrated waveguide and fiber taper," Opt. Express **13**(3), 801–820 (2005).

[21] Q. Lin, X. Jiang, M. Eichenfield, R. Camacho, P. Herring, K. J. Vahala, and O. Painter, "Giant opto-mechanical oscillations actuated by optical gradient forces," (2008). In preparation.

[22] B. Ilic, S. Krylov, K. Aubin, R. Reichenbach, and H. G. Craighead, "Optical excitation of nanoelectromechanical oscillators," Appl. Phys. Lett. **86**, 193114 (2005).

[23] C. Höhberger and K. Karrai, "Cavity cooling of a microlever," **432**(7020), 1002–1005 (2004).

[24] H. J. Metcalf and P. van der Straten, *Laser Cooling and Trapping*, Graduate Texts in Contemporary Physics (Springer, New York, NY, 1999).

[25] A. Schliesser, O. Arcizet, R. Riviere, G. Anetsberger, and T. J. Kippenberg, "Resolved-sideband cooling and position measurement of a micromechanical oscillator close to the Heisenberg uncertainty limit," Nature Physics **5**, 509–514 (2009).

[26] S. Gigan, H. R. Bohm, M. Paternostro, F. Blaser, G. Langer, J. B. Hertzberg, K. C. Schwab, D. Bauerle, M. Aspelmeyer, and A. Zeilinger, "Self-cooling of a micromirror by radiation pressure." Nature **444**(7115), 67–70 (2006).

[27] A. Schliesser, P. Del'Haye, N. Nooshi, K. J. Vahala, and T. J. Kippenberg, "Radiation pressure cooling of a micromechanical oscillator using dynamical backaction." Phys Rev Lett **97**(24), 243905 (2006).

[28] T. Corbitt, C. Wipf, T. Bodiya, D. Ottaway, D. Sigg, N. Smith, S. Whitcomb, and N. Mavalvala, "Optical Dilution and Feedback Cooling of a Gram-Scale Oscillator to 6.9 mK," Phys. Rev. Lett. **99**, 160801 (2007).

[29] J. D. Thompson, B. M. Zwickl, A. M. Jayich, F. Marquardt, S. M. Girvin, and J. G. E. Harris, "Strong dispersive coupling of a high-finesse cavity to micromechanical membrane," Nature **452**(6), 72–75 (2008).

[30] A. Schliesser, R. Riviere, G. Anetsberger, O. Arcizet, and T. J. Kippenberg, "Resolved-sideband cooling of a micromechanical oscillator," Nature Phys. **4**, 415–419 (2008).

[31] C. A. Regal, J. D. Tuefel, and K. W. Lehnert, "Measuring nanomechanical motion with a microwave cavity interferometer," Nature Phys. **4**, 555–560 (2008).

[32] T. D. Stowe, K. Yasumura, T. W. Kenny, D. Botkin, K. Wago, and D. Rugar, "Attonewton force detection using ultrathin silicon cantilevers," Appl. Phys. Lett. **71**(2), 288–290 (1997).

[33] M. L. Povinelli, M. Loncar, M. Ibanescu, E. J. Smythe, S. G. Johnson, F. Capasso, and J. D. Joannopoulos, "Evanescent-wave bonding between optical waveguides," Opt. Lett. **30**(22), 3042–3044 (2005).

[34] M. Notomi, H. Taniyama, S. Mitsugi, and E. Kuramochi, "Optomechanical Wavelength and Energy Conversion in High-$Q$ Double-Layer Cavities of Photonic Crystal Slabs," Phys. Rev. Lett. **97**, 023903 (2006).

[35] J. S. Foresi, P. R. Villeneuve, J. Ferrera, E. R. Thoen, G. Steinmeyer, S. Fan, J. D. Joannopoulos, L. C. Kimerling, H. I. Smith, and E. P. Ippen, "Photonic-Bandgap microcavities in optical waveguides," Nature **390**, 143–145 (1997).

[36] C. Sauvan, P. Lalanne, and J. P. Hugonin, "Slow-wave effect and mode-profile matching in photonic crystal microcavities," Phys. Rev. B **71**, 165118 (2005).

[37] A. R. Md Zain, N. P. Johnson, M. Sorel, and R. M. De La Rue, "Ultra high quality factor one-dimensional photonic crystal/photonic wire micro-cavities in silicon-on-insulator (SOI)," Opt. Express **16**(16), 12084–12089 (2008).

[38] P. Velha, J. C. Rodier, P. Lalanne, J. D. Hugonin, D. Peyrade, E. Picard, T. Charvolin, and E. Hadji, "Ultracompact silicon-on-insulator ridge-waveguide mirrors with high reflectance," Appl. Phys. Lett. **89**, 171121 (2006).

[39] M. Notomi, E. Kuramochi, and H. Taniyama, "Ultrahigh-Q Nanocavity with 1D Photonic Gap," Opt. Express **16**(15), 11905–11102 (2008).

[40] M. W. McCutcheon and M. Loncar, "Design of a silicon nitride photonic crystal nanocavity with a Quality factor of one million for coupling to a diamond nanocrystal," Opt. Express **16**(23), 19136–19145 (2008).

[41] O. Painter, K. Srinivasan, and P. E. Barclay, "A Wannier-like equation for photon states of locally perturbed photonic crystals," Phys. Rev. B **68**, 035214 (2003).

[42] P. E. Barclay, K. Srinivasan, O. Painter, B. Lev, and H. Mabuchi, "Integration of fiber-coupled high-$Q$ $SiN_x$ microdisks with atom chips," Appl. Phys. Lett. **89**(13), 131108 (2006).

[43] S. S. Verbridge, J. M. Parpia, R. B. Reichenbach, L. M. Bellan, and H. G. Craighead, "High quality factor resonance at room temperature with nanostrings under high tensile stress," **99**, 124304 (2006).

[44] S. S. Verbridge, H. G. Craighead, and J. M. Parpia, "A megahertz nanomechanical resonator with room temperature quality factor over a million," Appl. Phys. Lett. **92**, 013112 (2008).

[45] MIT Photonic Bands (MPB) is a free software package for the solution of the electromagnetic eigenmodes of periodic structures. MPB has been developed at MIT, http://ab-initio.mit.edu/wiki/index.php/MPB.

[46] COMSOL is a multiphysics software package for performing finite-element-method (FEM) simulations. See COMSOL AB, http://www.comsol.com/. We use the COMSOL multiphysics software package to perform both optical and mechanical numerical simulations of the zipper cavity.

[47] Lumerical FDTD Solutions is a finite-difference time-domain software package for performing electromagnetic simulations. See Lumerical Solutions, Inc., http://www.lumerical.com/.

[48] J. T. Robinson, C. Manolatou, L. Chen, and M. Lipson, "Ultrasmall Mode Volumes in Dielectric Optical Microcavities," Phys. Rev. Lett. **95**, 143901 (2005).

[49] M. Pinard and Y. Hadjar and A. Heidmann, "Effective mass in quantum effects of radiation pressure," Eur. Phys. J. D **7**, 107–116 (1999).

[50] S. G. Johnson, M. Ibanescu, M. A. Skorobogatiy, O. Weisberg, J. D. Joannopoulos, and Y. Fink, "Perturbation theory and Maxwell's equations with shifting material boundaries," Phys. Rev. E **65**, 066611 (2002).

[51] P. Meystre, E. M. Wright, J. D. McCullen, and E. Vignes, "Theory of radiation-pressure-driven interferometers," J. Opt. Soc. Am. B **2**(11), 1830–1840 (1985).

[52] M. Hossein-Zadeh and K. J. Vahala, "Observation of optical spring effect in a microtoroidal optomechanical resonator," Opt. Lett. **32**(12), 1611–1613 (2007).

[53] B. S. Sheard, M. B. Gray, C. M. Mow-Lowry, D. E. McClelland, and S. E. Whitcomb, "Observation and characterization of an optical spring," Phys. Rev. A **69**, 051801(R) (2004).

[54] O. Arcizet, P.-F. Cohadon, T. Briant, M. Pinard, and A. Heidmann, "Radiation-pressure cooling and optomechanical instability of a micromirror." Nature **444**(7115), 71–74 (2006).

[55] R. H. O. III and I. El-Kady, "Microfabricated phononic crystal devices and applications," Meas. Sci. Technol. **20**, 012002 (2008).

[56] A. Gruber, A. Dräbenstedt, C. Tietz, L. Fleury, J. Wratchtrup, and C. v. Borczyskowski, "Scanning confocal optical microscopy and magnetic resonance on single defect centers," Science **276**, 2012–2014 (1997).

[57] C. Santori, P. Tamarat, P. Neumann, J. Wrachtrup, D. Fattal, R. G. Beausoleil, J. Rabeau, P. Olivero, A. D. Greentree, S. Prawer, F. Jelezko, and P. Hemmer, "Coherent Population Trapping of Single Spins in Diamond under Optical Excitation," Phys. Rev. Lett. **97**(24), 247401 (2006).

[58] F. Jelezko, T. Gaebel, I. Popa, M. Domhan, A. Gruber, and J. Wrachtrup, "Observation of Coherent Oscillation of a Single Nuclear Spin and Realization of a Two-Qubit Conditional Quantum Gate," Phys. Rev. Lett. **93**(13), 130501 (2004).

[59] M. V. G. Dutt, L. Childress, L. Jiang, E. Togan, J. Maze, F. Jelezko, A. S. Zibrov, P. R. Hemmer, and M. D. Lukin, "Quantum Register Based on Individual Electronic and Nuclear Spin Qubits in Diamond," Science **316**(5829), 1312–1316 (2007).

[60] L. Childress, M. V. Gurudev Dutt, J. M. Taylor, A. S. Zibrov, F. Jelezko, J. Wrachtrup, P. R. Hemmer, and M. D. Lukin, "Coherent Dynamics of Coupled Electron and Nuclear Spin Qubits in Diamond," Science **314**(5797), 281–285 (2006).

[61] A. Beveratos, R. Brouri, T. Gacoin, J.-P. Poizat, and P. Grangier, "Nonclassical radiation from diamond nanocrystals," Phys. Rev. A **64**(6), 061802 (2001).

[62] S. Kühn and C. Hettich and C. Schmitt and J-PH. Poizat and V. Sandoghdar, "Diamond colour centres as a nanoscopic light source for scanning near field microscopy," J. Microsc. **202**(1), 2–6 (2001).

[63] S. Schietinger, T. Schroder, and O. Benson, "One-by-One Coupling of Single Defect Centers in Nanodiamonds to High-Q Modes of an Optical Microresonator," **8**(11), 3911–3915 (2008).

[64] P. E. Barclay, O. Painter, C. Santori, K.-M. Fu, and R. G. Beausoleil, "Coherent interference effects in a nano-assembled optical cavity-QED system," ArXiv:0812.4505 (2008).

[65] P. T. Rakich, M. A. Popovic, M. Soljacic, and E. P. Ippen, "Trapping, coralling and spectral bonding of optical resonances through optically induced potentials," Nature Photonics **1**(11), 658–665 (2007).

[66] M. Hossein-Zadeh and K. J. Vahala, "Photonic RF Down-Converter Based on Optomechanical Oscillation," IEEE Photonics Tech. Lett. **20**(4), 234–236 (2008).

[67] M. Eichenfield, C. P. Michael, R. Perahia, and O. Painter, "Actuation of Micro-Optomechanical Systems Via Cavity-Enhanced Optical Dipole Forces," Nature Photonics **1**(7) (2007).

[68] M. Li, W. H. P. Pernice, C. Xiong, T. Baehr-Jones, M. Hochberg, and H. X. Tang, "Harnessing optical forces in integrated photonic cicruits," Nature **456**(27), 480–484 (2008).

[69] A. Ashkin, "Histroy of Optical Trapping and Manipulation of Small-Neutral Particle, Atoms, and Molecules," IEEE J. Quan. Elec. **6**(6), 841–856 (2000).

[70] R. Miller, T. E. Northup, K. M. Birnbaum, A. Boca, A. D. Boozer, and H. J. Kimble, "Trapped atoms in cavity QED: coupling quantized light and matter," J. Phys. B: At. Mol. Opt. Phys. **38**(4), S551–S565 (2005).

[71] K. Srinivasan, P. E. Barclay, M. Borselli, and O. Painter, "An optical fiber-based probe for photonic crystal microcavities," IEEE J. on Sel. Area. in Comm. **23**(7), 1321–1329 (2005).

[72] B.-S. Song, S. Noda, T. Asano, and Y. Akahane, "Ultra-high-Q photonic double-heterostructure nanocavity," Nature Materials **4**, 207–210 (2005).

[73] S. S. Verbridge, R. Illic, H. G. Craighead, and J. M. Parpia, "Size and frequency dependent gas damping of nanomechanical resonators," Appl. Phys. Lett. **93**, 013101 (2008).

[74] M. Borselli, T. J. Johnson, and O. Painter, "Meausring the role of surface chemistry in silicon microphotonics," Appl. Phys. Lett. **88**, 13114 (2006).

[75] F. Marquardt, J. G. E. Harris, and S. M. Girvin, "Dynamical Multistability Induced by Radiation Pressure in High-Finesse Micromechanical Optical Cavities," Phys. Rev. Lett. **96**(10), 103901 (2006).

[76] J. B. Starr, "Squeeze-film damping in solid-state accelerometers," Techn. Digest IEEE Solid State Sensor and Acuator Workshop (Hilton Head Island, SC, 1990) pp. 44–47 (1990).

[77] M. Maldovan and E. L. Thomas, "Simultaneous localization of photons and phonons in two-dimensional periodic structures," Applied Physics Letters **88**(25), 251907 (pages 3) (2006).

[78] M. Trigo, A. Bruchhausen, A. Fainstein, B. Jusserand, and V. Thierry-Mieg, "Confinement of Acoustical Vibrations in a Semiconductor Planar Phonon Cavity," Phys. Rev. Lett. **89**(22), 227402 (2002).

[79] M. S. Kang, A. Nazarkin, A. Brenn, and P. S. J. Russell, "Tightly trapped acoustic phonons in photonic crystal fibres as highly nonlinear artificial Raman oscillators," Nat Phys **5**(4), 276–280 (2009).

[80] O. Painter, R. K. Lee, A. Yariv, A. Scherer, J. D. O'Brien, P. D. Dapkus, and I. Kim, "Two-dimensional photonic band-gap defect mode laser," Science **284**, 1819–1824 (1999).

[81] O. Arcizet, P.-F. Cohadon, T. Briant, M. Pinard, A. Heidmann, J. M. Mackowski, C. Michel, L. Pinard, O. Francais, and L. Rousseau, "High-Sensitivity Optical Monitoring of a Micromechanical Resonator with a Quantum-Limited Optomechanical Sensor," Phys. Rev. Lett. **97**, 133601 (2006).

[82] I. Tittonen, G. Breitenbach, T. Kalkbrenner, T. Müller, R. Conradt, S. Schiller, E. Steinsland, N. Blanc, and N. F. de Rooij, "Interferometric measurements of the position of a macroscopic body: Towards observation of quantum limits," Phys. Rev. A **59**(2), 1038–1044 (1999).

[83] V. B. Braginskiĭ, F. Y. Khalili, and K. S. Thorne, *Quantum measurement* (Cambridge University Press, Cambridge, 1992).

[84] V. Braginsky and S. P. Vyachanin, "Low quantum noise tranquilizer for Fabry Perot interferometer," Physics Letters A **293**(5-6), 228–234 (2002).

[85] D. Kleckner and D. Bouwmeester, "Sub-kelvin optical cooling of a micromechanical resonator." Nature **444**(7115), 75–78 (2006).

[86] V. B. Braginsky, S. E. Strigin, and S. P. Vyatchanin, "Parametric oscillatory instability in Fabry-Perot interferometer," Physics Letters A **287**(5-6), 331 – 338 (2001).

[87] T. J. Kippenberg, H. Rokhsari, T. Carmon, A. Scherer, and K. J. Vahala, "Analysis of radiation-pressure induced mechanical oscillation of an optical microcavity." Phys. Rev. Lett. **95**(3), 033901 (2005).

[88] K. J. Vahala, "Back-action limit of linewidth in an optomechanical oscillator," Physical Review A (Atomic, Molecular, and Optical Physics) **78**(2), 023832 (pages 4) (2008).

[89] Y.-C. Wen, L.-C. Chou, H.-H. Lin, V. Gusev, K.-H. Lin, and C.-K. Sun, "Efficient generation of coherent acoustic phonons in (111) InGaAs/GaAs multiple quantum wells through piezoelectric effects," Applied Physics Letters **90**(17), 172102 (pages 3) (2007).

[90] N. D. Lanzillotti-Kimura, A. Fainstein, A. Huynh, B. Perrin, B. Jusserand, A. Miard, and A. Lemaitre, "Coherent Generation of Acoustic Phonons in an Optical Microcavity," Physical Review Letters **99**(21), 217405 (pages 4) (2007).

[91] R. H. O. III, I. F. El-Kady, M. F. Su, M. R. Tuck, and J. G. Fleming, "Microfabricated VHF acoustic crystals and waveguides," Sensors and Actuators A: Physical **145-146**, 87 – 93 (2008).

[92] J. V. Sánchez-Pérez, D. Caballero, R. Mártinez-Sala, C. Rubio, J. Sánchez-Dehesa, F. Meseguer, J. Llinares, and F. Gálvez, "Sound Attenuation by a Two-Dimensional Array of Rigid Cylinders," Phys. Rev. Lett. **80**(24), 5325–5328 (1998).

[93] W. M. Robertson and J. F. R. III, "Measurement of acoustic stop bands in two-dimensional periodic scattering arrays," The Journal of the Acoustical Society of America **104**(2), 694–699 (1998).

[94] A. Khelif, B. Djafari-Rouhani, J. O. Vasseur, and P. A. Deymier, "Transmission and dispersion relations of perfect and defect-containing waveguide structures in phononic band gap materials," Phys. Rev. B **68**(2), 024302 (2003).

[95] A. Dorsel, J. McCullen, P. Meystre, E. Vignes, and H. Walther, "Optical Bistability and Mirror Confinement Induced by Radiation Pressure," Phys. Rev. Lett. **51**(17), 1550–1553 (1983).

[96] MIT Photonic Bands (MPB) is a free software package for the solution of the electromagnetic eigenmodes of periodic structures. MPB has been developed at MIT, http://ab-initio.mit.edu/wiki/index.php/MPB.

[97] COMSOL is a multiphysics software package for performing finite-element-method (FEM) simulations. See COMSOL AB, http://www.comsol.com/. We use the COMSOL multiphysics software package to perform both optical and mechanical numerical simulations of the optomechanical crystal systems.

[98] K. Srinivasan and O. Painter, "Momentum space design of high-Q photonic crystal optical cavities," Opt. Express **10**(15), 670–684 (2002).

[99] P. B. Deotare, M. W. McCutcheon, I. W. Frank, M. Khan, and M. LonCar, "Coupled photonic crystal nanobeam cavities," Applied Physics Letters **95**(3), 031102–3 (2009).

[100] T. Gorishnyy, J.-H. Jang, C. Koh, and E. L. Thomas, "Direct observation of a hypersonic band gap in two-dimensional single crystalline phononic structures," Applied Physics Letters **91**(12), 121915 (pages 3) (2007).

[101] M. S. Kushwaha, P. Halevi, L. Dobrzynski, and B. Djafari-Rouhani, "Acoustic band structure of periodic elastic composites," Phys. Rev. Lett. **71**(13), 2022–2025 (1993).

[102] F. R. Montero de Espinosa, E. Jiménez, and M. Torres, "Ultrasonic Band Gap in a Periodic Two-Dimensional Composite," Phys. Rev. Lett. **80**(6), 1208–1211 (1998).

[103] A. Cleland, *Foundations of Nanomechanics* (Springer-Verlag, 2003).

[104] H. Kolsky, *Stress waves in solids* (Dover Publications, Inc., 1963).

[105] B. H. Houston, D. M. Photiadis, M. H. Marcus, J. A. Bucaro, X. Liu, and J. F. Vignola, "Thermoelastic loss in microscale oscillators," Applied Physics Letters **80**(7), 1300–1302 (2002).

[106] Y. Yi, "Geometric effects on thermoelastic damping in MEMS resonators," Journal of Sound and Vibration **309**(3-5), 588 – 599 (2008).

[107] A. Duwel, J. Gorman, M. Weinstein, J. Borenstein, and P. Ward, "Experimental study of thermoelastic damping in MEMS gyros," Sensors and Actuators A: Physical **103**(1-2), 70 – 75 (2003).

[108] R. Lifshitz and M. L. Roukes, "Thermoelastic damping in micro- and nanomechanical systems," Physical Review B **61**(8) (2000).

[109] L. Landau and G. Rumer, "On the absorption of sound in solids," Phys. Zeit. Sowjet. **11**(18) (1937).

[110] W. Fon, K. C. Schwab, J. M. Worlock, and M. L. Roukes, "Phonon scattering mechanisms in suspended nanostructures from 4 to 40 K," Physical Review B **66**(4) (2002).

[111] T. A. Read, "The Internal Friction of Single Metal Crystals," Physical Review **58**(4) (1940).

[112] D. Bindel and S. Govindjee, "Elastic PMLs for resonator anchor loss simultaion," Tech report UCB/SEMM-2005/01. Submitted to IJNME **64**(6), 789–818 (2005).

[113] M. Maldovan and E. Thomas, "Simultaneous complete elastic and electromagnetic band gaps in periodic structures," Appl. Phys. B **83**(4), 595–600 (2006).

[114] S. Mohammadi, A. A. Eftekhar, and A. Adibi, "Large Simultaneous Band Gaps for Photonic and Phononic Crystal Slabs," in *Conference on Lasers and Electro-Optics/Quantum Electronics and Laser Science Conference and Photonic Applications Systems Technologies*, p. CFY1 (Optical Society of America, 2008).

[115] E. Yablonovitch, "Inhibited Spontaneous Emission in Solid-State Physics and Electronics," Phys. Rev. Lett. **58**(20), 2059–2062 (1987).

[116] R. F. Cregan, B. J. Mangan, J. C. Knight, T. A. Birks, P. S. J. Russell, P. J. Roberts, and D. C. Allan, "Single-mode photonic band gap guidance of light in air," Science **285**, 1537–1539 (1999).

[117] M. Notomi, K. Yamada, A. Shinya, J. Takahashi, C. Takahashi, and I. Yokohama, "Extremely Large Group-Velocity Dispersion of Line-Defect Waveguides in Photonic Crystal Slabs," Phys. Rev. Lett. **87**(25), 253902 (2001).

[118] Y. Akahane, T. Asano, B.-S. Song, and S. Noda, "Fine-tuned high-Q photonic-crystal nanocavity," Opt. Express **13**(4), 1202–1214 (2005).

[119] M. Soljačić, S. G. Johnson, S. Fan, M. Ibanescu, E. Ippen, and J. D. Joannopoulos, "Photonic-crystal slow-light enhancement of nonlinear phase sensitivity," J. Opt. Soc. Am. B **19**(9), 2052–2059 (2002).

[120] S. J. McNab, N. Moll, and Y. A. Vlasov, "Ultra-low loss photonic integrated circuit with membrane-type photonic crystal waveguides," Optics Express **11**(22), 2927–2939 (2003).

[121] M. S. Kang, A. Nazarkin, A. Brenn, and P. S. J. Russell, "Tightly trapped acoustic phonons in photonic crystal fibres as highly nonlinear artificial Raman oscillators," Nature Physics **5**, 276–280 (2009).

[122] P. Mohanty, D. A. Harrington, K. L. Ekinci, Y. T. Yang, M. J. Murphy, and M. L. Roukes, "Intrinsic dissipation in high-frequency micromechanical resonators," Phys. Rev. B **66**, 085416 (2002).

[123] D. Weinstein and S. A. Bhave, "Internal Dielectric Transduction of a 4.5 GHz Silicon Bar Resonator," IEEE Int. Electron Devices Meeting pp. 415–418 (2007).

[124] O. Arcizet, P.-F. Cohadon, T. Briant, M. Pinard, and A. Heidmann, "Radiation-pressure cooling and optomechanical instability of a micromirror." Nature **444**(7115), 71–74 (2006).

[125] S. Groblacher, J. B. Hertzberg, M. R. Vanner, G. D. Cole, S. Gigan, K. C. Schwab, and M. Aspelmeyer, "Demonstration of an ultracold micro-optomechanical oscillator in a cryogenic cavity," Nature Physics **5**, 485–488 (2009).

[126] Y. T. Yang, C. Callegari, X. L. Feng, K. L. Ekinci, and M. L. Roukes, "Zeptogram-Scale Nanomechanical Mass Sensing," Nano Letters **6**(4), 583–386 (2006).

[127] K. J. Vahala, "Back-action limit of linewidth in an optomechanical oscillator," Phys. Rev. A **78**(2), 023832 (2008).